Modeling and simulation of guided waves propagation in elastic mediums in the presence of uncertainties : Application to ultrasonic characterization

Antoisse Abdoulatuf

UNIVERSITÉ PARIS-EST

UNIVERSITÉ PARIS-EST

École Doctorale Sciences, Ingénierie et Environnement

THÈSE

présentée par

Antoisse ABDOULATUF

pour l'obtention du grade de

Docteur de l'Université Paris-Est

Spécialité : Sciences de l'Ingénieur

Sujet de la thèse :

Modélisation et simulation de la propagation d'ondes guidées dans des milieux élastiques en présence d'incertitudes.

Application à la caractérisation ultrasonore.

soutenue publiquement le 11 juillet 2017.

Composition du jury :

M. Christophe DESCELIERS	Professeur, Université Paris-Est Marne-la-Vallée	Président
M. Marc DESCHAMPS	Directeur de recherche CNRS, Université de Bordeaux 1	Rapporteur
M. Anas BATOU	Associate Professor, HDR, University of Liverpool (UK)	Rapporteur
Mme. Cécile BARON	Chargée de recherche CNRS, Université Aix Marseille	Examinatrice
M. Salah NAILI	Professeur, Université Paris-Est Créteil	Co-directeur de thèse
M. Vu-Hieu NGUYEN	Maître de conférences, HDR, Université Paris-Est Créteil	Co-directeur de thèse

Laboratoire Modélisation et Simulation Multi Echelle, MSME UMR 8208 CNRS, Université Paris-Est, 61, avenue du Général de Gaulle, 94010 Créteil Cedex - FRANCE

Version 1.0 - 28 juillet 2017

UNIVERSITÉ PARIS-EST
Communauté d'Universités et Établissements
UNIVERSITÉ PARIS-EST
ÉCOLE DOCTORALE UNIVERSITÉ PARIS-EST
Sciences, Ingénierie et Environnement

THESIS

submitted by

Antoisse ABDOULATUF

for the grade of

Doctor of Philosophy

Major : Engineering Sciences

Subject of thesis:

Modeling and simulation of guided waves propagation in elastic media with presence of uncertainties.

Application to ultrasonic characterization.

publicly defended July 11, 2017.

Composition of the jury:

Mr. Christophe DESCELIERS	Professor, Université Paris-Est Marne-la-Vallée	President
Mr. Marc DESCHAMPS	Directeur de recherche CNRS, Université de Bordeaux 1	Reviewer
Mr. Anas BATOU	Associate Professor, HDR, University of Liverpool (UK)	Reviewer
Ms. Cécile BARON	Chargée de recherche CNRS, Université Aix Marseille	Examiner
Mr. Salah NAILI	Professor, Université Paris-Est Créteil	PhD Co-Supervisor
Mr. Vu-Hieu NGUYEN	Maître de conférences, HDR, Université Paris-Est Créteil	PhD Co-Supervisor

Laboratoire Modélisation et Simulation Multi Echelle, MSME UMR 8208 CNRS, Université Paris-Est,
61, avenue du Général de Gaulle, 94010 Créteil Cedex - FRANCE

MSME Laboratoire Modélisation et Simulation Multi Echelle — cnrs

Version 1.0 - July 28, 2017

Une pensée plus profonde pour toi maman.

Je dédie cette thèse à la mémoire de ma mère. Nous ne t'oublierons jamais

Il y a dans la création des cieux et de la terre et dans la succession de la nuit et du jour, des signes pour ceux qui sont doués d'intelligence.

إِنَّ فِي خَلْقِ السَّمَاوَاتِ وَالْأَرْضِ وَاخْتِلَافِ اللَّيْلِ وَالنَّهَارِ لَآيَاتٍ لِّأُولِي الْأَلْبَابِ

[Coran ; Sourate 3 (La Famille d'imrân) verset 190]

Remerciements

"Il faut toujours remercier l'arbre à karité sous lequel on a ramassé de bons fruits pendant la bonne saison ."
[Ahmadou Kourouma]

Je tiens tout d'abord à exprimer toute ma reconnaissance à mes directeurs de thèse pour m'avoir proposé ce sujet de thèse et m'avoir encadré durant ces années de thèse. J'ai apprécié en outre leurs connaissances, leur disponibilité constante, leur rigueur, et la grande liberté qu'ils m'ont laissée au cours de ces années de recherches.

Merci au Professeur Salah NAILI, directeur du Laboratoire Modélisation et Simulation Multi Echelle, UMR CNRS 8208, pour m'avoir accueilli dans son laboratoire et fait confiance. Grâce à vous, j'ai pu réaliser mes travaux de M2 et ensuite de doctorat dans d'excellentes conditions. Merci d'avoir toujours favorisé mon travail de laboratoire et su trouver les ressources indispensables à cette recherche.

Merci à Vu-Hieu NGUYEN d'avoir écouté toutes mes questions, mes doutes, et d'avoir remis tant de mes réponses en questions. Nos discussions sont la clé de voûte des modèles développés durant ma thèse. Je ne me souviens pas d'être sorti de ton bureau sans au moins une ébauche de solution.

Mes remerciements vont ensuite aux membres du jury pour avoir accepté d'examiner et rapporter mes travaux de thèse en pleine période estivale. Je suis tout particulièrement reconnaissant à Marc DESCHAMPS et Anas BATOU d'avoir accepté d'être les rapporteurs de cette thèse. Merci pour vos commentaires constructifs et particulièrement pertinents sur le manuscrit.

Je tiens par ailleurs à remercier l'ensemble des personnes au sein du laboratoire ou de la faculté qui, d'une façon ou d'une autre, ont contribué à l'aboutissement de cette thèse. Un grand merci aux administratrices, secrétaires et personnel technique qui m'ont rendu de fiers services durant ces années. Merci à Henriette Peyrat, Isabelle BRIÉ–PATAKY, Didier BOTON et Isabelle JEANNARD pour leur aide précieuse.

Merci à Hung-Son PHAN sans qui le laboratoire ne pourrait pas fonctionner. Merci pour ton sens de l'humour et du juste mot, et d'être par ailleurs toujours disponible pour dissoudre mes soucis informatiques. Ce fut un bonheur, également, de partager avec toi ces discussions qui dépassaient le strict cadre du travail.

Je poursuis mes remerciements en saluant mes collègues thésards et autres post-docs que j'ai eu la chance de côtoyer durant ces années: Romain (mon confident), Adrien, Sarah, Seraphin, Davide, Son, Erica, Ilaria et Madge... À ceux qui ont déjà soutenu leur thèse, je leur souhaite un avenir radieux. Au reste des doctorant.e.s, beaucoup de courage. Je tiens aussi à remercier tous les membres du laboratoire MSME (permanents, post-docs, thésards, stagiaires) que je n'ai pas cités et que j'ai eu le plaisir de côtoyer.

En parallèle de mes travaux de recherche, j'ai effectué une mission d'enseignement de plus de 3 ans à la faculté des sciences et technologie de l'Université Paris-Est Créteil (UPEC). Je voudrais remercier l'ensemble des collègues avec lesquels j'ai collaboré pour les enseignements, de m'avoir dès le début considéré comme un collègue à part entière. J'ai aussi une pensée pour les étudiants que j'ai eu l'occasion d'encadrer. Ils m'ont un peu distrait de mes calculs quotidiens et m'ont obligé à prendre du recul, à ré-expliquer et re-comprendre des concepts, un peu différemment, un peu mieux.

———

Je conclurai par des remerciements plus personnels en saluant mes compatriotes, ami.e.s et membres de ma famille qui m'ont fait l'honneur d'assister à ma soutenance de thèse. Dans un contexte de grandes vacances, synonyme de jobs étudiants pour les uns et de voyage ou repos pour les autres, vous avez répondu présent. Merci du fond du cœur pour votre présence.

Mes pensées vont à ceux qui ont veillé sur moi depuis toujours, ceux qui m'ont fait confiance, qui m'ont soutenu sans faille dans tous mes projets et qui ont accepté mes choix sans pour autant toujours forcément les comprendre, merci à toute ma famille au sens large (mes parents et grands parents, mes frères et sœurs, mes cousins et cousines, mes neveux et nièces, ma femme et mes enfants) et mes ami.e.s pour leurs encouragements et soutiens.

Merci aux petits frères Boinaidi (ou "billo"), Alfane et Abbas pour vos encouragements. Je remercie aussi mes grands frères de m'avoir aidé financièrement pendant mon cursus scolaire. Merci à Abdourahim (ou "Bill") pour ton soutien, Ahmed (ou "Gerard") pour ton autorité, et Ali ("Ali physique" ou ingénieur selon le contexte) pour tes conseils. Merci à Chofera pour ta présence à la soutenance avec Soifia malgré la grossesse avancée. Merci à Nassur, Salami (ou Nizam) et Vendredi pour votre soutien.

Mes remerciements s'adressent aussi à Stella HUMBLOT, de m'avoir hébergé gratuitement à mon arrivé en France, et aidé administrativement à venir poursuivre mes études dans l'hexagone.

Même s'il y a peu de chances qu'ils lisent ces lignes, je tiens à témoigner ma profonde reconnaissance aux médecins des différents hôpitaux français (de Nice à Paris) où j'ai été hospitalisé pendant ma première année de thèse, ainsi qu'aux infirmiers et aides-soignants, pour leur travail remarquable et leur professionnalisme. J'estime qu'ils m'ont sauvé la vie, et, donc participé à l'aboutissement de mes travaux.

Mes dernières pensées vont à mes parents sans qui rien de tout cela n'aurait été possible. Je pense que c'est grâce à l'éducation que vous nous avez donnée à mes frères et moi que je suis arrivé jusqu'ici. C'est le premier doctorat de la famille, et, je suis résolument convaincu que ce n'est que le début. Merci papa, merci maman. Cette thèse je la dédie à la mémoire de ma mère. Nous ne t'oublierons jamais. Je la dédie à toi aussi papa. Tu as veillé sur moi jour et nuit pendant les périodes difficiles, et ce, malgré la

distance. Merci pour tes prières. Je tiens par ailleurs à te dire que je sais combien tu étais inquiet quand on t'a informé de mes soucis de santé (quelques mois après une inscription en thèse). Tes conseils, ton sens du dialogue et ton soutien inébranlable m'ont donné l'espoir et le courage de vaincre la maladie pour arriver à cette belle réussite. Je n'oublierai jamais cette expression, « Na msomé », devenue le préambule de nos réunions. Papa, tu as réussi! Nous avons tous réussi. C'est tout à ton honneur. Merci papa.

Enfin, le dernier mais non le moindre, je tiens à remercier ma femme Nissioita Said Omar (ou "Niss" pour les familiers). Je la remercie de tout mon cœur pour son soutien inlassable et sa présence à mes cotés pendant les moments les plus difficiles. Merci pour tout le bonheur qu'elle m'apporte. Je tiens à lui tirer également un coup de chapeau pour son abnégation et son courage puisqu'elle a relu mon manuscrit plein d'équations et de symboles incompréhensibles, chose ardue vous l'imaginez lorsque l'on est comptable et infirmière de formation. Cette thèse est aussi la sienne pour ses efforts et sacrifices. Merci aussi à ma belle famille.

Mon cursus scolaire aura été probablement l'un des plus beaux chapitres de ma vie. J'aimerais remercier celles et ceux qui d'une manière ou d'une autre ont participé à son écriture. Merci à celles et ceux qui m'ont été à mes débuts.

À celles et ceux qui iront plus loin que ces quelques lignes, je souhaite une très bonne lecture.

Antoisse Abdoulatuf

Juillet 2017

Table of Contents

Notation and table of symbols

The following list gathers the symbols and acronyms that are often used in this book. The number of the page on which a notation appears for the first time in the document is shown.

Global acronyms

AGW	Axial Guided Waves	p. 102
AT	Axial Transmission	p. 5
BMD	Bone Mineral Density	p. 5
BUA	Broadband Ultrasound Attenuation	p. 59
CGW	Circumferential Guided Waves	p. 102
CND	Contrôle Non-Destructif	p. 1
DOF	Degree Of Freedom	p. 64
DXA	Dual-Energy X-ray Absorptiometry	p. 5
FAS	First Arrival Signal	p. 59
FEM	Finite Element Method	p. 22
FGM	Functionally Graded Material	p. 33
GLW	Guided Lamb Waves	p. 59
MRI	Magnetic Resonance Imaging	p. 5
NDT	Non-Destructive Techniques	p. 59
PDF	Probability Density Functions	p. 108
QUS	Quantitative Ultrasound	p. 5

SAFE	Semi-Analytical Finite Element	p. 7
SAS	Second Arrival Signal	p. 59
SGW	Slow Guided Wave	p. 59
SOS	Speed Of Sound	p. 59

Global notations

$\mathbb{C}$	The set of complex numbers	p. 22
$\mathbb{R}$	The set of real numbers	p. 24
$\mathcal{R}(O;\mathbf{e}_1,\mathbf{e}_2,\mathbf{e}_3)$	be the Cartesian reference frame	p. 18
$\mathcal{R}(O;\mathbf{e}_r,\mathbf{e}_\theta,\mathbf{e}_z)$	Cylindrical reference system	p. 95

Mathematical operators

∂_i and ∂_i^2	partial derivatives of first and second operators	p. 96
$\int$	Integral operator	p. 22
∇	The gradient operator	p. 19
$\nabla\cdot$	The divergence operator	p. 19
∇^2	The Laplacian operator	p. 19
Tra	The trace operator	p. 24

Notations in chapter 2

$\boldsymbol{\sigma}$	Stress tensor	p. 19
δ	Dispersion parameter	p. 24
Γ_1^{bf}	Interfaces between the elastic layer Ω^b and the fluid domains Ω_1^f	p. 18
Γ_2^{bf}	Interfaces between the elastic layer Ω^b and the fluid domains Ω_2^f	p. 18
λ	Correlation length (m)	p. 24
$\mathbf{n}_\alpha^{bf}$	The normal unit vector of Ω^b at the interfaces Γ_α^{bf} $(\alpha=1,2)$	p. 20
$\mathbf{u}$	Displacement vector in the solid layer	p. 20
$\mathbf{u}^{(\alpha)}$	displacement vector in the fluid domain Ω_α^f $(\alpha=1,2)$	p. 19

ω	Angular frequency (rad/s)	p. 20
Ω^b	Elastic layer phisically mimicking cortical bone	p. 18
Ω_1^f	Half-space representing soft tissues	p. 18
Ω_2^f	Half-space representing marrow	p. 18
ρ	Mass density of the solid (kg.m^{-3})	p. 20
ρ_α	Mass density of the fluid domain Ω_α^f $(\alpha = 1, 2)$ (kg.m^{-3})	p. 19
θ	Angle of incidence (rad)	p. 18
c_α	Sound speed of the fluid domainΩ_α^f $(\alpha = 1, 2)$ (m/s)	p. 19
h	Bone thickness (m)	p. 18
n_r	The number of realizations	p. 25
p_α	Pressure field in fluid domain Ω_α^f $(\alpha = 1, 2)$	p. 19
P_I	Amplitude of the incident wave	p. 21
P_I	Amplitude of the transmitted wave	p. 21
p_I	Incident plane wave	p. 18
P_R	Amplitude of the reflected wave	p. 21
R	Reflection coefficient	p. 23
T	Trasmission coefficient	p. 23
h_2	The thickness of bone part with a gradient of material properties	p. 29

Notations in chapter 3

A	Anti-symmetric modes	p. 67
$att^{(m)}$	Attenuation (Np m^{-1})	p. 65
c_g	group velocity (m/s)	p. 65
C_{ph}	The wave's phase velocity (m/s)	p. 65
k_1	Wavenumber with respect to $\mathbf{e}_1$ (1/m)	p. 63
S	Symmetric modes	p. 67
$V_e^{(m)}$	Wave energy velocity (m/s)	p. 66

Notations in chapter 4

$F(n,m)$	Flexural Lamb mode	p. 103
k_z	Axial wave number (1/m)	p. 97
$L(0,m)$	Longitudinal mode	p. 103
n	Circumferential order	p. 97
R_e	External radius (m)	p. 95
R_i	Internal radius (m)	p. 95
$T(0,m)$	Torsional Lamb mode	p. 103

"On mesure l'intelligence d'un individu à la quantité d'incertitudes qu'il est capable de supporter ."

[Emmanuel Kant]

Chapitre 1

Introduction générale

"Il y a bien moins de difficultés à résoudre un problème qu'à le poser."

[Joseph de Maistre.]

1.1 Préambule

Le choix de la forme et du contenu de cette thèse, dont le résultat est une modeste contribution à un problème sans doute très complexe, est lié à un facteur de cohérence qu'il me semble utile de rappeler en préambule, afin d'aider le lecteur néophyte à naviguer aisément entre les chapitres. Ce préambule sera suivi d'une description plus détaillée du problème étudié et du contenu du manuscrit.

Du point de vue de la forme, le document est composé de cinq chapitres (introduction et conclusion incluses). Notons que le contenu du chapitre deux au chapitre quatre provient essentiellement de la rédaction d'articles scientifiques lesquels sont publiés, soumis pour publication ou à soumettre pour publication prochainement. Ces productions scientifiques étant initialement rédigées et/ou publiées en langue anglaise, nous avons fait le choix de rester sur la langue de Shakespeare, et ce, pour des raisons d'homogénéité sur les formulations, et de clarté sur les résultats présentés (tout en conservant notre attachement à la langue de Molière). Ainsi, les prochains chapitres sont rédigés en langue anglaise, et possèdent chacun une bibliographie, un sommaire et un résumé. En outre, les éléments ne pouvant pas figurer sur ces articles mais dont nous jugeons nécessaires à la compréhension du rapport, seront présentés en annexe. Enfin, un résumé long de la thèse est proposé en clôture de cette introduction générale.

1.2 Contexte de l'étude

En raison du besoin croissant de méthodes de diagnostic du tissu osseux, par exemple, pour diagnostiquer des pathologies osseuses comme l'ostéoporose ou d'autres ostéopénies, des méthodes dites de contrôle non-destructif (CND) par ultrasons ne cessent de susciter un engouement considérable dans la

communauté scientifique. De telles méthodes sont réputées être intéressantes pour évaluer la qualité du tissu osseux, de par leurs caractères non-invasif, peu couteux, facilement portable et non-ionisant. De plus, les ultrasons étant des ondes élastiques, elles sont susceptibles de présenter une sensibilité aux propriétés mécaniques du milieu dans lequel elles se propagent. Une telle sensibilité devrait permettre de remonter à des propriétés matérielles du tissu osseux souvent mal connues.

Cependant, utiliser des ultrasons dans le cadre de la caractérisation du tissu osseux, suppose une compréhension rigoureuse et poussée des différents phénomènes physiques mis en jeu lors de leur propagation. Des phénomènes tels que la dispersion, la réflexion/transmission, la diffusion ainsi que le rôle de la géométrie tridimensionnelle et des tissus mous demeurent encore à nos jours mal compris.

Cette thèse vise à développer des méthodes de diagnostic du tissu osseux en utilisant des méthodes ultrasonores. Elle s'inscrit dans le cadre général de l'évaluation quantitative de l'os pathologique ou sain. Il s'agit de développer un modèle de propagation d'ondes ultrasonores dans l'os cortical, capable de prendre en compte l'anisotropie, la forte hétérogénéité, la géométrie ainsi que les éventuelles fluctuations aléatoires des propriétés matérielles du tissu osseux. En particulier, nous souhaitons expliciter le rôle clef de l'hétérogénéité aléatoire du tissu osseux sur les phénomènes de propagation des ondes ultrasonores. Dans cette étude, seul le volet numérique sera étudié. L'objectif étant de poser des bases solides, en développant un modèle direct plus complet, lequel devrait permettre, à plus ou moins long terme, une reconstitution totale ou partielle des propriétés mécaniques et/ou géométriques de l'os par des mesures.

Les méthodes de modélisation et de simulations numériques utilisées dans notre approche peuvent être regroupées dans la thématique des "ondes ultrasonores dans un guide d'ondes aléatoire", thématique jalonnant plusieurs domaines scientifiques. Nous développerons nos modèles avec un esprit de mécanicien, visant une application sur le tissu osseux. Toutefois, ces modèles sont transposables à d'autres domaines scientifiques (par exemple, génie civil, aéronautique, naval, etc.).

1.3 Physiologie et méthodes de diagnostics du tissu osseux

1.3.1 Structure du tissu osseux

Dans cette section, on esquisse une brève présentation du tissu osseux, en particulier l'os humain. L'os étant un organe à géométrie et physiologie très complexes, nous ne donnerons ici que quelques éléments introductifs. De ce fait, nous considérerons l'os au sens du "mécanicien". Pour une description plus détaillée de ce tissu, le lecteur peut se référer à la littérature comme le livre de synthèse édité par Cowin (Cowin, 2001). Un exemple de pathologie osseuse sera donné, visant à rappeler les modifications et conséquences dues à ces types de pathologies.

Constitution de l'os. Le tissu osseux est un organe vivant constitué essentiellement d'une phase organique et d'une phase minérale. Il peut être vu comme un matériau composite composé d'eau, de sels minéraux et de substances organiques. La phase minérale, laquelle est composée principalement

de cristaux d'hydroxyapatite, confère à l'os son caractère de rigidité. La phase organique constituée de fibre de collagène, fournit à l'os ses propriétés élastiques. Notons que ce tissu vivant et dynamique est renouvelé constamment via le processus de remodelage effectué par des cellules osseuses (les ostéoblastes et les ostéoclastes), permettant ainsi à l'os de se régénérer, et d'adapter son architecture aux contraintes externes ou internes.

Le squelette (de sa fonction aux structures corticale et trabéculaire). Le squelette est composé de 206 os articulés assurant une double fonction, structurelle et métabolique. En conjonction avec les tissus mous (muscles, ligaments, tendons, etc.), le squelette forme un système robuste capable de supporter le corps, et de protéger certains organes sensibles (cœur, cerveau, poumon, etc.) tout en assurant une flexibilité du mouvement. De plus, l'os joue un rôle important dans la formation des cellules sanguines, il est considéré comme un réservoir de calcium et de minéraux pour l'organisme. Il va sans dire que la structure du tissu osseux est extrêmement complexe (cf. figure 1.1). Les os du squelette peuvent être regroupés en famille, selon leur taille et leur forme : les os courts, les os longs, les os plats et les os irréguliers. On distingue deux types de matériaux pour le tissu osseux : l'os cortical (appelé aussi os compact) et l'os trabéculaire (ou os spongieux).

L'os cortical. Le tissu cortical constitue principalement l'enveloppe externe des os, on le trouve dans la périphérie de la diaphyse (corps des os longs) et dans la constitution des os courts et plats. De part leur microstructure complexe en perpétuelle remodelage, le tissu cortical exhibe un comportement mécanique naturellement exceptionnel. Sa porosité est généralement comprise entre 5 et 10%, et il représente environs 80% de la masse osseuse. La structure de ce tissu est constituée essentiellement d'ostéons composés principalement de lamelles osseuses à géométrie cylindrique, empilées de façon concentrique autour des canaux de Havers (cf. figure 1.1).

L'os trabéculaire. Ce tissu trabéculaire se trouve principalement dans les épiphyses (extrémités des os longs), dans la métaphyse (zone intermédiaire entre l'épiphyse et la diaphyse), et dans les os courts et plats. Il est composé d'un système de lamelles osseuses irrégulières, appelées aussi travées ou trabécules. Sa structure est très poreuse, moins dense et moins rigide par rapport au tissu cortical.

Exemple de pathologie osseuse. Comme exemple de pathologie osseuse, on peut citer l'ostéoporose. Il s'agit d'une maladie qui survient généralement après une ostéopénie. Cette dernière est caractérisée par 'une fragilisation progressive du tissu osseux, menant peu à peu à l'ostéoporose proprement dite. Ils existent plusieurs variantes de cette pathologie (ostéoporoses de types I et II, etc.), mais nous ne définissons ici que le cas général, pour plus de détail, on peut se reporter à la littérature (Cowin, 2001). En général, l'ostéoporose se manifeste par une détérioration de la microstructure et/ou une perte de la masse osseuse, suivie d'une augmentation de la fragilité et du risque de fractures osseuses. Cette pathologie touche des millions de personnes dans le monde, plus particulièrement, les femmes post-ménopausées et les personnes âgées. Ainsi, son diagnostic demeure un défi majeur, à la fois social et économique.

Box 1.1. Composition du tissu osseux

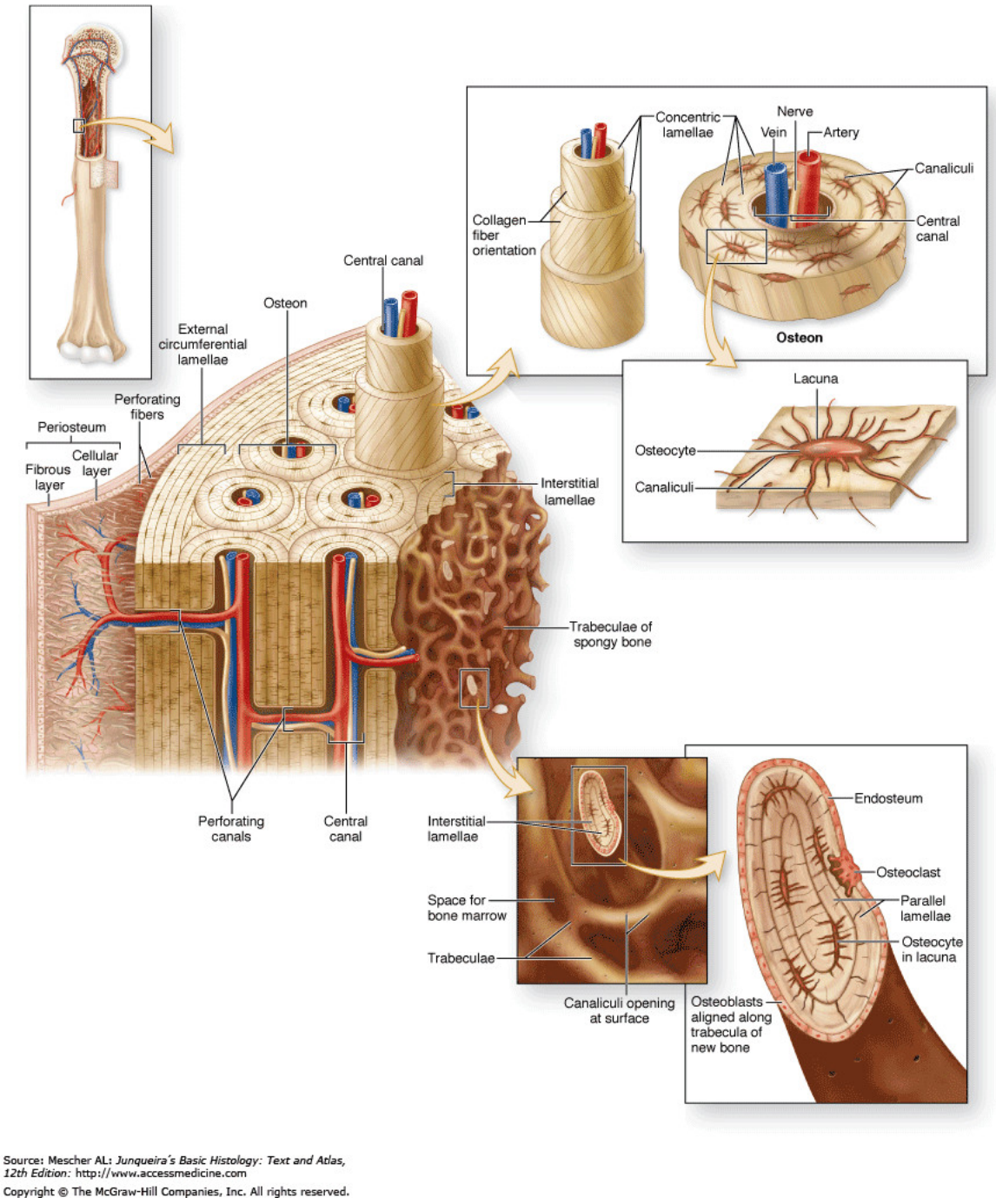

Figure 1.1: Structure de l'os cortical

1.3.2 Méthodes de diagnostic du tissu osseux

L'évaluation de la qualité de l'os passe par une meilleure compréhension des caractéristiques mécaniques et géométriques du tissu osseux. Caractériser ces différentes propriétés s'avère indispensable

au diagnostic de l'os pathologique ou sain. Ces dernières décennies, différentes méthodes de contrôle non-invasif (ou non-destructif) ont été développées pour l'évaluation quantitative de l'os. Des méthodes telles que l'absorption bi-photonique à rayon X (Dual-energy X-ray absorptiometry, DXA), la microtomographie à rayons X (Micro-CT), l'imagerie par résonance magnétique (Magnetic Resonance Imaging, MRI) et les ultrasons quantitatifs (Quantitative Ultrasound, QUS) ont vu le jour. Parmi ces techniques, la DXA est une technique de référence pour le diagnostic de l'ostéoporose, permettant de quantifier la densité minérale osseuse (Bone Mineral Density, BMD). Cependant, des propriétés déterminantes comme les caractéristiques mécaniques et micro-architecturales semblent difficilement accessibles via cette technique. Les ultrasons quantitatifs s'avèrent être une bonne alternative pour pallier cette insuffisance. Dans cette étude, notre attention sera portée sur les méthodes ultrasonores.

L'utilisation des ultrasons quantitatifs pour l'évaluation de la qualité osseuse a été proposée dès les années 80, et n'a cessé de progresser jusqu'à nos jours. De part leur nature d'ondes élastiques, les ultrasons sont sensibles aux propriétés mécaniques du tissus osseux. Une telle technique permet donc d'utiliser le potentiel des ondes élastiques pour explorer des propriétés mécaniques et géométriques de l'os. En outre, la technique ultrasonore présente l'avantage d'être non-ionisante, non-invasive, peu couteuse et portable.

En fonction de la nature des propriétés recherchées, un choix judicieux devra être fait sur le type de configuration, et de gammes de fréquences à utiliser afin d'arriver à un résultat optimal. En général, la technique ultrasonore est assujettie à trois méthodes de mesure : les mesures échographiques, la méthode de transmission transverse et la méthode de transmission axiale (Axial Transmission, AT). La technique de transmission transverse est dédiée à l'analyse du tissu trabéculaire tandis que la méthode de transmission axiale est utilisée pour l'évaluation du tissu cortical. Les dispositifs associés à ces méthodes, font appel à des sondes (émetteurs et/ou récepteurs) dont la gamme de fréquences est comprise en 250kHz et 2MHz. L'impulsion ultrasonore émise se propage dans la direction transversale ou longitudinale de l'os, selon la technique utilisée.

L'analyse des signaux enregistrés par les sondes, devrait, théoriquement, permettre de remonter à des propriétés mécaniques et géométriques du milieu traversé. On ne le dira jamais assez, du fait de la complexité de l'os, la caractérisation de ce tissu par des méthodes ultrasonores, suppose une compréhension précise et rigoureuse des phénomènes de propagation mis en jeu. L'analyse des ces phénomènes physiques est toujours un défi. Des modèles et méthodes numériques pertinents doivent être minutieusement développés. L'un des avantages d'une modélisation numérique est d'offrir la possibilité de mener une étude paramétrique permettant de faire varier simultanément ou successivement plusieurs paramètres du modèle, et suivre leur influence sur la réponse ultrasonore. Un tel modèle permettrait d'optimiser les dispositifs expérimentaux. De ce fait, des outils numériques robustes et précis, sont indispensables à l'interprétation des mesures expérimentales.

1.4 Modélisation numérique du tissu osseux

1.4.1 L'os vu comme un guide d'ondes ultrasonores

Stricto sensu, un guide d'ondes est un système physique capable de guider les ondes sur des longues distances sans perte d'énergie. Les techniques associées aux ultrasons quantitatifs, se basent sur la propagation des ondes ultrasonores dans une direction privilégiée, et dont l'énergie demeure confinée dans une zone délimitée. La géométrie du tissu osseux, couplée à sa structure confère à l'os le caractère de guide d'ondes ultrasonores.

Du point de vue physique, la célérité d'une onde est d'autant plus élevée que la durée de transmission de l'information d'une particule élémentaire constituant le matériau, à sa voisine est courte, et ce, suivant la cohésion de la matière aux plus petites échelles. De ce fait, les ultrasons se propagent plus rapidement dans le tissu osseux par rapport aux tissus mous ou à la moelle. L'onde peut être décrite par une grandeur scalaire ou vectorielle, selon la nature du milieu de propagation. Ainsi, dans le tissu cortical (solide), l'onde est entièrement décrite par le déplacement particulaire (des particules), tandis que dans les tissus mous et la moelle, elle est décrite par la pression.

Pour la modélisation de la propagation d'ondes dans le tissu osseux, l'os peut être modélisé comme une plaque libre (ou immergée dans le vide) ou par une plaque immergée dans deux demi-espaces fluides. Dans ce dernier cas, l'os est généralement pris en sandwich entre deux fluides représentant la moelle et les tissus mous. Dans le cas tridimensionnel, la structure osseuse est souvent modélisée par un cylindre libre ou chargé par deux fluides.

1.4.2 Comportement mécanique du tissu cortical

Propriétés déterministes. Du point de vue physique, l'os cortical est un matériau multiéchelle ayant une organisation structurelle très complexe (cf. figure 1.1), lui conférant des propriétés matérielles exceptionnelles. De part sa structure multiéchelle, son comportement mécanique varie selon les différents niveaux échelles. Dans cette thèse, l'os est modélisé à l'échelle du millimètre (c.-à-d. à l'échelle mésoscopique). À cette échelle, le tissu osseux est décrit comme un milieu hétérogène. En outre, du fait de l'orientation longitudinale de ses ostéons, l'os cortical adopte un comportement anisotrope. Il est généralement considéré comme un matériau transversalement isotrope, avec comme plan d'isotropie, un plan orthogonal à la direction axiale.

Propriétés aléatoires. Les caractéristiques décrites dans le paragraphe précédent supposent que les propriétés mécaniques du tissu osseux sont déterministes et connues (c.-à-d. fixées). Cependant, les hétérogénéités au niveau des petites échelles sont souvent de nature aléatoire, et peuvent causer une fluctuation des propriétés matérielles au plus grandes échelles. Dans le cas du tissu cortical, une fluctuation sur la distribution et la taille des pores est observée. Une telle fluctuation peut avoir des effets non négligeables sur la propagation des ondes ultrasonores, et devra être pris en compte dans nos modèles.

1.4.3 Méthodes numériques

Nombreuses sont les méthodes numériques développées dans le cadre de la propagation d'ondes ultrasonores. Selon le degré de complexité et de finesse requis, la méthode de résolution peut être de type analytique, semi-analytique ou purement numérique. On attend de ces méthodes qu'elles soient robustes, précises, et capables de prendre en compte les lois de comportement des systèmes étudiés. Idéalement, les méthodes numériques doivent être bâties sur un minimum de paramètres pertinents, tout en restant dans des coûts de calcul raisonnables. C'est dans cette optique que se fera le choix et/ou le développement des méthodes utilisées dans cette étude.

Généralement, si des méthodes analytiques existent, elles ne permettent de traiter que des cas limités, dont la configuration géométrique et le comportement mécanique (ou multi-physiques) sont relativement simples. Dans le cas de l'os, son comportement anisotrope et son caractère hétérogène empêchent toute tentative de recherche d'une solution analytique générale. Ainsi, les méthodes numériques, lesquelles permettent de prendre en compte l'anisotropie et l'hétérogénéité du matériau, se révèlent indispensables à l'étude de la propagation des ondes ultrasonores dans le tissu osseux.

Dans cette thèse, une approche basée sur la méthode des éléments finis semi-analytique (Semi-Analytical Finite Element, SAFE) est utilisée. Une telle approche permet de combiner les avantages offerts par les méthodes analytiques et celles des éléments finis. De plus, cette approche permet de modéliser la propagation des ultrasons aussi bien dans un milieu à propriétés continûment-variables que dans un multicouche. Dans ce travail, cette méthode sera plusieurs fois utilisée pour des modélisations bidimensionnelles et/ou tridimensionnelles de l'os cortical.

1.5 Résumé long de la thèse

Introduction. Dans cette étude, nous nous intéressons à la modélisation numérique de la propagation des ondes ultrasonores dans l'os cortical. Nous nous penchons plus particulièrement sur l'utilisation de la technique dite des ultrasons quantitatifs (Quantitative Ultrasound, QUS) pour évaluer la qualité du tissu osseux. Il s'agit d'une technique émergente dont l'application aux tissus biologiques se développe considérablement. Cette technique se base sur l'utilisation du potentiel des ondes ultrasonores lesquelles sont élastiques (mécaniques), pour sonder le tissu osseux, en espérant pouvoir remonter à des caractéristiques mécaniques et/ou géométriques du tissu osseux. Ce dernier étant un tissu vivant, il est sujet au vieillissement et aux maladies comme l'ostéoporose, susceptibles de conduire à des accidents graves. Pour éviter ces risques (ou du moins les minimiser), une surveillance de la qualité osseuse s'avère indispensable. Pour ce faire, différentes techniques connues sous l'appellation de contrôles non-destructifs (CND) existent pour diagnostiquer la qualité du tissu osseux. Ces techniques vont de l'utilisation des rayons X à l'utilisation des ultrasons pour quantifier les caractéristiques de l'os. Parmi ces techniques, celles utilisant les ondes ultrasonores se démarquent des autres, du fait de la nature physique des ultrasons (non-ionisant, ondes élastique, etc.) et de leur faible coût. Cependant, en raison de la complexité de la structure osseuse, la propagation de ces ultrasons dans l'os cortical met en jeu différents phénomènes physiques qui sont

encore mal compris (par exemple, la dispersion, le phénomène de réflexion/transmission, la multitude des modes, etc.). Ainsi, cette thèse vise à apporter une contribution à la compréhension de ces phénomènes, en développant des modèles numériques (bidimensionnels ou tridimensionnels) capables de prendre en compte les caractéristiques mécaniques et géométriques de l'os, ainsi que la nature aléatoire des fluctuations observées sur ses propriétés matérielles.

Le manuscrit comporte cinq chapitres (avec l'introduction et la conclusion). Le chapitre un est dédié à l'introduction générale de la thèse. Le contexte de l'étude y est présenté, et une description détaillée du problème étudié est proposée. Dans le chapitre deux, nous étudions les phénomènes de réflexion et de transmission des ultrasons à travers un modèle bidimensionnel prenant en compte le tissu mou et les incertitudes sur les propriétés élastiques de l'os. L'aspect lié au gradient de propriétés est inclus dans ce modèle, et ses caractéristiques et effets sont présentés et discutés. Le chapitre trois vise à explorer l'aspect modal des ondes. La dispersion des ondes de Lamb dans l'os est étudiée via un modèle stochastique bidimensionnel. Ensuite, pour s'approcher de la réalité tridimensionnelle de la géométrie de l'os, un modèle cylindrique est développé dans le chapitre quatre. Une étude modale est présentée, et l'effet de la géométrie est discuté. Enfin, dans le chapitre cinq, une conclusion est présentée et des perspectives sont proposées. Dans les paragraphes qui suivent, un résumé du contenu de chaque chapitre est proposé.

Réflexion et transmission des ultrasons dans l'os : Modèle bidimensionnel - (Chap. 2)

Contexte. Le point de départ de cette thèse est la caractérisation des propriétés matérielles d'un guide d'ondes via des méthodes ultrasonores. L'objectif visé étant une meilleure compréhension des phénomènes liés à la propagation des ondes ultrasonores dans l'os cortical. L'un des concepts physiques de base pour la quantification ultrasonore d'un guide d'ondes est l'estimation des coefficients de réflexion et de transmission des ondes sur ses interfaces. Dans ce contexte, nos premiers travaux se sont focalisés sur l'étude des ces coefficients d'intérêt dans une plaque d'os cortical. L'hétérogénéité et le comportement anisotrope du tissu osseux compliquent le calcul de ces coefficients ainsi que l'interprétation physique des phénomènes associés. Des solutions théoriques générales sont proposées dans la littérature pour des cas déterministes (Fedorov, 1968; Musgrave, 1970; Auld, 1990; Rokhlin et al., 1986; Deschamps and Hosten, 1992). Dans notre étude, l'effet lié à l'hétérogénéité aléatoire des propriétés mécaniques du tissu osseux est pris en compte. L'objectif étant de développer un modèle bidimensionnel capable d'extraire les coefficients de réflexion et de transmission d'un guide d'onde anisotrope et ayant une hétérogénéité aléatoire. Deux profils de propriétés mécaniques seront étudiés. Un premier cas où les propriétés matérielles moyennes du tissu osseux sont considérées comme homogènes, et un deuxième cas où un gradient de propriétés matérielles est introduit dans la direction transversale.

Méthode, modèles et résultats. Dans cette première étude, l'os cortical est modélisé par une plaque bidimensionnelle incluse dans un système tri-couche. La configuration géométrique adoptée est constituée d'une couche solide (représentant l'os) prise en sandwich entre deux autres couches fluides (représentants d'une part la moelle et d'autre part les tissus mous).

Dans un premier temps, nous avons étudié le cas où les propriétés matérielles moyennes de l'os sont supposées homogènes. Ainsi, dans le modèle déterministe, où les propriétés matérielles de l'os sont supposées connues, la couche solide est considérée comme un matériau homogène ayant un comportement isotrope transverse. Les propriétés mécaniques peuvent varier uniquement selon son épaisseur. Cependant, à l'échelle microscopique, des hétérogénéités souvent de nature aléatoire peuvent être la cause de fluctuations des propriétés matérielles à l'échelle de l'organe. Pour prendre en compte ces éventuelles fluctuations, nous avons proposé de modéliser l'os comme un matériau ayant une hétérogénéité aléatoire à l'échelle mésoscopique. Pour ce faire, un tenseur d'élasticité anisotrope aléatoire est généré par l'entremise d'un modèle probabiliste basé sur le principe du maximum d'entropie. Cette génération se fait à partir du tenseur moyen, lequel est isotrope transverse, et deux paramètres qui contrôlent la longueur de corrélation spatiale et la dispersion du champ stochastique. En gros, une simulation Monte-Carlo est utilisée pour générer plusieurs tenseurs d'élasticité. Pour chaque réalisation, une approche basée sur la méthode SAFE est utilisée pour calculer les coefficients de réflexion et de transmission. Une analyse de convergence stochastique est effectuée.

Une étude paramétrique est réalisée. Les coefficients d'intérêt (réflexion et transmission) sont calculés pour trois paramètres de dispersion, et ce, pour différentes valeurs de fréquences et d'angles d'incidence. Une très forte sensibilité de ces coefficients au paramètre de dispersion est observée, en particulier pour la gamme des hautes fréquences. En outre, les courbes des coefficients de réflexion et de transmission permettent d'identifier les plages d'angles et de fréquences pour lesquelles la dispersion est plus ou moins importante. Une telle sensibilité devrait permettre d'apporter une information complémentaire aux dispositifs expérimentaux, par exemple, sur le choix d'angles d'excitation appropriés à l'étude. Ces résultats seraient aussi utiles à la formulation du problème inverse.

Dans un deuxième temps, nous avons exploré le cas où le tissu osseux peut être considéré comme ayant un gradient de propriété matérielle dans sa direction transversale. En effet, le progrès sur le développement des techniques d'imagerie offre une nouvelle vue assez intéressante de la microstruture osseuse. Ainsi, des nouvelles caractéristiques du tissu osseux comme un gradient de porosité sur sa direction radiale, sont devenues visibles. Par exemple, il a été observé que la porosité intracorticale du fémur augmente du périoste à l'endoste (Bousson et al., 2001; Tatarinov et al., 2014, 2005; Thomas et al., 2005). Du point de vue mécanique, ce gradient de porosité devrait induire un gradient de propriétés mécaniques telles que la densité massique et la rigidité. On se propose donc, d'explorer l'effet de ce nouveau profil de propriétés, sur les phénomènes de réflexion et de transmission.

Durant cette dernière décennie, quelques travaux menés sur l'os, ont proposé de modéliser ce gradient de propriétés via une fonction affine (Haiat et al., 2009; Baron, 2011, 2012). Les résultats obtenus sont intéressants et nous encouragent à aller dans ce sens en essayant de proposer un gradient de propriétés pour se rapprocher de la réalité physique. Le gradient utilisé dans ce travail est basé sur un modèle proposé dans la littérature Desceliers et al. (2012), utilisé dans le cadre de l'évaluation utrasonore de l'os. La couche solide est scindée en deux couches, une couche homogène (représentant la zone du périoste) suivie d'une couche "poreuse" à gradient de propriétés. Une simulation Mont-Carlo est effectuée pour générer les tenseurs d'élasticité aléatoires anisotropes. Cette génération est basée sur le profil moyen du

gradient de propriétés. Ensuite, une étude de sensibilité aux paramètres du gradient est réalisée. Il a été observé que la prise en compte de ce gradient aboutit à des changements drastiques sur le comportement des coefficients de réflexion et de transmission. Ces résultats consolident le rôle que jouerait ce nouveau profil de propriétés sur les coefficients d'intérêt. Le travail présentée dans ce chapitre a donné lieu à la production de documents scientifiques, dont un article publié au journal *Wave Motion* (Nguyen et al., 2016).

Dispersion des ondes de Lamb dans l'os : Modèle bi-dimentionnel - (Chap. 3)

Contexte. Parmi les techniques ultrasonores souvent utilisées pour la caractérisation du tissu osseux, la technique de transmission axiale (Axial Transmission, AT) est considérée comme compétitive en raison de sa sensibilité aux caractéristiques mécaniques mais aussi géométriques du guide d'ondes (en l'occurrence, l'os). La propagation des ultrasons dans ces guides d'ondes, fait intervenir deux phénomènes physiques : la dispersion et une multitude de modes. Ces phénomènes s'expliquent du fait que plusieurs modes peuvent se propager dans le guide d'ondes à différentes vitesses, et ce, pour la même fréquence temporelle. Les ondes guidées associées à ces phénomènes sont appelées communément ondes de Lamb. La compréhension de ces phénomènes passe par la détermination des relations de dispersion souvent modélisées par des courbes dites de dispersion. Inutile de dire que dans le cas des milieux hétérogènes et anisotropes, obtenir ces relations de dispersion est toujours un défi. Des travaux apportant quelques réponses à ces questions peuvent être trouvés dans la littérature (Royer and Dieulesaint, 2000; Rose, 1999; Su and Ye, 2009; Nayfeh and Chimenti, 1989; Nayfeh, 1995; Neau, 2003; Nayfeh and Chimenti, 1988; Chimenti and Rokhlin, 1990) pour l'étude de structures homogènes et isotropes. Dans cette étude, on se propose d'explorer ces phénomènes dans le cadre de la propagation des ondes ultrasonores dans l'os cortical. Les courbes de dispersion correspondantes devraient dépendre principalement de la géométrie et du type de matériau. L'effet lié à l'hétérogénéité aléatoire des propriétés mécaniques sera minutieusement examiné.

Méthode, modèles et résultats. Dans ce travail, l'os cortical est modélisé par une plaque élastique libre (sans couplage avec des fluides). L'approche probabiliste utilisée dans le chapitre précédent, est de nouveau utilisée pour générer les tenseurs d'élasticité aléatoire à partir d'un tenseur déterministe et isotrope transverse. Ainsi, dans le modèle déterministe, la plaque est homogène transversalement isotrope, tandis que dans le modèle stochastique, elle est hétérogène avec un comportement totalement anisotrope. La formulation de la relation de dispersion conduit à un système non-linéaire en fonction du nombre d'ondes. Ce problème non-linéaire a été transformé en un problème aux valeurs propres. Une approche basée sur la méthode SAFE est proposée pour extraire les courbes de dispersion. L'approche est validée avec les résultats obtenus dans la littérature et via le logiciel Disperse (Lowe and Pavlakovic, 2013). La comparaison pour l'étude d'un multi-couche semble donner des résultats intéressants. Pour chaque réalisation aléatoire du tenseur d'élasticité, les caractéristiques de dispersions correspondantes sont extraites. En prenant en compte les incertitudes sur les propriétés matérielles, il est observé que l'approche SAFE permet d'extraire plus de modes. Contrairement à ce à quoi l'on pouvait s'attendre, les courbes de dispersion dans le cas stochastique exhibent des branches quasi-complètes. De ce fait, le modèle proposé

pourrait être d'une aide précieuse à la compréhension des courbes expérimentales. Il est généralement connu que ces courbes ont des branches souvent incomplètes, rendant ainsi, l'interprétation plus délicate. Le modèle proposé devrait permettre de compléter les branches manquantes dans les courbes de dispersion générées expérimentalement. Du point de vue probabiliste, les modes fondamentaux $A0$ et $S0$ sont dispersifs. La fluctuation du premier mode quasi-symétrique est plus importante par rapport à celle du premier mode quasi-antisymétrique. Enfin, ces modes sont aussi sensibles à une modification de l'épaisseur corticale. L'étude présentée dans ce chapitre 3 a donné lieu à la rédaction d'un article lequel est soumis pour publication au journal *Philosophical Transactions of the Royal Society A : Mathematical, Physical and Engineering Sciences* [S1].

Modèle tridimensionnel cylindrique - (Chap. 4)

Contexte. À ce stade, la situation est la suivante. Une modélisation bidimensionnelle est proposée pour la propagation des ondes ultrasonores dans l'os cortical. Les phénomènes de réflexion/transmission et de dispersion sont étudiés. De plus, quelques caractéristiques du tissu osseux sont prises en compte par la modélisation d'un gradient de propriétés et l'introduction d'une hétérogénéité aléatoire de ce tissu vivant. Des résultats prometteurs sont observés dans le cas de l'étude de la dispersion des ondes de Lamb d'une plaque d'os ayant des propriétés aléatoires. Par exemple, les courbes de dispersion correspondantes présentent des branches quasi-complètes. Une modélisation stochastique couplée à la méthode SAFE semble être pertinente quant à l'étude de la propagation des ultrasons dans le tissu cortical. Une sensibilité aux différentes caractéristiques du modèle est observée (du moins pour le cas 2D). Mais qu'en est-il dans le cas d'une géométrie tridimensionnelle, dont la nature pourrait changer la donne? C'est en partie pour répondre à cette question, qu'une modélisation tridimensionnelle cylindrique est proposée dans le chapitre quatre. L'objectif est de développer un modèle tridimensionnel cylindrique capable d'extraire les relations de dispersion des ondes guidées dans le tissu cortical. L'hétérogénéité aléatoire sera aussi prise en compte. La motivation de cette étude est de donner naissance à un outil numérique permettant de comprendre les relations de dispersion d'un guide d'ondes cylindrique ayant une hétérogénéité aléatoire. Nous nous focaliserons sur l'étude des ondes guidées qui s'y propagent.

Méthode, modèles et résultats. Une modélisation tridimensionnelle est proposée dans cette étude. Dans le modèle déterministe, l'os est modélisé par un cylindre creux et homogène ayant un comportement isotrope transverse. Il sera modélisé par un cylindre anisotrope et hétérogène dès lors que les incertitudes sur les propriétés matérielles seront prises en compte. Le cylindre est considéré comme homogène dans sa direction longitudinale (axiale) avec une hétérogénéité aléatoire dans sa direction radiale. Une formulation basée sur la méthode semi-analytique des éléments finis est proposée, puis validée avec les résultats donnés par le logiciel Disperse. L'effet de la géométrie tridimensionnelle est exploré en effectuant une étude paramétrique. Force est de constater que les résultats obtenus par ce modèle (par exemple, les courbes de dispersion de la vitesse de phase) convergent vers ceux obtenus par notre modèle bidimensionnel (cf. chapitre 3) lorsqu'on augmente le rayon interne du cylindre. Une discussion est menée pour expliquer

rigoureusement cette tendance. Toutefois, une légère différence est observée pour les basses fréquences. Ensuite, nous avons exploré la possibilité d'utiliser ces ondes guidées pour détecter une éventuelle perte intra-corticale. Une légère sensibilité des modes à une détérioration intra-corticale est constatée. Les premiers modes de respiration $T(0,1)$, $L(0,1)$ et $L(0,2)$ semblent être appropriés à l'évaluation ultrasonores de l'os. De plus, le premier mode de torsion $T(0,1)$, lequel ne présente pas une dépendance fréquentielle (non dispersif) est désormais dispersif du point de vu probabiliste. La prise en compte des incertitudes sur les propriétés matérielles du cylindre, aboutit à l'extraction de courbes de dispersion ayant des branches quasi-complètes. Ainsi, la conjonction des résultats obtenus laisse présager que le modèle proposé serait intéressant dans le cadre d'une évaluation quantitative de l'os par des méthodes ultrasonores. Les résultats de cette étude seront soumis pour publication prochainement [P1].

Conclusion.

Dans ce manuscrit nous avons présenté les modèles développés durant ces années de thèse. Il s'agit d'une contribution à la compréhension des phénomènes physiques (ou multi-physique) mis en jeu lors de la propagation des ondes ultrasonores dans le tissu osseux. L'étude se place dans le contexte général de la caractérisation quantitative de l'os par des méthodes ultrasonores. Plus précisément, le travail s'articule autour de la thématique de la modélisation numérique dédiée à la propagation des ondes ultrasonores dans des guides d'ondes multidimensionnels (bidimensionnels ou tridimensionnels), hétérogènes, anisotropes, et composés de matériaux dont les hétérogénéités peuvent être de nature aléatoire. Ces mots-clés jalonnent presque tous les chapitres de ce document et constituent ainsi le fil conducteur des modèles proposés.

À travers les modèles numériques présentés dans ce manuscrit, nous avons pu mesurer la complexité des phénomènes liés à la propagation des ultrasons dans le tissu cortical. Le choix de modélisation et les études paramétriques menées, semblent donner des résultats prometteurs dans la perspective d'une évaluation quantitative de l'os par des mesures expérimentales. Enfin, le travail présenté dans ce document constitue un ensemble de recherches originales qui contribue à la compréhension des phénomènes impliqués dans la propagation des ondes ultrasonores dans le tissu cortical.

Bibliographie

B.A. Auld. *Acoustic field and waves in solids*, volume I and II. Krieger Publishing, Malabar, 2nd edition, 1990.

C. Baron. Propagation of elastic waves in an anisotropic functionally graded hollow cylinder in vacuum. *Ultrasonics*, 51(2):123 – 130, 2011.

C. Baron. Using the gradient of human cortical bone properties to determine age-related bone changes via ultrasonic guided waves. *Ultrasound in Medicine & Biology*, 38(6):972 – 981, 2012.

V. Bousson, A. Meunier, C. Bergot, E. Vicaut, M.A. Rocha, M.H. Morais, A.M. Laval-Jeantet, and J.D. Laredo. Distribution of intracortical porosity in human midfemoral cortex by age and gender. *J. Bone Miner Res.*, 16:1308–11317, 2001.

D.E. Chimenti and S.I. Rokhlin. Relationship between leaky lamb modes and reflection coefficient zeroes for a fluid coupled elastic layer. *The Journal of the Acoustical Society of America*, 88(3):1603–1611, 1990.

S.C. Cowin. *Bone mechanics handbook*. CRC Press, Boca Raton, FL, 2nd edition, 2001.

C. Desceliers, C. Soize, S. Naili, and G. Haiat. Probabilistic model of the human cortical bone with mechanical alterations in ultrasonic range. *Mechanical Systems and Signal Processing*, 32:170 – 177, 2012.

M. Deschamps and B. Hosten. The effects of viscoelasticity on the reflection and transmission of ultrasonic waves by an orthotropic plate. *The Journal of the Acoustical Society of America*, 91(4):2007–2015, 1992.

F.I. Fedorov. *Theory of elastic waves in crystals*. Plenum Press, 1968.

G. Haiat, S. Naili, Q. Grimal, M. Talmant, C. Desceliers, and C. Soize. Influence of a gradient of material properties on ultrasonic wave propagation in cortical bone: Application to axial transmission. *The Journal of the Acoustical Society of America*, 125(6):4043–4052, 2009.

M. Lowe and B. Pavlakovic. DISPERSE. *User's Manual*, 2013.

M.P.J. Musgrave. *Crystal acoustics*. Holden Day, San Francisco, 1970.

A.H. Nayfeh and D.E. Chimenti. Ultrasonic wave reflection from liquid-coupled orthotropic plates with application to fibrous composites. *Journal of A*, 55:863–870, 1988.

A.H. Nayfeh and D.E. Chimenti. Free wave propagation in plates of general anisotropic media. *Journal of Applied Mechanics*, 56:881–886, 1989.

H.A. Nayfeh. *Wave Propagation in Layered Anisotropic Media*. Elsevier, 1995.

G. Neau. *Lamb waves in anisotropic vicooelastic plates. Study of the wave fronts and attenuation*. PhD thesis, Université Bordeaux 1, 2003.

V.-H. Nguyen, A. Abdoulatuf, C. Desceliers, and S. Naili. A probabilistic study of reflection and transmission coefficients of random anisotropic elastic plates. *Wave Motion*, 64:103 – 118, 2016.

S.I. Rokhlin, T.K. Bolland, and L. Adler. Reflection and refraction of elastic waves on a plane interface between two generally anisotropic media. *The Journal of the Acoustical Society of America*, 79:906–918, 1986.

J.L. Rose. *Ultrasonic waves in solid media*. Cambridge University Press, 1999.

D. Royer and E. Dieulesaint. *Elastic wave in solids I. free and guides propagation*. Springer, 2000.

Z. Su and L. Ye. *Identification of Damage Using Lamb Waves*, volume 48. Springer-Verlag London, 2009.

A. Tatarinov, N. Sarvazyan, and A. Sarvazyan. Use of multiple acoustic wave modes for assessment of long bones: Model study. *Ultrasonics*, 43(8):672 – 680, 2005.

A. Tatarinov, V. Egorov, N. Sarvazyan, and A. Sarvazyan. Multi-frequency axial transmission bone ultrasonometer. *Ultrasonics*, 54(5):1162 – 1169, 2014.

C.D. Thomas, S.A. Feik, and J.G. Clement. Regional variation of intracortical porosity in the midshaft of the human femur: age and sex differences. *J. Anat.*, 206:115–125, 2005.

Chapter 2

A probabilistic study of Reflection and Transmission coefficients of random anisotropic elastic plates

"Les grandes choses peuvent se manifester par de petits signes."

[Sigmund Freud.]

CHAPTER INFORMATION

Keywords:
Random properties
Reflection coefficient
Transmission coefficient
Semi-analytical finite element method
Cortical bone
Ultrasound

Publication:
The work presented in this chapter has led to the writing of a scientific article which is published in the journal *Wave Motion* [A1].

ABSTRACT

This chapter presents a probabilistic framework to analyze wave reflection and transmission through anisotropic elastic plates. The elastic plate is sandwiched between two homogeneous fluids and has randomly varied elastic properties in the through-thickness direction. By introducing a stochastic model for quantitative description of heterogeneous elastic properties in the plate, the effects of material heterogeneity on reflected and transmitted waves may be investigated from a probability point of view. The reflection and transmission coefficients are computed *via* the semi-analytical finite element (SAFE) method. A sensitivity study is presented, highlighting effects of the uncertainty of elasticity properties on the reflection and transmission coefficients measured from different angles of incidence.

Contents

2.1 Introduction

A large variety of the natural and artificial materials have unidirectional varying elastic properties. Mantel crust, oceans, composites or bone materials are some of these functionally graded media. For artificial materials, many studies focused on the advantages presented by this type of materials in terms of mechanical behavior High-tech industries have exploited these properties and developed applications in many fields of the biomaterial and material engineering in the past decades. Consequently, the development of non-destructive evaluation techniques to characterize mechanical behaviors of these materials is a key issue.

A common setup for ultrasonic testings of this kind of structure consists of an elastic layer sandwiched between two fluids. One of the basic physical concepts for ultrasound quantification of the plate bases on the estimation of reflection and transmission coefficients of ultrasonic waves on its interfaces. While simple and well-documented for testing of isotropic materials, reflection and transmission phenomena for anisotropic and heterogeneous materials are much more complicated from both physical interpretation and technical calculation points of view. General theoretical results on the reflection and transmission phenomena can be found in the comprehensive books of Fedorov (1968), Musgrave (1970) and Auld (1990). Solutions of the reflection and transmission problem have been studied by Rokhlin et al. (1986), Lanceleur et al. (1993) for anisotropic elastic plates and by Deschamps and Hosten (1992) for orthotropic viscoelastic plates.

The deterministic models assume that the modeling parameters are perfectly known. However, most of the time, only partial information is available on these parameters and the actual values which are obtained *via* experimental measurements. So, it is useful to consider these parameters as uncertain. Among other approaches, probability theory provides an effective and robust framework to take into account such uncertainties. The uncertainty introduced on the parameters allows, in particular, to assess its impact on the interest parameters. In this work, we aim to assess the impact of the anisotropic and heterogeneity of elastic properties of the solid layer on the measured reflection and transmission coefficients. A parametric probabilistic method, which is based on the maximum entropy principle, will be used to generate an optimal probabilistic model by using a minimal parameter number to describe uncertain elasticity field. Moreover, the semi-analytical finite element (SAFE) method will be used to compute the reflection and transmission coefficients of anisotropic heterogeneous solid plates.

In this study, we are interested mainly on ultrasonic characterization of cortical bone. In this context, some models have been developed by Desceliers et al. (2009b, 2012) to evaluate the first arriving velocity in bones by using the axial transmission technique. Here, we will study a three-layer model consisting of a cortical bone solid layer immersed in two fluids. The material properties of the fluids and the bone mass density are supposed to be deterministic. The elasticity tensor of bone tissue is randomly varied in the thickness direction. We investigate the global reflection and transmission coefficients of ultrasonic waves through the cortical bone. A sensitivity analysis of material properties will be performed. In the deterministic model from which the stochastic model is constructed, the cortical bone plate is assumed to be homogeneous and transversely isotropic elastic. Whereas in the stochastic model, the plate is anisotropic

and heterogeneous with material properties that vary along the thickness axis. In principle, it will be possible to estimate the physical parameters of bone from the acoustic response. This can be done by solving an inverse problem which will require appropriate resolution strategy. This study presents therefore the first step in the modeling of the direct problem which is indispensable to the identification of material properties.

After this introduction, this chapter is organized as follows. In section 2.2, the elastoacoustic problem in the solid-fluid coupling is formulated. In section 2.3, a numerical approach is proposed for determining the mean reflection and transmission coefficients, which are associated with the deterministic model. The probabilistic model of the elasticity tensor and the estimated mean values of these coefficients are presented in section 2.4. Then, in section 2.5, the validation of the SAFE formulation and the convergence analysis of the proposed stochastic method are presented. Section 2.6, presents some numerical results simulating a test on a cortical bone specimen immersed in the fluid. Two kind of bone material properties are investigated : homogeneous mean properties (see. subsection 2.6.1) and functionally graded mean material properties (see. subsection 2.6.2). Finally, conclusions will be drawn in section 2.7.

2.2 Problem statement

2.2.1 Description of geometrical configuration

Let $\mathcal{R}(O;\mathbf{e}_1,\mathbf{e}_2,\mathbf{e}_3)$ the cartesian reference frame, where O is the origin of the space and $(\mathbf{e}_1,\mathbf{e}_2,\mathbf{e}_3)$ is the orthonormal basis for this space. The coordinates of a point M are specified by (x_1,x_2,x_3) in $\mathcal{R}$. Figure 2.1 presents a two-dimensional geometrical description of the considered problem for which both the incident wave and the mechanical system are assumed to be invariant with respect to x_3. An elastic layer with constant thickness h, which occupies the unbounded domain Ω^b in $\mathbf{e}_1$-axis, is surrounded by two fluid half-spaces Ω_1^f and Ω_2^f. The interfaces between the elastic layer Ω^b and the fluid domains Ω_1^f and Ω_2^f are assumed to be flat and denoted by Γ_1^{bf} and Γ_2^{bf}, respectively, as shown in Fig. 2.1.

The system is excited by an incident plane and harmonic wave p_I propagating with a pulsation ω in the upper fluid domain Ω_1^f and arriving to the interface Γ_1^{bf} from an angle θ as shown in Fig. 2.1.

Due to the nature of the source and to the geometrical configuration, the components in the $\mathbf{e}_3$-direction of the displacement vectors in the solid and fluid domains will be zeros and the elastoacoustic wave motion will be independent of x_3. Hence, all derivatives with respect to x_3 vanish in the partial differential equations that govern the wave motion. Consequently, the coordinate x_3 is implicit in the mathematical expressions to follow. The present study is conducted in the plane $(O;\mathbf{e}_1,\mathbf{e}_2)$. These conditions are associated with the plane strain model.

As a result, the domains Ω_1^f, Ω_2^f and Ω^b may be defined by:

$$\begin{aligned}\Omega_1^f &= \{M(x_1,x_2); x_2 \geq 0\}\,,\\ \Omega_2^f &= \{M(x_1,x_2); x_2 \leq -h\}\,,\\ \Omega^b &= \{M(x_1,x_2); -h \leq x_2 \leq 0\}\,.\end{aligned} \tag{2.1}$$

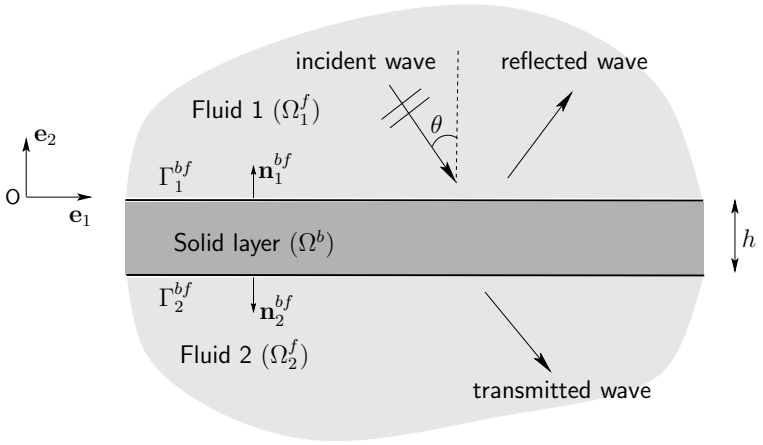

Figure 2.1: Description of geometrical configuration

2.2.2 Governing equations

In this section, we present the equations of motion for the three domains Ω_1^f, Ω_2^f and Ω^b. In what follows, we note respectively ∇ , $\nabla\cdot$ and ∇^2 the gradient, divergence and Laplacian operators in two-dimensional space (2D). The time derivative is denoted by a dot superimposed. We denote respectively by ∂_i and ∂_i^2 the partial derivatives of first and second operators with respect to x_i. In general, the boldface symbols are used to designate the matrices, the fields of vectors and tensors in two-dimensional and three-dimensional spaces.

2.2.2.1 Equations in the fluid domains

The fluid occupying the domain Ω_α^f $(\alpha = 1, 2)$ is considered non-dissipative and homogeneous. The mass density and sound speed of these domains are denoted by ρ_α and c_α, respectively. In the context of linearized theory, and neglecting the body forces, the wave equation in the domain Ω_α^f reads:

$$\frac{1}{c_\alpha^2}\ddot{p}_\alpha - \nabla^2 p_\alpha = 0, \quad \forall M \in \Omega_\alpha^f \quad (\alpha = 1, 2), \tag{2.2}$$

where p_α denotes the pressure in the fluid. The velocity vector $\mathbf{v}_\alpha(M, t)$ is related to the pressure field $p_\alpha(M, t)$ by the Euler equation:

$$\rho_\alpha \dot{\mathbf{v}}_\alpha + \nabla p_\alpha = \mathbf{0}, \quad \forall M \in \Omega_\alpha^f \quad (\alpha = 1, 2), \tag{2.3}$$

where $\dot{\mathbf{v}}_\alpha = \ddot{\mathbf{u}}^{(\alpha)}$ and $\mathbf{u}^{(\alpha)}$ denotes the displacement vector in the fluid.

2.2.2.2 Equations in the solid layer

By neglecting body forces, the equation of motion in Ω^b is given by:

$$\rho\ddot{\mathbf{u}} - \nabla\cdot\boldsymbol{\sigma} = \mathbf{0}, \quad \forall M \in \Omega^b, \tag{2.4}$$

which may be written in the vectorial form:

$$\rho\ddot{\mathbf{u}} - \mathbf{L}^T\mathbf{s} = \mathbf{0}, \quad \forall M \in \Omega^b, \tag{2.5}$$

where ρ is the mass density of the solid, $\mathbf{u} = (u_1, u_2)^T$ is the displacement vector in which the superscript "T" denotes the transpose operator, the vector $\mathbf{s}$ contains the components of the stress tensor $\boldsymbol{\sigma}$ and is denoted by $\mathbf{s} = (\sigma_{11}, \sigma_{22}, \sigma_{12})^T$. The operator $\mathbf{L}$ is defined by:

$$\mathbf{L} = \mathbf{L}_1\partial_1 + \mathbf{L}_2\partial_2, \quad \mathbf{L}_1 = \begin{bmatrix} 1 & 0 \\ 0 & 0 \\ 0 & 1 \end{bmatrix}, \quad \mathbf{L}_2 = \begin{bmatrix} 0 & 0 \\ 0 & 1 \\ 1 & 0 \end{bmatrix}. \tag{2.6}$$

Using the notation of Voigt, the Hooke law reads: $\mathbf{s} = \mathbf{c}\mathbf{e}$ where $\mathbf{e}$ is a vector containing the strain components which are given by $\mathbf{e} = (\epsilon_{11}, \epsilon_{22}, 2\epsilon_{12})^T = \mathbf{L}\mathbf{u}$, and $\mathbf{c}$ is the matrix containing the components of the anisotropic elasticity tensor *via* the Voigt notation:

$$\mathbf{c} = \begin{bmatrix} c_{11} & c_{12} & c_{16} \\ c_{12} & c_{22} & c_{26} \\ c_{16} & c_{26} & c_{66} \end{bmatrix}. \tag{2.7}$$

In this model, it is assumed that the physical properties of the solid only depend on x_2, *i.e.* $\mathbf{c} = \mathbf{c}(x_2)$.

2.2.2.3 Continuity conditions at interfaces

The continuity conditions at the fluid-solid interfaces Γ_1^{bf} and Γ_2^{bf} can written in the same way. The continuity condition of the normal velocity and of the traction at the interfaces requires:

$$\begin{aligned} &\nabla p_\alpha \cdot \mathbf{n}_\alpha^{bf} = -\rho_\alpha \ddot{\mathbf{u}}^{(\alpha)} \cdot \mathbf{n}_\alpha^{bf}, \\ &\boldsymbol{\sigma}\mathbf{n}_\alpha^{bf} = -p_\alpha \mathbf{n}_\alpha^{bf}, \end{aligned} \qquad \forall M \in \Gamma_\alpha^{bf} \quad (\alpha = 1, 2), \tag{2.8}$$

where $\mathbf{n}_\alpha^{bf}$ is the normal unit vector of Ω^b at the interfaces Γ_α^{bf}. Seeing that $\mathbf{n}_1^{bf} = -\mathbf{n}_2^{bf} = (0, 1)^T$, Eqs (2.8) may be written as follows:

$$\begin{aligned} &\partial_2 p_\alpha = -\rho_\alpha \ddot{u}_2^{(\alpha)}, \\ &\mathbf{t} = (0, -p_\alpha)^T, \end{aligned} \qquad \forall M \in \Gamma_\alpha^{bf} \qquad (\alpha = 1, 2), \tag{2.9}$$

where $\mathbf{t} = (\sigma_{12}, \sigma_{22})^T = \mathbf{L}_2^T\mathbf{s}$.

2.3 Solution of the mean problem by using the SAFE method

2.3.1 Wave field in the fluids

Let us consider an incident plane and harmonic wave with an amplitude P_I and an angular frequency ω, propagating in Ω_1^f, which is incident under angle θ to the interface Γ_1^{bf} (see Fig. 2.1). As the system is homogeneous along $\mathbf{e}_1$, we look for the plane wave solution in the fluids (see Eq. (2.2)) in the form:

$$p_\alpha(M, t) = \hat{p}_\alpha(x_2)\exp(\mathrm{i}(k_1 x_1 - \omega t)), \quad \forall M \in \Omega_\alpha^f \ (\alpha = 1, 2), \tag{2.10}$$

where $\mathrm{i}^2 = -1$. Substituting Eq. (2.10) into Eqs. (2.2) and (2.9) leads to the following equation:

$$\partial_2^2 \hat{p}_\alpha + \left(\frac{\omega^2}{c_\alpha^2} - k_1^2\right) \hat{p}_\alpha = 0, \quad \forall M \in \Omega_\alpha^f \quad (\alpha = 1, 2). \tag{2.11}$$

The solutions in Ω_1^f is a superposition of the incident and reflected wave fields of which the amplitudes are denoted by P_I and P_R, respectively:

$$\hat{p}_1 = P_I \exp(\mathrm{i} k_2^{(1)} x_2) + P_R \exp(-\mathrm{i} k_2^{(1)} x_2), \tag{2.12}$$

where $k_1^2 + (k_2^{(1)})^2 = (\omega/c_1)^2 = k_0^2$. Note that the angle of incidence is θ, the wavenumbers with respect to $\mathbf{e}_1$ and $\mathbf{e}_2$ are respectively given by: $k_1 = k_0 \sin\theta$ and $k_2^{(1)} = -k_0 \cos\theta$.

Similarly with the solutions in Ω_2^f, the transmitted wave field is sought in the form:

$$\hat{p}_2 = P_T \exp(\mathrm{i} k_2^{(2)} (x_2 + h)), \tag{2.13}$$

where $k_2^{(2)} = -\sqrt{(\omega/c_2)^2 - k_1^2}$. P_T

2.3.2 Wave field in the solid layer

By seeking the plane wave solution in the solid (see Eq. (2.5)) in the following form:

$$\mathbf{u}(M, t) = \hat{\mathbf{u}}(x_2) \exp[\mathrm{i}(k_1 x_1 - \omega t)], \quad \forall M \in \Omega^b, \tag{2.14}$$

where $\hat{\mathbf{u}} = (\hat{u}_1, \hat{u}_2)^T$, the equation of motion (2.5) can be written as a system of partial differential equations on the displacement $\hat{\mathbf{u}}$ with respect only to x_2:

$$\left(-\omega^2 \mathbf{A}_1 + k_1^2 \mathbf{A}_2\right) \hat{\mathbf{u}} - \mathrm{i} k_1 \mathbf{A}_3^T \partial_2 \hat{\mathbf{u}} - \partial_2 \mathbf{t} = \mathbf{0}, \quad \forall x_2 \in [-h, 0], \tag{2.15}$$

where $\mathbf{t} = (i k_1 \mathbf{A}_3 + \mathbf{A}_4 \partial_2)\hat{\mathbf{u}}$, and the two-by-two matrices $\mathbf{A}_i$ $(i = 1, ..., 4)$ are defined by:

$$\mathbf{A}_1 = \rho \mathbf{I}_d, \quad \mathbf{A}_2 = \mathbf{L}_1^T \mathbf{c} \mathbf{L}_1, \quad \mathbf{A}_3 = \mathbf{L}_2^T \mathbf{c} \mathbf{L}_1, \quad \mathbf{A}_4 = \mathbf{L}_2^T \mathbf{c} \mathbf{L}_2, \tag{2.16}$$

where $\mathbf{I}_d$ is the two-by-two identity matrix. The boundary conditions (2.9) may be expressed as:

$$\hat{u}_2(0) = \frac{1}{\rho_1 \omega^2} \partial_2 \hat{p}_1(0), \quad \hat{u}_2(-h) = \frac{1}{\rho_2 \omega^2} \partial_2 \hat{p}_2(-h), \tag{2.17}$$

$$\mathbf{t}(0) = (0, -\hat{p}_1(0))^T, \quad \mathbf{t}(-h) = (0, -\hat{p}_2(-h))^T, \tag{2.18}$$

or by using the general solutions given by Eqs. (2.12) and (2.13), the boundary conditions (2.17) and (2.18) read:

$$\hat{u}_2(0) = \frac{(P_I - P_R)}{\alpha_1}, \quad \hat{u}_2(-h) = \frac{P_T}{\alpha_2}, \tag{2.19}$$

$$\mathbf{t}(0) = -(0, P_I + P_R)^T, \quad \mathbf{t}(-h) = -(0, P_T)^T, \tag{2.20}$$

where the constants α_1 and α_2 are given by:

$$\alpha_1 = \frac{\mathrm{i}k_2^{(1)}}{\rho_1\omega^2}, \quad \alpha_2 = \frac{\mathrm{i}k_2^{(2)}}{\rho_2\omega^2}. \tag{2.21}$$

By eliminating P_R and P_T in Eqs. (2.19) and (2.20), one may deduce the impedance conditions as follows:

$$\mathbf{t}(0) = \mathbf{F}_0 - \mathbf{P}_1\hat{\mathbf{u}}(0), \quad \mathbf{t}(-h) = \mathbf{P}_2\hat{\mathbf{u}}(-h), \tag{2.22}$$

where

$$\mathbf{F}_0 = \begin{pmatrix} 0 \\ -2P_I \end{pmatrix}, \quad \mathbf{P}_1 = \begin{bmatrix} 0 & 0 \\ 0 & -\alpha_1 \end{bmatrix}, \quad \mathbf{P}_2 = \begin{bmatrix} 0 & 0 \\ 0 & -\alpha_2 \end{bmatrix}. \tag{2.23}$$

2.3.3 Weak formulation and finite element implementation

The weak formulation of the problem defined from Eq. (2.15) may be derived using standard procedure (Bathe, 1996). Let $\mathcal{C}^{ad}$ be the admissible function space constituted by all sufficiently smooth complex-valued functions $x_2 \in]-h, 0[\rightarrow \delta\mathbf{u}(x_2) \in \mathbb{C} \times \mathbb{C}$, where $\mathbb{C}$ denotes the set of complex numbers. The conjugate transpose of $\delta\mathbf{u}$ is denoted $\delta\mathbf{u}^*$. By multiplying the Eq. (2.15) with the test function $\delta\mathbf{u}^* \in C^{ad}$ and integrating by parts, we obtain:

$$\begin{aligned} &\int_{-h}^{0} \delta\mathbf{u}^* \left(-\omega^2\mathbf{A}_1 + k_1^2\mathbf{A}_2 - \mathrm{i}k_1\mathbf{A}_3^T\partial_2\right)\hat{\mathbf{u}}\, dx_2 \\ &\qquad + \int_{-h}^{0} \partial_2(\delta\mathbf{u}^*)\mathbf{t}\, dx_2 - [\delta\mathbf{u}^*\mathbf{t}]_{-h}^{0} = 0 \end{aligned} \tag{2.24}$$

The last term in Eq. (2.24) may be calculated by using the boundary conditions (2.22). Thus the weak formulation of the problem is: Find $\mathbf{u}(x_2) \in \mathcal{C}^{ad}$ such that:

$$\begin{aligned} &\int_{-h}^{0} \delta\mathbf{u}^* \left(-\omega^2\mathbf{A}_1 + k_1^2\mathbf{A}_2 - \mathrm{i}k_1\mathbf{A}_3^T\partial_2\right)\hat{\mathbf{u}}\, dx_2 \\ &\qquad + \int_{-h}^{0} \partial_2(\delta\mathbf{u}^*)\left(\mathrm{i}k_1\mathbf{A}_3 + \mathbf{A}_4\partial_2\right)\hat{\mathbf{u}}\, dx_2 \\ &\qquad + \delta\mathbf{u}^*(0)\mathbf{P}_1\hat{\mathbf{u}}(0) + \delta\mathbf{u}^*(-h)\mathbf{P}_2\hat{\mathbf{u}}(-h) = \delta\mathbf{u}^*\mathbf{F}_0, \end{aligned} \tag{2.25}$$

for all $\delta\mathbf{u}^* \in C^{ad}$. In order to solve the problem (see Eq. (2.25)) by using the FEM, we discretize the domain $[-h, 0]$ into a mesh which contains n^{el} elements Ω_e : $[-h, 0] = \bigcup_e (e = 1, ..., n^{el})$. Using the Galerkin method, the two functions $\mathbf{u}$ and $\delta\mathbf{u}$ in each element e are approximated using the same interpolation function:

$$\hat{\mathbf{u}}(x_2) = \mathbf{N}_e\mathbf{U}_e, \quad \delta\mathbf{u}(x_2) = \mathbf{N}_e\delta\mathbf{U}_e, \quad \forall x_2 \in \Omega_e, \tag{2.26}$$

where $\mathbf{N}_e$ is the interpolation function, $\mathbf{U}_e$ and $\delta\mathbf{U}_e$ are respectively the vectors of nodal solutions of $\mathbf{u}$ and $\delta\mathbf{u}$ in Ω_e. Substituting Eq. (2.26) into Eq. (2.25) and assembling the elementary matrices, we obtain the following system of linear equations:

$$(\mathbf{K} + \mathbf{K}^{\Gamma})\mathbf{U} = \mathbf{F}, \tag{2.27}$$

where $\mathbf{U}$ is the global nodal displacement vector, $\mathbf{K}$ is the global "stiffness matrix" of the solid, $\mathbf{K}^{\Gamma}$ represents the coupling operator between the fluid and the solid, and $\mathbf{F}$ is the force vector:

$$\mathbf{K} = -\omega^2 \mathbf{K}_1 + k_1^2 \mathbf{K}_2 + \mathrm{i} k_1 \mathbf{K}_3 + \mathbf{K}_4, \tag{2.28}$$

$$\mathbf{K}^{\Gamma} = \mathrm{Diag}\left\{0, -\frac{\rho_2 \omega^2}{\alpha_2}, 0, ..., 0, -\frac{\rho_1 \omega^2}{\alpha_1}\right\}, \tag{2.29}$$

$$\mathbf{F} = \{0, ..., 0, -2P_I\}^T, \tag{2.30}$$

and:

$$\begin{aligned} \mathbf{K}_1 &= \bigcup_e \int_{\Omega_e} \mathbf{N}_e^T \mathbf{A}_1 \mathbf{N}_e dx_2, \quad \mathbf{K}_2 = \bigcup_e \int_{\Omega_e} \mathbf{N}_e^T \mathbf{A}_2 \mathbf{N}_e dx_2, \\ \mathbf{K}_3 &= \bigcup_e \int_{\Omega_e} 2\left[\mathbf{N}_e'^T \mathbf{A}_3 \mathbf{N}_e\right]_a dx_2, \quad \mathbf{K}_4 = \bigcup_e \int_{\Omega_e} \mathbf{N}_e'^T \mathbf{A}_4 \mathbf{N}_e' dx_2, \end{aligned} \tag{2.31}$$

where the notation $[\star]_a$ denotes the antisymmetric part of $[\star]$ and $\star'$ the derivative with respect to x_2. In this study, Gauss quadrature rule has been used for computing the integrations over the elements.

2.3.3.1 Reflection and transmission coefficients

The reflection and transmission coefficients are defined by the ratio between the amplitudes of the reflected and transmitted waves to the amplitude of the incident wave, respectively, and may be computed by using (see Eqs. (2.19) and (2.20)):

$$R = \left|\frac{P_R}{P_I}\right| = \left|1 - \frac{\alpha_1 \hat{u}_2(0)}{P_I}\right|, \quad T = \left|\frac{P_T}{P_I}\right| = \left|\frac{\alpha_2 \hat{u}(-h)}{P_I}\right|, \tag{2.32}$$

where $\hat{u}_2(0)$ and $\hat{u}_2(-h)$ are obtained by solving the system of linear equations (2.27).

2.4 Stochastic model

2.4.1 Probabilistic model of the elasticity tensor

In order to describe the heterogeneity which is randomly varied in the solid layer along the $\mathbf{e}_2$ direction, we use a probabilistic model which has been proposed by Soize (2006) for the construction of the random elastic tensor. This model is constructed by using the maximum entropy principle (Jaynes, 1957a,b) and the random matrix theory (Mehta, 2004) in three dimension. Note that the solid layer is assumed to be homogeneous along $\mathbf{e}_3$ direction. As a result, a two dimensional model could be used for studying the wave propagation problem instead of 3D model. In this study, the random elasticity tensor has first been generated in three dimensions (21 components) with a high value of the spatial correlation length in $\mathbf{e}_3$ direction. Then only heterogeneous six components, which correspond to the ones defined in the plane $(\mathbf{e}_1, \mathbf{e}_2)$, are extracted to be used for the 2D simulation. In this chapter, we only sketch out the main features of the model in the context of this study. A more detailed description may be found in Soize (2006).

By using the Voigt notation, we denote by $\mathbf{C}(x_2)$ the random elastic matrix at x_2 and by $\mathbf{c}(x_2)$ its mean value, respectively, and for which the following relationship is satisfied $\mathbb{E}\{\mathbf{C}(x_2)\} = \mathbf{c}(x_2)$, where $\mathbb{E}\{\star\}$ designates the mathematical expectation. Note that $\mathbf{C}(x_2)$ and $\mathbf{c}(x_2) \in \mathbf{M}_n^+(\mathbb{R})$ where $\mathbf{M}_n^+(\mathbb{R})$ is the set of all the $(n \times n)$ real symmetric positive-definite matrices and $\mathbb{R}$ is the set of real numbers. As indicated above, the random elasticity tensor is defined in the three dimensional space and the Voigt notation is used, as a result, the study is carried out with $n = 6$. The matrix $\mathbf{c}(x_2) \in \mathbf{M}_n^+(\mathbb{R})$ can be decomposed into a product of a unique upper triangular real matrix $\boldsymbol{\mathcal{L}}(x_2)$ with strictly positive diagonal entries and its transpose:

$$\mathbf{c}(x_2) = \boldsymbol{\mathcal{L}}^T(x_2)\, \boldsymbol{\mathcal{L}}(x_2). \tag{2.33}$$

Using this model, the random matrix $\mathbf{C}(x_2)$ is parameterized by its mean value $\mathbf{c}(x_2)$, the dispersion level δ and the correlation length λ in the $\mathbf{e}_2$-direction, which is denoted by $\mathbf{C}(x_2; \mathbf{c}, \delta, \lambda)$ and may be decomposed into the following form:

$$\mathbf{C}(x_2; \mathbf{c}, \delta, \lambda) = \boldsymbol{\mathcal{L}}^T(x_2)\, \mathbf{G}(x_2; \mathbf{c}, \delta, \lambda)\, \boldsymbol{\mathcal{L}}(x_2), \tag{2.34}$$

where $\mathbf{G}(x_2; \mathbf{c}, \delta, \lambda)$, called the stochastic germ matrix, is a homogeneous and normalized non-Gaussian positive-definite matrix-valued second-order random field with values in $\mathbb{M}_n^+(\mathbf{R})$.

The dispersion parameter δ, which is a scalar, controls the dispersion of the random matrix $\mathbf{G}(x_2; \mathbf{c}, \delta, \lambda)$ and must satisfy the following inequality $0 < \delta < \sqrt{(n+1)/(n+5)}$, which allows the mean-square convergence condition for the germ matrix to be hold (Soize, 2001). It is proved that the dispersion parameter δ is related to a parameter δ_C which evaluates the dispersion of the random matrix $\mathbf{C}(x_2)$ by the relation given by:

$$\delta_C(x_2) = \frac{\delta}{\sqrt{n+1}} \left\{ 1 + \frac{\{\mathrm{Tra}(\mathbf{c}(x_2))\}^2}{\mathrm{Tra}([\mathbf{c}(x_2)]^2)} \right\}^{1/2}, \tag{2.35}$$

where Tra is the trace operator. Note that the dispersion of the random matrix $\mathbf{C}(x_2)$ is a scalar field and depends on x_2, n and δ.

Note that the elastic plate is assumed to be invariant in the $\mathbf{e}_3$-direction and homogeneous in the $\mathbf{e}_1$-direction. As a result, a two dimensional model could be used for studying the wave propagation problem instead of 3D model. However, the random elasticity tensor has first been generated in three dimensions (21 components) with a high value of the spatial correlation lengths in the $\mathbf{e}_1$ and $\mathbf{e}_3$ directions. Then, only heterogeneous six components, which correspond to the ones defined in the plane $(\mathbf{e}_1, \mathbf{e}_2)$, are extracted to be used for the simulations.

The correlation length λ, which is a scalar, is a measure of the distance up to which one has spatial memory of the spatial variations in the material properties. There is no unique definition of this length scale, but from a phenomenological point of view it can be defined as the length scale up to which the effect of a small local perturbation in the system may be felt. This is due to the fluctuation which links the response of the system to a local perturbation and the large scale behavior of the two-point correlation function.

2.4.2 Stochastic solver for the uncertain mechanical system

2.4.2.1 Random reflection and transmission coefficients

The stochastic solver used is based on the Monte Carlo simulation. For a given parameter set $\mathbf{c}$, h, δ and λ, we begin with the discretization of the 1D domain $[-h, 0]$ by using quadratic Lagrangian elements. The global x_2-coordinates of the Gauss points in all elements are denoted by x_2^k for $k = 1, ..., n_{gp}$, where n_{gp} is the total number of the Gauss points in the mesh.

Let n_r be the total number of realizations, we may construct the set of the independent realizations ϕ_j, for $j = 1, ..., n_r$, defined by:

$$\mathcal{S} = \left\{ \left\{ \mathbf{C}(x_2^k, \phi_1) \right\}_{k=1,...,n_{pg}}, ..., \left\{ \mathbf{C}(x_2^k, \phi_{n_r}) \right\}_{k=1,...,n_{pg}} \right\} \tag{2.36}$$

in which $\left\{ \mathbf{C}(x_2^k, \phi_j) \right\}_{k=1,...,n_{pg}}$ are n_{pg} samples at points x_2^k of one realization of random matrix field $\mathbf{C}(x_2; \mathbf{c}, \delta, \lambda)$ as described in Section 2.4.1 (see Soize (2006) and Desceliers et al. (2012)). 2.36. The procedure is summarized in Appendix A of chapter 2 (p51), and implemented in Matlab.

For each statistical independent realization ϕ_j, for $j = 1, ..., n_r$, by using $\left\{ \mathbf{C}(x_2^k, \phi_j) \right\}_{k=1,...,n_{pg}}$, n_r statistical independent realizations of the random reflection and transmission coefficients, $R(\phi_j)$ and $T(\phi_j)$ respectively, may be calculated following the SAFE procedure presented in Section 2.3.

The required total number of realizations n_r is determined by performing convergence analyses of the statistical estimates of the second order moments of R and T. Finally, the confidence regions of random reflection and transmission coefficients R and T for a probability level P_c can be determined.

2.4.2.2 Convergence analysis

The convergence analysis with respect to the number of realizations n_r is carried out in studying the convergence of statistical estimates of the second-order moments of R and T, respectively denoted by $\mathrm{m}_{R,2} = \mathbb{E}\left\{R^2\right\}$ and $\mathrm{m}_{T,2} = \mathbb{E}\left\{T^2\right\}$. The statistical estimates $\mathrm{Conv}_R(n_r)$ and $\mathrm{Conv}_T(n_r)$ of $\mathrm{m}_{R,2}$ and $\mathrm{m}_{T,2}$ respectively are defined by:

$$\mathrm{Conv}_R(n_r) = \left(\frac{1}{n_r} \sum_{j=1}^{n_r} R^2(\phi_j) \right)^{1/2}, \quad \mathrm{Conv}_T(n_r) = \left(\frac{1}{n_r} \sum_{j=1}^{n_r} T^2(\phi_j) \right)^{1/2}. \tag{2.37}$$

To determine whether a sequence is convergent to a limit, we need to define a distance function (or metric) which measures the distance between the terms of the sequence. The concept of close to each other can be made fully rigorous using the notion of a metric. Therefore, discussing convergence of a sequence of random variables boils down to discussing what metrics can be used to measure the distance between two random variables. The mean-square convergence analysis of every statistical estimators is carried out with respect to the number of samples in the Monte Carlo numerical simulation. The objective of such convergence analysis is double. Indeed, such a convergence also implies a convergence in probability and a convergence in law. As a consequence, the estimation of the probability density functions of such

random variables makes sense. In addition, such a convergence analysis allows calculating the number of simulations required for estimating every second-order statistics of these random variables.

2.4.2.3 Confidence regions

A procedure based on the quantile method is performed for estimating the confidence regions of both random variables R and T. The confidence region of R is limited by a lower envelope and an upper envelope, denoted by r^- and r^+, respectively:

$$\mathbb{P}(r^- < R \leq r^+) = P_c, \tag{2.38}$$

where $\mathbb{P}(A)$ denotes the probability measure of an event A.

Let F_R be the cumulative distribution function of R defined by $F_R(r) = \mathbb{P}(R \leq r)$. The p-th quantile ($p \in]0, 1[$) of F_R is defined by:

$$\zeta(p) = \inf \{r : F_R(r) \geq p\}. \tag{2.39}$$

The lower and upper envelopes r^- and r^+ are defined by:

$$r^- = \zeta\left(\frac{1 - P_c}{2}\right), \quad r^+ = \zeta\left(\frac{1 + P_c}{2}\right). \tag{2.40}$$

Let $\tilde{r}_1 < ... < \tilde{r}_n$ be the order statistics associated with $R(\phi_1), ..., R(\phi_{n_r})$, we have the following estimations:

$$r^- \simeq \tilde{r}_{j^-}, \quad j^- = \text{fix}[n_r(1 - P_c)/2], \tag{2.41}$$

$$r^+ \simeq \tilde{r}_{j^+}, \quad j^+ = \text{fix}[n_r(1 + P_c)/2], \tag{2.42}$$

in which $\text{fix}(z)$ denotes the integer part of the real number z.

2.5 Numerical parameters and validation

2.5.1 Bone as a Functionally Graded Material properties waveguide.

Although the method presented in previous sections can be used for a wide variety of media having unidirectional varying elastic properties, our attention here will focus on studying cortical bone plates in the context of diagnostic of bone tissues using qualitative ultrasound techniques. The purpose of ultrasonic measurements of bones is to identify individuals with excessive bone fragility and fracture risk associated with various pathologies. Bone tissue has been shown to be a heterogeneous, anisotropic and porous material. Bone tissues may be distinguished into two different kinds: the cortical bone and the cancellous bone. Although there may be different shapes of bones that have functions, they are mostly composed of an outer layer of cortical bone and an inner layer of cancellous bone. An exception to this configuration is the vertebrae that protect the spinal chord. It has been shown that osteoporosis in cortical long bones

may reduce bone layer thickness, modify the material properties by increasing porosity, namely in the endosteal region, and degrade the mineral content of bone matrix.

Basically, the wave propagation in long bones using the ultrasound technique may be modeled by using a coupled system which consists of a constant-thickness plate-like or cylindrical-like solid (for representing the cortical bone) surrounded by fluids (for representing soft tissues and marrow). In most studies, modeling of guided waves in long bones has been carried out by using fluid-loaded homogeneous plate or cylindrical models. For the wave propagation modeling in long bones, an important factor which should be attentively considered, is the heterogeneity of bone properties in the bone cross-section. In recent decades, progress on imaging techniques offer an accurate view of the bone microstructures. As result, newly visible bone characteristic, such as a gradient of porosity is emerging. Imaging of microstructures of long bone cross sections at all ages, and for both genders, shows that the mean porosity in the endosteal region (inner part) is significantly higher than the porosity in the periosteal region (outer part) (Bousson et al., 2001; Thomas et al., 2005; Sansalone et al., 2010). In other words, the porosity decreases from the endosteal to the periosteal part. From elasticity point of view, such gradient of porosity is expected to induce a gradient of intracortical bone material properties such as mass density and stiffness. Normally, when porosity decreases, the mean mass density and elastic constants should increase. However, for the best of our knowledge, we don't know precisely how the intracortical porosity varies, and, how its affects the mesoscopic as well as macroscopic material properties. Recently, in Gräsel et al. (2017) an approach for porosity measurement of human cortical bone using a new device is investigated.

Wave phenomena in functionally-graded bone structures have been studied by somes authors in the frequency-domain (Baron and Naili, 2008, 2010; Baron, 2012) or in the time-domain (Desceliers et al., 2008; Haiat et al., 2009; Nguyen and Naili, 2012, 2013). According to results obtained in such studies, the gradient of properties can provides some information on material properties. It has been shown that the gradient of properties can provide supplementary information to better understand ultrasound guided wave in cortical bones. For instance, in Baron (2012), where cortical bone is modeled by a cylinder having functionally graded material properties in the radial direction, the proposed model seems to be relevant to evaluating age-related changes in intracortical bone. In most studies, the cortical bone material has been considered as a deterministic (visco-)elastic medium. The ultrasonic response of random bone plates have been recently studied in Desceliers et al. (2009b) and Naili et al. (2015) but only in the time-domain. As far as we know, the reflection of ultrasonic waves on a random bone plate has still not been addressed in the literature.

The mass density and material properties used for the simulation have usually been empirically obtained from experimental or numerical studies which were carried out on many bone samples (Dong and Guo, 2004).

2.5.2 Numerical parameters

2.5.2.1 Mean homogeneous material properties.

We are motivated by modeling biological materials that typically feature an anisotropic elastic plate sandwiched between two homogeneous fluids. In the context of bone evaluation, the solid and fluid layers in the model represent bone and soft tissues (soft tissue and marrow), respectively.

In this study, we are interested in modeling of an *in vitro* ultrasonic test of anisotropic elastic bone plates. The bone phantom has a constant thickness $h = 4$ mm and is submerged in water. The mechanical properties of the fluid ($\rho_1 = \rho_2$ and $c_1 = c_2$) are shown in Tab. 2.1. The bone plate is assumed to have a transversely isotropic elastic behavior. The mass density of the bone and the essential components of the elastic matrix are given in Tab. 2.1, which are taken from the mechanical test results obtained by Dong and Guo (2004). Note that the other components of the elasticity matrix are given by: $c_{22} = c_{33}, c_{12} = c_{13} = c_{21} = c_{31}, c_{23} = c_{32}$ and $c_{55} = c_{66}$. In what follows, bone tissue can be assumed to have a functionally graded material properties, but when a portion of bone tissue is assumed to be a homogeneous elastic medium, its material properties will be those presented in Tab. 2.1.

Table 2.1: Mechanical parameters for the mean model.

Fluid material properties		Solid material properties					
$\rho_1 = \rho_2$	$c_1 = c_2$	ρ	c_{11}	c_{22}	c_{12}	c_{66}	$c_{16} = c_{26}$
$(kg.m^{-3})$	$(m.s^{-1})$	$(kg.m^{-3})$	(GPa)	(GPa)	(GPa)	(GPa)	(GPa)
1000	1500	1722	23.05	15.10	8.71	4.7	0

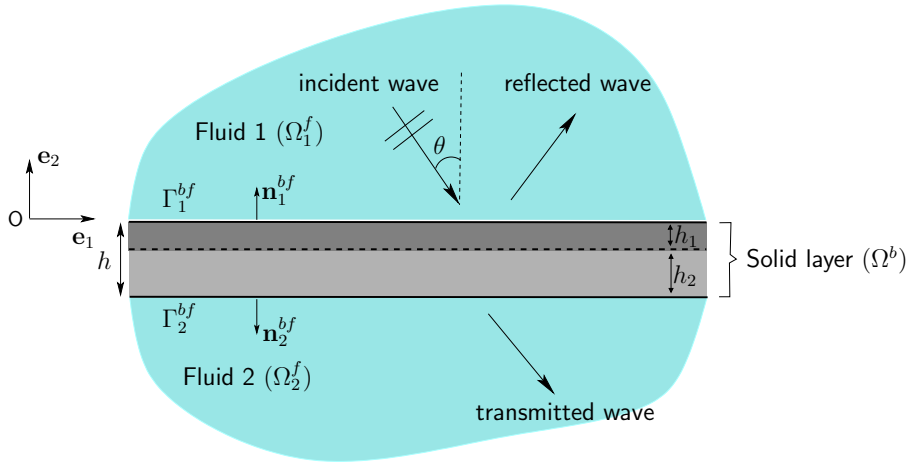

Figure 2.2: Description of geometrical configuration when cortical is modeled as a functionally graded material waveguide.

2.5.2.2 Functionally Graded Material properties.

As discussed in the previous section, the cortical bone can be assumed to have Functionally Graded Material properties in the transversal direction. Most of time, the simple realistic gradient of properties profile explored is an affine spacial variation. As described in Bousson et al. (2001), the spacial organization of the microstructure driven by the size and the spatial concentration of different pores can affect the macroscopic behavior of bone. As result, it would be more relevant to propose a gradient of properties which can approximately take into account this difference (directly or indirectly). Among the models proposed in the literature, the one proposed in Desceliers et al. (2012) seems to be interesting. In such model, the variation is not introduced in the global porosity but in a portion corresponding to the endosteal region. In this study, we use a gradient model based on the one proposed in Desceliers et al. (2012) in which a cortical bone plate with a mechanical alteration is studied in a statistical sens. The solid layer which represents the cortical bone is split into two layers, a homogeneous layer (representing the periosteal region) and a "porous" layer having functionally graded material properties. The solid layer is immersed in fluids. Thus, the model proposed in this study involves an anisotropic solid layer sandwiched between two homogeneous fluids and having functionally graded material properties in the transversal direction (i.e., through-thickness direction).

In Fig. 2.2, the thickness h_1, represents the portion of the cortical bone having homogeneous mean material properties, and h_2, the part considered heterogeneous with a gradient of physical properties. The gradient profile is modeled in next paragraphs.

Gradient modeling. The gradient of material properties used in this study is modeled as follows. Let a and b two real as $-h \leq b \leq a \leq 0$, $h_2 = |a-b|$ and $h_1 = |a|$. The elasticity tensor and the mass density of bone part having gradient properties are defined by:

$$\mathbf{c}(x_2) = \begin{cases} [1-g(x_2)]\mathbf{c}^s + g(x_2)\mathbf{c}^f & \forall\, x_2 \in]b, a[, \\ \mathbf{c}^s & \forall\, x_2 \in [a, 0], \\ \mathbf{c}^f & \forall\, x_2 \in [-h, b], \end{cases}$$
$$\rho(x_2) = \begin{cases} [1-g(x_2)]\rho^s + g(x_2)\rho_2 & \forall\, x_2 \in]b, a[, \\ \rho^s & \forall\, x_2 \in [a, 0], \\ \rho_2 & \forall\, x_2 \in [-h, b], \end{cases} \tag{2.43}$$

and:

$$\begin{aligned} &g(x_2) = d_0 + d_1 x_2 + d_2 x_2^2 + d_3 x_2^3, \\ &d_0 = a^2(a-3b)/(a-b)^3, \quad d_1 = 6ab/(a-b)^3, \\ &d_2 = -3(a+b)/(a-b)^3, \quad d_3 = 2/(a-b)^3. \end{aligned} \tag{2.44}$$

This model is such that $\mathbf{c}(a) = \mathbf{c}^s$, $\mathbf{c}(b) = \mathbf{c}^f$ and for $x_2 = a$ or $x_2 = b$, $\partial_2 \mathbf{c}(x_2) = 0$ and $\partial_2 \rho(x_2) = 0$. The quantities $\mathbf{c}^s$ and ρ^s are respectively the mean elastic tensor and the mass density of the portion of bone having constant physical properties. These quantities are those given in Tab. 2.1 for the solid material properties. The quantity $\mathbf{c}^f$ can be seen as the "elasticity tensor" of the fluid medium representing the

marrow (Desceliers et al., 2012). All components of $\mathbf{c}^f$ are zero except $c^f_{11}, c^f_{12}, c^f_{13}, c^f_{21}, c^f_{22}, c^f_{23}, c^f_{31}, c^f_{32}$ et c^f_{33} that are all equal to $K_1 = \rho_2 c_2^2$. Fig. 2.3 shows the profile of the mean tensor of elasticity with different values of h_2.

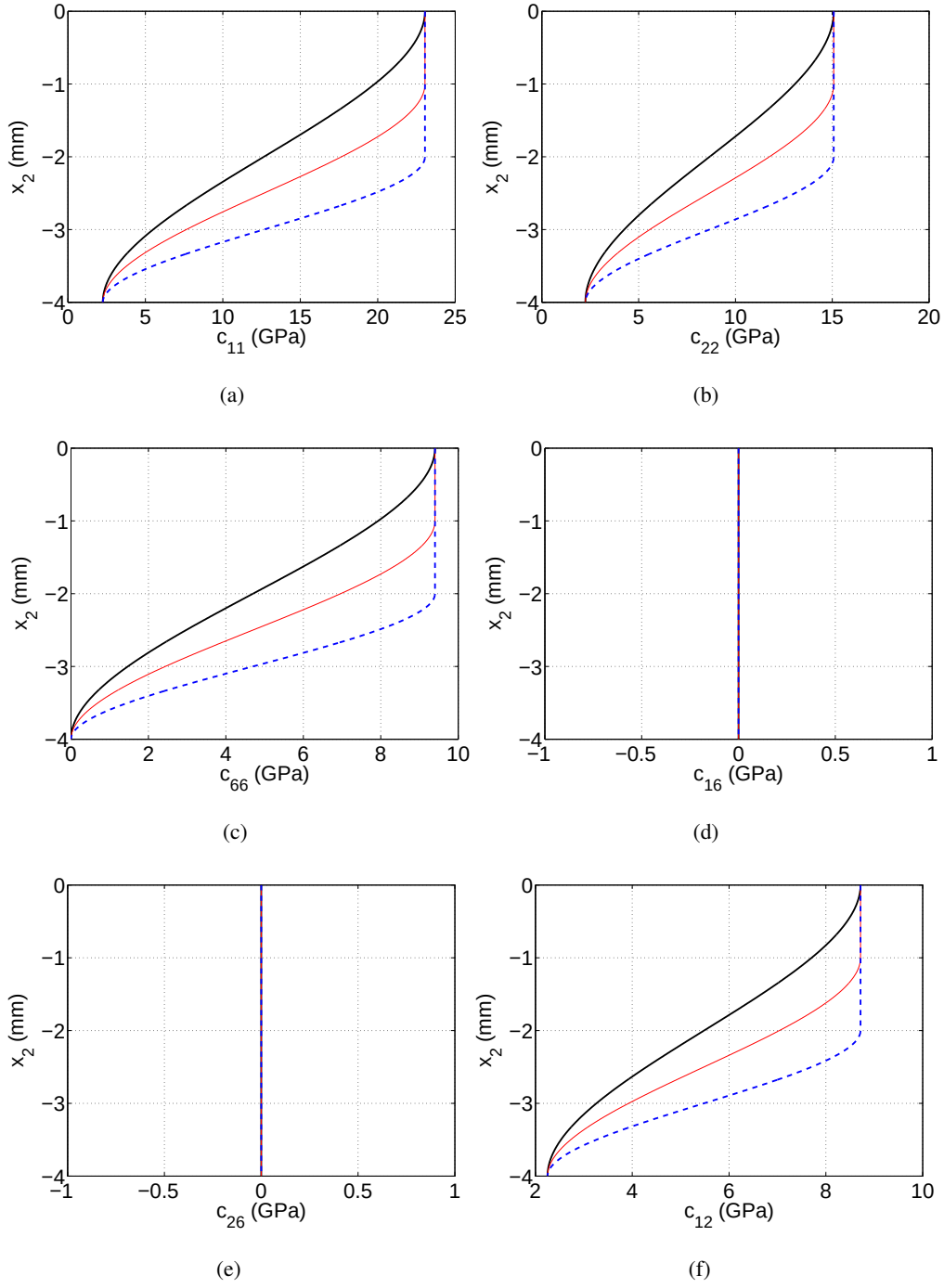

Figure 2.3: Profiles properties. Graphs of functions $x_2 \longrightarrow \mathbf{c}(x_2)$ when $h_2 = 2$ mm (dotted line), $h_2 = 3$ mm (thin solid line) and $h_2 = h = 4$ mm (thick solid line).

2.5.2.3 Parameters for the uncertain elasticity model

(i) Generation from homogeneous mean material properties This study is restricted to only consider the one dimensional uncertain heterogeneous in the direction $\mathbf{e}_2$. Thus, only the dispersion δ and one correlation length λ need to be introduced to control the statistical fluctuations of the elasticity field in the $\mathbf{e}_2$-direction. For this study, a fixed correlation length $\lambda = 0.1$ mm will be used, which may be seen as a center-to-center distance between osteons in cortical bone (see Cowin (2001), Wang et al. (1999) and Nguyen et al. (2010)). When a portion of bone is assumed to be homogeneous, the random elasticity tensor $\mathbf{C}(x_2; \mathbf{c}, \delta, \lambda)$ is generated from the mean homogeneous material properties defined in Tab. 2.1. Three different values of the dispersion $\delta = 0.1, 0.2$ and 0.3 will be investigated. The coefficient δ_C which evaluates the dispersion of the random field $\mathbf{C}$ is defined by Eq. (2.35). Note that three different values of the dispersion $\delta = 0.1, 0.2$ and 0.3 lead to three different values of the dispersion $\delta_C = 0.1251, 0.2431$ and 0.3647 at any points localized on the interface Γ_1^{bf}.

(ii) Generation from heterogeneous mean material properties When bone is modeled as a functionally graded material waveguide, the random elasticity tensor $\mathbf{C}(x_2; \mathbf{c}, \delta, \lambda)$ is generated from the mean gradient profile of properties $\mathbf{c}(x_2)$ defined in the previous section, which is parametrized by a, b, $\mathbf{c}^s$ and $\mathbf{c}^f$, denoted by $\mathbf{c}(x_2; a, b, \mathbf{c}^s, \mathbf{c}^f)$. The spatial correlation length λ is still set at 100 μm. Different values of gradient parameters are investigated, performing a parametric study. The level of fluctuation of material properties will be controlled using different values of dispersion parameter δ.

2.5.3 Validation of the SAFE formulation

A convergence study is firstly performed in order to verify the SAFE formulation. For this purpose, we consider a homogeneous bone layer. The material properties of the solid layer are the ones of the mean model presented in Tab. 2.1. The frequency of the incident wave is 2 MHz. In this case, the analytic solution can be obtained by solving the system of equations (2.15)-(2.21).

Figure 2.4 presents the reflection (see Fig. 2.4(a)) and transmission coefficients (see Fig. 2.4(b)) when $\theta = 30°$, with respect to the parameter of the spatial discretization given by number of elements n^{el}. In these graphs, the dashed and solid lines are respectively associated with the analytical solution and the SAFE solution. For $n^{el} \geq 50$, the finite element results of both coefficients R and T converge to their analytic solutions with errors less than 0.01%. Under such conditions, the element size is lower than $1/10$ of the shortest wavelength in the medium, which is in accordance with the usual requirements in conventional finite element analysis (Bathe, 1996).

2.5.4 Stochastic convergence analysis

The stochastic convergence analysis seeks to determine the minimal number of realizations by the Monte Carlo solver to calculate in order to do the statistics on the interest quantities given by R nd T. For this test, we consider a 4mm-thickness solid layer meshed by 200 quadratic elements. Note

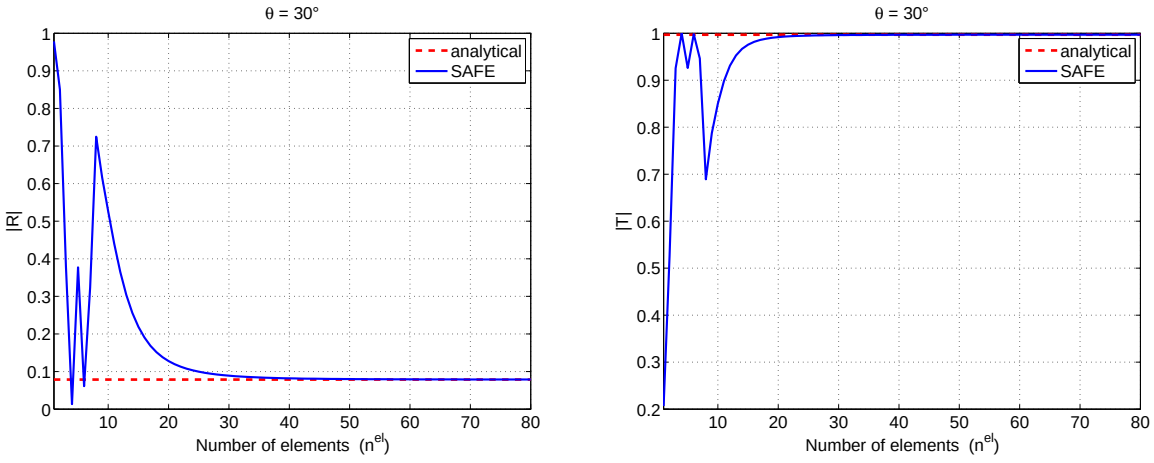

(a) (b)

Figure 2.4: (Color online) Variation of the reflection and transmission coefficients *versus* the parameter of the spatial discretization given by number of elements n^{el} for $\theta = 30°$. The solid line is associated with the SAFE formulation and the dashed line is associated with the analytic solution. (a) reflection coefficient; (b) transmission coefficient.

that this discretization allows us to satisfy the requirement that at least 5 elements per correlation length ($\lambda = 0.1$ mm) are needed.

Figure 2.5(a) shows an illustration of a realization of the spatial variation of the components of the random field $\mathbf{C}(x_2)$ with respect to x_2 when $\delta = 0.1$. The probability density function allows the description of the relative likelihood for this random variable to take on a given value. The probability of the random variable falling within a particular range of values is given by the integral of this variable density over that range. As such, the information obtained from the probability density function reflects behavior expectations in the material properties. These statements may also be seen in Fig. 2.5(b) in which the probability density functions of random elasticity matrix components $\mathbf{C}(x_2)$ on the interface Γ_1^{bf} are computed and presented. These functions are obtained when $\delta = 0.1$. One may verify that the mean values of the $\mathbf{C}$'s components are equal to the values given for the mean model (see Section 2.3). In particular, the mean of c_{16} and c_{26} are equal to zero (transversely isotropic model).

Figure 2.6 shows the graphs of functions $n_r \rightarrow \mathrm{Conv}_R(n_r)$ and $n_r \rightarrow \mathrm{Conv}_T(n_r)$ defined in Sec. 2.4.2.2 in the case of normal incidence ($\theta = 0°$). For the case $\delta = 0.1$ (see Fig. 2.6(a)), the second-order moments of R and of T are converged for $n_r \geq 500$. Indeed, one may check that for more than 500 realizations, $0.697 \leq \mathrm{Conv}_R(n_r) \leq 0.698$ and $0.717 \leq \mathrm{Conv}_T(n_r) \leq 0.718$, which are approximately equivalent to 0.1% of variation. For $\delta = 0.2$ (see Fig. 2.6(b)) and $\delta = 0.3$ (see Fig. 2.6(c)), the convergence is achieved for $n_r \geq 600$ and $n_r \geq 700$, respectively.

From Fig. 2.6, it can be seen that the fluctuations of the statistical estimators of the variance of random reflection and random transmission coefficients decrease with the number of realizations. In addition, the statistical estimators converge to deterministic values which are the variances of the random reflection

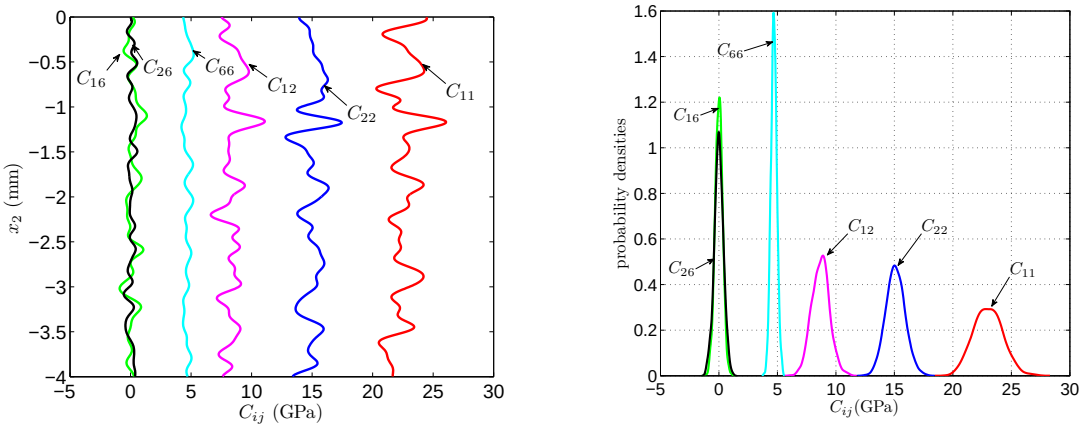

(a) (b)

Figure 2.5: (Color online) (a): x_2-profiles of C_{ij} components when $\delta = 0.1$. (b): Probability density functions of the components of the random elastic tensor on boundaries Γ_1^{bf} when $\delta = 0.1$.

and transmission coefficients. We show only the convergence analysis of the statistical estimators for the variance as an example. Nevertheless, such a convergence analysis has also been carried out for every other statistics of the random output of the probabilistic model (probability density functions, confidence regions, etc.).

2.6 Numerical results and discussion

In this section, we present some numerical results simulating a test on a cortical bone immersed in fluid. Two kind of cortical bone material properties are investigated. The bone tissue can be assumed to have homogeneous mean properties or functionally graded mean material properties. The corresponding results are presented and discussed in sections 2.6.1 and 2.6.2, for homogeneous properties and FGM properties, respectively.

2.6.1 Application to bone tissue with homogeneous mean material properties

2.6.1.1 Sensitivity of reflection and transmission coefficients to the dispersion parameter

We investigate the effects of the fluctuation of bone elasticity which is represented by the dispersion parameter δ and allows to control the statistical fluctuation level. Afterwards, we can assess the impact of this fluctuation on the acoustic responses R and T. The 4mm-thickness bone plate described above has been studied.

Table 2.2 presents the mean values $\mathbb{E}(R)$ and $\mathbb{E}(T)$ calculated by the Monte Carlo numerical method of R and T respectively corresponding to different incident angles. For comparison purposes, the deterministic solutions obtained by mean model are also presented. For instance, we may notice that the mean

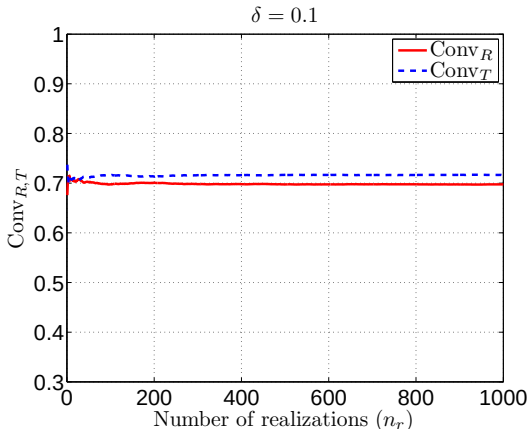

(a)

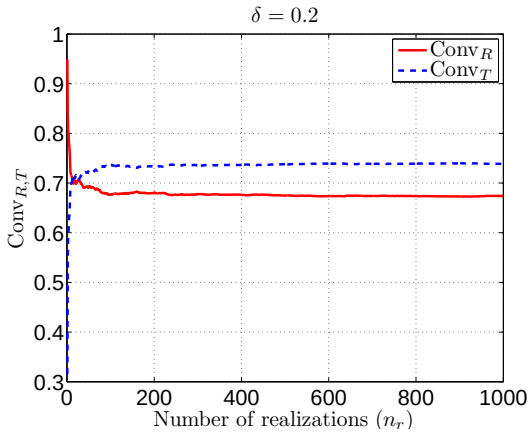

(b)

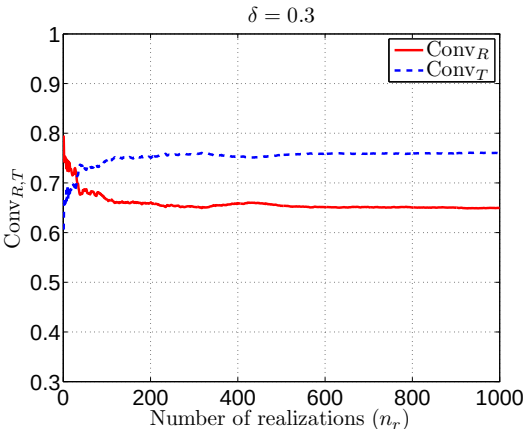

(c)

Figure 2.6: (Color online) Stochastic convergence analysis for the case $\theta = 0°$ and $f = 1$ MHz. Graphs of functions $n_r \to \mathrm{Conv}_R(n_r)$ and $n_r \to \mathrm{Conv}_T(n_r)$. The solid and dashed lines are respectively associated with the functions $\mathrm{Conv}_R(n_r)$ and $\mathrm{Conv}_T(n_r)$. (a) $\delta = 0.1$; (b) $\delta = 0.2$; (c) $\delta = 0.3$.

value of the reflection coefficient $\mathbb{E}(R)$ for an angle of incidence $\theta = 0°$ is lower than the deterministic ones, and it slightly decreases with larger dispersion δ. On the contrary, the mean values $\mathbb{E}(T)$ are greater

than the deterministic ones, and it increases while δ increases.

Table 2.2: Mean values of the reflection and transmission coefficients R and T. These results are obtained with $f = 1$ MHz.

	$\mathbb{E}(R)$				$\mathbb{E}(T)$			
δ	$\theta = 0°$	$\theta = 30°$	$\theta = 45°$	$\theta = 60°$	$\theta = 0°$	$\theta = 30°$	$\theta = 45°$	$\theta = 60°$
0.1	0.697	0.651	0.081	0.676	0.716	0.760	0.997	0.731
0.2	0.670	0.647	0.125	0.671	0.735	0.766	0.995	0.719
0.3	0.633	0.638	0.176	0.672	0.748	0.777	0.990	0.698
Mean model	0.704	0.651	0.066	0.678	0.709	0.758	0.997	0.734

Figure 2.7 presents the confidence regions of the reflection and transmission coefficients for a probability level $P_c = 0.95$. The case of an angle for incidence $\theta = 0°$ is shown. The mean values of these coefficients are represented by a thick line (black line, color online) while the ones obtained with the deterministic model are represented by a thin line (red line, color online). These results show that the width of the confidence regions increases with the dispersion. One may also note that the upper envelope and lower envelope are not symmetrical with respect to the mean value. The presence of heterogeneities in the bone layer may lead to underestimated (or overestimated) R (or of T, respectively).

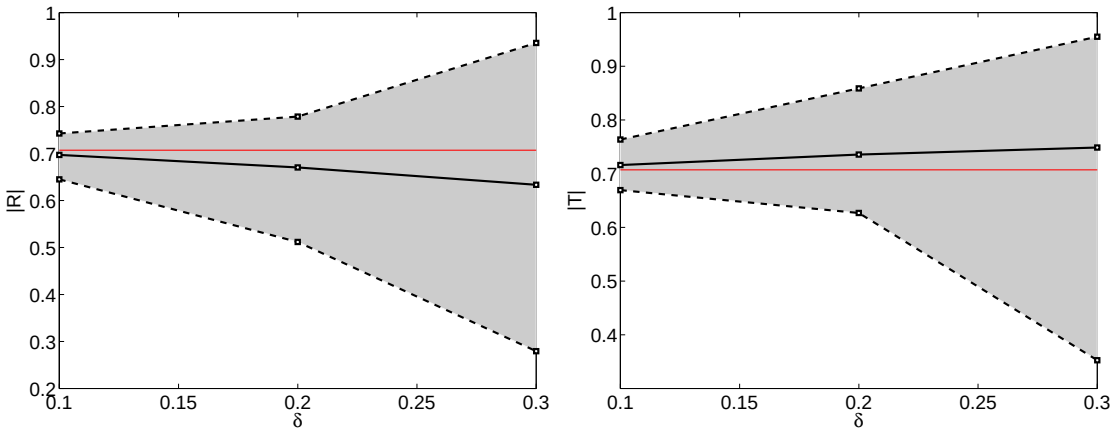

(a) (b)

Figure 2.7: (Color online) Confidence region (colored in grey domain between the dashed lines) associated with a probability level $P_c = 0.95$ and mean values (thick and black line) of reflection and transmission coefficients with respect to the dispersion coefficient δ of random elasticity tensor. The coefficients R and T obtained with the deterministic model are plotted with the thin lines (red line). (a) reflection coefficient R; (b) transmission coefficient T. These results are obtained with $f = 1$ MHz.

Figures 2.8 and 2.9 show the confidence regions of the reflection and transmission coefficients *versus* frequency from 50 Hz to 2 MHz for the incidence angles $\theta = 0°$ and $\theta = 30°$ respectively when $\delta = 0.1$.

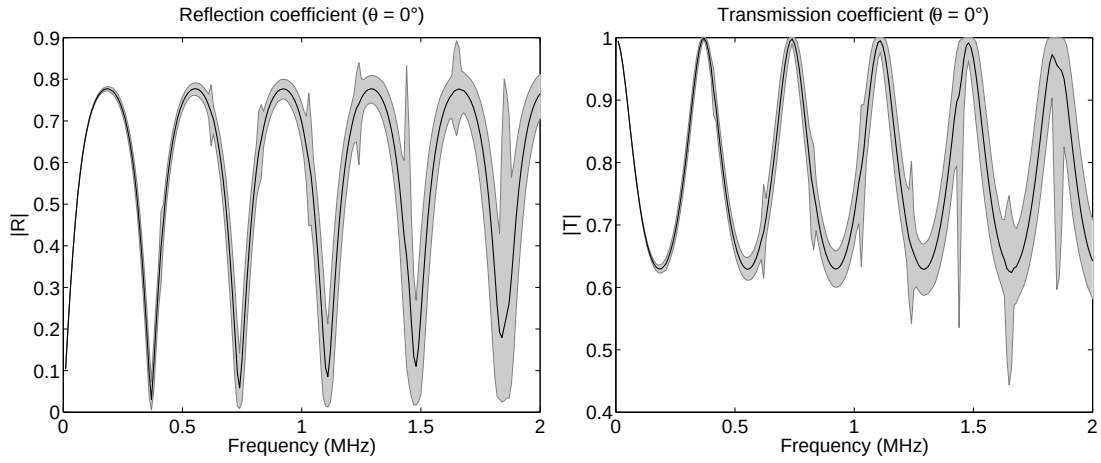

(a) (b)

Figure 2.8: Confidence regions of reflection and transmission coefficients with respect to frequency when $\delta = 0.1$. The confidence regions are colored in grey while the reflection and transmission coefficients obtained *via* the deterministic model are plotted in thick solid line. Incidence angle $\theta = 0°$: (a) reflection coefficient R; (b) transmission coefficient T.

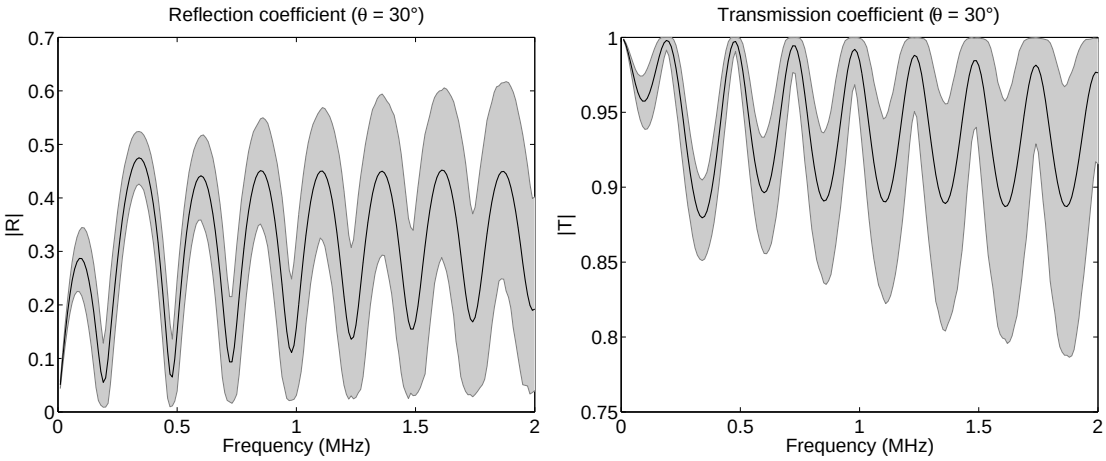

(a) (b)

Figure 2.9: See caption of Fig. 2.8. Incidence angle $\theta = 30°$: (a) reflection coefficient R; (b) transmission coefficient T.

The confidence regions are colored in gray while the reflection and transmission coefficients obtained *via* the deterministic model are plotted in thick solid line. These figures show that the width of the confidence region increases with frequency. This width is more important for the incidence $\theta = 30°$. For a normal incidence (see Fig. 2.8), some peaks may be observed on the envelops characterizing the confidence regions of both coefficients of reflection and transmission. These peaks are due to the shear modes that exist when the material properties become fully anisotropic. However, these peaks are quasi nonexistent when $\theta = 30°$ for both coefficients.

In Figs. 2.10 and 2.11, the probability density functions of the reflection and transmission coefficients are presented for two frequencies given by $f = 250$ kHz and $f = 1$ MHz respectively when $\delta = 0.1$. For each frequency and each coefficient of reflection and transmission, the probability density function is plotted for four incidence angles $\theta = 0°, 30°, 45°$ and $60°$. By comparing Figs. 2.10 and 2.11, the findings show that the dispersion and the asymmetry degree of the probability density functions increase with f for all incidence angles.

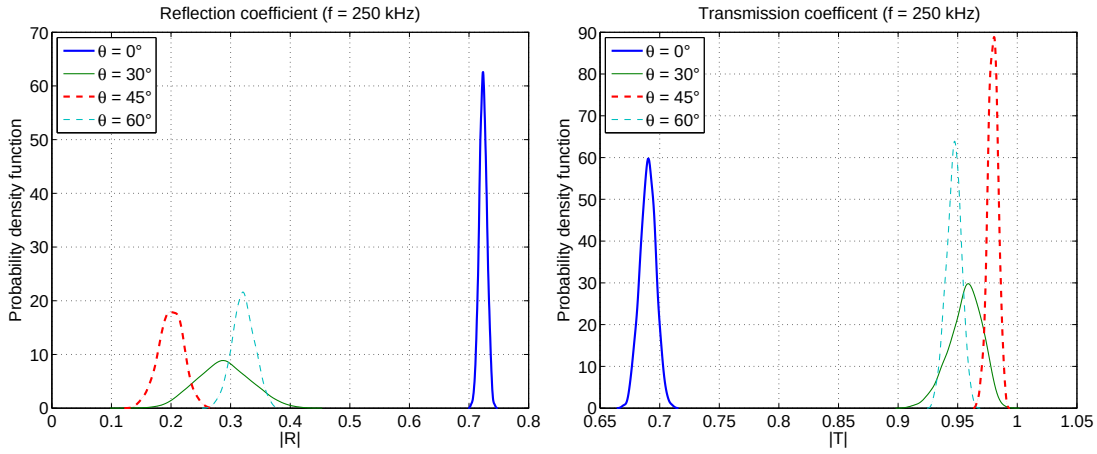

(a) (b)

Figure 2.10: (Color online) Probability density function for four incidence angles given by $\theta = 0^o, 30^o, 45^o$ and 60^o when $\delta = 0.1$. These results are obtained with $f = 250$ kHz. (a) reflection coefficient R; (b) transmission coefficient T.

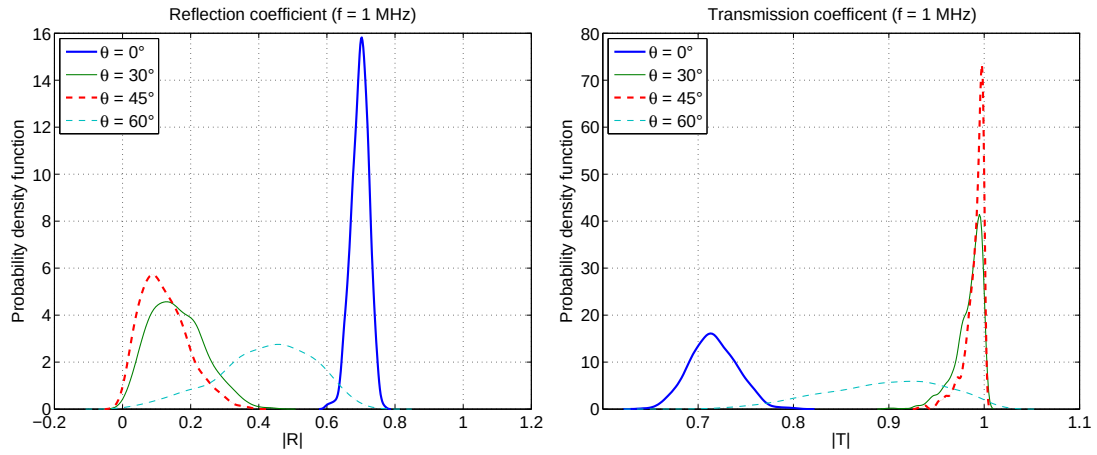

(a) (b)

Figure 2.11: See caption of Fig. 2.10. These results are obtained with $f = 1$ MHz.

2.6.1.2 Sensitivity analysis with respect to the angle of incidence

Comparison between the mean and stochastic models

In this section, the results obtained with the mean model using the values defined in Section 2.5.2.1 are compared to the ones obtained with the stochastic model. In Figs. 2.12 and 2.13, the reflection and transmission coefficients are respectively plotted as a function of the incidence angle for the three values of the dispersion ($\delta = 0.1$ (thin line), $\delta = 0.2$ (dotted line) and $\delta = 0.3$ (dashed line)) and two frequencies ($f = 250$ kHz and $f = 1$ MHz). The mean values of the reflection and transmission coefficients are calculated for each incidence angle for $\theta \in [0, 90[$ with a step of $1°$. Likewise, these coefficients obtained with the mean model are plotted with thick solid lines.

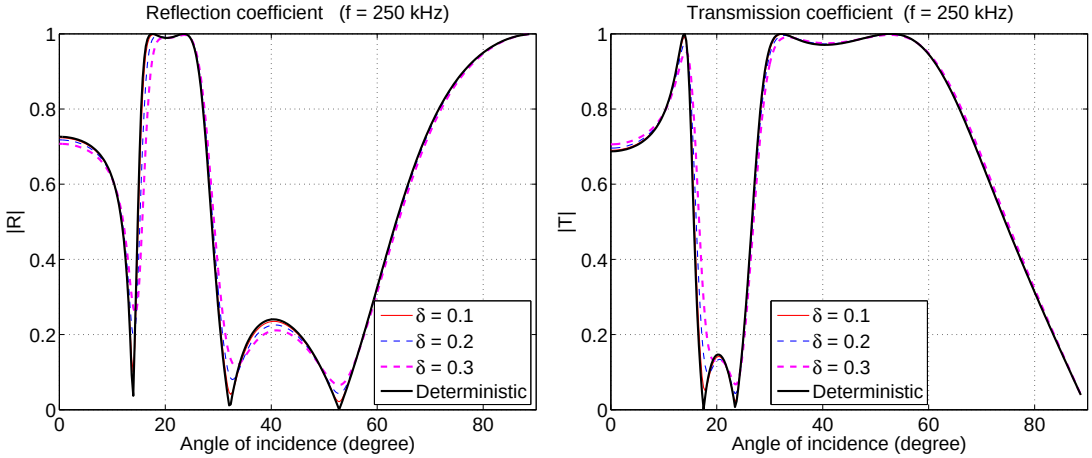

(a) (b)

Figure 2.12: (Color online) Mean estimated values of the reflection and transmission coefficients when $\delta = 0.1$ (thin line), $\delta = 0.2$ (thin line) and $\delta = 0.3$ (dashed line). The thick solid line is obtained with the mean model. These results are obtained with $f = 250$ kHz. (a) reflection coefficient R; (b) transmission coefficient T.

When $f = 250$ kHz and $\delta = 0.1$, the curves of the estimated mean (thin line) and mean model (thick line) for the reflection and transmission coefficients R and T are almost superimposed. However, when $\delta = 0.2$ and $\delta = 0.3$ the difference is more significant, especially when the angle of incidence is less than $10°$ degrees or comprised between $25°$ and $40°$.

When $f = 1$ MHz, the difference between the estimated mean values (thin line) and values of mean model (thick line) for the reflection and transmission coefficients R and T is significant even when $\delta = 0.1$. This difference is amplified when $\delta = 0.2$ and 0.3.

The concept of critical angles is usually introduced in the framework of an interface separating two half-spaces to evaluate angles for which the angle of incidence produces a total reflection. This concept is used in this work. With the values defined for the deterministic model, the velocities of longitudinal elastic waves in $\mathbf{e}_1$ and $\mathbf{e}_2$ -directions are respectively $c_{p1} = \sqrt{c_{11}/\rho} = 3660$ m.s^{-1} and $c_{p2} = \sqrt{c_{22}/\rho} =$

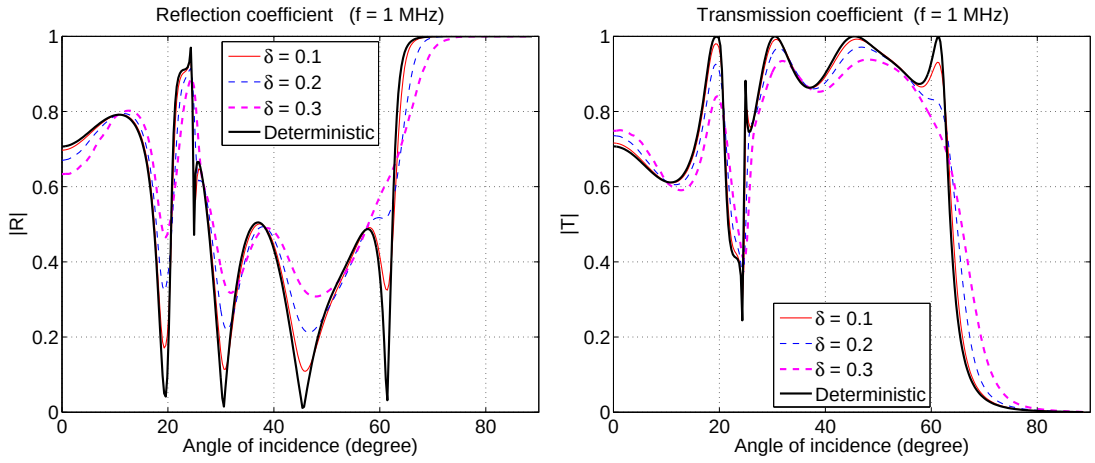

(a) (b)

Figure 2.13: See caption of Fig. 2.12. These results are obtained with $f = 1$ MHz.

2961 m.s^{-1}. The velocity of shear elastic wave is given by $c_t = \sqrt{c_{44}/\rho} = 1652.08$ m.s^{-1}. The two critical angles of longitudinal and shear elastic waves are respectively $\theta_{cl} = \arcsin(c_1/cl) = 24.19°$ and $\theta_{ct} = \arcsin(c_1/ct) = 65.23°$ where $cl = \max(c_{p1}, c_{p2})$. The amplitude of the reflection coefficient R is maximal near the first critical angle $\theta_{cl} = 24.19°$.

Note that both these values are found from Fig. 2.13(a) in the case of the deterministic model. The uncertainty on the material properties leads to a lightly different behavior on the first critical angles.

Confidence regions

In this section, the confidence regions associated with a probability level P_c for random fields R and T are calculated. Figures 2.14 and 2.15 represent confidence regions associated with a probability level $P_c = 0.95$ of random fields $\theta \longrightarrow \{R(\theta)\}$ and $\theta \to \{T(\theta)\}$ when $\theta \in [0, 90[$.

The upper envelope and lower envelope are constructed using equations (2.41) and (2.42). Two similar solid lines represent the functions $\theta \to \{r^-(\theta)\}$ and $\theta \to \{r^+(\theta)\}$ ($\theta \to \{t^-(\theta)\}$ and $\theta \to \{t^+(\theta)\}$, respectively) delimiting the confidence region of the reflection coefficient (transmission coefficient, respectively) obtained with the stochastic model when $\delta = 0.1$ (black region), $\delta = 0.2$ (dark gray region) and $\delta = 0.3$ (light gray region). The dotted line represents the function $\theta \to \{R(\theta)\}$ ($\theta \to \{T(\theta)\}$ respectively) obtained with the deterministic model.

It is observed that the width of the confidence interval is not constant over all incidence angles θ increases with the dispersion δ. The width of the confidence interval is large relative to angle of incidence between the two critical angles θ_{cl} and θ_{ct} or close to these two angles.

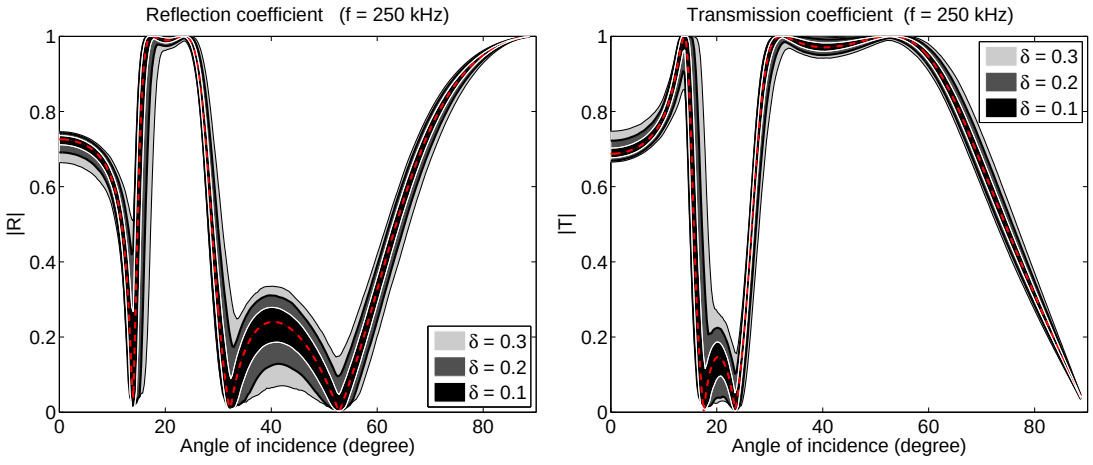

(a) (b)

Figure 2.14: Confidence regions of the reflection and transmission coefficients when $f = 250$ kHz. The dotted line represents the deterministic solutions of R and T

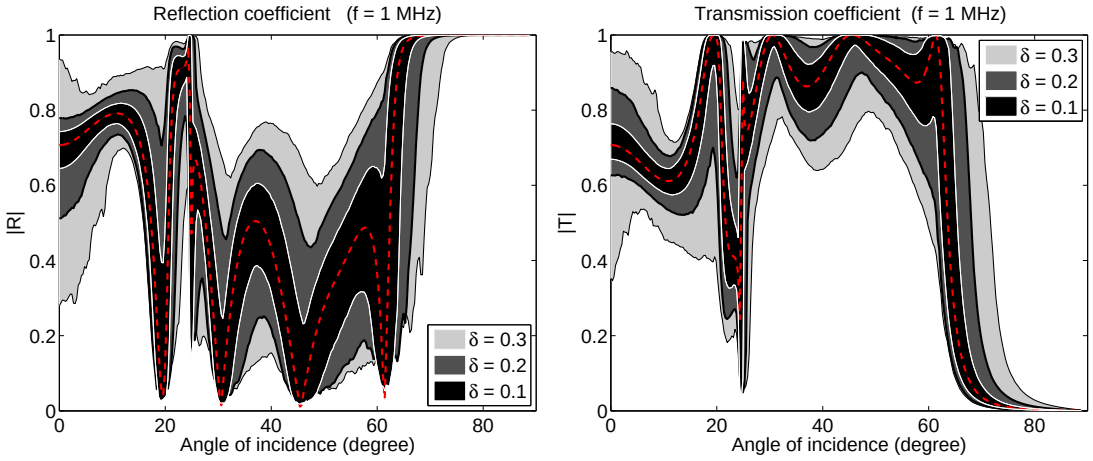

(a) (b)

Figure 2.15: Confidence regions of the reflection and transmission coefficients when $f = 1$ MHz. The dotted line represents the deterministic solutions of R and T

2.6.2 Application to bone tissue with FGM mean properties

2.6.2.1 Sensitivity of R/T coefficients to the dispersion parameter and to the gradient

In this section, we investigate the effects of the gradient and the fluctuation of bone material properties. Note that the gradient is parametrized by h_2 which represents the thickness of the gradient part. The fluctuation of bone elasticity is represented by the dispersion parameter δ and allows to control the statistical fluctuation level. The purpose is to assess the impact of these parameters on the acoustic responses R and T. The 4mm-thickness bone plate described above has been studied. Their material properties are those defined in section 2.5.2.2.

Tab. 2.3 presents the mean values $\mathbb{E}(R)$ and $\mathbb{E}(T)$ calculated by the the Monte Carlo numerical method of R and T respectively corresponding to different incident angles for different values of thickness h_2 (gradient part). For comparison purpose, the deterministic solutions obtained by mean model are also presented. For instance, we may notice that for $h_2 = 4$ mm, the mean value of the reflection coefficient $\mathbb{E}(R)$ for an angle of incidence $\theta = 0°$ is higher than the deterministic ones, and it slightly increases with large δ. On contrary, the mean values $\mathbb{E}(T)$ is smaller than the deterministic ones, and it decreases with large δ. For an angle of incidence $\theta = 0°$ and a dispersion parameter $\delta = 0.1$ or $\delta = 0.2$, we may notice that the mean value of the reflection coefficient $\mathbb{E}(R)$ increases with small h_2. On contrary, the mean values $\mathbb{E}(T)$ decreases with small h_2.

Table 2.3: Mean values of reflection and transmission coefficients with respect to δ and h_2 (length of the gradient portion) for different values of θ when $f = 1$ MHz.

		$\mathbb{E}(R)$				$\mathbb{E}(T)$			
h_2	δ	θ= 0°	$\theta = 30°$	$\theta = 45°$	$\theta = 60°$	$\theta = 0°$	$\theta = 30°$	$\theta = 45°$	$\theta = 60°$
4 mm	0.1	0.410	0.985	0.989	0.997	0.908	0.150	0.123	0.067
	0.2	0.428	0.948	0.967	0.982	0.891	0.274	0.215	0.156
	0.3	0.454	0.901	0.937	0.958	0.872	0.374	0.294	0.240
	Mean model	0.402	0.999	1.000	1.000	0.915	0.044	0.002	0.008
3 mm	0.1	0.450	0.989	0.992	0.998	0.892	0.126	0.106	0.051
	0.2	0.445	0.965	0.975	0.990	0.890	0.226	0.188	0.115
	0.3	0.450	0.925	0.949	0.968	0.879	0.326	0.267	0.199
	Mean model	0.451	0.999	0.999	0.999	0.892	0.022	0.035	0.023
2 mm	0.1	0.551	0.989	0.986	0.986	0.833	0.131	0.151	0.151
	0.2	0.547	0.972	0.975	0.976	0.832	0.203	0.197	0.183
	0.3	0.546	0.940	0.950	0.967	0.820	0.290	0.269	0.209
	Mean model	0.552	0.994	0.989	0.990	0.833	0.107	0.144	0.135

Fig. 2.16 presents the confidence regions of the reflection and transmission coefficients for a probability level $P_c = 0.95$ on a low frequency ($f = 250$ kHz). The case of an angle of incidence $\theta = 0°$ is highlighted. The mean values of these coefficients are represented by a thick line (black line, color online) while the ones obtained with the deterministic model are represented by a thin line (red line, color online). These results show that the width of the confidence regions increases with the dispersion. One may also note that the upper and lower envelopes are not symmetrical with respect to the mean value. The presence of heterogeneities in the bone layer may lead to underestimated (or overestimated) of R (or of T, respectively).

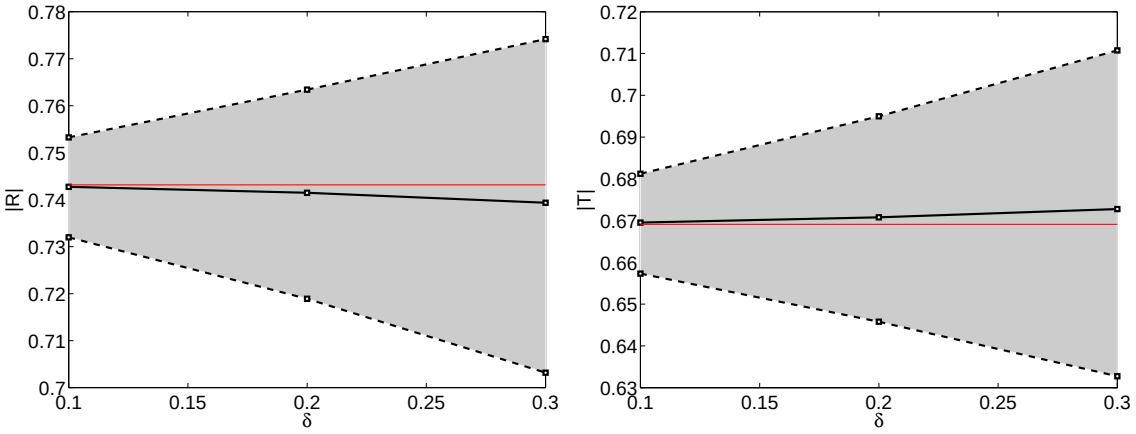

(a) (b)

Figure 2.16: (Color online) Confidence region (colored in grey domain between the dashed lines) associated with a probability level $P_c = 0.95$ and mean values (thick and black line) of reflection and transmission coefficients with respect to the dispersion coefficient δ of random elasticity tensor. The coefficients R and T obtained with the deterministic model are plotted with the thin lines (red line). (a) reflection coefficient R; (b) transmission coefficient T when $f = 250$ kHz and h_2 =3 mm.

Figures 2.17 to 2.19 show the confidence regions of the reflection and transmission coefficients *versus* frequency from 50 Hz to 2 MHz for the incidence angles $\theta = 0°$ and $\theta = 30°$ respectively when $\delta = 0.1$. It can be observed from these figures that the width of the confidence region increases with frequency. Compared with the case of normal incidence, the width of confidence region become more important with oblique incidence, *e.g.* $\theta = 30°$ (see Fig. 2.19). For a normal incidence (see Fig. 2.17), some peaks may be observed on the envelops characterizing the confidence regions of both coefficients of reflection and transmission. These peaks are due to the shear modes that are existed when the material properties become fully anisotropic.

In Fig. 2.19(b), difference between the mean transmission coefficient and the deterministic one become more significant when increasing the frequency. For frequencies more than 700 kHz, the transmission coefficient is not zero despite the total reflection. This phenomenon may be due to the fact that the critical angle changes when the material properties become fully anisotropic. In addition, we may notes that for high frequencies more than 1.25 MHz, the deterministic transmission coefficients are not inside the confidence region.

In Figs. 2.21 and 2.22, the probability density functions of the reflection and transmission coefficients are presented for two frequencies given by $f = 250$ kHz and $f = 1$ MHz ,respectively when $\delta = 0.1$. For each frequency and each coefficient of reflection and transmission, the probability density function is plotted for three incidence angles $\theta = 0°, 30°$ and $45°$. By comparing Figs. 2.21 and 2.22, the findings show that the dispersion and the asymmetry degree of the probability density functions are increased with f for all incidence angles.

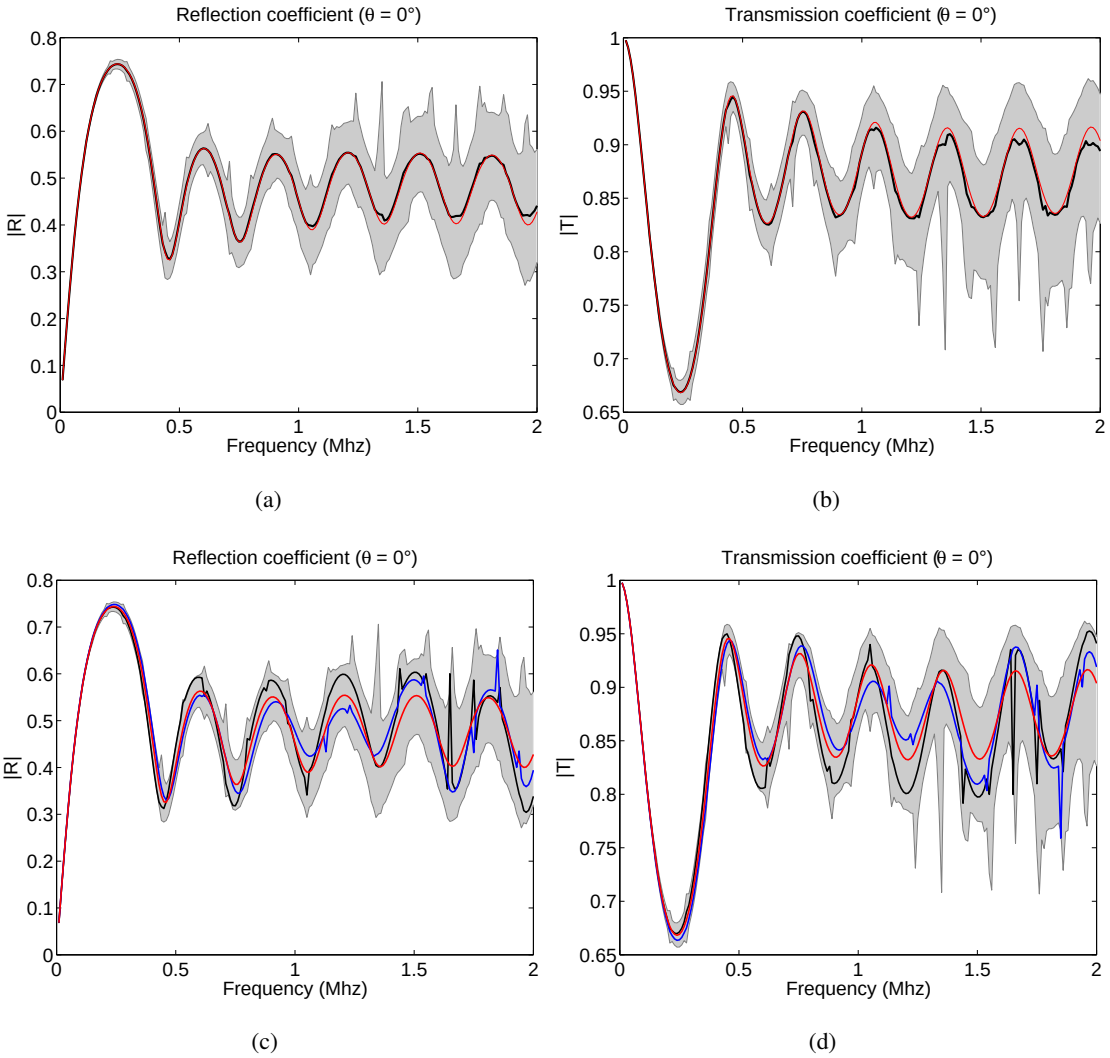

Figure 2.17: (Color online) Confidence regions of reflection and transmission coefficients with respect to frequency when $\delta = 0.1$. The confidence regions are colored in grey. The estimated mean values of the reflection and transmission coefficients are plotted in thick solid line while those obtained *via* the deterministic model are plotted in thin red solid line. Incidence angle $\theta = 0°$ and $h_2 = 3$ mm: (a) reflection coefficient R; (b) transmission coefficient T.

2.6.2.2 Sensitivity analysis with respect to the angle of incidence

Comparison between the mean and stochastic models.

In this section, the results obtained with the mean model using the values defined in Section 2.5.2.2 are compared to the ones obtained with the stochastic model. In Figs. 2.23 and 2.24, the reflection and transmission coefficients are respectively plotted as function of the incidence angle for the three values of the dispersion ($\delta = 0.1$ (thin line), $\delta = 0.2$ (dotted line) and $\delta = 0.3$ (dashed line)) and two frequencies ($f = 250$ kHz and $f = 1$ MHz). The mean values of the reflection and transmission coefficients are calculated for each incidence angle for $\theta \in [0, 90[$ with a step of $0.3°$. Likewise, these coefficients

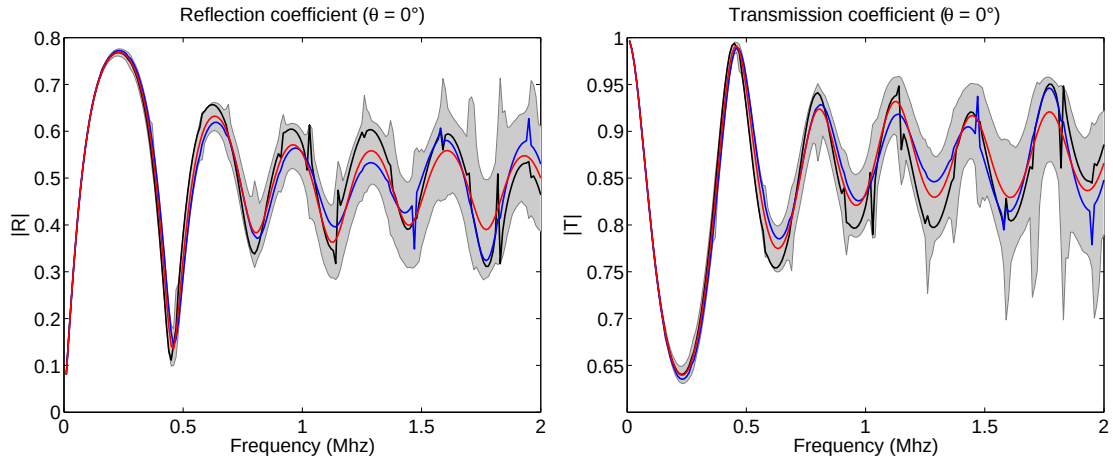

(a) (b)

Figure 2.18: See caption of Fig. 2.17. Incidence angle $\theta = 0°$ and $h_2 = 2$ mm: (a) reflection coefficient R; (b) transmission coefficient T.

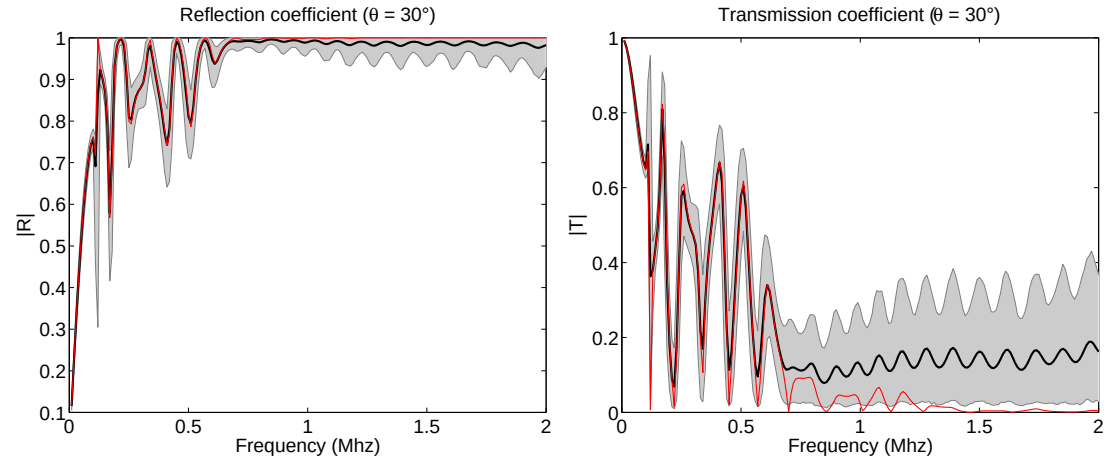

(a) (b)

Figure 2.19: See caption of Fig. 2.17. Incidence angle $\theta = 30°$ and $h_2 = 3$ mm: (a) reflection coefficient R; (b) transmission coefficient T.

obtained with the mean model are plotted with thick solid lines.

When $f = 250$ kHz and $\delta = 0.1$, the curves of the estimated mean (thin line) and mean model (thick line) for the reflection coefficient R are almost superimposed, while those of the transmission coefficient T are superimposed only for angles below $60°$. However, when $\delta = 0.2$ and $\delta = 0.3$ the difference is more significant for the two coefficients, especially when the angle of incidence is more than $40°$ degrees.

When $f = 1$ MHz, the difference between the estimated mean values (thin line) and values of mean model (thick line) for the reflection and transmission coefficients R and T is significant even when $\delta = 0.1$. This difference is amplified when $\delta = 0.2$ and 0.3.

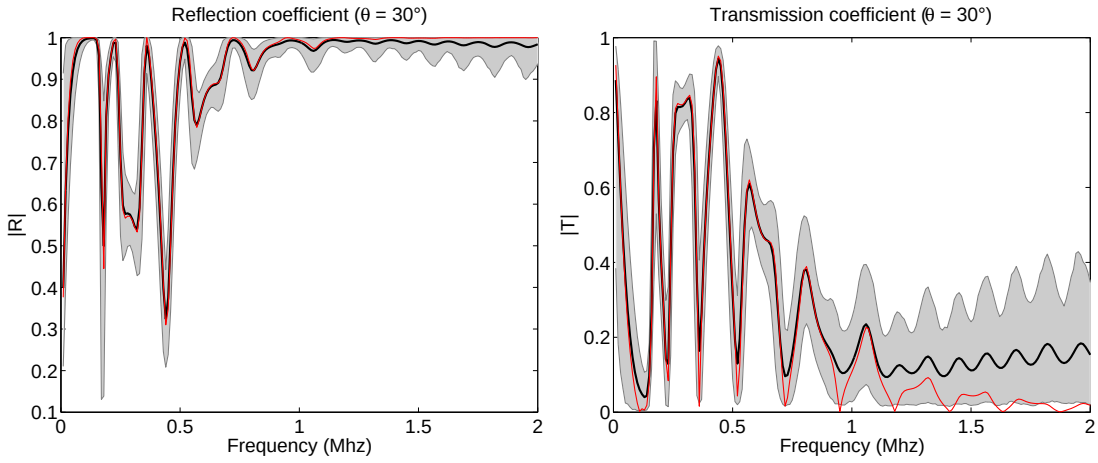

(a) (b)

Figure 2.20: See caption of Fig. 2.17. Incidence angle $\theta = 30°$ and $h_2 = 2$ mm: (a) reflection coefficient R; (b) transmission coefficient T.

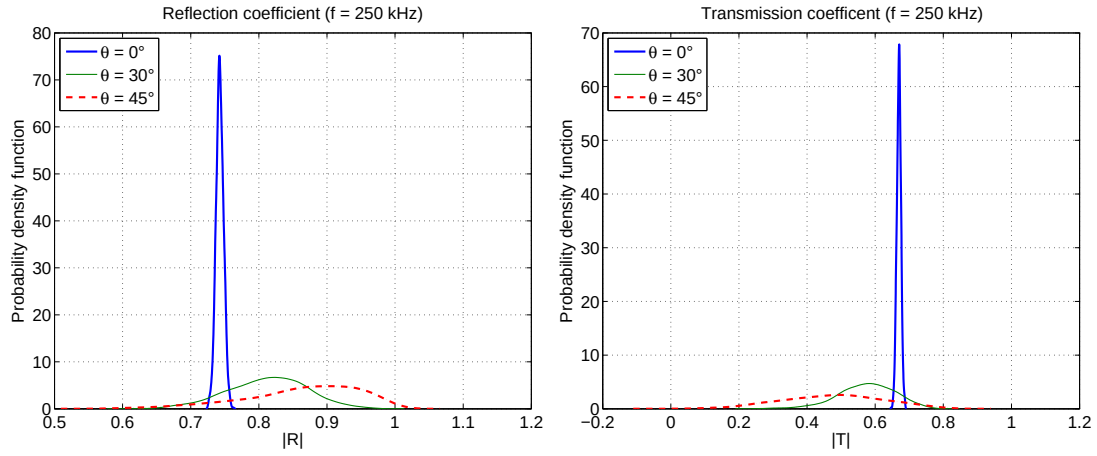

(a) (b)

Figure 2.21: (Color online) Probability density function for four incidence angles given by $\theta = 0^o, 30^o$ and 45^o when $\delta = 0.1$. These results are obtained with $f = 250$ kHz. (a) reflection coefficient R; (b) transmission coefficient T.

Confidence regions.

In this section, the confidence regions associated with a probability level P_c for random fields R and T are calculated. Figures 2.25 and 2.26 represent confidence regions associated with a probability level $P_c = 0.95$ of random fields $\theta \longrightarrow \{R(\theta)\}$ and $\theta \rightarrow \{T(\theta)\}$ when $\theta \in [0, 90[$.

The upper and lower envelopes are constructed using equations (2.41) and (2.42). Two similar solid lines represent the functions $\theta \rightarrow \{r^-(\theta)\}$ and $\theta \rightarrow \{r^+(\theta)\}$ ($\theta \rightarrow \{t^-(\theta)\}$ and $\theta \rightarrow \{t^+(\theta)\}$, respectively) delimiting the confidence region of the reflection coefficient (transmission coefficient, respectively)

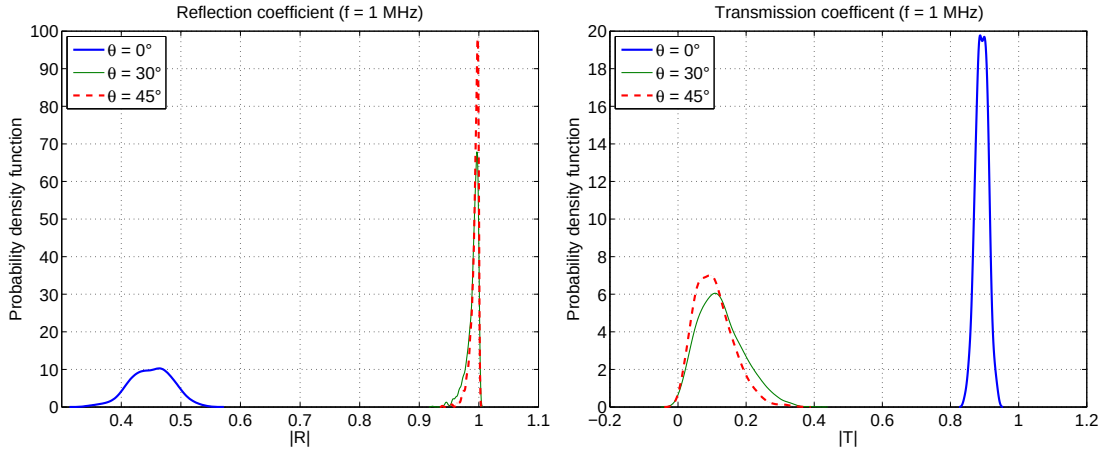

(a) (b)

Figure 2.22: See caption of Fig. 2.21. These results are obtained with $f = 1$ MHz.

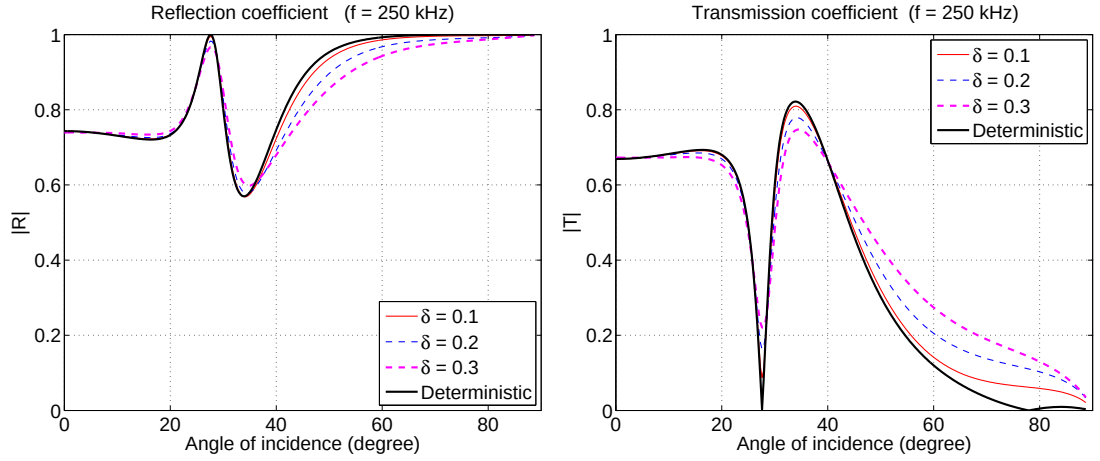

(a) (b)

Figure 2.23: (Color online) Mean estimated values of the reflection and transmission coefficients when $\delta = 0.1$ (thin line), $\delta = 0.2$ (thin line) and $\delta = 0.3$ (dashed line). The thick solid line is obtained with the mean model. These results are obtained with $f = 250$ kHz. (a) reflection coefficient R; (b) transmission coefficient T.

obtained with the stochastic model when $\delta = 0.1$ (black region), $\delta = 0.2$ (dark gray region) and $\delta = 0.3$ (light gray region). The dotted line represents the function $\theta \rightarrow \{R(\theta)\}$ ($\theta \rightarrow \{T(\theta)\}$ respectively) obtained with the deterministic model.

It is observed that the width of the confidence interval is not constant over all incidence angles θ increases with the dispersion δ.

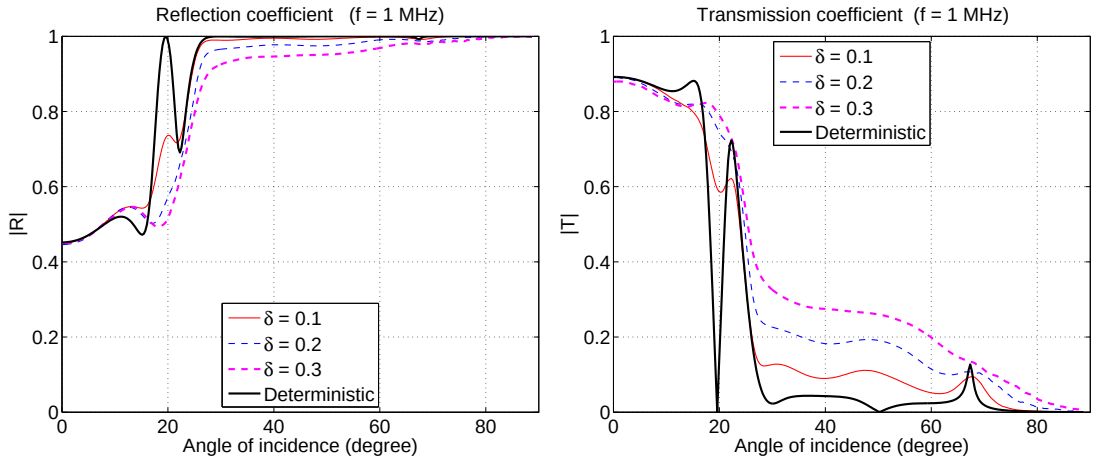

(a) (b)

Figure 2.24: See caption of Fig. 2.23. These results are obtained with $f = 1$ MHz.

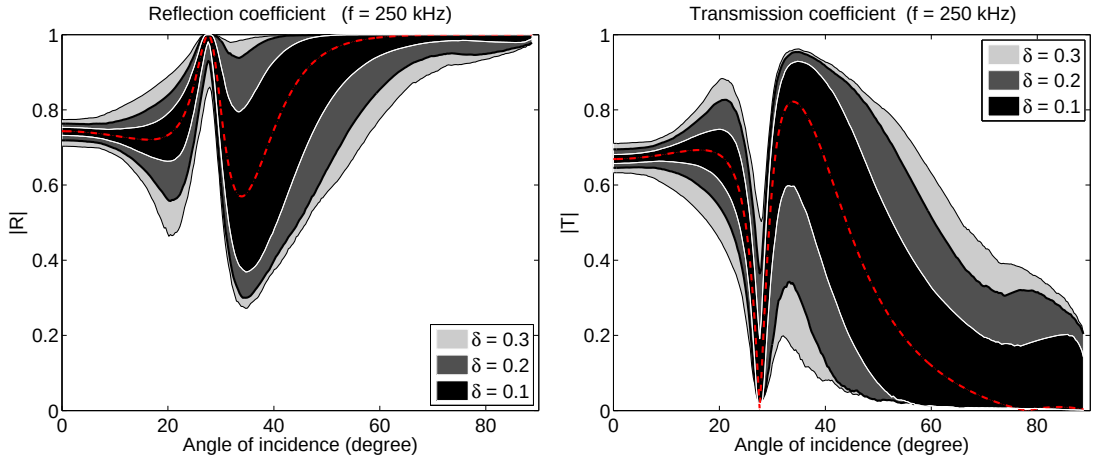

(a) (b)

Figure 2.25: Confidence regions of the reflection and transmission coefficients when $f = 250$ kHz. The dotted line represents the deterministic solutions of R and T

2.6.3 Impact of the findings on the determination of the material properties

The study proposed in the work fits into the context of the nondestructive ultrasonic methods to determine the material properties of heterogeneous and anisotropic solid layers. In this method, the solid layer is immersed in a liquid tank and insonifying it with an acoustic beam at various incident angles and frequencies. This experimental method therefore allows to generate dispersion curves which are then fitted by adjusting the material properties of the solid layer in the theoretical model until good agreement is obtained between the theoretically and experimentally generated curves. Note that the minima (or maxima) of reflection (or transmission) coefficients are directly correlated to dispersion curves. This procedure involves constructing an appropriate functional in an optimization process of material proper-

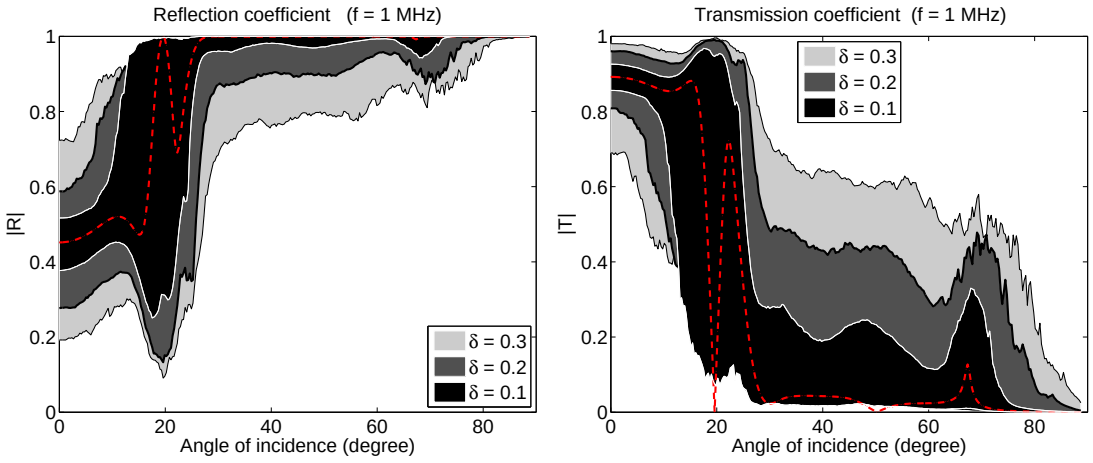

(a) (b)

Figure 2.26: Confidence regions of the reflection and transmission coefficients when $f = 1$ MHz. The dotted line represents the deterministic solutions of R and T

ties *via* iteratively minimizing the squares of the differences between the theoretically and experimentally generated dispersion curves (Karim et al., 1990; Rokhlin and Chimenti, 1990). The accuracy of the technique is usually reported to be quite good but care must be taken to include a large enough portion of the dispersion curves since it is known that different regions of the curves are more sensitive to certain material properties than others. As a result, the curves of the coefficients of reflection and transmission should allow us to identify the ranges of angles and frequencies for which the dispersion is least important but also to formulate the optimization problem in the probabilistic framework. The solution of this optimization problem yields an optimal probabilistic model in order to take into account the uncertainties related to the material properties. This approach was successfully led with the axial transmission method which provides the velocity of ultrasonic waves axially transmitted along compact cortical bone through a linear arrangement of transmitters and receivers placed on the same side of the skeletal site (Desceliers et al., 2009a).

2.7 Conclusion

In this chapter a new approach is proposed for the determination of the reflection and transmission coefficients of a two-dimensional waveguide wherein the elastic properties are uncertain. As a consequence, probabilistic approaches are good candidates to investigate these problems. In this approach, the values of each interest parameter are considered as random and are associated with a probability density function. The results show that the reflection and transmission coefficients are sensitive to material properties. In addition, the results obtained in the present chapter show that the angle of incidence has an influence on the estimation of the probability density of reflection and transmission coefficients. That being said, the positions allowing better discrimination of material properties of the bone tissue may be highlighted.

In this chapter, we propose a numerical framework for investigating the reflection and transmission coefficients of ultrasonic waves from a two-dimensional waveguide wherein the elastic properties are uncertain in the thickness direction. A parametric probabilistic method, which is based on the maximum entropy principle, has been employed to model the random elasticity field in the plate. The quantities of interest (reflection and transmission coefficients) were statistically studied by using the Monte-Carlo simulation. A semi-finite element formulation has been developed. Numerical validations show that SAFE method is very efficient for dealing with arbitrary mechanical heterogeneity in the plate, even in the high frequency domain.

The case of *in vitro* ultrasonic testing on a cortical bone plate has been studied for illustration purpose. It has been shown that both coefficients are very sensitive to the dispersion parameter which represents the random fluctuation level of elastic properties in the plate. Moreover, the effects of random properties may become much more important for higher frequency of the emitted wave. The parametric studies show that the reflection and transmission coefficients are both sensitive to the parameters of the gradient model. It has been observed that taking into account this gradient, leads to drastic changes in the behavior of the reflection and transmission coefficients. These results confirm the relevance of taking into account this new profile of property for the estimation of the coefficients of interest. In addition, the findings show that the confidence regions may be less large or larger depending on the angle of incidence, which can be useful to develop a strategy in the experimental method of measurement of the reflection and transmission coefficients in order to minimize the errors due to heterogeneity. All these results have great importance on the identification of material properties by solving an inverse problem which will be presented in forthcoming publications.

Appendices

A Generation of the random elasticity tensors

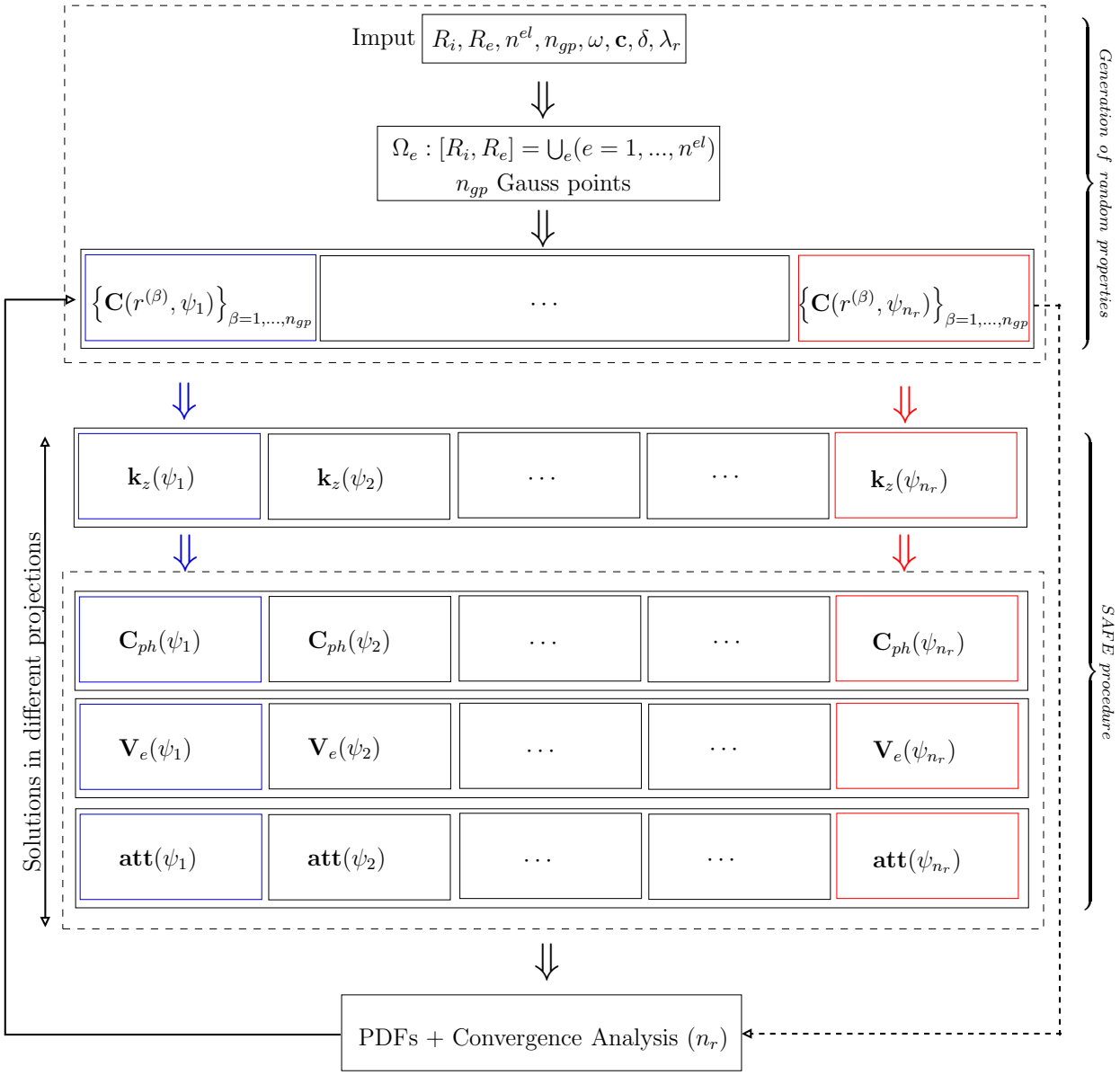

Figure 2.27: Steps for estimation the probabilistic characteristics of solutions.

B Results for other values of h_2

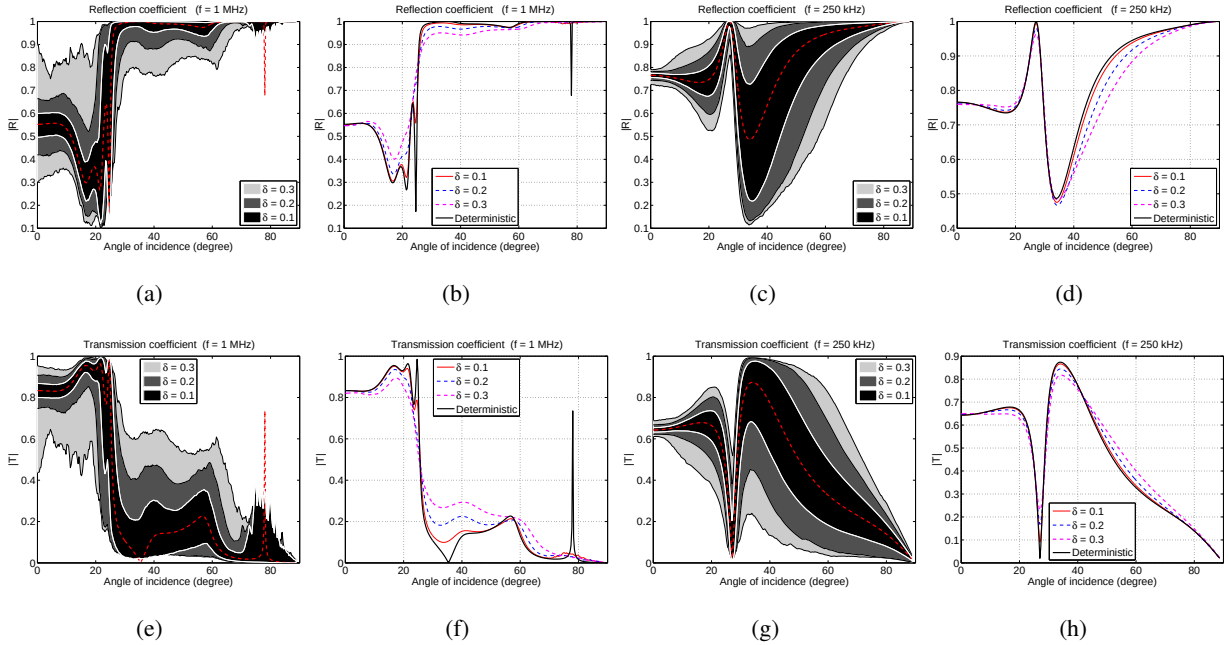

(a) (b) (c) (d)

(e) (f) (g) (h)

Figure 2.28: Confidence region prediction for the random reflection and transmission coefficient when $h_2 = 2\ mm$.

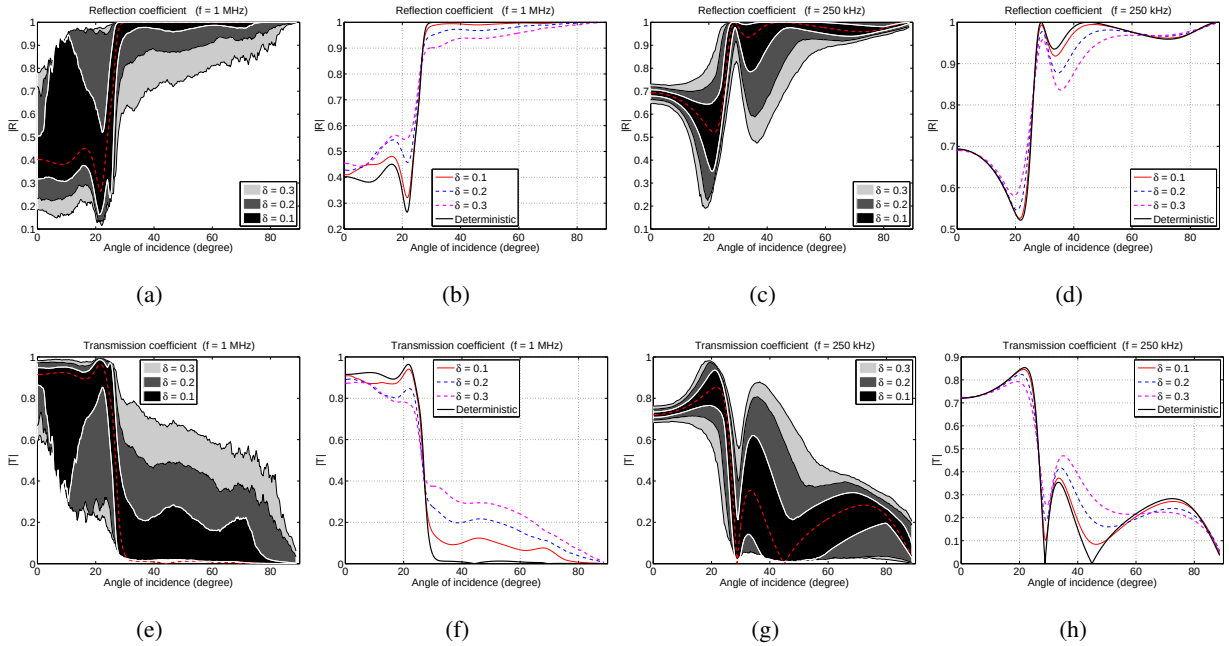

(a) (b) (c) (d)

(e) (f) (g) (h)

Figure 2.29: Confidence region prediction for the random reflection and transmission coefficient when $h_2 = 4\ mm$.

Bibliography

B.A. Auld. *Acoustic field and waves in solids*, volume I and II. Krieger Publishing, Malabar, 2nd edition, 1990.

C. Baron. Using the gradient of human cortical bone properties to determine age-related bone changes via ultrasonic guided waves. *Ultrasound in Medicine & Biology*, 38(6):972 – 981, 2012.

C. Baron and S. Naili. Elastic wave propagation in a fluid-loaded anisotropic waveguide with laterally varying properties. *C.R. Mécanique*, 336:772–730, 2008.

C. Baron and S. Naili. Propagation of elastic waves in a fluid-loaded anisotropic functionally graded waveguide: Application to ultrasound characterization. *The Journal of the Acoustical Society of America*, 127(3):1307–1317, 2010.

K.J. Bathe. *Finite Element Procedures*. Prentice-hall, 1996.

V. Bousson, A. Meunier, C. Bergot, E. Vicaut, M.A. Rocha, M.H. Morais, A.M. Laval-Jeantet, and J.D. Laredo. Distribution of intracortical porosity in human midfemoral cortex by age and gender. *J. Bone Miner Res.*, 16:1308–11317, 2001.

S.C. Cowin. *Bone mechanics handbook*. CRC Press, Boca Raton, FL, 2nd edition, 2001.

C. Desceliers, C. Soize, Q. Grimal, G. Haiat, and S. Naili. A time-domain method to solve transient elastic wave propagation in a multilayer medium with a hybrid spectral-finite element space approximation. *Wave Motion*, 45(4):383 – 399, 2008.

C. Desceliers, C. Soize, Q. Grimal, M. Talmant, and S. Naili. Identification of an anisotropic elasticity tensor for an elastic layer using transient wave propagation in a fluid-solid multilayer. model with uncertainties and experiments. *The Journal of the Acoustical Society of America*, 125(4):2027–2034, 2009a.

C. Desceliers, C. Soize, S. Naili, and G. Haiat. Determination of the random anisotropic elasticity layer using transient wave propagation in a fluid-solid multilayer: Model and experiments. *The Journal of the Acoustical Society of America*, 125(4):2027–2034, 2009b.

C. Desceliers, C. Soize, S. Naili, and G. Haiat. Probabilistic model of the human cortical bone with mechanical alterations in ultrasonic range. *Mechanical Systems and Signal Processing*, 32:170 – 177, 2012.

M. Deschamps and B. Hosten. The effects of viscoelasticity on the reflection and transmission of ultrasonic waves by an orthotropic plate. *The Journal of the Acoustical Society of America*, 91(4):2007–2015, 1992.

X.N. Dong and X.E. Guo. The dependence of transversaly isotropic elasticity of human femoral cortical bone on porosity. *Journal of Biomechanics*, 37:1281–1287, 2004.

F.I. Fedorov. *Theory of elastic waves in crystals*. Plenum Press, 1968.

M. Gräsel, C.-C. Glüer, and R. Barkmann. Characterization of a new ultrasound device designed for measuring cortical porosity at the human tibia: A phantom study. *Ultrasonics*, 76:183 – 191, 2017.

G. Haiat, S. Naili, Q. Grimal, M. Talmant, C. Desceliers, and C. Soize. Influence of a gradient of material properties on ultrasonic wave propagation in cortical bone: Application to axial transmission. *The Journal of the Acoustical Society of America*, 125(6):4043–4052, 2009.

E.T. Jaynes. Information theory and statistical mechanics. *The Physical Review*, 106(4):620–630, 1957a.

E.T. Jaynes. Information theory and statistical mechanics. II. *The Physical Review*, 108(2):171–190, 1957b.

M.R. Karim, A.K. Mal, and Y. Bar-Cohen. Inversion of leaky lamb wave data by simplex algorithm. *The Journal of the Acoustical Society of America*, 88(1):482–491, 1990.

P. Lanceleur, H. Ribeiro, and J.-F. De Belleval. The use of inhomogeneous waves in the reflection-transmission problem at a plane interface between two anisotropic media. *The Journal of the Acoustical Society of America*, 93:1882–1892, 1993.

M.L. Mehta. *Random Matrices*. Academic Press, 2004.

M.P.J. Musgrave. *Crystal acoustics*. Holden Day, San Francisco, 1970.

S. Naili, V.-H. Nguyen, M.-B Vu, C. Desceliers, and C. Soize. Modeling of transient wave propagation in a heterogeneous solid layer coupled with fluid: Application to long bones. *The Journal of the Acoustical Society of America*, 137(2):668–678, 2015.

V.-H. Nguyen and S. Naili. Simulation of ultrasonic wave propagation in anisotropic poroelastic bone plate using hybrid spectral/finite element method. *International Journal for Numerical Methods in Biomedical Engineering*, 28(8):861–876, 2012.

V.-H. Nguyen and S. Naili. Ultrasonic wave propagation in viscoelastic cortical bone plate coupled with fluids: a spectral finite element study. *Computer Methods in Biomechanics and Biomedical Engineering*, 16(9):963–974, 2013.

V.-H. Nguyen, T. Lemaire, and S. Naili. Poroelastic behaviour of cortical bone under harmonic axial loading: A finite element study at the osteonal scale. *Medical Engineering & Physics*, 32(4):384 – 390, 2010.

S.I. Rokhlin and D.E. Chimenti. *Reconstruction of elastic constants from ultrasonic reflectivity data in a fluid coupled composite plate*, pages 1411–1418. Springer US, Boston, MA, 1990.

S.I. Rokhlin, T.K. Bolland, and L. Adler. Reflection and refraction of elastic waves on a plane interface between two generally anisotropic media. *The Journal of the Acoustical Society of America*, 79:906–918, 1986.

V. Sansalone, S. Naili, V. Bousson, C. Bergot, F. Peyrin, J. Zarka, J.D. Laredo, and G. Haiat. Determination of the heterogeneous anisotropic elastic properties of human femoral bone: from nanoscopic to organ scale. *J. Biomech.*, 43:1857–1863, 2010.

C. Soize. Maximum entropy approach for modeling random uncertainties in transient elastodyanmics. *The Journal of the Acoustical Society of America*, 109(5):1979–1996, 2001.

C. Soize. Non-gaussian positive-definite matrix-valued random fields for elliptic stochastic partial differential operators. *Computer Methods in Applied Mechanics and Engineering*, 195(1-3):26–64, 2006.

C.D. Thomas, S.A. Feik, and J.G. Clement. Regional variation of intracortical porosity in the midshaft of the human femur: age and sex differences. *J. Anat.*, 206:115–125, 2005.

L. Wang, S.P. Fritton, S.C. Cowin, and S. Weinbaum. Fluid pressure relaxation depends upon osteonal microstructure: modeling an oscillatory bending experiment. *Journal of Biomechanics*, 32:663–672, 1999.

Chapter 3

Dispersion of Lamb waves in anisotropic random plates: Application to cortical bone tissues diagnosis

"La terre a été longtemps plus grande que l'homme, et elle a imposé à l'humanité la loi de la dispersion."

[Jean Jaurès.]

CHAPTER INFORMATION

Keywords:
random properties
Lamb waves
dispersion curves
ultrasound
SAFE method
cortical bone

Publication:
The work presented in this chapter led to the writing of a scientific article which is submitted for publication in the journal *Philosophical Transactions of the Royal Society A* [S1].

ABSTRACT

In this chapter, we present a probabilistic study to analyse Lamb waves of anisotropic elastic plates. The elastic plate has randomly varied elastic properties in the through-thickness direction. By introducing a stochastic model for quantitative description of heterogeneous elastic properties in the plate, the effect of material heterogeneity on Lamb modes may be investigated from a stochastic point of view. Different plate thicknesses are considered and associated dispersion curves are computed. A sensitivity study is performed, highlighting effect of the uncertainty of elasticity properties on the fluctuation of Lamb modes *via* phase velocities, energy velocities and modes shapes. Next, we discussed the relevancy of introducing random media to identify branches associated with experimental dispersion curves.

Contents

3.1 Introduction

Due to the increasing needs for monitoring the human bone health status, for example to diagnosis different metabolic diseases such as osteoporosis or other bone osteopenia, a variety of non-destructive techniques (NDT) for quantitative bone assessment is developed. Thus, techniques such as Dual-energy X-ray absorptiometry (DXA), magnetic resonance imaging (MRI) and quantitative ultrasound (QUS) have emerged. This last one, but not the least, stands out from the others. Indeed, QUS has been regarded as a promising good candidate for quantitative bone evaluation, owing to its advantageous nature of non-radiation, portability, sensitivity to the mechanical elasticity of bone tissues and low-expense.

Ultrasonic waves in bone can be captured in different measurement configurations, axial transmission (AT), through-transmission or transverse transmission and pulse echo (Nguyen et al., 2010b; Vallet et al., 2016). Hence, bone properties can be evaluated in various aspects by using these different techniques. Applying the transverse transmission technique for the cancellous bone, waves can propagate into the bone structure and captured after they propagate across the bone cross-section. Thus, speed of sound (SOS) as well as the broadband ultrasound attenuation (BUA) can be measured. In cortical bone, ultrasonic waves are mainly measured by the axial transmission technique, in which probes are placed along the body part over the examined bone and radiate ultrasound waves into the cortical layer through the surface layer of soft tissues. Thereby, the first arrival signal (FAS) propagating along and near below the cortical bone surface and the second arrival signal (SAS) so-called slow guided wave (SGW) arriving after the FAS can be evaluated (Chen and Su, 2014; Lee and Yoon, 2016). The AT technique remains competitive, due to its capability to reflect not only material properties but also bone microstructure (Nicholson et al., 2002; Moilanen, 2008).

Meanwhile, in the light of success in the use of ultrasonic guided wave method in non-destructive evaluation applying on other domains than the ones of the health, recent studies have shown interesting results in bone assessment by this approach. It has been shown that guided waves provide significant information in the bone evaluation. In this study, our attention is focused on the guided Lamb waves (GLW) in an anisotropic elastic plate mimicking a cortical bone layer.

The fundamentals and analysis of Lamb waves can be found in many books (for instance Royer and Dieulesaint (2000); Rose (1999); Su and Ye (2009)). In a free plate, the dispersion of Lamb waves has been investigated for instance in Royer and Dieulesaint (2000) and Rose (1999) for isotropic plates and for instance in Nayfeh and Chimenti (1989), Nayfeh (1995) for anisotropic plates. When the plate is loaded by fluids, partially or totally immersed in fluids, Lamb waves are radiated on fluids and are leaked. This case is known as leaky Lamb waves. It has been shown that high density fluids have significant influences on the Lamb wave dispersion (Nayfeh and Chimenti, 1988; Chimenti and Rokhlin, 1990).

In the context of the bone evaluation, a number of recent researches on the guided Lamb waves has been published (Tatarinov et al., 2005; Ta et al., 2006; Chen et al., 2013). Among these works, Xu et al. (2014) have investigated the guided modes in fractured long bones, and point out the fact that reflection energy and transmission coefficient of the symmetrical and antisymmetric zero-order modes, denoted S_0 and A_0 respectively, can be used to evaluate bone status. Thakare et al. (2015) use the semi-

analytical finite element (SAFE) method to obtain the guided wave velocity and show that the velocity is sensitive on geometric conditions such as thickness. A method that allows a simultaneous estimation of the thickness and the longitudinal wave velocity has been proposed in Tasinkevych et al. (2016). In the three dimensional case, Chen and Su (2014) Baron (2011), Lee and Yoon (2016) have studied Lamb waves in a cylindrical tube as cortical-bone-mimicking phantoms. Recently, Lee and Yoon (2016) and Vallet et al. (2016) paid attention on time-reversed Lamb waves in bone and characterisation of cortical bone using guided waves, respectively.

However, in the literature, most of studies about Lamb waves are carried out in a deterministic framework. In particular, the material properties are fixed and perfectly known. Nevertheless, for certain materials as the bone, information available is uncertain. For instance, bone material properties depend on clinical history of the patient. As result, it is interesting to not consider these properties as deterministic but rather uncertain. The uncertainty is introduced on the heterogeneity of bone using only the available information. Obviously, guided Lamb waves in random media is a key issue due to the lack of information on the material properties of complex media (Parra et al., 1999; Bal and Ryzhik, 2001; Ichchou et al., 2011; Bouchoucha et al., 2013; Ben Souf et al., 2013; Fabro et al., 2015). In the case of bone, recent studies are carried out in randomly layered medium (Cieszko et al., 2016) and random plates (Desceliers et al., 2012; Nguyen et al., 2016; Gilbert et al., 2013; Naili et al., 2015). To the authors best knowledge, dispersion curves of Lamb waves on random bone plate using the semi-analytical finite element (SAFE) method is not yet considered in the literature.

This study aims to investigate Lamb waves dispersion curves in an elastic plate with uncertain material properties. The probabilistic framework presented in our previous work (Nguyen et al., 2016) for studying the reflection and transmission coefficients is used to analyse Lamb waves in random plate mimicking a cortical bone layer. The elasticity tensor of bone tissue is randomly varied in the thickness direction. When the deterministic model is considered, bone tissue is assumed to be homogeneous with transversely isotropic elastic material properties. Whereas, in the stochastic model, the plate is anisotropic and heterogeneous with material properties randomly varied along the thickness axis. A sensitivity analysis of material and geometric properties is performed. In principle, it is possible to estimate the material properties of the plate from guided Lamb modes.

The chapter is organized as follows. After this introduction on the rationale about Lamb waves and dispersion curves, in the next section, the geometry description is presented and governing equations are described. In section 3.3, a finite element method is proposed to formulate dispersion relation. A numerical approach is proposed for determining dispersion curves. The methodology used to generate the random elasticity tensor and the stochastic solver are presented in section 3.4. Next, some numerical examples presenting a simulation test in cortical bone are displayed and detailed discussion is provided in section 3.5. Finally, some concluding remarks are made in section 3.6.

3.2 Problem statement

3.2.1 Geometry description

We consider an infinite solid layer occupying the domain Ω^b that represents a plate with a constant thickness h, placed in vacuum. The upper and lower plane interfaces between the plate (Ω^b) and vacuum are denoted by Γ_1^{bv} and Γ_2^{bv}, respectively, as shown in Fig. 3.1. Let $\mathcal{R}(O;\mathbf{e}_1,\mathbf{e}_2,\mathbf{e}_3)$ be the Cartesian reference system, where O is the origin of the space and $(\mathbf{e}_1,\mathbf{e}_2,\mathbf{e}_3)$ is the orthonormal basis. The coordinates of a point M are specified by (x_1,x_2,x_3) in $\mathcal{R}$. Due to the geometrical configuration, the components in the $\mathbf{e}_3$-direction of the displacement vectors in the solid will be zeros and the elastoacoustic wave motion will be independent of x_3. The present study is conducted in the plane $(O;\mathbf{e}_1,\mathbf{e}_2)$. These conditions are associated with the plane strain model.

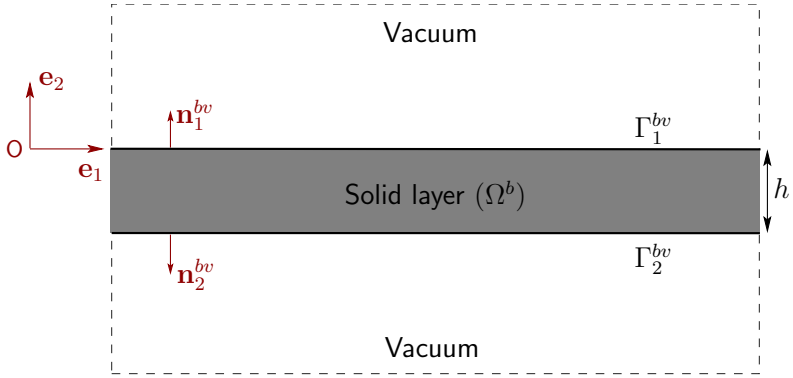

Figure 3.1: Description of the geometrical configuration.

3.2.2 Governing equations

In what follows, we note respectively ∇, $\nabla\cdot$ and ∇^2 the gradient, divergence and Laplacian operators in two-dimensional space (2D). The time derivative is denoted by a dot superimposed. We denote respectively by ∂_i and ∂_i^2 the partial derivatives of first and second operators with respect to x_i. In general, the boldface symbols are used to designate the matrices, the fields of vectors and tensors in two-dimensional and three-dimensional spaces.

3.2.2.1 Equation in bone layer

We denote by $\mathbf{u}(M,t)=(u_1,u_2)^T$ the displacement vector at a point M located in the solid domain Ω^b in which the superscript "T" denotes the transpose operator. By neglecting body forces, the equations of motion in Ω^b is given by:

$$\rho\ddot{\mathbf{u}} - \nabla\cdot\boldsymbol{\sigma} = \mathbf{0}, \quad \forall M\in\Omega^b, \tag{3.1}$$

where ρ is the mass density of the solid. This equation can be rewritten in a vectorial form:

$$\rho\ddot{\mathbf{u}} - \mathbf{L}^T\mathbf{s} = \mathbf{0}, \quad \forall M \in \Omega^b, \tag{3.2}$$

where the vector $\mathbf{s}$ contains the components of the stress tensor $\boldsymbol{\sigma}$ and is denoted by $\mathbf{s} = (\sigma_{11}, \sigma_{22}, \sigma_{12})^T$. The operator $\mathbf{L}$ is defined by:

$$\mathbf{L} = \mathbf{L}_1\partial_1 + \mathbf{L}_2\partial_2, \quad \mathbf{L}_1 = \begin{bmatrix} 1 & 0 \\ 0 & 0 \\ 0 & 1 \end{bmatrix}, \quad \mathbf{L}_2 = \begin{bmatrix} 0 & 0 \\ 0 & 1 \\ 1 & 0 \end{bmatrix}. \tag{3.3}$$

Using the notation of Voigt, the Hooke law reads: $\mathbf{s} = \mathbf{ce}$ where $\mathbf{e}$ is a vector containing the components of the infinitesimal strain tensor which are given by $\mathbf{e} = (\epsilon_{11}, \epsilon_{22}, 2\epsilon_{12})^T = \mathbf{Lu}$, and $\mathbf{c}$ is the matrix containing the components of the anisotropic elasticity tensor *via* the Voigt notation:

$$\mathbf{c} = \begin{bmatrix} c_{11} & c_{12} & c_{16} \\ c_{12} & c_{22} & c_{26} \\ c_{16} & c_{26} & c_{66} \end{bmatrix}. \tag{3.4}$$

It is assumed that the physical properties of the solid only depend on x_2, *i.e.* $\mathbf{c} = \mathbf{c}(x_2)$.

3.2.2.2 Boundary conditions

The plane interfaces between the solid surfaces and vacuum domains are referred to as free surfaces. On these surfaces, the surface traction vectors are continuous, since as an infinite acceleration would be required to maintain a traction discontinuity. Inasmuch as a vacuum cannot sustain any stress, we get the free-surfaces boundary conditions interfaces Γ_1^{bv} and Γ_2^{bv}:

$$\boldsymbol{\sigma}\mathbf{n}_\alpha^{bv} = \mathbf{0}, \qquad \forall M \in \Gamma_\alpha^{bv} \quad (\alpha = 1, 2), \tag{3.5}$$

where $\mathbf{n}_\alpha^{bv}$ is a normal unit vector of Ω^b at the interfaces Γ_α^{bv}. Seeing that $\mathbf{n}_1^{bf} = -\mathbf{n}_2^{bv} = (0, 1)^T$, Eq. (3.5) may be written as follows:

$$\mathbf{t} = \mathbf{0}, \quad \text{at } x_2 = 0 \text{ and } x_2 = -h, \tag{3.6}$$

where $\mathbf{t} = (\sigma_{12}, \sigma_{22})^T = \mathbf{L}_2^T\mathbf{s}$. Seeing that $\mathbf{s} = \mathbf{ce}$ and $\mathbf{e} = \mathbf{Lu}$, the surface traction vector $\mathbf{t}$ may be written in the following expanded form:

$$\mathbf{t} = (\mathbf{L}_2^T\mathbf{c}\mathbf{L}_1\partial_1 + \mathbf{L}_2^T\mathbf{c}\mathbf{L}_2\partial_2)\mathbf{u}. \tag{3.7}$$

3.3 Dispersion analysis by using finite element method

3.3.1 Equations in the frequency-wavenumber domain

We look for the solution of an harmonic wave propagating along the axial direction. The plane wave solution in the solid may be expressed in the following form:

$$\mathbf{u}(M,t) = \hat{\mathbf{u}}(x_2)\exp[\mathrm{i}(k_1 x_1 - \omega t)], \quad \forall M \in \Omega^b, \tag{3.8}$$

where the pure imaginary number i is defined by $\mathrm{i}^2 = -1$, $\hat{\mathbf{u}} = (\hat{u}_1, \hat{u}_2)^T$, k_1 and ω denote the wavenumber with respect to $\mathbf{e}_1$ and the angular frequency, respectively. As result, the time derivative and the spatial differential operations with respect to x_1 turn into simple factors:

$$\partial_t(*) \longrightarrow -\mathrm{i}\omega(*), \quad \partial_1 \longrightarrow \mathrm{i}k_1(*). \tag{3.9}$$

Consequently, the equation of motion (3.2) can be written as a system of partial differential equations on the displacement $\hat{\mathbf{u}}$ with respect only to x_2:

$$\left(-\omega^2\mathbf{A}_1 + k_1^2\mathbf{A}_2\right)\hat{\mathbf{u}} - \mathrm{i}k_1\mathbf{A}_3^T\partial_2\hat{\mathbf{u}} - \partial_2\mathbf{t} = \mathbf{0}, \quad \forall x_2 \in [-h, 0], \tag{3.10}$$

where $\mathbf{t} = (ik_1\mathbf{A}_3 + \mathbf{A}_4\partial_2)\hat{\mathbf{u}}$, and the two-by-two matrices $\mathbf{A}_i$ $(i = 1, ..., 4)$ are defined by:

$$\mathbf{A}_1 = \rho\mathbf{I}_d, \quad \mathbf{A}_2 = \mathbf{L}_1^T\mathbf{c}\mathbf{L}_1, \quad \mathbf{A}_3 = \mathbf{L}_2^T\mathbf{c}\mathbf{L}_1, \quad \mathbf{A}_4 = \mathbf{L}_2^T\mathbf{c}\mathbf{L}_2, \tag{3.11}$$

where $\mathbf{I}_d$ is the two-by-two identity matrix.

3.3.2 Weak formulation and finite element implementation

3.3.2.1 Weak formulation

The weak formulation of the problem defined from Eq. (3.10) may be derived using standard procedure (Bathe, 1996). Let $\mathcal{C}^{ad}$ be the admissible function space constituted by all sufficient smooth complex-valued functions $x_2 \in]-h, 0[\rightarrow \delta\mathbf{u}(x_2) \in \mathbb{C}\times\mathbb{C}$, where $\mathbb{C}$ denotes the set of complex numbers. The conjugate transpose of $\delta\mathbf{u}$ is denoted $\delta\mathbf{u}^*$. By multiplying the equation (3.10) with the test function $\delta\mathbf{u}^* \in C^{ad}$ and integrating by parts, we obtain:

$$\int_{-h}^{0} \delta\mathbf{u}^*\left(-\omega^2\mathbf{A}_1 + k_1^2\mathbf{A}_2 - \mathrm{i}k_1\mathbf{A}_3^T\partial_2\right)\hat{\mathbf{u}}\,dx_2 + \int_{-h}^{0}\partial_2(\delta\mathbf{u}^*)\mathbf{t}\,dx_2 - [\delta\mathbf{u}^*\mathbf{t}]_{-h}^{0} = 0. \tag{3.12}$$

The last term in Eq. (3.12) may vanish by using the free-surfaces boundary conditions (3.6). Thus the weak formulation of the problem is: Find $\mathbf{u}(x_2) \in \mathcal{C}^{ad}$ such that:

$$\int_{-h}^{0} \delta\mathbf{u}^*\left(-\omega^2\mathbf{A}_1 + k_1^2\mathbf{A}_2 - \mathrm{i}k_1\mathbf{A}_3^T\partial_2\right)\hat{\mathbf{u}}\,dx_2 + \int_{-h}^{0}\partial_2(\delta\mathbf{u}^*)\left(\mathrm{i}k_1\mathbf{A}_3 + \mathbf{A}_4\partial_2\right)\hat{\mathbf{u}}\,dx_2 = 0, \tag{3.13}$$

for all $\delta\mathbf{u}^* \in C^{ad}$.

3.3.2.2 Finite element formulation

We proceed by introducing a finite element mesh of the domain $[-h, 0]$ which contains n^{el} elements Ω_e: $[-h, 0] = \bigcup_e \Omega_e$ $(e = 1, .., n^{el})$. By the Galerkin finite element method, both functions $\tilde{\mathbf{u}}$ and $\delta\tilde{\mathbf{u}}$ in each element e are approximated using the same interpolation function:

$$\hat{\mathbf{u}}(x_2) = \mathbf{N}_e\mathbf{U}_e, \quad \delta\mathbf{u}(x_2) = \mathbf{N}_e\delta\mathbf{U}_e, \quad \forall x_2 \in \Omega_e, \tag{3.14}$$

where $\mathbf{N}_e$ is the interpolation function, $\mathbf{U}_e$ and $\delta\mathbf{U}_e$ are respectively the vectors of nodal solutions of $\mathbf{u}$ and $\delta\mathbf{u}$ in Ω_e. Substituting Eq. (3.14) into Eq. (3.13) and assembling the elementary matrices, we obtain the following system of linear equations:

$$\mathbf{K}\mathbf{U} = \mathbf{0}, \tag{3.15}$$

where $\mathbf{U}$ is the global nodal displacement vector and $\mathbf{K}$ is the global "stiffness matrix" of the solid defined by:

$$\mathbf{K} = [-\omega^2\mathbf{K}_1 + k_1^2\mathbf{K}_2 + \mathrm{i}k_1\mathbf{K}_3 + \mathbf{K}_4], \tag{3.16}$$

where

$$\begin{aligned} \mathbf{K}_1 &= \bigcup_e \int_{\Omega_e} \mathbf{N}_e^T\mathbf{A}_1\mathbf{N}_e dx_2, \quad \mathbf{K}_2 = \bigcup_e \int_{\Omega_e} \mathbf{N}_e^T\mathbf{A}_2\mathbf{N}_e dx_2, \\ \mathbf{K}_3 &= \bigcup_e \int_{\Omega_e} 2\left[\mathbf{N}_e'^T\mathbf{A}_3\mathbf{N}_e\right]_a dx_2, \quad \mathbf{K}_4 = \bigcup_e \int_{\Omega_e} \mathbf{N}_e'^T\mathbf{A}_4\mathbf{N}_e' dx_2, \end{aligned} \tag{3.17}$$

In Eq. (3.17), the notation $[\star]_a$ denotes the antisymmetric part of $[\star]$ and $\star'$ the derivative with respect to x_2. The dimension of system defined by Eq. (3.15) is denoted by N which corresponds to the degree of freedom (DoF) of the finite element mesh Ω_e. In this study, Gauss quadrature rule has been used for computing the integrations over the elements.

3.3.3 Dispersion relation

Equation (3.15) has two parameters, the angular frequency ω and the axial wavenumber k_1. Therefore, this problem may be solved in two approaches: (*i*) by first fixing the axial wavenumber k_1, and solving for angular frequency ω, or (*ii*) by first fixing the angular frequency ω, and solving for axial wavenumber k_1. Using approach (*ii*), and performing same manipulations, Eq. (3.15) can be rewritten as the following linearized eigenvalue problem:

$$[\mathbf{A}(\omega) - k_1\mathbf{B}(\omega)]\,\hat{\mathbf{V}} = \mathbf{0}, \tag{3.18}$$

where $\mathbf{A}(\omega)$ and $\mathbf{B}(\omega)$ are complex matrices and $\hat{\mathbf{V}}$ is the eigenvector corresponding to the eigenvalue k_1:

$$\mathbf{A}(\omega) = \begin{bmatrix} \mathbf{0} & \mathbf{C} \\ \mathbf{C} & \mathbf{D} \end{bmatrix}, \quad \mathbf{B}(\omega) = \begin{bmatrix} \mathbf{C} & \mathbf{0} \\ \mathbf{0} & -\mathbf{K}_2 \end{bmatrix}, \quad \hat{\mathbf{V}} = \begin{bmatrix} \hat{\mathbf{u}} \\ k_1\hat{\mathbf{u}} \end{bmatrix}, \tag{3.19}$$

where

$$\mathbf{C} = -\omega^2 \mathbf{K}_1 + \mathbf{K}_4, \quad \mathbf{D} = \mathrm{i}\mathbf{K}_3. \tag{3.20}$$

Note that the eigenvector $\hat{\mathbf{V}}$ of Eq. (3.18) is twice the size of the original eigenvector $\hat{\mathbf{U}}$. From Eq. (3.18), at a given real angular frequency ω, $2N$ complex eigenvalues $k_1^{(m)}$ $(m = 1, ..., 2N)$ and $\hat{\mathbf{V}}^{(m)}$ eigenvectors are obtained. The quantity $k_1^{(m)} = \mathrm{Re}[k_1^{(m)}] + \mathrm{i}\ \mathrm{Im}[k_1^{(m)}]$ represents the axial wavenumber for all modes existing at a given angular frequency. Note that the real part $\mathrm{Re}[k_1^{(m)}]$ and imaginary part $\mathrm{Im}[k_1^{(m)}]$ describe the wave spatial frequency in $\mathbf{e}_1$-direction and the wave amplitude decay, respectively. Half of the $2N$ eigenvalues is physically related to travelling waves in the positive $\mathbf{e}_1$-axis while the other half express the backward waves.

3.3.4 Phase velocity and attenuation

For a given angular frequency ω, the wave phase velocity $C_{ph}^{(m)}$ and the attenuation $att^{(m)}$ for the m-th guided wave may be computed by using:

$$C_{ph}^{(m)} = \frac{\omega}{\mathrm{Re}[k_1^{(m)}]} \quad [\text{in m.s}^{-1}], \qquad att^{(m)} = \mathrm{Im}[k_1^{(m)}] \quad [\text{in Np.m}^{-1}]. \tag{3.21}$$

By definition, the phase velocity of a wave is the rate at which the phase of this wave propagates in space domain. In other words, C_{ph} is the velocity at which the phase of any one frequency component of the wave travels. The quantity att is the attenuation whose the physical dimension is the Nepers per metre. The attenuation is the gradual loss in intensity of the wave which means that a unit amplitude decays to an amplitude $\exp(-att)$ after travelling one metre. It is more useful and practical to describe attenuation in other units as Decibel per metre. Wave attenuation in Decibel per metre (dB.m^{-1}) can be obtained from Nepers per metre unit by using the following fixed linear ratio:

$$1\ \text{Np.m}^{-1} \equiv \frac{20}{\ln(10)} \quad [\text{in dB.m}^{-1}], \tag{3.22}$$

where $\ln$ designates the natural logarithm function.

3.3.5 Energy velocity

The wave energy velocity can be seen as the velocity at which a guided wave travels along the waveguide. The velocity of a group of waves with a similar frequency (*i.e.* wave packet) is given by the group velocity:

$$c_g = \frac{\partial \omega}{\partial k_1} \tag{3.23}$$

As reported in many works, this group velocity definition is not valid in absorbing plates (Bernard et al., 2001). In this case, the wavenumber is complex and the differentiation is no longer possible. It has been shown that if the differentiation is made with respect to the real part of the complex wavenumber, then the group velocity calculation yields non-physical solutions such as infinite velocities at some locations

of the dispersion curves. Bernard et al. (2001) have shown that there is a rigourous identity between the velocity group defined by (3.23) and velocity energy in with or without absorbing medium.

By definition, the wave energy velocity vector is equal to the Poynting vector (*i.e.* the power flow density vector) divide by the total energy (kinetic and strain) per unit volume. For the m-th mode, the temporal average of the kinetic and strain energy densities at a point $M(x_1, x_2)$ may be expressed, respectively, as (see *e.g.* Royer and Dieulesaint (2000)):

$$\left\langle e_k^{(m)} \right\rangle_T = \frac{1}{2}\,\rho \left\langle \mathrm{Re}[\dot{\mathbf{u}}^{(m)}]^T \mathrm{Re}[\dot{\mathbf{u}}^{(m)}]^* \right\rangle_T \quad [\text{in J.m}^{-3}], \tag{3.24}$$

$$\left\langle e_p^{(m)} \right\rangle_T = \frac{1}{2} \left\langle \mathrm{Re}[\boldsymbol{\sigma}^{(m)}]^T \mathrm{Re}[\mathbf{e}^{(m)}]^* \right\rangle_T \quad [\text{in J.m}^{-3}], \tag{3.25}$$

where

$$\langle \star \rangle_T = \frac{1}{T} \int_0^T (\star) dt, \tag{3.26}$$

is the temporal average operator over a unit period of time $T = 2\pi/\omega$. The subscript $[\star]^*$ refers to the complex conjugate.

Let us introduce the local complex Poynting vector $\mathbf{P}^{(m)}$ (power flow density vector) at a point $M(x_1, x_2)$ for the m-th mode whose the components are denoted by $(P_1^{(m)}, P_2^{(m)})^T$:

$$\mathbf{P}^{(m)} = -\frac{1}{2}\,\mathrm{Re}\left([\boldsymbol{\sigma}^{(m)}][\hat{\dot{\mathbf{u}}}^{(m)}]^* \right) \quad [\text{J.s}^{-1}.\text{m}^{-2}]. \tag{3.27}$$

Note that due to the guided wave propagating in $\mathbf{e_1}$-direction and the absence of leakage or dissipation, the component of the Poynting vector in $\mathbf{e_2}$-direction is zero. As result, the power flow is entirely in the direction of the wave propagation.

Using the Hooke law and the time derivative defined in Eq. (3.9), the power flow density vector, the temporal average of the kinetic and strain energy densities can be rewritten as:

$$\mathbf{P}^{(m)} = -\frac{1}{2}\omega\,\mathrm{Re}\left([\hat{\mathbf{s}}^{(m)}][\hat{\mathbf{u}}^{(m)}]^* \right) \quad [\text{in J.s}^{-1}.\text{m}^{-2}], \tag{3.28}$$

$$\left\langle e_k^{(m)} \right\rangle_T = \frac{1}{4}\,\rho\omega^2 \mathrm{Re}\left([\hat{\mathbf{u}}^{(m)}]^T [\hat{\mathbf{u}}^{(m)}]^* \right) \quad [\text{in J.m}^{-3}], \tag{3.29}$$

$$\left\langle e_p^{(m)} \right\rangle_T = \frac{1}{4}\,\mathrm{Re}\left([\hat{\mathbf{s}}^{(m)}]^T [\hat{\mathbf{e}}^{(m)}]^* \right) \quad [\text{in J.m}^{-3}]. \tag{3.30}$$

The wave energy velocity in $\mathbf{e_1}$-direction is then obtained by:

$$V_e^{(m)} = \frac{\int_{-h}^{0} \left[\mathbf{P}^{(m)} \cdot \mathbf{e_1} \right] dx_2}{\int_{-h}^{0} \left[\langle e_k^{(m)} \rangle_T + \langle e_p^{(m)} \rangle_T \right] dx_2} \quad [\text{in m.s}^{-1}]. \tag{3.31}$$

The operator and matrices defined in Eq. (3.3) are used for rewriting Eq. (3.28)-(3.29) in matrix forms, next, Gauss quadrature rule has been used for computing the integrations of total energy and Poynting vector over thickness in Eq. (3.31).

3.3.6 Separating Lamb modes approach

In the deterministic model, the plate is assumed to be homogeneous and transversely isotropic elastic. Thus, the symmetric S and antisymmetric A modes exist and can be differentiated by investigate the displacement vector which is obtained by solving Eq (3.15). To illustrate how modes can be separated, the displacements of two symmetrical material points with respect to the mean plane of the plate (*i.e.* $x_2 = -h/2$), $M_1(x_1, -h/2 + x_2)$ and $M_2(x_1, -h/2 - x_2)$ are compared for different modes.

In the stochastic model, the plate material properties are anisotropic and heterogeneous which vary along the $\mathbf{e_2}$-axis. Hence, the modes, denoted S and A, exhibit quasi-symmetric and quasi-antisymmetric displacements distribution with respect to half thickness. They are known as quasi-symmetric and quasi-antisymmetric modes (or pseudo-symmetric and pseudo-antisymmetric modes).

The relationship between the displacement vector components and mode types are given in Tab. 3.1. Due to numerical computation and heterogeneous properties, exact equality values as given in Tab. 3.1 are not obtained. Therefore, tolerance values ξ is considered to differentiate the modes.

Table 3.1: Relationship between displacement vector components and mode types on the material points M_1 and M_2.

Quasi-symmetric mode S	Quasi-antisymmetric mode A
$u_1(M1) \sim u_1(M2)$	$u_1(M1) \sim -u_1(M2)$
$u_2(M1) \sim -u_2(M2)$	$u_2(M1) \sim u_2(M2)$

3.4 Stochastic model

3.4.1 Probabilistic model of the elasticity tensor

This section provides a brief description of the probabilistic model of random elastic matrix. We only sketch out the main features of the model in the context of this study. This model is proposed by Soize (2006) for the construction of the random elastic tensor in order to describe the random heterogeneity in the solid layer along the $\mathbf{e}_2$-direction. The maximum entropy principle (Jaynes, 1957a,b) and the random matrix theory (Mehta, 2004) are used in three dimension to describe the model. Although, the random elasticity tensor $(n \times n)$ has been generated in three dimensions ($n = 6$) with a high value of the spatial correlation lengths in the $\mathbf{e}_1$ and $\mathbf{e}_3$ -directions, only heterogeneous six components, which correspond to the ones defined in the plane $(\mathbf{e}_1, \mathbf{e}_2)$, are extracted to be used for the simulations. Indeed, the solid layer is assumed to be invariant in the $\mathbf{e}_3$-direction and homogeneous in the $\mathbf{e}_1$-direction.

We denote by $\mathbf{C}(x_2) \in \mathbf{M}_n^+(\mathbb{R})$ the random elastic matrix at x_2 and by $\mathbf{c}(x_2) \in \mathbf{M}_n^+(\mathbb{R})$ its mean value, respectively, and for which the following relationship is satisfied $\mathbb{E}\{\mathbf{C}(x_2)\} = \mathbf{c}(x_2)$, where $\mathbb{E}\{\star\}$ designates the mathematical expectation, $\mathbf{M}_n^+(\mathbb{R})$ the set of all the $(n \times n)$ real symmetric positive-definite

matrices and $\mathbb{R}$ the set of real numbers. The matrix $\mathbf{c}(x_2)$ can be decomposed into a product of a unique upper triangular real matrix $\boldsymbol{\mathcal{L}}(x_2)$ with strictly positive diagonal entries and its transpose:

$$\mathbf{c}(x_2) = \boldsymbol{\mathcal{L}}^T(x_2)\,\boldsymbol{\mathcal{L}}(x_2). \tag{3.32}$$

The random matrix $\mathbf{C}(x_2)$ is parameterised by its mean value $\mathbf{c}(x_2)$, the dispersion level δ and the correlation length λ in the $\mathbf{e}_2$-direction, which is denoted by $\mathbf{C}(x_2;\mathbf{c},\delta,\lambda)$ and may be decomposed into the following form:

$$\mathbf{C}(x_2;\mathbf{c},\delta,\lambda) = \boldsymbol{\mathcal{L}}^T(x_2)\,\mathbf{G}(x_2;\mathbf{c},\delta,\lambda)\,\boldsymbol{\mathcal{L}}(x_2), \tag{3.33}$$

where $\mathbf{G}(x_2;\mathbf{c},\delta,\lambda)$, called the stochastic germ matrix, is a homogeneous and normalised non-Gaussian positive-definite matrix-valued second-order random field with values in $\mathbb{M}_n^+(\mathbf{R})$. The dispersion parameter δ, which is a scalar, controls the dispersion of the random matrix $\mathbf{G}(x_2;\mathbf{c},\delta,\lambda)$ and must satisfy the following inequality $0 < \delta < \sqrt{(n+1)/(n+5)}$, which allows the mean-square convergence condition for the germ matrix to be hold (Soize, 2001). It is proved that the dispersion parameter δ is related to a parameter δ_C which evaluates the dispersion of the random matrix $\mathbf{C}(x_2)$ by the relation given by:

$$\delta_C(x_2) = \frac{\delta}{\sqrt{n+1}} \left\{ 1 + \frac{\{\mathrm{Tra}(\mathbf{c}(x_2))\}^2}{\mathrm{Tra}([\mathbf{c}(x_2)]^2)} \right\}^{1/2}, \tag{3.34}$$

The correlation length λ, which is a scalar, is a measure of the distance up to which one has spatial memory of the spatial variations in the material properties.

3.4.2 Stochastic solver and convergence analysis

The Monte Carlo simulation is used for the reliability analysis. For a given parameter set $\mathbf{c}$, h, δ and λ, the 1D domain $[-h, 0]$ is discretized by using quadratic Lagrangian elements. The global x_2-coordinates of the Gauss points in all elements are denoted by x_2^β for $\beta = 1, ..., n_{gp}$, where n_{gp} is the total number of the Gauss points in the mesh.

Let n_r be the total number of realisations, we may construct the set of the independent realisations ψ_j, for $j = 1, ..., n_r$, defined by:

$$\mathcal{A} = \left\{ \left\{ \mathbf{C}(x_2^\beta, \psi_1) \right\}_{\beta=1,...,n_{gp}}, ..., \left\{ \mathbf{C}(x_2^\beta, \psi_{n_r}) \right\}_{\beta=1,...,n_{gp}} \right\} \tag{3.35}$$

in which $\left\{ \mathbf{C}(x_2^\beta, \psi_j) \right\}_{\beta=1,...,n_{gp}}$ are n_{gp} samples at points x_2^β of one realization of random matrice field $\mathbf{C}(x_2;\mathbf{c},\delta,\lambda)$ as described in Section 3.4.1 (see Soize (2006) and Desceliers et al. (2012)). For each statistical independent realisation ψ_j, n_r statistical independent realisations of the random phase velocity $C_{ph}(\psi_j)$, energy velocity $V_e(\psi_j)$ and displacement $\mathbf{u}(\psi_j)$ may be calculated following the the semi-analytical finite element (SAFE) method presented in previous sections.

Convergence analysis with respect to the number of realisations n_r may be performed by studying the convergence of statistical estimates of the second-order moments of random fields (phase velocity, energy

velocity and displacement). For instance, the second-order moment of random phase velocity of a given Lamb mode at a fixed frequency is defined by:

$$\mathrm{Conv}_{C_{ph}}(n_r) = \left\{ \frac{1}{n_r} \sum_{j=1}^{n_r} [C_{ph}(\psi_j)]^2 \right\}^{1/2} . \tag{3.36}$$

3.5 Results and discussion

3.5.1 Numerical parameters

In this model, the elastic solid plate represents cortical bone layer having a constant thickness h. The mean bone mechanical properties are shown in Tab. 3.2, which are taken from the mechanical test results obtained by Dong and Guo (2004). In the deterministic model, bone plate is assumed to have a transversally isotropic elastic properties. The isotropy plane is an orthogonal plane on the $\mathbf{e_1}$-direction. Note that the other components of the elasticity matrix are given by: $c_{22} = c_{33}, c_{12} = c_{13} = c_{21} = c_{31}, c_{23} = c_{32}$ and $c_{55} = c_{66}$.

Table 3.2: Mechanical parameters for the mean model.

Bone material properties					
ρ (kg.m^{-3})	c_{11} (GPa)	c_{22} (GPa)	c_{12} (GPa)	c_{66} (GPa)	$c_{16} = c_{26}$ (GPa)
1722	23.05	15.10	8.71	4.7	0

In the stochastic model, the dispersion δ and one correlation length λ are necessary to control the statistical fluctuations of the elasticity tensor in the $\mathbf{e}_2$-direction. A fixed correlation length $\lambda = 0.1$ mm is used, which may be seen as a center-to-center distance between osteons in cortical bone (see Cowin (2001), Wang et al. (1999) and Nguyen et al. (2010a)). In this study, different dispersion parameters are investigated.

3.5.2 Validation of the SAFE formulation

In this section, we provide a validation of SAFE formulation in the determination of the dispersion curves. Firstly, isotropic homogeneous plates are considered and the validation is made by comparing our results with those in literature. Secondly, anisotropic case is introduced and the comparison is made by using the dispersion curves obtained with DISPERSE software which was created by Mike Lowe and Brian Pavlakovic from Imperial College at London in United Kingdom.

3.5.2.1 Wave modes of homogeneous isotropic plates

It exists an analytical expression for obtaining Lamb wave dispersion curves of free isotropic elastic plates. Dispersion curves are obtained from the following equation:

$$\frac{\tan(ph/2)}{\tan(qh/2)} + \left[\frac{(k_1^2 - q^2)^2}{4pqk_1^2}\right]^{\pm 1} = 0, \tag{3.37}$$

$$k_1^2 = \frac{\omega^2}{C_{ph}^2}, \quad p^2 = \frac{\omega^2}{c_L^2} - k_1^2, \quad q^2 = \frac{\omega^2}{c_T^2} - k_1^2, \tag{3.38}$$

where h, C_{ph}, k_1 and ω are the plate thickness, phase velocity, wavenumber and angular frequency, respectively. The exponent $+1$ and -1 in Eq. (3.37) relates to the symmetric and antisymmetric modes, respectively. The quantities c_L and c_S are the velocities of longitudinal and shear wave modes in the plate, respectively. Equation (3.37) is known as the *Rayleigh-Lamb equation* (Royer and Dieulesaint, 2000). Despite its simple appearance, this equation does not generally have analytical solutions and require awkward numerical root searching techniques to find k_1 values for a given ω.

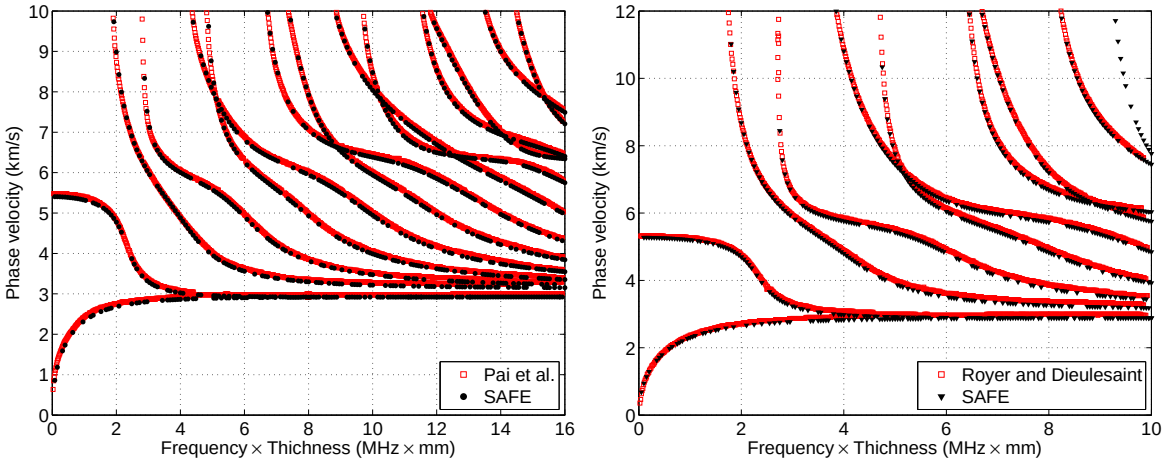

(a) (b)

Figure 3.2: (a): Dispersion curves of homogeneous isotropic aluminum plate. (b): Dispersion curves of homogeneous isotropic steel plate.

Figures 3.2(a) and 3.2(b) show a comparison between the method presented in this paper and results obtain in Pai et al. (2015) and by Royer and Dieulesaint (2000) for an isotropic plate. As compared with the results of Pai et al. (2015) where damage inspection is studied, the SAFE method applied on 4mm-thickness solid layer meshed by 50 elements extracts perfectly similar curves (see Fig. 3.2(a)). On the other hand, in Fig. 3.2(b) the SAFE results and Royer and Dieulesaint (2000) dispersion curves of isotropic steel plate are plotted. It can be seen a good agreement on the two results. However, it seems that on the chosen frequency window, the SAFE method detects the branch of a mode dispersion curve which is not obviously detected in Royer and Dieulesaint (2000). It is not known whether these authors have plotted all modes present on the frequency windows or whether this mode is not detected by the algorithm used in DISPERSE for this frequency range.

3.5.2.2 Wave modes of homogeneous/heterogeneous anisotropic plates

For the cortical bone, the anisotropic and heterogeneous nature of bone tissue further hinders any attempt to seek analytical solution to Eq. (3.37). The SAFE method is one of the efficient approaches to semi-analytically provide accurate dispersion curves and different modes without such difficulties. The method is tested by extracting dispersion curves of transversally isotropic plates (see Fig. 3.3). The results are compared with those obtained using DISPERSE software for plate having material properties presented in Tab. 3.2. Note that in the DISPERSE software, the global matrix method is implemented. From Fig. 3.3, it can be seen a good agreement between our results and those obtained *via* DISPERSE.

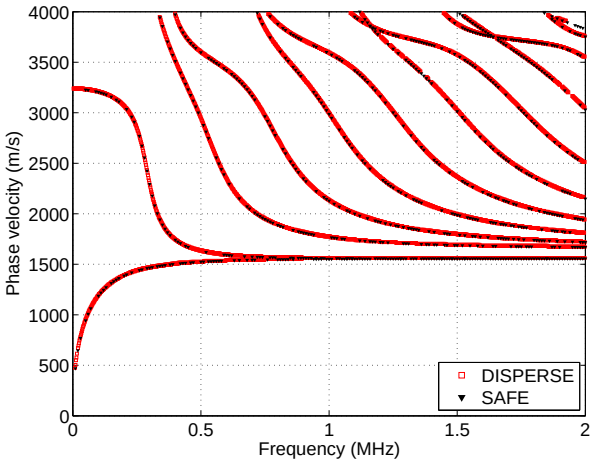

Figure 3.3: (color online) Dispersion curves of homogeneous transversally isotropic plate obtained using SAFE method (triangle black marker) and using DISPERSE software (square red marker).

3.5.2.3 Validation of the approach in multilayered anisotropic plates

In this section, the relevant of the proposed approach is explored for numerical calculation of dispersion curves in multilayered anisotropic (or isotropic) plates. To check the validity of our approach in multilayered plates, the method was first implemented on a bi-layer isotropic plate (measuring 2 mm in global thickness). The plate is composed of an aluminum layer and a brass layer measuring 1 mm each (see Tab. 3.3). Then, the method was further applied to a 4 mm-thickness quardi-layer transversally isotropic plate, which is made of two bones layers and two graphite-epoxy layers measuring 1 mm in thickness each. Layers are arranged in the following sequence: bone-graphite-bone-graphite. Their properties are given in Tab. 3.3. Dispersion curves obtained in these two cases are plotted in Fig. 3.4 for comparison with the results obtained from DISPERSE. The findings show that our solutions agree well with those calculated by DISPERSE. From Fig. 3.4(a) where we study the isotropic bilayer plate, our approach extracts the same dispersion curves as the DISPERSE software, the curves are well superimposed. In Fig. 3.4(b) in which transversally isotropic quadri-layer is tested, our approach agree well with DISPERSE results. However, DISPERSE software does not obviously detect two modes which are well detected by our method. Indeed, in the frequency windows studied, we detect 16 modes whereas

DISPERSE extracts only 14 modes in the anisotropic multilayer. That is to say, the proposed approach may be well suitable to study Lamb waves of heterogeneous multilayered such composites which is a key issue in many domains.

Table 3.3: Isotropic and transversally isotropic layers properties.

Property	ρ (kg.m^{-3})	c_{11} (GPa)	c_{22} (GPa)	c_{12} (GPa)	c_{66} (GPa)	$c_{16} = c_{26}$ (GPa)
Brass	8400	162.6	81.3	162.6	40.7	0.0
Aluminum	2700	107.8	54.94	107.8	26.45	0.0
Bone	1722	23.05	15.10	8.71	4.7	0.0
Graphite-Epoxy	1600	155.6	15.95	3.7	7.46	0.0

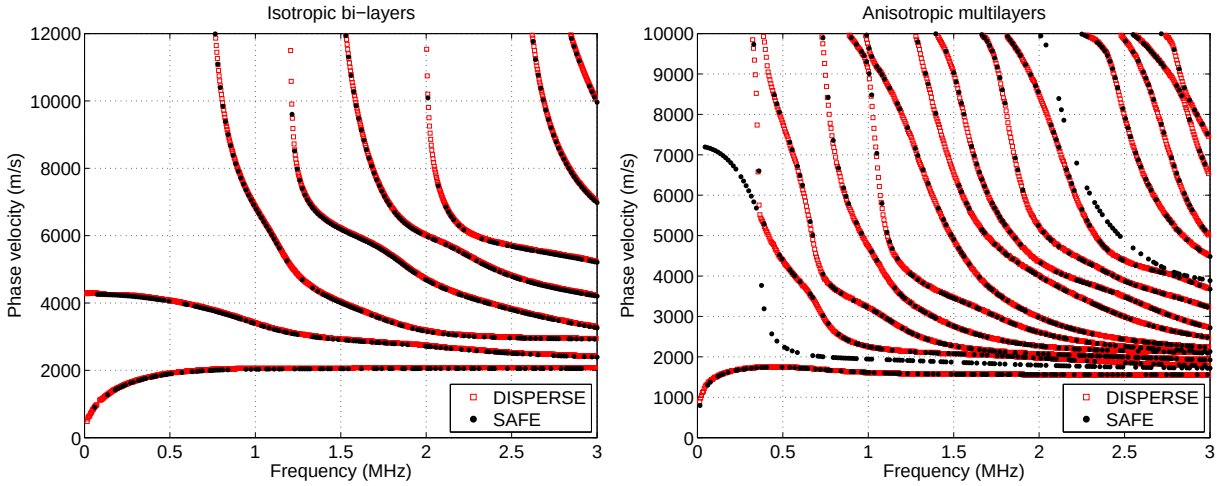

(a) (b)

Figure 3.4: (color online) (a) Dispersion curves of bi-ilayered isotropic plate obtained using SAFE method (circle black marker) and using DISPERSE software (square red marker). (b) Dispersion curves of quadri-layered transversally isotropic plate obtained using SAFE method (circle black marker) and using DISPERSE software (square red marker).

3.5.3 Stochastic convergence analysis

In order to do the statistics on the interest quantities, a stochastic convergence analysis must firstly be carried out. Convergence with respect to number of realisations n_r is carried out in studying the convergence of the estimated second-order moment. This convergence leads to determine the minimal number of realisations to do simulation by using the Monte Carlo solver. For this analysis, we consider a 1 mm-thickness solid layer meshed by 50 quadratic elements which allows us to satisfy the requirement that at least 5 elements per correlation length ($\lambda = 0.1$ mm) are required. Figure 3.5 shows the graphs

of function $n_r \rightarrow \mathrm{Conv}_{\mathrm{C_{ph}}}(\mathrm{n_r})$ for symmetric zero-order mode A_0 (see Fig. 3.5(a)) and antisymmetric zero-order mode S_0 (see Fig. 3.5(b)) at a fixed frequency. The dispersion parameter is fixed at $\delta = 0.3$.

From Fig. 3.5 one can see that the second order moment of phase velocity decreases with the number of realisations. Convergence is reached for $n_r \geq 200$ and $n_r \geq 300$ for A_0 and S_0 modes, respectively. As compared to Fig. 3.5(a), the fluctuation of statistical estimator of the variance of random phase velocity in Fig. 3.5(b) is more important. This behaviour is confirmed in Fig. 3.6 where probability density functions of A_0 and S_0 modes are plotted. Result shows that from statistical point of view S_0 mode is more dispersive than A_0.

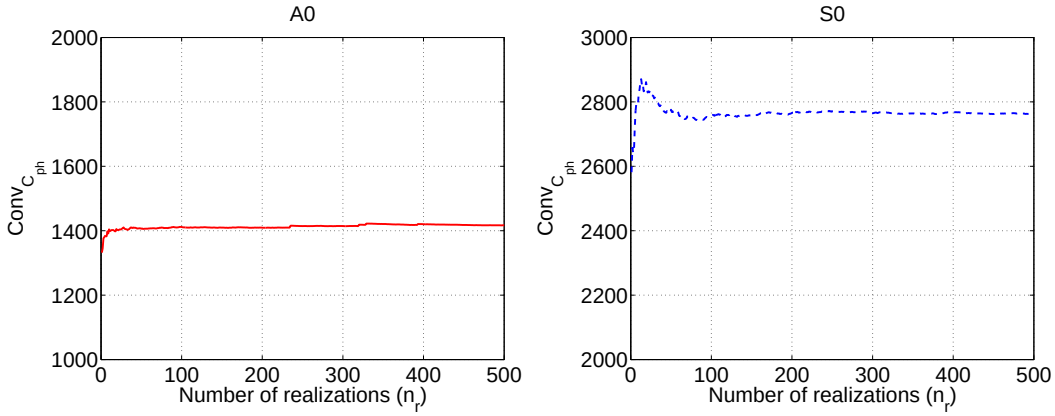

(a) (b)

Figure 3.5: (a): antisymmetric zero-order mode A_0. (b): symmetric zero-order mode S_0. $f = 1$ MHz and $\delta = 0.1$.

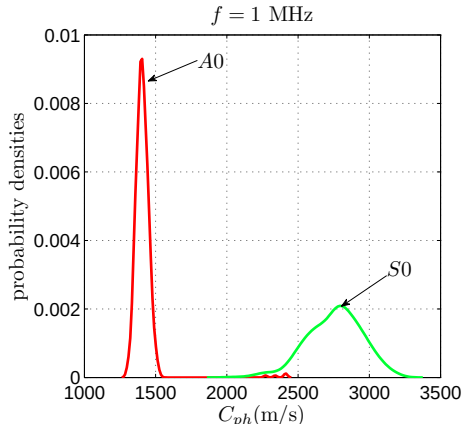

Figure 3.6: (Color online) Probability density functions (PDF) of A_0 and S_0 modes at a given frequency $f = 1$ MHz when $\delta = 0.1$.

3.5.4 Phase velocity

3.5.4.1 Mode separation

The quasi-symmetric and quasi-antisymmetric dispersion curves are plotted in Fig. 3.7 for one realisation of the elasticity tensor when $\delta = 0.1$. In this case, the plate is fully anisotropic and heterogeneous with material properties that vary along the $\mathbf{e_2}$-direction. As result, quasi-symmetric and quasi-antisymmetric modes appear.

The relationship between displacement vector components and mode types are given in Tab. 3.1. A tolerance value ξ of the order of 10^{-6} in the deterministic case, which varies in the stochastic case, is considered for each given dispersion parameter in order to differentiate the modes type using conditions given in Tab. 3.1.

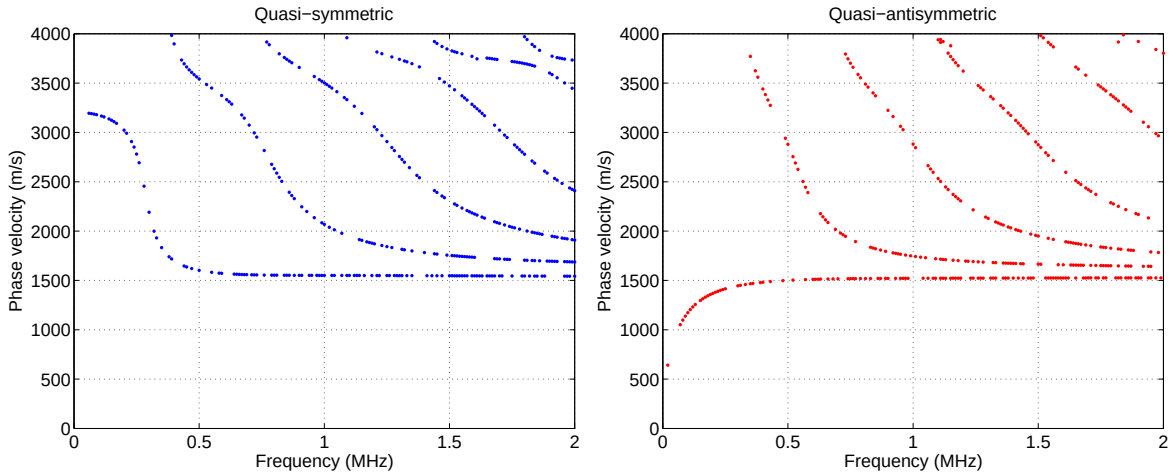

(a) (b)

Figure 3.7: (a): Phase velocity for quasi-symmetric modes. (b): Phase velocity for quasi-antisymmetric modes. These curves are plotted for one realisation when $\delta = 0.1$ with $h = 4$ mm.

3.5.4.2 Sensitivity with respect to bone thickness

Here, we attempt to explore the feasibility of using the guided waves to estimate the plate thickness. We examine Lamb waves of the plate with different thicknesses from $h \sim 1$ mm to $h = 4$ mm. The phase velocity dispersion curves obtained for three thicknesses are presented in Fig. 3.8(a). It can be seen that the curves of high-order A_i and S_i, for $i \geq 1$, modes are translated with respect to the thickness. Hence, when increasing the thickness, high-order modes appear at high cutoff frequencies, *i.e.* the smallest frequencies at which these Lamb waves exist. In other words, a thickness variation yields a translation of high-order modes. Moreover, a increase of the thickness leads to an increase of Lamb mode number.

Next, we paid our attention on the sensitivity of fundamental modes A_0 and S_0 which exist at all frequencies. Figure 3.8(a) reveals that at a given low frequency, *i.e.* $f \leq 250$ kHz, the fundamental quasi-

antisymmetric A_0 mode is more sensitive to thickness value than quasi-symmetric S_0 mode. Indeed, at a fixed frequency, the phase velocity of A_0 mode increases with respect to the thickness, while those of S_0 exhibit a slightly decrease. Nevertheless, we observe frequency ranges on which A_0 and S_0 modes are sensitive to the thickness, for instance from $f = 750$ kHz to $f = 1$ MHz.

In the same way as the phase velocity, the energy velocity dispersion curves show a similar behaviour on fundamental modes as well as on higher order modes (see Fig. 3.8(b)). As seen in Fig. 3.8(a) and (b), A_0 and S_0 modes may be the suitable modes for the determining bone thickness using guided waves. In principle, the plate thickness can be obtained from such model by simulating A_0 and S_0 dispersion curves until there is a good match between numerical and possible experimental results. Thus, a phenomenon such a degradation of the material properties or a modification of the thickness can be detected by guided waves. Note that in the clinical applications for monitoring the human bone health status, there is an unmet need in identifying population having the osteoporosis, in particular women who should receive a preventive treatment (Herrero and Pico, 2016; Invernizzi et al., 2016). Guided Lamb waves are deemed to be a good candidate.

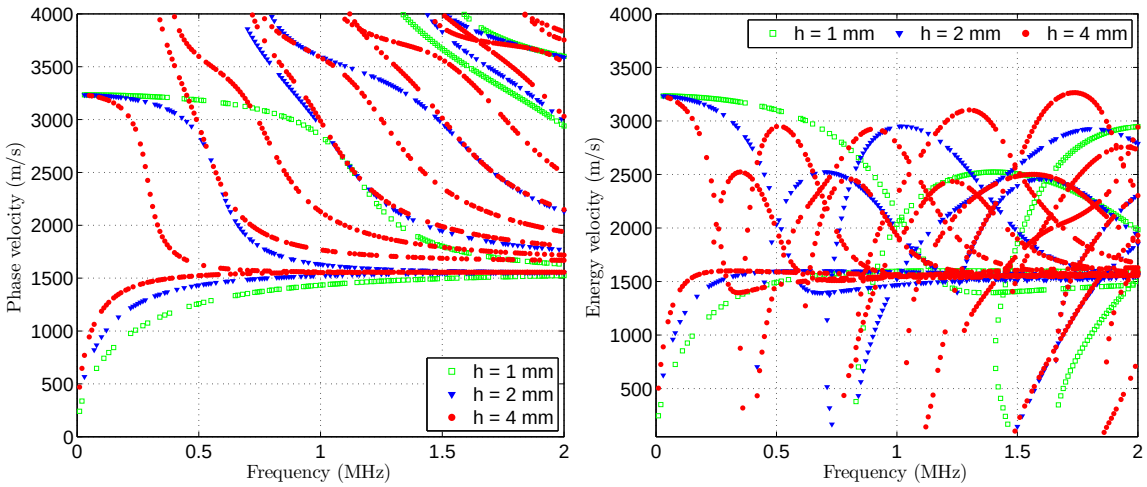

(a) (b)

Figure 3.8: (a) Phase velocity dispersion curves in deterministic models. (b) Energy velocity dispersion curves in deterministic models.

3.5.4.3 Fluctuation on phase velocity

In order to point out the impact of uncertainties in material properties on Lamb waves, a parametric study is proposed. Figure 3.9 shows phase velocity dispersion curves for three bone thicknesses ($h = 1$ mm, $h = 2$ mm and $h = 4$ mm) in frequency range from 0 to 2 MHz. Three dispersion parameters ($\delta = 0.1$, $\delta = 0.2$ and $\delta = 0.3$) are used to generate random properties. For these thicknesses, the probability density functions of fundamental modes are plotted at fixed frequencies in Fig. 3.10.

Due to the random material properties of the plate, the phase velocity exhibits a complementary dispersion behaviour in addition on the one observed in deterministic case, *i.e.* the dispersion of the phase

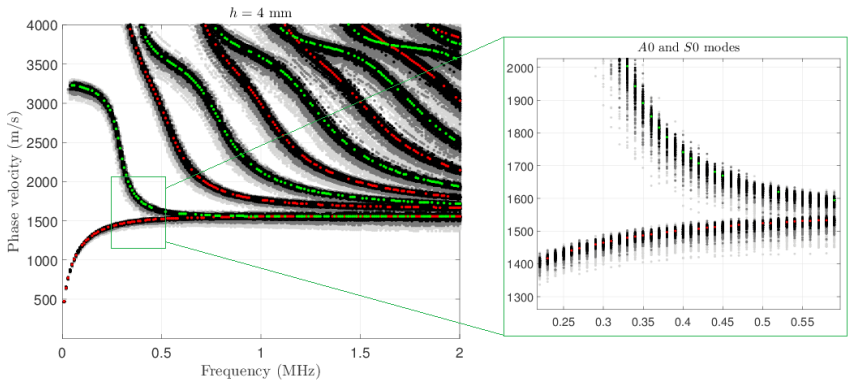

(a)

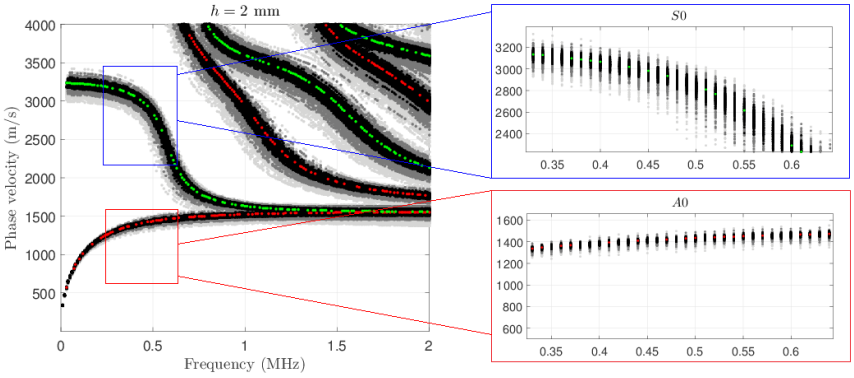

(b)

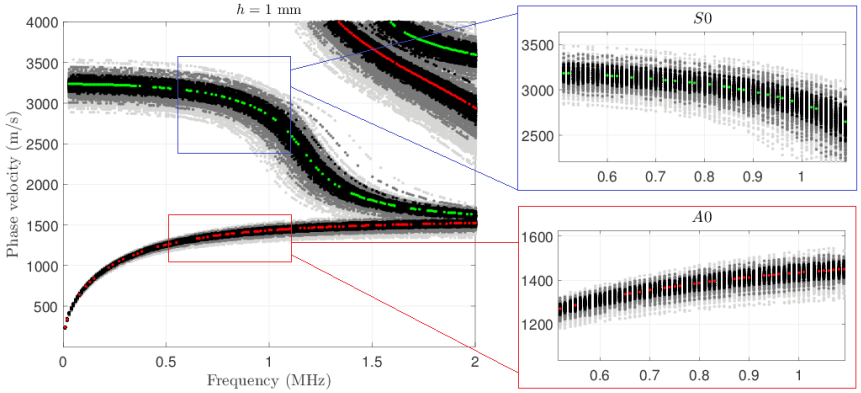

(c)

Figure 3.9: (Color online) Phase velocity dispersion curves when $h = 4$ mm (a), $h = 2$ mm (b) and $h = 1$ mm (c), in which, $\delta = 0.1$ (black region), $\delta = 0.2$ (dark gray region) and $\delta = 0.3$ (light gray region).

velocity with respect to frequency. Hence, for all realisations of the random elasticity tensor, the phase velocity is dispersive for each Lamb mode as shown in Fig. 3.9. All dispersion curves of each realisation of the random medium are extracted. From Fig. 3.9, it can be seen that dispersion curves are affected by the random material properties of the plate. By paying our attention to the fundamental modes, Fig. 3.9(a), (b) and (c) are zoomed. The finding reveals that, for a given dispersion parameter, the mode S_0 is more

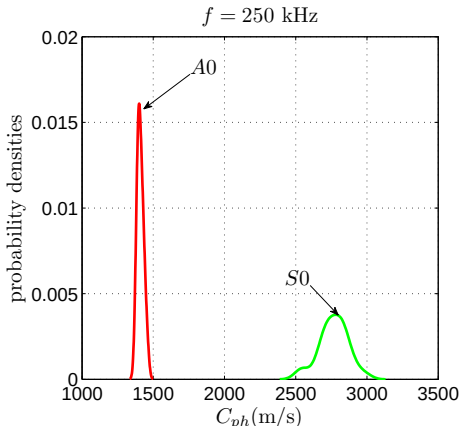

(a)

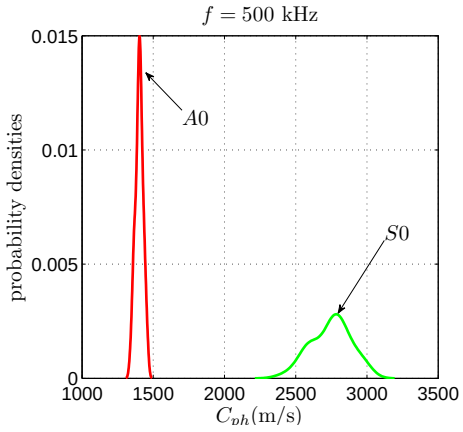

(b)

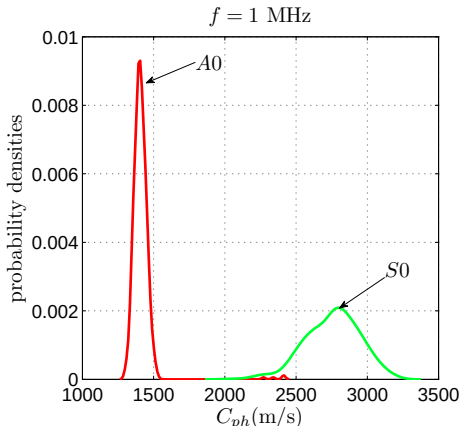

(c)

Figure 3.10: (Color online) Probability density functions of fundamental modes are plotted at fixed frequencies when $h = 4$ mm (a), $h = 2$ mm (b) and $h = 1$ mm (c).

dispersive than mode A_0 on all frequency ranges. For illustration purpose, the probability density functions of phase velocities of modes A_0 and S_0 at fixed frequencies and low dispersion parameter $\delta = 0.1$ are plotted in Fig. 3.10(a), (b) and (c). As compared to the mode A_0, it can be seen that the dispersion and the asymmetric degree of the PDFs of the mode S_0 are more important.

Besides, it can be seen that dispersion curves have about complete branches at each random trajectory. In general, it is very difficult, if not impossible, to detect and plot all the Lamb modes present on a given frequency window. In most of time, branches of the dispersion curves often remain incomplete. This difficulty is encountered in homogeneous as well as heterogeneous medium. In this study, the plate is assumed having random material properties. Thus, random medium having heterogeneous material properties in the thickness are generated *via* a probabilistic model. From Fig. 3.9, it can be seen that all modes have about complete branches on their dispersion curves, *i.e.* at least a point is captured on each frequency. The prominent feature of this result is that the number of Lamb modes captured is more important and the quality of dispersion curves is greatly enhanced when random medium is considered. This observation, which is at first sight counter-intuitive, can be explained by the fact that by generating random and heterogeneous medium, quasi-symmetric and quasi-antisymmetric modes whose the behaviours are close to those of the A and S modes may appear. From a numerical point of view, this can be achieved by obtaining real or complex eigenvalues with a small imaginary part, *i.e.* a small attenuation. Hence, these modes may be captured and added on dispersion curves.

Such model can allow to complete the missing branches or at least to predict an interval in which these missing points should be recovered on the experimental dispersion curves. Indeed, it has been shown that experimentally generated dispersion curves present a large number of incomplete branches (Harb and Yuan, 2015; Lee, 2001; Vallet et al., 2016; Lee and Yoon, 2016). Fitting the missed branches remain a challenge.

3.5.5 Mode shapes

3.5.5.1 Displacement vector at a fixed frequency

Figure 3.11 shows normalised displacement. Some points taken on the dispersion curves are selected to plot the displacement vector. The dotted line presents the displacement in the $\mathbf{e_1}$-direction denoted u_1 whereas solid line shows those on $\mathbf{e_2}$-direction denoted u_2. These figures are plotted for illustration. The material properties are taken on one realisation among all those of the elasticity tensor obtained *via* a Monte Carlo simulation. Note that relations between the displacements of all symmetrical material points with respect to the mean plane of the plate, *i.e.* $x_2 = -2$ mm, are those presented on Tab. 3.1. Figure 3.11 confirms the quasi-symmetric and quasi-antisymmetric behavior of displacement vector on the random heterogeneous media. Indeed, in the mode S (respectively A), the component u_1 of displacement vector is quasi-symmetric (respectively quasi-antisymmetric) with respect to the mean plane of the plate. Whereas in the mode A (respectively S), the component u_2 of displacement vector is quasi-antisymmetric (respectively quasi-symmetric) with respect to the mean plane of the plate. On these figures, the red solid line represents the displacement u_2, the dotted line shows the one u_1. The mode shapes obtained in the deterministic case are presented in Figure 3.12. One may notice that compared to the stochastic case where displacement vector is not fully symmetric (respectively antisymmetric), in the deterministic case, the displacement vector exhibit a fully symmetric (respectively anti-symmetric) behavior.

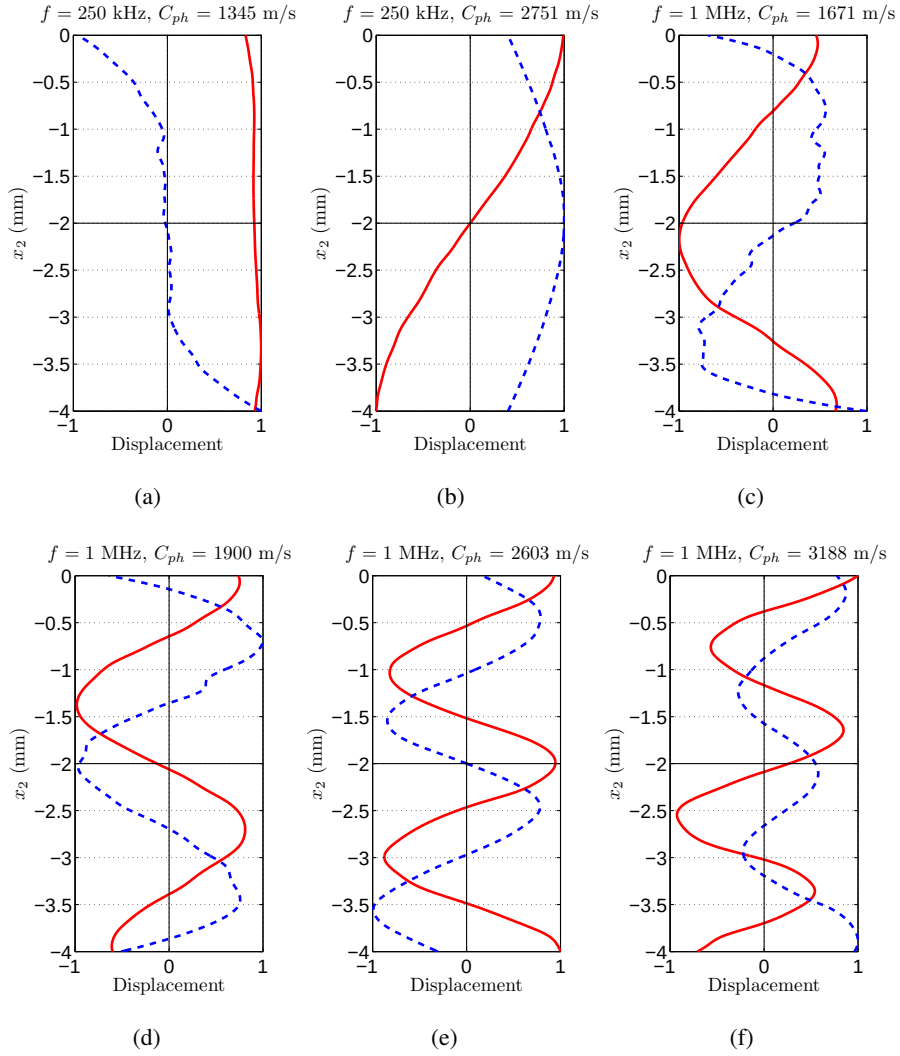

Figure 3.11: (Color online) Normalized displacement at six points taken on the dispersion curves of 4 mm-thickness bone plate. Dispersion parameter is fixed at $\delta = 0.3$. Dotted blue line presents the component u_1 and the solid red line shows the u_2 one. From (a) to (f) are plotted A_0, S_0, A_1, S_1, A_2 and S_2 modes, respectively.

3.5.5.2 Confidence regions

In Figures 3.13 and 3.14, the confidence regions of displacement vector are shown. Confidence regions associated with a probability level $P_c = 0.95$ for random fields u_1 and u_2 are calculated by using the quantile method (see Appendix A). The six first modes are considered to plot these confidence regions. These results allow us to confirm the nature of captured modes. Indeed, a quasi-symmetric mode that would be picked up by mistake instead of another quasi-antisymmetric one would exhibit a incoherent confidence region. Moreover, as observed for the phase velocity, from probability point of view, the mode shape S is more dispersive than mode shape A. Indeed, the expanse of the confidence region is more width in the mode shapes S.

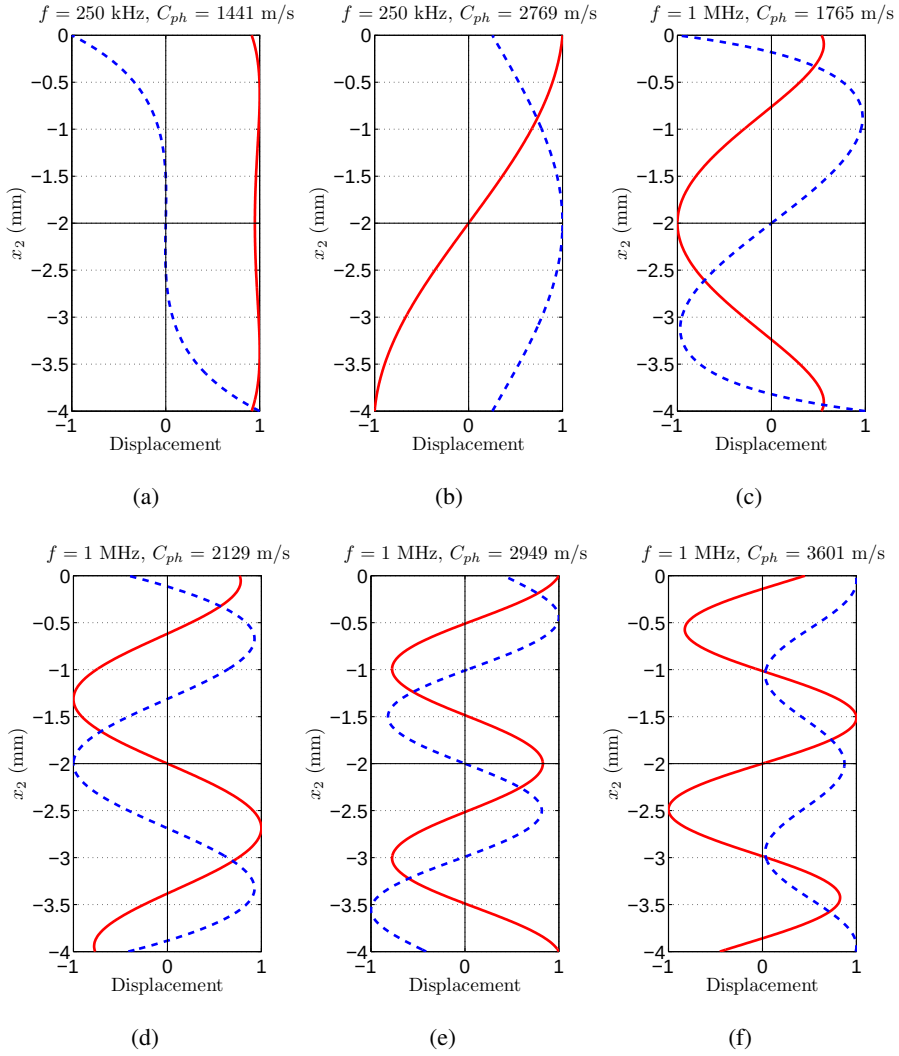

Figure 3.12: See caption of Fig. 3.11. These curves are obtained using the deterministic model.

3.5.6 Energy contribution and attenuation

3.5.6.1 Energy velocity

In order to illustrate the behaviour of the energy velocity travelling across the cross section of the plate, the energy velocity V_e on the random plate is presented. For each realisation of random elasticity tensor, by using Eq. (3.31), we can extract energy velocity dispersion curves. For illustration purpose, the energy velocities for a random plate is presented in Fig. 3.15. The velocities obtained in the deterministic model are plotted in cyan colour marker. For each frequency, Fig. 3.16 allows to know the velocities at which Lamb waves travel along the plate waveguide.

In order to explore the energy contribution when random properties are assumed, we plot energy velocities of all Lamb modes detected at a fixed frequency windows. Thus, velocities $V_e^{(m)}$ for the m-th guided waves are plotted when $\delta = 0.1$ (black region), $\delta = 0.2$ (dark gray region) and $\delta = 0.3$ (light gray region). From Fig. 3.15 and 3.16, it can be seen that, as for the phase velocity dispersion curves, the

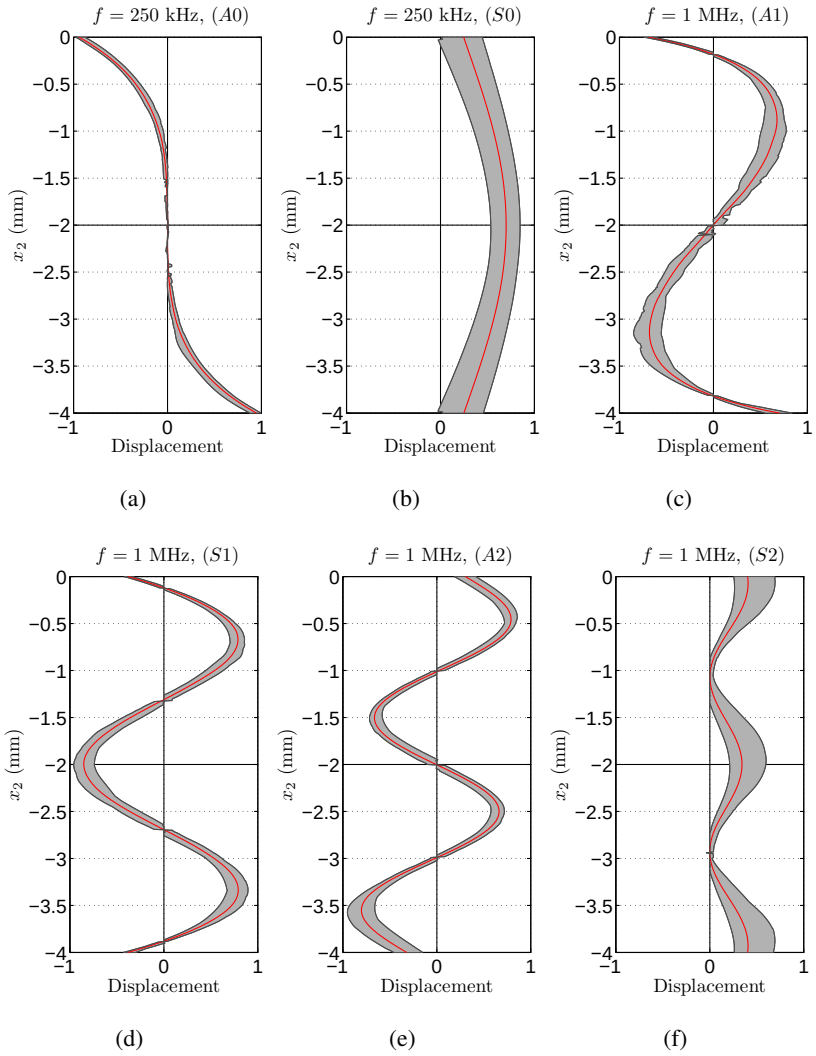

Figure 3.13: Confidence regions of the displacement u_1 at low and high frequencies. The red solid line represents the mean estimated solutions when $\delta = 0.1$. From (a) to (f) are plotted A_0, S_0, A_1, S_1, A_2 and S_2 modes, respectively

energy velocity dispersion curves have about complete branches when random properties are assumed. Moreover, by increasing the dispersion parameter, the complementary dispersion, *i.e.* dispersion due to the random fields, increases. Nevertheless, the obtained curves remain coherent with the deterministic results. That is to say, prediction on unknown velocities can also be performed. Hence, this would make it possible to predict without overestimating or underestimating the rate at which the energy contribution is propagating in the waveguide.

3.5.6.2 Attenuation of Lamb waves

In this section, we explore a possible attenuation of the Lamb waves. In general, Lamb waves can be attenuated by two mechanisms: (*i*) material absorption; (*ii*) Lamb waves leakage. The first mechanism happens when waves are propagating in the absorbing material; their energy is absorbed by material

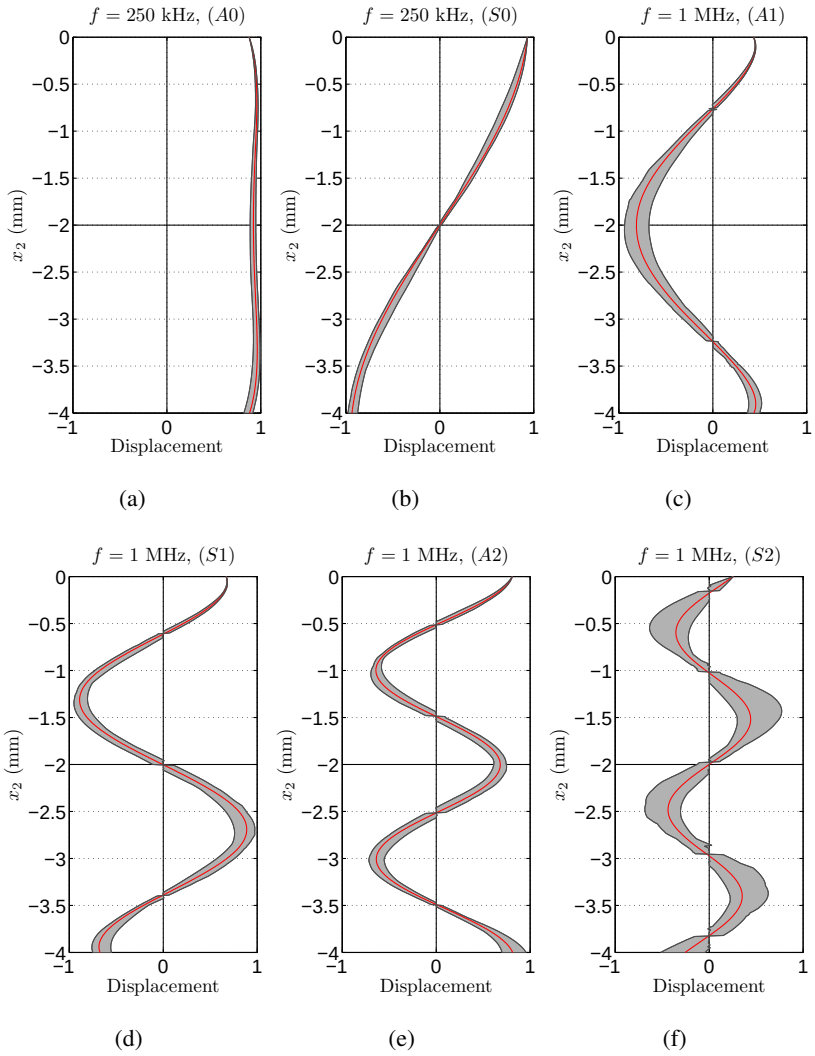

Figure 3.14: Confidence regions of the displacement u_2 at low and high frequencies. The red solid line represents the mean estimated solutions when $\delta = 0.1$. From (a) to (f) are plotted A_0, S_0, A_1, S_1, A_2 and S_2 modes, respectively.

via friction between material particles. Thus, wave energy is converted to heat when the Lamb waves propagate. This attenuation occurs mainly when the plate has viscoelastic material properties. Note that all materials possess some degrees of viscoelasticity, but in the frequency range used in this study, *i.e.* ultrasonic range, this effect is assumed to be negligible in bone tissues. The second mechanism occurs for example when Lamb waves are propagating in plate loaded by a half space medium. In this case, parts of waves are transmitted ("leak") into the half space and will never come back to the plate. They are known as *leaky Lamb waves*. In this study, plate is surrounded by vacuum, *i.e.* free plate, so there is no leakage on Lamb waves energy. In summary, elastic properties and free bone plate are assumed. As result, in the present study, lamb waves should undergo no attenuation of the least no significant. To confirm this prediction on the attenuation, we plot the attenuation defined in Eq. (3.21) on Fig. 3.17(a). The result shows that there is a very negligible attenuation in the frequency range below 4 kHz. At

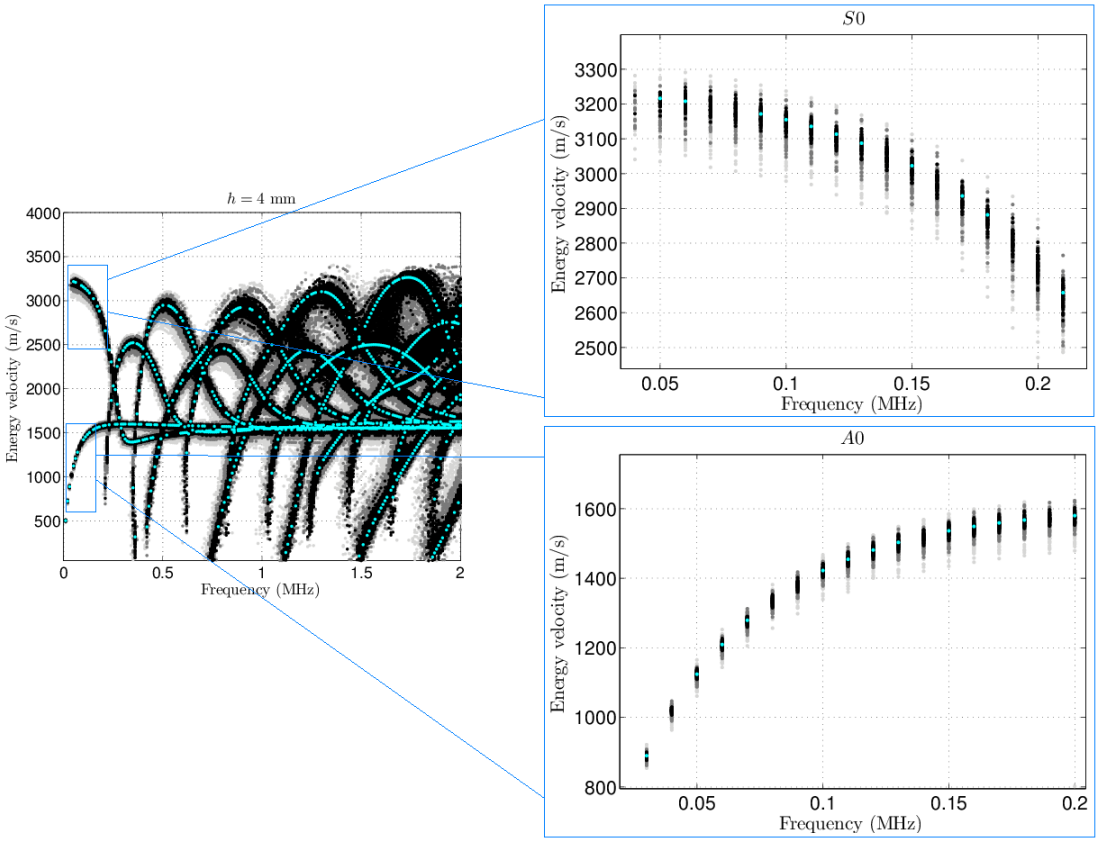

Figure 3.15: (color online) Energy velocity dispersion curves of thick plate. Deterministic results are plotted in cyan color.

most, Lamb waves are attenuated by about 8×10^{-5} Decibel per metre, *i.e.* 0.008 dB/cm, so negligible. For illustration, we plot the attenuation occurs in viscoelastic transversally isotopic plate (see Fig.3.17(b)). The difference between theses two kind of materials properties is tangible, attenuation can reach 180 dB/m (or 20.7233 Np/m) in the viscoelastic homogeneous plate.

3.6 Conclusion

Wave dispersion is a complex phenomenon occurs when waves propagate in heterogeneous material such as bone. Due to the dynamic and its strong frequency dependence, modeling of this phenomenon, *e.g.* Lamb waves, is tricky. The nonlinear problem with respect to wavenumber was deformed in linear eigenvalue problem. The dispersion curves calculated with the SAFE method agreed well with those obtained in the literature and by theoretical solutions in simple cases, which proves the validity as well as the accuracy of this approach. In addition, it is shown that the proposed approach gives very accurate results for multilayered anisotropic plates.

Next, we discussed dispersion curves and displacement field for fundamental modes which are affected by random heterogeneity in the plate. The obtained results are promising and the SAFE method

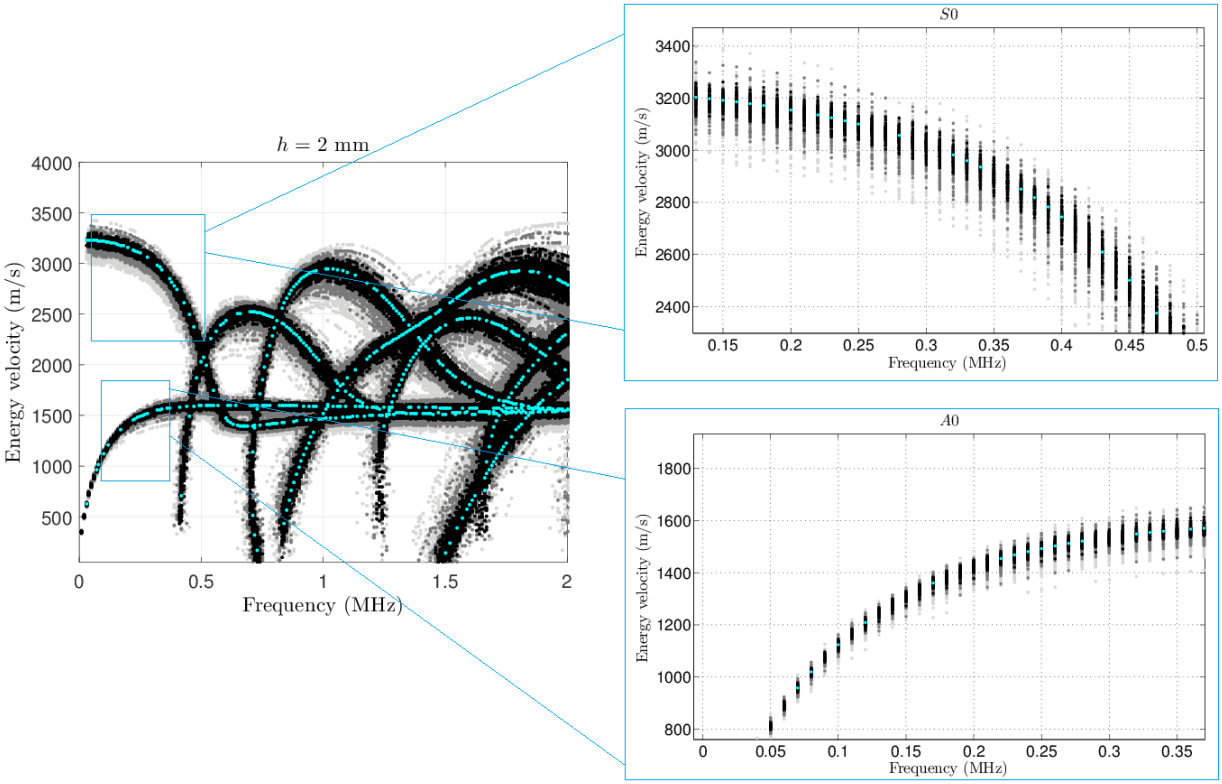

Figure 3.16: (color online) Energy velocity dispersion curves of thin plate.

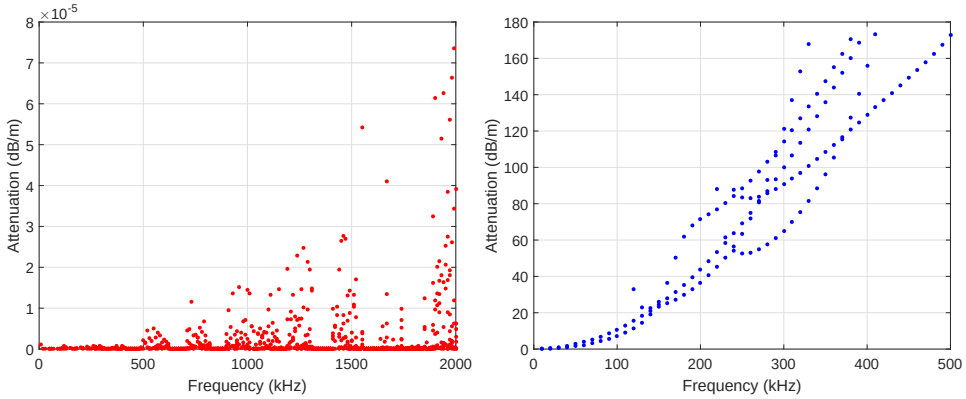

(a) (b)

Figure 3.17: (a) Attenuation of Lamb waves in a free elastic 4mm-waveguide. (b): Attenuation of Lamb waves in a free viscoelastic 4mm-waveguide.

coupling with stochastic model seems to be well suited to be employed for bone characterisation. Moreover, by introducing uncertainties on material properties, the findings show that the SAFE method extracts more completes branches of dispersion curves. As result, such model may help to overcome the lack of experimental data. Thus, one can fit experimental dispersion curves by predicting a confidence region where missing branches should be recovered.

Beside, from a probabilistic point of view, the two fundamental modes are both dispersive, but the fluctuation of S_0 mode is much larger than that of A_0. It has been shown that A_0 and S_0 modes are the more sensitive when the thickness changes. Hence, these modes should be the more suitable for thickness evaluation and material properties determination.

However, this study has some limitations. For example, we considered a free bone plate, so this configuration is only possible for *in vitro* studies. In *in vivo* evaluation, the effect of soft tissue and marrow should be taken into account, even though it has been observed in the literature that soft tissue does not have much effect on estimation of the cortical thickness. In addition, we considered the two-dimensional case to validate this preliminary approach. Hence, it would be interesting to see the relevance of such approach in a tree-dimensional geometry. This is precisely the aim of a forthcoming study, which is devoted to the study of guided waves in 3D cylindrical waveguide mimicking bone having random properties on the radial direction.

It should be noted that, the numerical model proposed here does not exhaust the potential of this approach in bone. Such approach allows also determination of dispersion properties for other macroscopic random medium.

Appendices

A Confidence regions *via* the quantile method

A procedure based on the quantile method is performed for estimating the confidence regions of random variables displacement U_1 and U_2. The confidence region of u_1 is limited by a lower envelope and an upper envelope, denoted by u_1^- and u_1^+, respectively:

$$\mathbb{P}(u_1^- < U_1 \leq u_1^+) = P_c, \tag{3.39}$$

where $\mathbb{P}(A)$ denotes the probability measure of an event A.

Let F_{U_1} be the cumulative distribution function of U_1 defined by $F_{U_1}(u_1) = \mathbb{P}(U_1 \leq u_1)$. The p-th quantile ($p \in]0,1[$) of F_{U_1} is defined by:

$$\zeta(p) = \inf\{r : F_{U_1}(u_1) \geq p\}. \tag{3.40}$$

The lower and upper envelopes u_1^- and u_1^+ are defined by:

$$u_1^- = \zeta\left(\frac{1-P_c}{2}\right), \quad u_1^+ = \zeta\left(\frac{1+P_c}{2}\right). \tag{3.41}$$

Let $\tilde{u_1}_{(1)} < ... < \tilde{u_1}_{(n_r)}$ be the order statistics associated with $U_1(\phi_1), ..., U_1(\phi_{n_r})$, we have the following estimations:

$$u_1^- \simeq \tilde{u_1}_{j^-}, \quad j^- = \text{fix}[n_r(1-P_c)/2], \tag{3.42}$$

$$u_1^+ \simeq \tilde{u_1}_{j^+}, \quad j^+ = \text{fix}[n_r(1+P_c)/2], \tag{3.43}$$

in which $\text{fix}[\star]$ denotes the integer part of the real number $[\star]$.

Bibliography

G. Bal and L. Ryzhik. Time reversal for classical waves in random media. *Comptes Rendus de l'Académie des Sciences - Series I - Mathematics*, 333(11):1041 – 1046, 2001.

C. Baron. Propagation of elastic waves in an anisotropic functionally graded hollow cylinder in vacuum. *Ultrasonics*, 51(2):123 – 130, 2011.

K.J. Bathe. *Finite Element Procedures*. Prentice-hall, 1996.

M.A. Ben Souf, O. Bareille, M.N. Ichchou, F. Bouchoucha, and M. Haddar. Waves and energy in random elastic guided media through the stochastic wave finite element method. *Physics Letters A*, 377(37): 2255 – 2264, 2013.

A. Bernard, M.J.S. Lowe, and M. Deschamps. Guided waves energy velocity in absorbing and non-absorbing plates. *The Journal of the Acoustical Society of America*, 110(1):186–196, 2001.

F. Bouchoucha, M.N. Ichchou, and M. Haddar. Guided wave propagation in uncertain elastic media. *Ultrasonics*, 53(2):303 – 312, 2013.

J. Chen and Z. Su. On ultrasound waves guided by bones with coupled soft tissues: A mechanism study and *in vitro* calibration. *Ultrasonics*, 54(5):1186 – 1196, 2014.

J. Chen, L. Cheng, Z. Su, and L. Qin. Modeling elastic waves in coupled media: Estimate of soft tissue influence and application to quantitative ultrasound. *Ultrasonics*, 53(2):350 – 362, 2013.

D.E. Chimenti and S.I. Rokhlin. Relationship between leaky lamb modes and reflection coefficient zeroes for a fluid coupled elastic layer. *The Journal of the Acoustical Society of America*, 88(3):1603–1611, 1990.

M. Cieszko, R. Drelich, and M. Pakuła. Wave dispersion in randomly layered materials. *Wave Motion*, 64:52 – 67, 2016.

S.C. Cowin. *Bone mechanics handbook*. CRC Press, Boca Raton, FL, 2nd edition, 2001.

C. Desceliers, C. Soize, S. Naili, and G. Haiat. Probabilistic model of the human cortical bone with mechanical alterations in ultrasonic range. *Mechanical Systems and Signal Processing*, 32:170 – 177, 2012.

X.N. Dong and X.E. Guo. The dependence of transversaly isotropic elasticity of human femoral cortical bone on porosity. *Journal of Biomechanics*, 37:1281–1287, 2004.

A.T. Fabro, N.S. Ferguson, T. Jain, R. Halkyard, and B.R. Mace. Wave propagation in one-dimensional waveguides with slowly varying random spatially correlated variability. *Journal of Sound and Vibration*, 343:20 – 48, 2015.

R.P. Gilbert, P. Guyenne, and J. Li. A viscoelastic model for random ultrasound propagation in cancellous bone. *Computers & Mathematics with Applications*, 66(6):943 – 964, 2013.

M.S. Harb and F.G. Yuan. A rapid, fully non-contact, hybrid system for generating lamb wave dispersion curves. *Ultrasonics*, 61:62 – 70, 2015.

S. Herrero and Y. Pico. Treatments for post-menopausal osteoporotic women, what's new? how can we manage long-term treatment? *European Journal of Pharmacology*, 779:8 – 21, 2016.

M.N. Ichchou, F. Bouchoucha, M.A. Ben Souf, O. Dessombz, and M. Haddar. Stochastic wave finite element for random periodic media through first-order perturbation. *Computer Methods in Applied Mechanics and Engineering*, 200(4):2805 – 2813, 2011.

M. Invernizzi, M. Noale, G. Iolascon, G.L. Mauro, P. Falaschi, G. Arioli, S. Maggi, and C. Cisari. Vertebral fractures, function and cognitive status in osteoporotic hip fractured women: The {FOCUS} study. *European Geriatric Medicine*, 8(1):48–53, 2016.

E.T. Jaynes. Information theory and statistical mechanics. *The Physical Review*, 106(4):620–630, 1957a.

E.T. Jaynes. Information theory and statistical mechanics. II. *The Physical Review*, 108(2):171–190, 1957b.

K.I. Lee and S.W. Yoon. Propagation of time-reversed lamb waves in acrylic cylindrical tubes as cortical-bone-mimicking phantoms. *Applied Acoustics*, 112:10 – 13, 2016.

Y.-C. Lee. Measurements of dispersion curves of leaky lamb waves using a lens-less line-focus transducer. *Ultrasonics*, 39(4):297 – 306, 2001.

M.L. Mehta. *Random Matrices*. Academic Press, 2004.

P. Moilanen. Ultrasonic guided waves in bone. *IEEE Transactions of Ultrasonics, Ferroelectrics, and Frequency Control*, 55(6):1277–1286, 2008.

S. Naili, V.-H. Nguyen, M.-B Vu, C. Desceliers, and C. Soize. Modeling of transient wave propagation in a heterogeneous solid layer coupled with fluid: Application to long bones. *The Journal of the Acoustical Society of America*, 137(2):668–678, 2015.

A.H. Nayfeh and D.E. Chimenti. Ultrasonic wave reflection from liquid-coupled orthotropic plates with application to fibrous composites. *Journal of A*, 55:863–870, 1988.

A.H. Nayfeh and D.E. Chimenti. Free wave propagation in plates of general anisotropic media. *Journal of Applied Mechanics*, 56:881–886, 1989.

H.A. Nayfeh. *Wave Propagation in Layered Anisotropic Media*. Elsevier, 1995.

V.-H. Nguyen, T. Lemaire, and S. Naili. Poroelastic behaviour of cortical bone under harmonic axial loading: A finite element study at the osteonal scale. *Medical Engineering & Physics*, 32(4):384 – 390, 2010a.

V.-H. Nguyen, S. Naili, and V. Sansalone. A closed-form solution for in vitro transient ultrasonic wave propagation in cancellous bone. *Mechanics Research Communications*, 37(4):377 – 383, 2010b.

V.-H. Nguyen, A. Abdoulatuf, C. Desceliers, and S. Naili. A probabilistic study of reflection and transmission coefficients of random anisotropic elastic plates. *Wave Motion*, 64:103 – 118, 2016.

P.H.F. Nicholson, P. Moilanen, T. Karkkainen, J. Timonen, and S. Cheng. Guided ultrasonic waves in long bones: modelling, experiment and *in vivo* application. *Physiological Measurement*, 23(4):755–768, 2002.

P.F. Pai, H. Deng, and M.J. Sundaresan. Time-frequency characterization of lamb waves for material evaluation and damage inspection of plates. *Mechanical Systems and Signal Processing*, 62-63:183–206, 2015.

J.O. Parra, C.L. Hackert, R. Ababou, and M.J. Sablik. Dispersion and attenuation of acoustic waves in randomly heterogeneous media. *Journal of Applied Geophysics*, 42(2):99 – 115, 1999.

J.L. Rose. *Ultrasonic waves in solid media*. Cambridge University Press, 1999.

D. Royer and E. Dieulesaint. *Elastic wave in solids I. free and guides propagation*. Springer, 2000.

C. Soize. Maximum entropy approach for modeling random uncertainties in transient elastodyanmics. *The Journal of the Acoustical Society of America*, 109(5):1979–1996, 2001.

C. Soize. Non-gaussian positive-definite matrix-valued random fields for elliptic stochastic partial differential operators. *Computer Methods in Applied Mechanics and Engineering*, 195(1-3):26–64, 2006.

Z. Su and L. Ye. *Identification of Damage Using Lamb Waves*, volume 48. Springer-Verlag London, 2009.

D.-A. Ta, K. Huang, W.-Q. Wang, Y.-Y. Wang, and L.H. Le. Identification and analysis of multimode guided waves in tibia cortical bone. *Ultrasonics*, 44, Supplement:e279 – e284, 2006. Proceedings of Ultrasonics International (UI'05) and World Congress on Ultrasonics (WCU).

Y. Tasinkevych, J. Podhajecki, K. Falińska, and J. Litniewski. Simultaneous estimation of cortical bone thickness and acoustic wave velocity using a multivariable optimization approach: Bone phantom and in-vitro study. *Ultrasonics*, 65:105 – 112, 2016.

A. Tatarinov, N. Sarvazyan, and A. Sarvazyan. Use of multiple acoustic wave modes for assessment of long bones: Model study. *Ultrasonics*, 43(8):672 – 680, 2005.

D.R. Thakare, P. Belanger, and P. Rajagopal. Effect of dimensional degradation on ultrasonic guided waves in bone system. *Physics Procedia*, 70:1131 – 1134, 2015.

Q. Vallet, N. Bochud, C. Chappard, P. Laugier, and J.G. Minonzio. *In vivo* characterization of cortical bone using guided waves measured by axial transmission. *IEEE Transactions on Ultrasonics, Ferroelectrics, and Frequency Control*, 63(9):1361–1371, 2016.

L. Wang, S.P. Fritton, S.C. Cowin, and S. Weinbaum. Fluid pressure relaxation depends upon osteonal microstructure: modeling an oscillatory bending experiment. *Journal of Biomechanics*, 32:663–672, 1999.

K. Xu, D. Liu, D.-A. Ta, B. Hu, and W. Wang. Quantification of guided mode propagation in fractured long bones. *Ultrasonics*, 54(5):1210 – 1218, 2014.

Chapter 4

Dispersion of guided waves in random anisotropic elastic cylinders: Application to ultrasound characterization of long bones

"La géométrie n'est pas vrai,
elle est avantageuse."
[Henri Poincaré.]

CHAPTER INFORMATION

Keywords:
random properties
guides waves
dispersion curves
cortical bone
ultrasound
SAFE method
cylindrical guided wave

Publication:
The work presented in this chapter led to the writing of a scientific article which is intended to be submitted for publication [P1].

ABSTRACT

This chapter presents an extension of the previous work wherein a two-dimensional model is proposed for investigate the behavior of Lamb waves in random cortical bone plate. Here we aim to study the dispersion of ultrasound waves propagating in a cylindrical wave-guide in which the elastic properties in the cross-section are randomly heterogeneous. First, we present the development of a Semi-Analytical Finite Element formulation to solve the wave propagation problem in considered system. Next, stochastic model is employed by introducing random heterogeneity of elastic properties. The solutions obtained by SAFE method were validated for homogeneous structures for which the solutions may be obtained using analytical method (DISPERSE). Parametric study has been performed to highlight the effects of three-dimensional geometry and random properties on the dispersion of the phase velocity and the attenuation. Comparison between plate and cylindrical models are also discussed.

Contents

4.1 Introduction

The subject of guided waves in cylinder were first studied in the late 19th century. Chree (1889) and Pochlammer (1876) were the first to mathematically investigate this problem and their names are still associated with the equation describing the modes of solid cylinder. The first general solution of waves propagation in an infinity hollow cylinder is proposed by Gazis (1959). His pilot work included the basis analysis of non-axisymmetric flexural modes, as well as axisymmetric, longitudinal and torsional modes in cylinder waveguide. Studies that followed were largely based on his work.

Focusing on QUS bone evaluation which is our interest problem, recent studies are performed by modeling bone as a cylindrical waveguide. For homogeneous bone cylinder model, Protopappas et al. (2007) studied the healing long bone *via* the dispersion of guided modes. Their results suggest that monitoring of bone fracture healing can be enhanced by analyzing the characteristics of the higher-order longitudinal modes. Lee and Yoon (2016) investigate the propagation of time-reversed guides waves in cylinder cortical bone by using a modified time-reversal method. It has been shown that the time-reversed Lamb wave would essentially behave as A0 Lamb wave. Chen and Su (2014) evaluated the precision and accuracy of QUS assessment for human bone when soft tissue is taken into account. On the Nauleau (2013) thesis, the feasibility of using circumferential guided wave to characterize femoral neck is investigated.

Taking into account the heterogeneities in bone material properties, Baron (2011) modeled bone as a Functionally Graded Material cylindrical waveguide. She investigated the influence of curvature of waveguides on guides waves propagation. In Baron (2012), the gradient of cylindrical cortical bone seems to be relevant to evaluating age-related changes in cortical bone in the context of osteoporosis and therapeutic follow-up. Charalambopoulos et al. (2012) proposed a three-dimensional framework to model wave propagation in cylindrical waveguides exhibiting microstructures such cortical bones with a gradient. All these previous bone cylindrical models are assumed that bone material properties are fixed and perfectly known.

However, from QUS bone assessment point of view, cortical bone material properties exhibit random fluctuation Desceliers et al. (2012). Indeed, it is well known that bone properties depend on many factors such genetic, environmental, physiological and pathological. In addition, due to a lack of more *in vivo* data, statistical and repeatability studies are still limited. Taking into account the uncertainties on material properties is become a key issue in the modeling of mechanical structures, as evidenced by the increase in publications (Gomez, 2009; Lunéville and Mercier, 2010; Parra et al., 1999; Bal and Ryzhik, 2001; Ichchou et al., 2011; Bouchoucha et al., 2013; Ben Souf et al., 2013; Fabro et al., 2015)

In recent years, numerical studies investigated ultrasound propagating in random bone, but only the two-dimensional case is considered (i.e., random cortical bone plate). In such 2D stochastic models, the first application on bone can be found in Macocco et al. (2006), where the prediction of measured longitudinal velocity by AT technique is investigated in probabilistic point of view. The bone is considered to have random material properties. In Desceliers et al. (2009) a simplistic two-dimensional bone plate model coupled with a stochastic modeling of bone elasticity tensor seems to be suitable to recover the

experimental measurements. In Desceliers et al. (2012) a probabilistic model is proposed to model the gradient of bone properties derived to a gradient of porosity in the thickness. Mézière et al. (2013) model trabecular bone by 2D and 3D (a cube) models. Their results validate the relevancy of using random media in the context of two-wave propagation in trabecular bone. They explore the possibility to describe outside Biot's framework, two longitudinal waves arising from propagation in a random medium. Gilbert et al. (2013) investigate ultrasound propagation in random viscoelastic cancellous bone. Their results show that ultrasounds are attenuated by both viscosity and random inhomogeneity of the propagating medium. Recently, in Naili et al. (2015) the bone is modeled as a two-dimensional randomly heterogeneous plate in the context of AT technique. It is shown that the first arrival signal (FAS) is very sensitive to dispersion of the bone's elasticity tensor in a statistical sense. Subsequently, in our previous works Nguyen et al. (2016) and Abdoulatuf et al. (2015) we proposed a probabilistic framework for studying reflection and transmission (R/T) coefficients on random cortical bone. The effect of uncertainty of elasticity properties on the R/T coefficients measured from different angle of incidence is highlighted. In a recent study, by introducing uncertainty in bone material properties, we studied guides waves dispersion from probabilistic point of view (results are presented in the previous chapter). We showed the relevancy of introducing random properties to identify more branches on the experimental dispersion curves.

Despite uncertainties on bone physical properties, it appear that, in contrast to deterministic bone cylindrical waveguides and 2D random plates waveguides, for which research studies have been evolving, no research work (for our knowledge) has been conducted for random bone cylindrical waveguide. To our knowledge, the present work is probably the first example, which discusses the possible modeling of bone as random cylindrical waveguide in the context of bone evaluation. By random cylindrical waveguides we mean that the bone material properties are randomly varied on the radial direction. As results, the generated medium will be a cylinder having random heterogeneity.

Strictly speaking, in this work, we extend our previous numerical study by addressing a more realistic geometry. The three-dimensional cylindrical geometry of cortical bone is taken into account. The aims of this study are i) to propose a numerical framework for studying Lamb modes in random cylinder ii) to elucidated the influence of three-dimensional geometry on dispersion characteristics iii) to explore the effect of uncertainties on the output random quantities iv) to investigate the sensitivity of guides waves on random material properties. In this respect, we first examine an homogeneous deterministic bone cylinder. Next uncertainties on properties is introduced.

The remaining part of the chapter focuses on the formulation, implementation, validation and application of the proposed approach to guides waves in the context of QUS bone evaluation. In the next section, the tree-dimensional geometry is presented and governing equations are described. In section 4.3, using the SAFE method, we give a general formulation for studying guides waves in cylindrical waveguide. In section 4.4 The methodology used to generate the random elasticity tensor in three dimensions is presented and a stochastic solver is proposed. In section 4.5 we verify and validate the proposed approach, and some numerical examples presenting a simulation test in cortical bone are displayed. Finally, a summary and some concluding remarks are presented in section 4.6.

4.2 Problem formulation

4.2.1 Model specification

Let us consider a cylindrical reference system $\mathcal{R}(O;\mathbf{e}_r,\mathbf{e}_\theta,\mathbf{e}_z)$, where O is the origin of the space and $(\mathbf{e}_r,\mathbf{e}_\theta,\mathbf{e}_z)$ is the orthonormal basis. The coordinates of an arbitrary point M are specified by (r,θ,z) in $\mathcal{R}$. A solid cylindrical layer with constant thickness h, which represents cortical bone and occupies the unbounded domain Ω^b in $\mathbf{e}_z$-axis, is placed in vacuum. The waveguide cross section is set in the $(\mathbf{e}_r,\mathbf{e}_\theta)$ plane and the $\mathbf{e}_z$-axis coincides with the axis of the waveguide, as illustrated in Fig. 4.1. The domain Ω^b may be defined by:

$$\Omega^b = \{M(r,\theta,z); R_i \leq r \leq R_e\}\,, \tag{4.1}$$

where, R_i and R_e denote the internal and external radius, respectively, as shown in Fig. 4.1. Note that the elastic solid cylinder is assumed to be homogeneous in the $\mathbf{e}_z$-direction and $\mathbf{e}_\theta$-direction, but may be varied along the $\mathbf{e}_r$-direction.

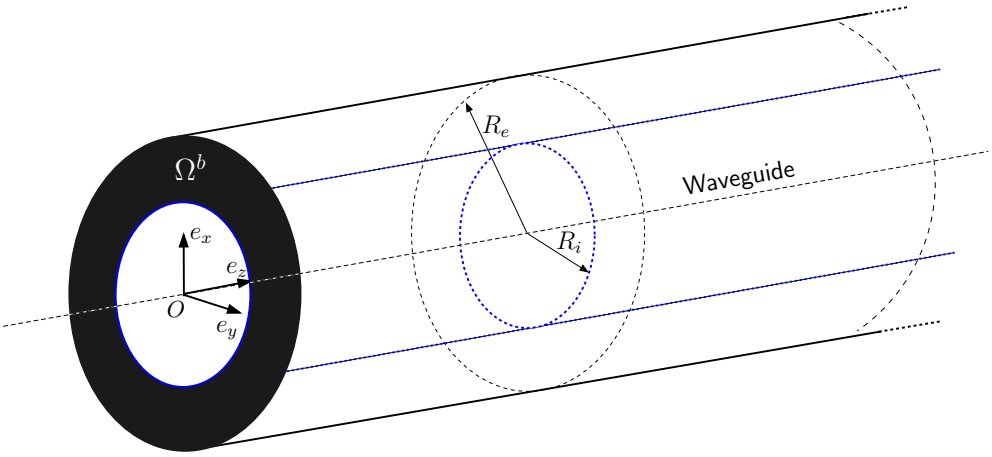

(a)

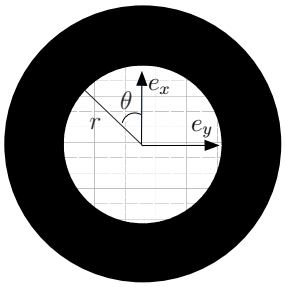

(b)

Figure 4.1: A sketch showing the three-dimensional cylindrical waveguide physically mimicking bone.

4.2.2 Governing equations

In what follows, we denote, respectively, by ∇, $\nabla.$ and ∇^2 the gradient, divergence and Laplacian operators in cylindrical three-dimensional space (3D). We denote respectively by ∂_i and ∂_i^2 the partial derivatives of first and second operators with respect to κ ($\kappa = r, \theta, z$,...). The time derivative is denoted by a dot superimposed. The boldface symbols are used to designate the matrices, the fields of vectors and tensors in two-dimensional and three-dimensional spaces.

By neglecting body forces, the equation of motion in Ω^b is given by:

$$\rho\ddot{\mathbf{u}} - \nabla \cdot \boldsymbol{\sigma} = \mathbf{0}, \quad \forall M \in \Omega^b, \tag{4.2}$$

which may be written in the vectorial form:

$$\rho\ddot{\mathbf{u}} - \mathbf{L}_\sigma^T \mathbf{s} = \mathbf{0}, \quad \forall M \in \Omega^b, \tag{4.3}$$

where ρ is the mass density of the solid cylinder, $\mathbf{u}(M,t) = (u_r, u_\theta, u_z)^T$ is the displacement vector in which the superscript "T" denotes the transpose operator, the vector $\mathbf{s}$ contains the components of the stress tensor $\boldsymbol{\sigma}$ and is denoted by $\mathbf{s} = (\sigma_{rr}, \sigma_{\theta\theta}, \sigma_{zz}, \sigma_{\theta z}, \sigma_{rz}, \sigma_{r\theta})^T$. The operator $\mathbf{L}_\sigma$ is defined by:

$$\mathbf{L}_\sigma = \mathbf{L}_r\partial_r + \mathbf{L}_\theta\frac{1}{r}\partial_\theta + \mathbf{L}_z\partial_z + (\mathbf{L}_r - \mathbf{L}_0)\frac{1}{r}, \tag{4.4}$$

$$\mathbf{L}_r = \begin{bmatrix} 1 & 0 & 0 \\ 0 & 0 & 0 \\ 0 & 0 & 0 \\ 0 & 0 & 0 \\ 0 & 0 & 1 \\ 0 & 1 & 0 \end{bmatrix}, \quad \mathbf{L}_\theta = \begin{bmatrix} 0 & 0 & 0 \\ 0 & 1 & 0 \\ 0 & 0 & 0 \\ 0 & 0 & 1 \\ 0 & 0 & 0 \\ 1 & 0 & 0 \end{bmatrix}, \quad \mathbf{L}_z = \begin{bmatrix} 0 & 0 & 0 \\ 0 & 0 & 0 \\ 0 & 0 & 1 \\ 0 & 1 & 0 \\ 1 & 0 & 0 \\ 0 & 0 & 0 \end{bmatrix}, \quad \mathbf{L}_0 = \begin{bmatrix} 0 & 0 & 0 \\ 1 & 0 & 0 \\ 0 & 0 & 0 \\ 0 & 0 & 0 \\ 0 & 0 & 0 \\ 0 & -1 & 0 \end{bmatrix}. \tag{4.5}$$

Using the notation of Voigt, the Hooke law reads: $\mathbf{s} = \mathbf{c}\mathbf{e}$ where $\mathbf{e}$ is a vector containing the strain components which are given by $\mathbf{e} = (\epsilon_{rr}, \epsilon_{\theta\theta}, \epsilon_{zz}, 2\epsilon_{\theta z}, 2\epsilon_{rz}, 2\epsilon_{r\theta})^T = \mathbf{L}_\epsilon\mathbf{u}$, and $\mathbf{c}$ is the matrix containing the components of the anisotropic elasticity tensor expressed *via* the Voigt notation:

$$\mathbf{c} = \begin{bmatrix} c_{11} & c_{12} & c_{13} & c_{14} & c_{15} & c_{16} \\ c_{21} & c_{22} & c_{23} & c_{24} & c_{25} & c_{26} \\ c_{31} & c_{32} & c_{33} & c_{34} & c_{35} & c_{36} \\ c_{41} & c_{42} & c_{43} & c_{44} & c_{45} & c_{46} \\ c_{51} & c_{52} & c_{53} & c_{54} & c_{55} & c_{56} \\ c_{61} & c_{62} & c_{63} & c_{64} & c_{65} & c_{66} \end{bmatrix}. \tag{4.6}$$

The operator $\mathbf{L}_\epsilon$ is defined as follows:

$$\mathbf{L}_\epsilon = \mathbf{L}_r\partial_r + \mathbf{L}_\theta\frac{1}{r}\partial_\theta + \mathbf{L}_z\partial_z + \mathbf{L}_0\frac{1}{r}. \tag{4.7}$$

In this model, it is assumed that the physical properties of the solid only depend on r, *i.e.* $\mathbf{c} = \mathbf{c}(r)$.

The cylindrical internal interfaces Γ_i^{bv} (resp. external Γ_e^{bv}) between the solid bone surfaces and vacuum domains are referred to as free surfaces. Thus, we get the free-surfaces boundary conditions on internal and external interfaces Γ_i^{bv} and Γ_e^{bv}, respectively:

$$\boldsymbol{\sigma}\mathbf{n}_\alpha^{bv} = \mathbf{0}, \qquad \forall M \in \Gamma_\alpha^{bv} \quad (\alpha = i, e), \tag{4.8}$$

where $\mathbf{n}_\alpha^{bv}$ is a normal unit vector of Ω^b at the interfaces Γ_α^{bv}. Seeing that $\mathbf{n}_e^{bv} = -\mathbf{n}_i^{bv} = \{1,0,0\}^T$, Eq. (4.8) may be written as follows:

$$\mathbf{t} = \{0,0,0\}^T, \quad \text{at } r = R_e \text{ and } r = R_i, \tag{4.9}$$

where $\mathbf{t} = \mathbf{L}_r^T\mathbf{s} = \{\sigma_{rr}, \sigma_{r\theta}, \sigma_{rz}\}^T$. Seeing that $\mathbf{s} = \mathbf{c}\mathbf{e}$ and $\mathbf{e} = \mathbf{L}_\epsilon\mathbf{u}$, the traction vector $\mathbf{t}$ may be written in the following expanded form:

$$\mathbf{t} = (\mathbf{L}_r^T\mathbf{c}\mathbf{L}_r\partial_r + \frac{1}{r}\mathbf{L}_r^T\mathbf{c}\mathbf{L}_\theta\partial_\theta + \mathbf{L}_r^T\mathbf{c}\mathbf{L}_z\partial_z + \frac{1}{r}\mathbf{L}_r^T\mathbf{c}\mathbf{L}_0)\mathbf{u}, \tag{4.10}$$

4.3 Solution of the three-dimensional mean problem

4.3.1 Wave field in the solid cylinder

We look for the plane wave solution in the solid (see Eq. (4.3)) in the following form:

$$\mathbf{u}(M,t) = \hat{\mathbf{u}}_n(r)\exp(\mathrm{i}n\theta)\exp[\mathrm{i}(k_z z - \omega t)], \quad \forall M \in \Omega^b, \tag{4.11}$$

where, k_z, ω and n denote the axial wavenumber, the angular frequency and the circumferential wave number, respectively. Note that $\hat{\mathbf{u}}_n = (\hat{u}_r^{(n)}, \hat{u}_\theta^{(n)}, \hat{u}_z^{(n)})^T$. Consequently, the time derivative and the spatial differential operations with respect to z and θ turn into simple factors:

$$\partial_t(*) \longrightarrow -\mathrm{i}\omega(*), \quad \partial_z \longrightarrow \mathrm{i}k_z(*) \quad , \quad \partial_\theta \longrightarrow \mathrm{i}n(*) \tag{4.12}$$

As result, the equation of motion Eq. (4.3) can be written as a system of partial differential equations on the displacement $\hat{\mathbf{u}}_n$ with respect only to r. At each circumferential mode n, this equation leads to:

$$\begin{aligned}
&\Big[-\omega^2\mathbf{A}_\rho + (k_z)^2\mathbf{A}_{zz} + \frac{1}{r^2}\Big(\mathbf{A}_{11} + n^2\mathbf{A}_{\theta\theta} + \mathrm{i}n(\mathbf{A}_{\theta 1}^T - \mathbf{A}_{\theta 1})\Big) \\
&+ k_z\frac{1}{r}\Big(\mathrm{i}\mathbf{A}_{z1}^T - \mathrm{i}\mathbf{A}_{z1} + n(\mathbf{A}_{\theta z} + \mathbf{A}_{\theta z}^T)\Big)\Big]\hat{\mathbf{u}}_n \\
&+ \Big[\frac{1}{r}(\mathbf{A}_{r0}^T - \mathrm{i}n\mathbf{A}_{r\theta}^T) - \mathrm{i}k_z\mathbf{A}_{rz}^T\Big]\partial_r\hat{\mathbf{u}}_n - (\frac{1}{r} + \partial_r)\mathbf{t}_n = \mathbf{0}, \quad \forall r \in [R_i, R_e],
\end{aligned} \tag{4.13}$$

where $\mathbf{t}_n = (\mathbf{A}_{rr}\partial_r + \mathrm{i}n\frac{1}{r}\mathbf{A}_{r\theta} + \mathrm{i}k_z\mathbf{A}_{rz} + \frac{1}{r}\mathbf{A}_{r0})\hat{\mathbf{u}}_n$. The three-by-three matrices $\mathbf{A}_\rho$, $\mathbf{A}_{r0}$, $\mathbf{A}_{rr}$, $\mathbf{A}_{r\theta}$, $\mathbf{A}_{rz}$, $\mathbf{A}_{\theta 1}$, $\mathbf{A}_{\theta\theta}$, $\mathbf{A}_{\theta z}$, $\mathbf{A}_{z1}$, $\mathbf{A}_{11}$ and $\mathbf{A}_{zz}$ depend only on the physical properties and are defined by:

$$\begin{aligned}
&\mathbf{A}_{r0} = \mathbf{L}_r^T\mathbf{c}\mathbf{L}_0, \quad \mathbf{A}_{rr} = \mathbf{L}_r^T\mathbf{c}\mathbf{L}_r, \quad \mathbf{A}_{r\theta} = \mathbf{L}_r^T\mathbf{c}\mathbf{L}_\theta, \quad \mathbf{A}_\rho = \rho\mathbf{I}_d, \\
&\mathbf{A}_{rz} = \mathbf{L}_r^T\mathbf{c}\mathbf{L}_z, \quad \mathbf{A}_{\theta 1} = \mathbf{L}_\theta^T\mathbf{c}\mathbf{L}_0, \quad \mathbf{A}_{\theta\theta} = \mathbf{L}_\theta^T\mathbf{c}\mathbf{L}_\theta, \quad \mathbf{A}_{\theta z} = \mathbf{L}_\theta^T\mathbf{c}\mathbf{L}_z, \\
&\mathbf{A}_{z1} = \mathbf{L}_z^T\mathbf{c}\mathbf{L}_0, \quad \mathbf{A}_{11} = \mathbf{L}_0^T\mathbf{c}\mathbf{L}_0, \quad \mathbf{A}_{zz} = \mathbf{L}_z^T\mathbf{c}\mathbf{L}_z,
\end{aligned} \tag{4.14}$$

where $\mathbf{I}_d$ is the three-by-three identity matrix. The explicit forms of these sub-matrices can be found in Appendix A (Box. 4.1).

4.3.2 Weak formulation

The weak formulation of the problem defined from Eq. (4.13) may be derived using standard procedure (Bathe, 1996). Let $\mathcal{C}^{ad}$ be the admissible function space constituted by all sufficient smooth complex-valued functions $r \in]R_i, R_e[\rightarrow \delta\mathbf{u}_n(r) \in \mathbb{C} \times \mathbb{C} \times \mathbb{C}$, where $\mathbb{C}$ denotes the set of complex numbers. The conjugate transpose of $\delta\mathbf{u}_n$ is denoted $\delta\mathbf{u}_n^*$. By multiplying the Eq. (4.13) with the test function $\delta\mathbf{u}_n^* \in C^{ad}$ and integrating by parts, we obtain:

$$\begin{aligned}
&\int_{R_i}^{R_e} \delta\mathbf{u}_n^* \Big[-\omega^2 \mathbf{A}_\rho + (k_z)^2 \mathbf{A}_{zz} + \frac{1}{r^2}\Big(\mathbf{A}_{11} + n^2\mathbf{A}_{\theta\theta} - \mathrm{i}n\mathbf{A}_{r\theta} - \mathbf{A}_{r0} + \mathrm{i}n(\mathbf{A}_{\theta 1}^T - \mathbf{A}_{\theta 1})\Big) \\
&+ k_z \frac{1}{r}\Big(\mathrm{i}\mathbf{A}_{z1}^T - \mathrm{i}\mathbf{A}_{z1} + n(\mathbf{A}_{\theta z} + \mathbf{A}_{\theta z}^T)\Big) + \frac{1}{r}(\mathbf{A}_{r0}^T\partial_r - \mathrm{i}n\mathbf{A}_{r\theta}^T\partial_r) - \mathrm{i}k_z\mathbf{A}_{rz}^T\partial_r \\
&- \frac{1}{r}(\mathbf{A}_{rr}\partial_r + \mathrm{i}k_z\mathbf{A}_{rz})\Big]\hat{\mathbf{u}}_n \,\mathrm{d}r + \int_{R_i}^{R_e} \partial_r\delta\mathbf{u}_n^*\mathbf{t}_n \,\mathrm{d}r - \big[\delta\mathbf{u}_n^*\mathbf{t}_n\big]_{R_i}^{R_e} = 0\,,
\end{aligned} \tag{4.15}$$

The last term in Eq. (4.15) may vanish by using the free-surfaces boundary conditions defined in Eq. (4.9). Thus, the weak formulation of the problem is: Find $\hat{\mathbf{u}}_n(r) \in \mathcal{C}^{ad}$ such that:

$$\begin{aligned}
&\int_{R_i}^{R_e} -\delta\mathbf{u}_n^*\omega^2\mathbf{A}_\rho\hat{\mathbf{u}}_n \,\mathrm{d}r + \int_{R_i}^{R_e} \delta\mathbf{u}_n^*\Big[(k_z)^2\mathbf{A}_{zz} + \frac{1}{r^2}\Big(\mathbf{A}_{11} + n^2\mathbf{A}_{\theta\theta} - \mathrm{i}n\mathbf{A}_{r\theta} - \mathbf{A}_{r0} + \mathrm{i}n(\mathbf{A}_{\theta 1}^T - \mathbf{A}_{\theta 1})\Big) \\
&+ k_z\frac{1}{r}\Big(\mathrm{i}\mathbf{A}_{z1}^T - \mathrm{i}\mathbf{A}_{z1} - \mathrm{i}\mathbf{A}_{rz} + n(\mathbf{A}_{\theta z} + \mathbf{A}_{\theta z}^T)\Big)\Big]\hat{\mathbf{u}}_n \,\mathrm{d}r + \int_{R_i}^{R_i} \partial_r\delta\mathbf{u}_n^*\left[\frac{\mathrm{i}n}{r}\mathbf{A}_{r\theta} + \mathrm{i}k_z\mathbf{A}_{rz}\right]\hat{\mathbf{u}}_n \,\mathrm{d}r \\
&- \int_{R_i}^{R_e} \delta\mathbf{u}_n^*\left[\frac{\mathrm{i}n}{r}\mathbf{A}_{r\theta} + \mathrm{i}(k_z)\mathbf{A}_{rz}\right]^T \partial_r\hat{\mathbf{u}}_n \,\mathrm{d}r + \int_{R_i}^{R_e} \frac{1}{r}\left[\partial_r\delta\mathbf{u}_n^*\mathbf{A}_{r0}\hat{\mathbf{u}}_n + \delta\mathbf{u}_n^*\mathbf{A}_{r0}^T\partial_r\delta\mathbf{u}_n^*\right]\mathrm{d}r \\
&+ \int_{R_i}^{R_e} \partial_r\delta\mathbf{u}_n^*\mathbf{A}_{rr}\partial_r\hat{\mathbf{u}}_n \,\mathrm{d}r - \int_{R_i}^{R_e} \delta\mathbf{u}_n^*\frac{1}{r}\mathbf{A}_{rr}\partial_r\hat{\mathbf{u}}_n \,\mathrm{d}r = 0,
\end{aligned} \tag{4.16}$$

for all $\delta\mathbf{u}_n^* \in C^{ad}$.

4.3.3 Finite element implementation

Due to constant cross-section and homogeneous material properties along $\mathbf{e}_z$-direction, the displacement field can be interpolated in the radial direction only. Thus, using the finite element method (FEM), we discretized the domain $[R_i, R_e]$ into a mesh which contains n^{el} mono-dimensional elements with 3 degrees of freedom (DOF) per node, and n_{nd} nodes per element $\Omega_e : [R_i, R_e] = \bigcup_e (e = 1, ..., n^{el})$. Note that the 3 DOF per node are associated to the displacements components u_r, u_θ, and u_z. Using the Galerkin method, the two functions $\mathbf{u}_n$ and $\delta\mathbf{u}_n$ in each element e are approximated using the same interpolation function:

$$\hat{\mathbf{u}}_n(r) = \mathbf{N}_e\mathbf{U}_e, \quad \delta\hat{\mathbf{u}}_n(r) = \mathbf{N}_e\delta\mathbf{U}_e, \quad \forall r \in \Omega_e, \tag{4.17}$$

where $\mathbf{N}_e$ is a $3 \times 3n_{nd}$ matrix containing the element quadratic interpolation functions N_j, for $j = 1, ..., n_{nd}$. $\mathbf{U}_e$ and $\delta\mathbf{U}_e$ are respectively the $3n_{nd} \times 1$ column vectors of nodal solutions of $\hat{\mathbf{u}}_n$ and $\delta\hat{\mathbf{u}}_n$ in Ω_e.

$$\mathbf{N}_e = \begin{bmatrix} N_1 & & N_2 & & \ddots & & N_{n_{nd}} & \\ & N_1 & & N_2 & & \ddots & & N_{n_{nd}} \\ & & N_1 & & N_2 & & \ddots & \end{bmatrix}, \tag{4.18}$$

and:

$$\mathbf{U}_e = \begin{bmatrix} u_r^{[1]} & u_\theta^{[1]} & u_z^{[1]} & u_r^{[2]} & u_\theta^{[2]} & u_z^{[2]} & \cdots & \cdots & \cdots & u_r^{[n_{nd}]} & u_\theta^{[n_{nd}]} & u_z^{[n_{nd}]} \end{bmatrix}^T. \tag{4.19}$$

Substituting Eq. (4.17) into Eq. (4.16) and assembling the elementary matrices, we obtain the following system of linear equations:

$$\mathbf{M}\mathbf{U} = \mathbf{0}, \tag{4.20}$$

where $\mathbf{U}$ is the global nodal displacement vector and $\mathbf{M}$ the global "stiffness matrix" of the solid:

$$\mathbf{M} = \left[-\omega^2\mathbf{B}_1 + \mathbf{B}_2 + \mathrm{i}k_z\mathbf{B}_3 + k_z^2\mathbf{B}_4 + \mathrm{i}n\mathbf{B}_5 + n^2\mathbf{B}_6 + nk_z\mathbf{B}_7\right]_N, \tag{4.21}$$

and:

$$\begin{aligned}
\mathbf{B}_1 &= \bigcup_e \int_{\Omega_e} \mathbf{N}_e^T \mathbf{A}_\rho \mathbf{N}_e \,\mathrm{d}r, \quad \mathbf{B}_3 = \bigcup_e \int_{\Omega_e} \left[\frac{1}{r}\mathbf{N}_e^T\left(\mathbf{A}_{z1}^T - \mathbf{A}_{z1} - \mathbf{A}_{rz}\right)\mathbf{N}_e - 2\left[\mathbf{N}_e'^T \mathbf{A}_{rz}\mathbf{N}_e\right]_a\right] \mathrm{d}r, \\
\mathbf{B}_2 &= \bigcup_e \int_{\Omega_e} \left[\frac{1}{r^2}\mathbf{N}_e^T\left(\mathbf{A}_{11} - \mathbf{A}_{r0}\right)\mathbf{N}_e + \frac{2}{r}\left[\mathbf{N}_e'^T \mathbf{A}_{r0}\mathbf{N}_e\right]_s + \left(\mathbf{N}_e'^T - \frac{1}{r}\mathbf{N}_e^T\right)\mathbf{A}_{rr}\mathbf{N}_e'\right] \mathrm{d}r, \\
\mathbf{B}_4 &= \bigcup_e \int_{\Omega_e} \mathbf{N}_e^T \mathbf{A}_{zz} \mathbf{N}_e \,\mathrm{d}r, \quad \mathbf{B}_5 = \bigcup_e \int_{\Omega_e} \left[\frac{1}{r^2}\mathbf{N}_e^T\left(\mathbf{A}_{\theta 1}^T - \mathbf{A}_{\theta 1} - \mathbf{A}_{r\theta}\right)\mathbf{N}_e + \frac{2}{r}\left[\mathbf{N}_e'^T \mathbf{A}_{r\theta}\mathbf{N}_e\right]_a\right] \mathrm{d}r, \\
\mathbf{B}_6 &= \bigcup_e \int_{\Omega_e} \frac{1}{r^2}\mathbf{N}_e^T \mathbf{A}_{\theta\theta}\mathbf{N}_e \mathrm{d}r, \quad \mathbf{B}_7 = \bigcup_e \int_{\Omega_e} \frac{1}{r}\mathbf{N}_e^T\left(\mathbf{A}_{\theta z} + \mathbf{A}_{\theta z}^T\right)\mathbf{N}_e \,\mathrm{d}r
\end{aligned} \tag{4.22}$$

where the notation $[\star]_s$ and $[\star]_a$ denote the symmetric and antisymmetric parts of $[\star]$, respectively. The notation $\star'$ denotes the derivative with respect to r. The subscript N in Eq. (4.21) denotes the dimension of the matrices in Eq. (4.20) which corresponds to the DOF (degree of freedom) of the finite element mesh Ω_e. In this study, Gauss quadrature rule has been used for computing the integrations over the elements.

4.3.4 Extraction of dispersive solutions

4.3.4.1 Solution strategy

For an assigned circumferential wavenumber, Eq. (4.20) has two unknown parameters, the angular frequency ω and the axial wave number k_z. Therefore, this problem may be solved by first fixing the angular frequency ω, and solving for unknown axial wave number k_z. Performing same manipulations on the nonlinear problem, Eq. (4.20) can be rewritten as the following linearized eigenvalue problem:

$$\left[\mathbf{Y}(n,\omega) - k_z\mathbf{Z}(n,\omega)\right]\hat{\mathbf{W}}_n = \mathbf{0}, \tag{4.23}$$

where $\mathbf{Y}(n,\omega)$ and $\mathbf{Z}(n,\omega)$ are complex matrices and $\hat{\mathbf{W}}_n$ is the eigenvector corresponding to the eigenvalue k_z:

$$\mathbf{Y}(n,\omega) = \begin{bmatrix} \mathbf{0} & -\omega^2\mathbf{B}_1 + \mathbf{B}_2 + \mathrm{i}n\mathbf{B}_5 + n^2\mathbf{B}_6 \\ -\omega^2\mathbf{B}_1 + \mathbf{B}_2 + \mathrm{i}n\mathbf{B}_5 + n^2\mathbf{B}_6 & \mathrm{i}\mathbf{B}_3 + n\mathbf{B}_7 \end{bmatrix}_{2N}, \quad \hat{\mathbf{W}}_n = \begin{bmatrix} \hat{\mathbf{u}}_n \\ k_z\hat{\mathbf{u}}_n \end{bmatrix}_{2N}. \tag{4.24}$$

$$\mathbf{Z}(n,\omega) = \begin{bmatrix} -\omega^2\mathbf{B}_1 + \mathbf{B}_2 + \mathrm{i}n\mathbf{B}_5 + n^2\mathbf{B}_6 & \mathbf{0} \\ \mathbf{0} & -\mathbf{B}_4 \end{bmatrix}_{2N}. \tag{4.25}$$

From Eq. (4.23), at a given real angular frequency ω, $2N$ complex eigenvalues $k_z^{(m)}$ ($m = 1, ..., 2N$) and $\hat{\mathbf{W}}_n^{(m)}$ eigenvectors are obtained. The quantities $k_z^{(m)} = \mathrm{Re}[k_z^{(m)}] + \mathrm{i}\ \mathrm{Im}[k_z^{(m)}]$ represent the axial wavenumbers for all modes existing at a given angular frequency with the circumferential wavenumber n. The real part of the axial wavenumber $k_z^{(m)}$ expresses the wave spatial frequency in $\mathbf{e}_z$-direction, while its imaginary part describes the wave amplitude decay.

The solutions of the problem defined by Eq. (4.23) can be viewed in different projections. Each of these latter can reveal different information about the dispersive characteristics of solutions. In general, dispersion curves can be presented in five projections: real wave number, phase velocity, energy velocity (or group velocity when possible) and attenuation. These fours different projections are described in the next sections.

4.3.4.2 Phase velocity

The phase velocity of a guided wave is the rate at which the phase of a wave propagates in space domain. The phase velocity dispersion curves view will be the projection most frequently shown in this study. This view is more convenient to use for ultrasonic testing such AT techniques. The wave phase velocity $C_{ph}(\omega)$ which is parametrized by its circumferential wavenumber n and the mode number m (for the m-th mode), may be computed as a function of angular frequency ω by using:

$$C_{ph}(\omega; n, m) = \frac{\omega}{\mathrm{Re}[k_z^{(n,m)}]}\ (\mathrm{m\ s^{-1}}). \tag{4.26}$$

4.3.4.3 Real wave number

In this projection, the dispersion curves displays wavenumber, more precisely, the real part of axial wavenumber $k_z^{(n,m)}$, as a function of frequency. The real wavenumber $\mathrm{Re}[k_z^{(n,m)}]$ is related to the wavelength of the guide wave λ by:

$$\lambda = \frac{2\pi}{\mathrm{Re}[k_z^{(n,m)}]}\ (\mathrm{m}). \tag{4.27}$$

Thus, relationship between the spatially and temporally variation of guided modes characteristics along the propagation direction (i.e., $\mathbf{e}_z$-direction) can be highlighted. Dispersion curves appear more linear in this projection (e.g. see Fig. 4.8(b)).

4.3.4.4 Attenuation

The attenuation dispersion curves allows the decay of guides waves to be investigated. In most of time, guided waves are attenuated by material absorption or guides waves leakage. Absorption occurs mainly in viscoelastic material, while leakage phenomenon appears in embedded structures such as fluid loading. Attenuation is known as the imaginary part of the axial wavenumber:

$$att(\omega; n, m) = \text{Im}[k_z^{(m)}] \text{ (Np m}^{-1}\text{)}. \tag{4.28}$$

An attenuation of η Nepers per meter means that a wave with a unit amplitude is decayed to an amplitude $\exp(-\eta)$ after traveling one meter. It is more useful and practical to describe attenuation in other units as Decibel per meter. Attenuation can be expressed in familiar units such as decibels per meter ($1 \text{ Np m}^{-1} \equiv 20/\ln(10) \text{ dB m}^{-1} = 8.68 \text{ dB m}^{-1}$).

4.3.4.5 Energy velocity

By definition, the wave energy velocity vector is equal to the power flow density vector divide by the total energy. This last, is composed by kinetic energy and strain energy (which can be seen as a potential energy) per unit volume. The wave energy velocity can be seen as the velocity at which a guided wave travels along the waveguide. The time-averaged m-th strain and kinetic energy densities at a point $M(r, \theta, z)$ may be expressed, respectively, as:

$$\left\langle E_s^{(m)} \right\rangle_T = \frac{1}{2} \left\langle \text{Re}[\boldsymbol{\sigma}^{(m)}]^T \text{Re}[\mathbf{e}^{(m)}]^* \right\rangle_T \text{ (J m}^{-3}\text{)}, \quad \left\langle E_k^{(m)} \right\rangle_T = \frac{1}{2} \rho \left\langle \text{Re}[\dot{\mathbf{u}}^{(m)}]^T \text{Re}[\dot{\mathbf{u}}^{(m)}]^* \right\rangle_T \text{ (J m}^{-3}\text{)}, \tag{4.29}$$

where $\langle \star \rangle_T = \frac{1}{T} \int_0^T (\star) dt$ is the time-averaging operator over a unit period of time $T = 2\pi/\omega$. Let us introduce the local complex Poynting vector (power flow density vector) at a point $M(r, \theta, z)$ for the m-th mode $\mathbf{P}^{(m)} = [P_r^{(m)}, P_\theta^{(m)}, P_z^{(m)}]^T$ as:

$$\mathbf{P}^{(m)} = -\frac{1}{2} \text{Re} \left([\boldsymbol{\sigma}^{(m)}][\hat{\dot{\mathbf{u}}}^{(m)}]^* \right) \text{ (J s}^{-1}\text{m}^{-2}\text{)}, \tag{4.30}$$

Due to the guided wave propagating in $\mathbf{e_z}$ direction, and the absence of leakage or absorption assumed, the power flows entirely in the $\mathbf{e_z}$ direction and the components of the Poynting vector in the circumferential and radial directions are zero $P_\theta^{(m)} = 0$ and $P_r^{(m)} = 0$.

Using Hooke law and the time derivative defined in Eq. (4.12), the power flow density vector and both kinetic and potential energy in each element e can be rewritten as:

$$\mathbf{P}^{(m)} = -\frac{1}{2} \omega \text{Re} \left([\hat{\mathbf{s}}^{(m)}][\hat{\mathbf{u}}^{(m)}]^* \right) \text{ (J s}^{-1}\text{m}^{-2}\text{)}, \tag{4.31}$$

$$\left\langle E_s^{(m)} \right\rangle_T = \frac{1}{4} \text{Re} \left([\hat{\mathbf{s}}^{(m)}]^T [\hat{\mathbf{e}}^{(m)}]^* \right) \text{ (J m}^{-3}\text{)}, \tag{4.32}$$

$$\left\langle E_k^{(m)} \right\rangle_T = \frac{1}{4} \rho \omega^2 \text{Re} \left([\hat{\mathbf{u}}^{(m)}]^T [\hat{\mathbf{u}}^{(m)}]^* \right) \text{ (J m}^{-3}\text{)}, \tag{4.33}$$

and:

$$\hat{\mathbf{u}}^{(m)} = \mathbf{N}_e \mathbf{U}_e, \quad \hat{\mathbf{e}}^{(m)} = \hat{\mathbf{L}}_\epsilon \mathbf{N}_e \mathbf{U}_e = \left[\mathbf{L}_r \partial_r + \mathrm{i}n\mathbf{L}_\theta \frac{1}{r} + \mathrm{i}k_z \mathbf{L}_z + \mathbf{L}_0 \frac{1}{r} \right] \mathbf{N}_e \mathbf{U}_e, \quad \hat{\mathbf{s}}^{(m)} = \mathbf{c}\hat{\mathbf{e}}^{(m)}. \tag{4.34}$$

The wave energy velocity vector is then calculated as:

$$V_e(\omega; n, m) = \frac{\bigcup_e \int_{\Omega_e} \left[\mathbf{P}^{(m)}.\mathbf{e}_z \right] r \, \mathrm{d}r}{\bigcup_e \int_{\Omega_e} \left[\langle E_k^{(m)} \rangle_T + \langle E_p^{(m)} \rangle_T \right] r \, \mathrm{d}r} \, (\mathrm{m\,s^{-1}}), \tag{4.35}$$

Using Gauss quadrature rule the integrations of total energy and Poynting vector has been computed and evaluated over the waveguide cross section.

4.3.5 Nature of the guided waves in cylinder

In bone cylinder, two types of guided waves propagation are distinguished: the circumferential guided waves (CGW) and axial guided waves (AGW) as illustrated in Fig. 4.2.

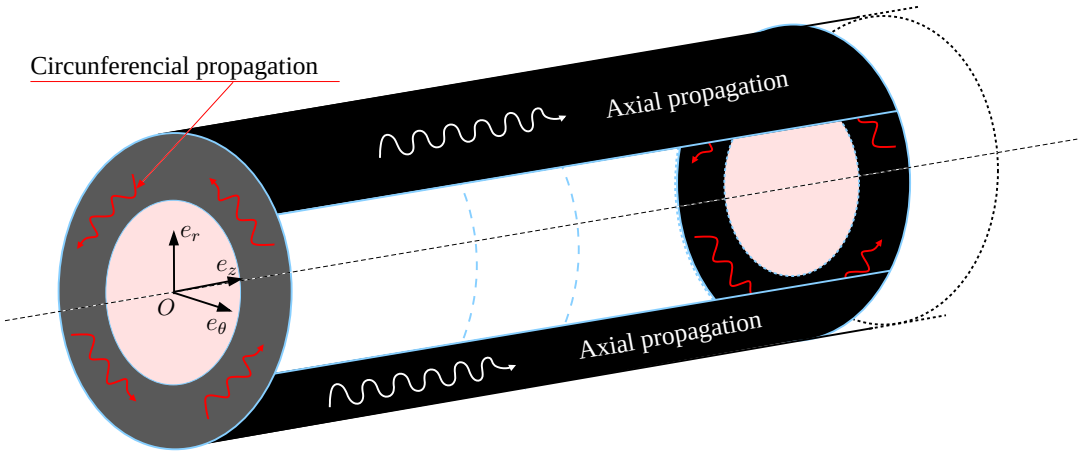

Figure 4.2: Illustration of circumferential and axial guided waves propagations.

The circumferential waves are traveling in the plane$(\mathbf{e}_r, \mathbf{e}_\theta)$ perpendicular to the cylinder axis direction, while the axial waves are those traveling along the axis direction. Due to its nature, circumferential propagation can be used to study short bones (e.g. calcaneus, femoral neck). This propagation being assumed to be invariant along the axis of the cylinder, thus, the component of displacement u_z , and axial wavenumber k_z are zero, it is a plane problem. Whereas, the axial propagation can be exploited to the characterization of long bones such as the tibia, femur, radius or humerus. In this study, we focus on axial waves. A description of guides waves propagation in the axial direction is presented in the next subsections.

4.3.5.1 Convention

The propagation characteristics of guides waves in a cortical bone cylinder are analogous to those in cortical bone plate, except that some supplementary complexities arise. Guides waves in a cylindrical

bone are different from those in bone plates in some aspects. Strictly speaking, unlike the symmetric (S) or antisymmetric (A) Lamb modes in a plate, three different families of guides waves are present in cylindrical waveguides: longitudinal (L), torsional (T) and flexural (F) modes, depending mainly on their displacement field. Cylindrical guided waves are usually labeled with a double index (n, m), where the former being the circumferential order (i.e., circumferential wavenumber) which is associated with the geometric properties of the cylinder structure. The second index is a counter variable ($m = 1, 2, ...$) used in order to distinguish the modes of one family, at a given order n. This classification is that adopted in many studies following the Gazis (1959) work. Note that other relevant classification exists in the literature for isotropic medium but is not valid on anisotropic structures (Nishino et al., 2001).

4.3.5.2 Identification approach of modes in bone cylinder

The displacement fields of every mode have a characteristic radial distribution, known as the mode shapes. In order to better understand the behavior of Lamb modes, it is quite indispensable to understand the modes shapes by studying the displacement field (called also *wavestructures*). Circumferential order $n = 0$ indicates that the cylinder is axially symmetric (axisymmetric). Thus, Longitudinal and Torsional guided waves, being axially symmetric, can be calculated for $n = 0$, and are labeled as $L(0, m)$ and $T(0, m)$, respectively. The flexural guided waves $F(n, m)$ are characterized by a non-axially symmetric displacement field, and can be obtained for non-zero circumferential orders $n \geq 1$.

The different mode families can be best separated by considering the components of their displacement vector (see. Tab. 4.1). Note that due to numerical computation, exact equality values as given in Tab. 4.1 are not obtained.

Table 4.1: Relationship between displacement vector components and mode types.

Longitudinal mode ($L(0, m)$)	Torsional mode ($T(0, m)$)	Flexural mode ($F(n, m)$)
$u_r(r) \neq 0$	$u_r(r) = 0$	$u_r(r) \neq 0$
$u_\theta(r) = 0$	$u_\theta(r) \neq 0$	$u_\theta(r) \neq 0$
$u_z(r) \neq 0$	$u_z(r) = 0$	$u_z(r) \neq 0$

In the homogeneous deterministic model, in which the cortical bone cylinder is assumed to be transversely isotropic elastic, displacement field can be axially symmetric and Lamb modes can be distinguished by investigate the displacement vector. However, in the stochastic model, the cylinder is anisotropic and heterogeneous with material properties that vary along the radial $\mathbf{e_r}$-axis. Hence, the bone cylinder is in this case quasi-axially symmetric (or pseudo-axially symmetric).

4.4 Three-dimensional stochastic model

4.4.1 Random elasticity tensor

In this section, we describe briefly the probabilistic model used to generate the random medias. As recalled in previous sections, cortical bone can be modeled by a cylinder having random properties in the radial direction. The uncertainties are introduced *via* the heterogeneity which is randomly varied in the bone layer along the $\mathbf{e}_r$ direction A probabilistic model which has been developed in Soize (2006) is deemed to be more suitable for such problem (Nguyen, 2013; Desceliers et al., 2009, 2012). Note that this model is mainly constructed to generate random elastic tensors by using two ingredients: the maximum entropy principle (Jaynes, 1957a,b) and the random matrix theory (Mehta, 2004) in three dimension (21 components). In this paper, we only sketch out the main features of the model in the context of cortical bone study, a more detailed description may be found in Soize (2006).

Henceforth, the writing in upper and lowercase will be used to denote random and mean quantities, respectively. As result, we denote by $\mathbf{C}(r)$ the random elastic matrix at a material point $M(r,\theta,z)$ and by $\mathbf{c}(r)$ its mean value, respectively. The following relationship is satisfied $\mathbb{E}\{\mathbf{C}(r)\} = \mathbf{c}(r)$, where $\mathbb{E}\{\star\}$ designates the mathematical expectation. Moreover, the random and mean elastic tensors both belong in set of all the (6×6) real symmetric positive-definite matrices $\mathbf{M}_6^+(\mathbb{R})$. Since $\mathbf{c}(r)$ is definite positive, matrix $\mathbf{c}(r)$ can be written using the Cholesky decomposition as

$$\mathbf{c}(r) = \begin{bmatrix} l_{11} & 0 & 0 & 0 & 0 & 0 \\ l_{12} & l_{22} & 0 & 0 & 0 & 0 \\ l_{13} & l_{23} & l_{33} & 0 & 0 & 0 \\ l_{14} & l_{24} & l_{34} & l_{44} & 0 & 0 \\ l_{15} & l_{25} & l_{35} & l_{45} & l_{55} & 0 \\ l_{16} & l_{26} & l_{36} & l_{46} & l_{56} & l_{66} \end{bmatrix} \begin{bmatrix} l_{11} & l_{12} & l_{13} & l_{14} & l_{15} & l_{16} \\ 0 & l_{22} & l_{23} & l_{24} & l_{25} & l_{26} \\ 0 & 0 & l_{33} & l_{34} & l_{35} & l_{36} \\ 0 & 0 & 0 & l_{44} & l_{45} & l_{46} \\ 0 & 0 & 0 & 0 & l_{55} & l_{56} \\ 0 & 0 & 0 & 0 & 0 & l_{66} \end{bmatrix}, \tag{4.36}$$

in which the upper triangular real matrix contains 21 deterministic components and will be denoted by $\boldsymbol{\mathcal{L}}(r)$, the lower triangular one is its transpose.

The random matrix $\mathbf{C}(r)$ is parameterized by its mean value $\mathbf{c}(r)$, the dispersion level δ and three spacial correlation length λ_r, λ_θ and λ_z in the $\mathbf{e}_r$, $\mathbf{e}_\theta$ and $\mathbf{e}_z$-direction, respectively. However, material properties in the bone cylinder being assumed to be homogeneous is the $\mathbf{e}_z$-axis and invariant in the circumferential $\mathbf{e}_\theta$-directions, $\mathbf{C}(r)$ has been generated in three dimensions (21 components) with a high value of the spatial correlation lengths in the $\mathbf{e}_z$ and $\mathbf{e}_\theta$-directions. Strictly speaking, the random matrix $\mathbf{C}(r)$ is parameterized by its mean value $\mathbf{c}(r)$, the dispersion level δ and the correlation length λ_r in the $\mathbf{e}_r$-direction, which is denoted by $\mathbf{C}(r;\mathbf{c},\delta,\lambda_r)$ and can be decomposed in following form:

$$\mathbf{C}(r;\mathbf{c},\delta,\lambda_r) = \boldsymbol{\mathcal{L}}^T(r)\,\mathbf{G}(r;\mathbf{c},\delta,\lambda_r)\,\boldsymbol{\mathcal{L}}(r), \tag{4.37}$$

where $\mathbf{G}(r;\mathbf{c},\delta,\lambda_r)$, is a stochastic field called the stochastic germ matrix, which is a homogeneous and normalized non-Gaussian positive-definite matrix-valued second-order random field with values in

$\mathbb{M}_6^+(\mathbf{R})$. The explicit form of this application defined in Soize (2006) is written as

$$\mathbf{G}(r;\mathbf{c},\delta,\lambda_r) = \mathbf{L}^T(r;\mathbf{c},\delta,\lambda_r)\,\mathbf{L}((r;\mathbf{c},\delta,\lambda_r), \tag{4.38}$$

where $\mathbf{L}(r;\mathbf{c},\delta,\lambda_r)$ is a 6×6 random upper triangular matrix.

$$\mathbf{L}(r;\mathbf{c},\delta,\lambda_r) = \begin{bmatrix} L_{11} & L_{12} & L_{13} & L_{14} & L_{15} & L_{16} \\ 0 & L_{22} & L_{23} & L_{24} & L_{25} & L_{26} \\ 0 & 0 & L_{33} & L_{34} & L_{35} & L_{36} \\ 0 & 0 & 0 & L_{44} & L_{45} & L_{46} \\ 0 & 0 & 0 & 0 & L_{55} & L_{56} \\ 0 & 0 & 0 & 0 & 0 & L_{66} \end{bmatrix}, \tag{4.39}$$

The 21 components of this upper triangular matrix are rigorously defined in the pilot paper (Soize, 2006) using a nonlinear transformation and an autocorrelation function judiciously chosen.

The dispersion parameter δ, controls the dispersion of the random matrix $\mathbf{G}(r;\mathbf{c},\delta,\lambda_r)$ and must satisfy the following inequality

$$0 < \delta < \delta_p, \quad \delta_p = \sqrt{(p+1)(p+5)^{-1}} < 1, \tag{4.40}$$

in which p denotes the size of the $(p\times p)$ square matrix $\mathbf{G}(r;\mathbf{c},\delta,\lambda_r)$. It is proved that the dispersion parameter δ is related to a parameter δ_C which evaluates the dispersion of the random matrix $\mathbf{C}(r)$ by the relation given by:

$$\delta_C(r) = \frac{\delta}{\sqrt{p+1}} \left\{ 1 + \frac{\{\mathrm{Tra}(\mathbf{c}(r))\}^2}{\mathrm{Tra}([\mathbf{c}(r)]^2)} \right\}^{1/2}, \tag{4.41}$$

where Tra is the trace operator. In this three-dimensional study, $p = 6$.

4.4.2 Stochastic response and convergence analysis

In this section, we describe the procedure for obtaining random responses derived from bone random heterogeneity. The Monte Carlo simulation is used as stochastic solver. For a given parameters set $\mathbf{c}$, R_i, R_e, δ and λ_r, the 1D domain $[R_i, R_e]$ is discretized by using quadratic Lagrangian elements. The global $\mathbf{e}_r$-coordinates of the Gauss points in all elements are denoted by r^β for $\beta = 1,...,n_{gp}$, where n_{gp} is the total number of the Gauss points in the mesh. Let n_r be the total number of realizations, we may construct the set of the independent realizations ψ_j, of random matrices field $\left\{\mathbf{C}(r^{(\beta)},\psi_j)\right\}_{\beta=1,...,n_{gp}}$, for $j = 1,...,n_r$, as described in previous section. For each statistical independent realization ψ_j, n_r statistical independent realizations of the random complex axial wavenumber $k_z(\psi_j)$ may be calculated at a given angular frequency ω, following the SAFE procedure presented in subsection 4.3.4.1. Then, the random phase velocity $C_{ph}(\psi_j)$, energy velocity $V_e(\psi_j)$ and attenuation $att(\psi_j)$ can be extracted.

Next, convergence analysis with respect to the number of realizations n_r may be performed by studying the convergence of statistical estimates of the second-order moments of random fields (phase velocity,

energy velocity and displacement). For instance, the second-order moment of random phase velocity of a given Lamb mode at a fixed frequency is defined by:

$$\mathrm{Conv}_{V_e}(n_r) = \sqrt{\frac{1}{n_r}\sum_{j=1}^{n_r}[V_e(\psi_j)]^2}. \tag{4.42}$$

4.5 Results

4.5.1 Material properties and numerical parameters

Bone material properties

In this subsection, the material properties related to the mean model are presented. In this regard, an anisotropic class of bone elasticity tensor is chosen according to realistic behavior. As describe by different authors, cortical bone material properties can be assumed to be transversely isotropic. This behavior has been experimentally validated, and deemed to be a realistic approximation of bone material properties. Modeling bone as homogeneous structure, we can use the data given in Eq. (4.43), which are those obtained by Dong and Guo (2004), who extracts the homogenized bone material properties from a mechanical testing on different human bone samples. In this study, bone is assumed to be a transversely isotropic medium for which the plane $(\mathbf{e}_r, \mathbf{e}_\theta)$ is the plane of isotropy. The correspondence of the traditional material principal axes 1 - 2 - 3 with the reference system axes $\mathbf{e}_r$ - $\mathbf{e}_\theta$ - $\mathbf{e}_z$ is recalled in Fig. 4.3.

$$\rho = 1722\ (\mathrm{kg.m^{-3}}), \quad \mathbf{c} = \begin{bmatrix} 15.1 & 8.4 & 8.7 & 0 & 0 & 0 \\ & 15.1 & 8.7 & 0 & 0 & 0 \\ & & 23.05 & 0 & 0 & 0 \\ & \mathrm{Sym} & & 4.7 & 0 & 0 \\ & & & & 4.7 & 0 \\ & & & & & 3.3 \end{bmatrix} \ (\mathrm{GPa}). \tag{4.43}$$

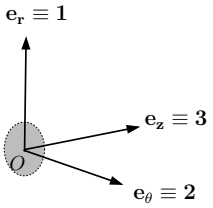

Figure 4.3: Correspondence between material principal axes and reference system axes.

Parameters for the uncertain elasticity model

The mean elasticity tensor $\mathbf{c}(r)$ used to generate the random one $\mathbf{C}(r;\mathbf{c},\delta,\lambda_r)$ is that given in Eq. (4.43). As described in subsection 4.4.1, the dispersion δ and one correlation length λ_r need to be introduced to control the statistical fluctuations of the elasticity field in the $\mathbf{e}_r$-direction . A fixed spacial correlation length $\lambda_r = 100$ μm will be used, which may be seen as a center-to-center distance between osteons in cortical bone (see Cowin (2001), Wang et al. (1999) and Nguyen et al. (2010)). Three different values of dispersion $\delta = 0.1, 0.2$ and 0.3 will be investigated, these three values lead to three different values of the dispersion $\delta_C = 0.1251, 0.2431$ and 0.3647 at material points $M(R_e,\theta,z)$.

4.5.2 Convergence analysis

4.5.2.1 Mesh convergence study

In this section we perform a mesh convergence analysis in order to verify the convergence of results deriving to SAFE Method. As describe in previous sections, at a given angular frequency, by using the SAFE formulation, the solutions of the dispersion eigenvalue problem (see. Eq. (4.23)) can be determined. As results, the complex wavenumbers which are none other than the eigenvalues solutions can be extracted. Since, all solutions in the different projections derived to the axial wavenumber, it more relevant to perform the convergence analysis on this quantity.

Fig. 4.4 presents the complex axial wavenumber solutions corresponding to fours modes detected at frequency $f = 2$ MHz, with zero and one circumferential order. Real and imaginary parts of the axial wavenumber are plotted with respect to the spatial discretization parameter piloted by the number of elements n^{el}. In general, the spatial discretization (mesh) should be sufficiently fine to accurately present nodal solutions at the highest frequency of interest. As shown in these graphs, for $n \geq 25$, the real part as well as imaginary part converge and remain almost constants. Such conditions are in accordance with the usual requirement in finite element analysis (Bathe, 1996). The element size must be lower than $1/10$ of the shortest wavelength in a 4 mm thickness medium.

4.5.2.2 Stochastic convergence analysis

Using the procedure defined in section 4.4, $n_r = 200$ independent realizations of the random variable $\mathbf{C}(r)$ are constructed. Computation is performed with $\delta = 0.1$, $\lambda_r = 100$ μm and the deterministic homogeneous elasticity tensor defined $\mathbf{c}(r)$. In this convergence analysis, we consider a 1 mm-thickness cylindrical layer discretized by 50 quadratic elements. This meshing allows as to satisfy the requirement of at least 5 elements per spatial correlation length are needed. In addition mesh convergence conditions expressed in the previous section is satisfied.

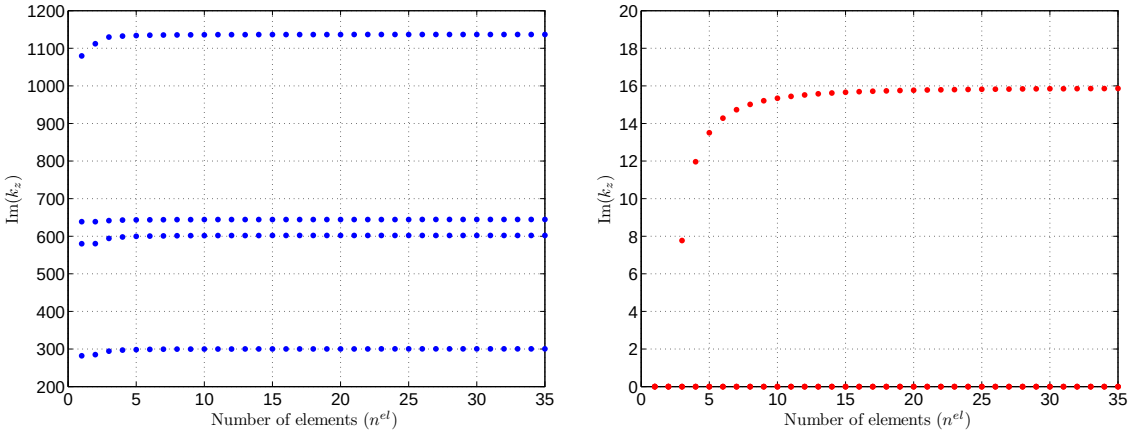

(a) (b)

Figure 4.4: (a) Real part of axial wavenumber. (b) Imaginary part of the axial wavenumber.

(i) Mean estimated elasticity tensor Using a Monte Carlo simulation, the estimation of mean elasticity tensor give the following result:

$$\mathbb{E}\{\mathbf{C}(r=0)\} \simeq \begin{bmatrix} 15.077 & 8.4802 & 8.7181 & 0.0005 & 0.0007 & 0.0035 \\ & 15.079 & 8.7175 & 0.0023 & 0.0018 & 0.0041 \\ & & 23.045 & 0.0003 & 0.0026 & 0.0003 \\ & \text{Sym} & & 4.7000 & 0.0010 & 0.0011 \\ & & & & 4.7000 & 0.0005 \\ & & & & & 3.2974 \end{bmatrix} \text{(GPa)}, \tag{4.44}$$

which has to be compared with the deterministic mean elasticity tensor $\mathbf{c}(r)$. We have a good agreement with the deterministic homogeneous properties given in Eq. (4.43). For illustration, the mean estimated components of random elasticity tensor in the cross section are presented in Fig. 4.5 for "homogeneous" properties.

(ii) Convergence on phase velocity Here, stochastic convergence is performed on output random quantities, especially on phase velocity. Such convergence lead to determine the minimal number of realization n_r necessary to perform statistical study on the random output quantities and make sense from a statistical point of view. We consider a bone cylinder having the homogeneous material properties presented in Eq. (4.43).

Using a Monte Carlo simulation, the phase velocities of the axisymmetric modes $L(0,1)$, $L(0,2)$, $T(0,1)$ and non-axisymmetric modes $F(1,1)$, $F(1,2)$, $F(1,3)$ are calculated for 200 realizations, when $\delta = 0.1$. For longitudinal and torsional modes, the corresponding probability density functions (PDF) of phase velocity are shown in Fig. 4.6(a). The PDFs of flexural modes phase velocity are presented In Fig. 4.6(b). One may verify that the mean values of the random phase velocity are approximately equal to deterministic ones. It can be seen that the firsts non-axisymmetric modes $F(1,1)$, $F(1,2)$ and $F(1,3)$

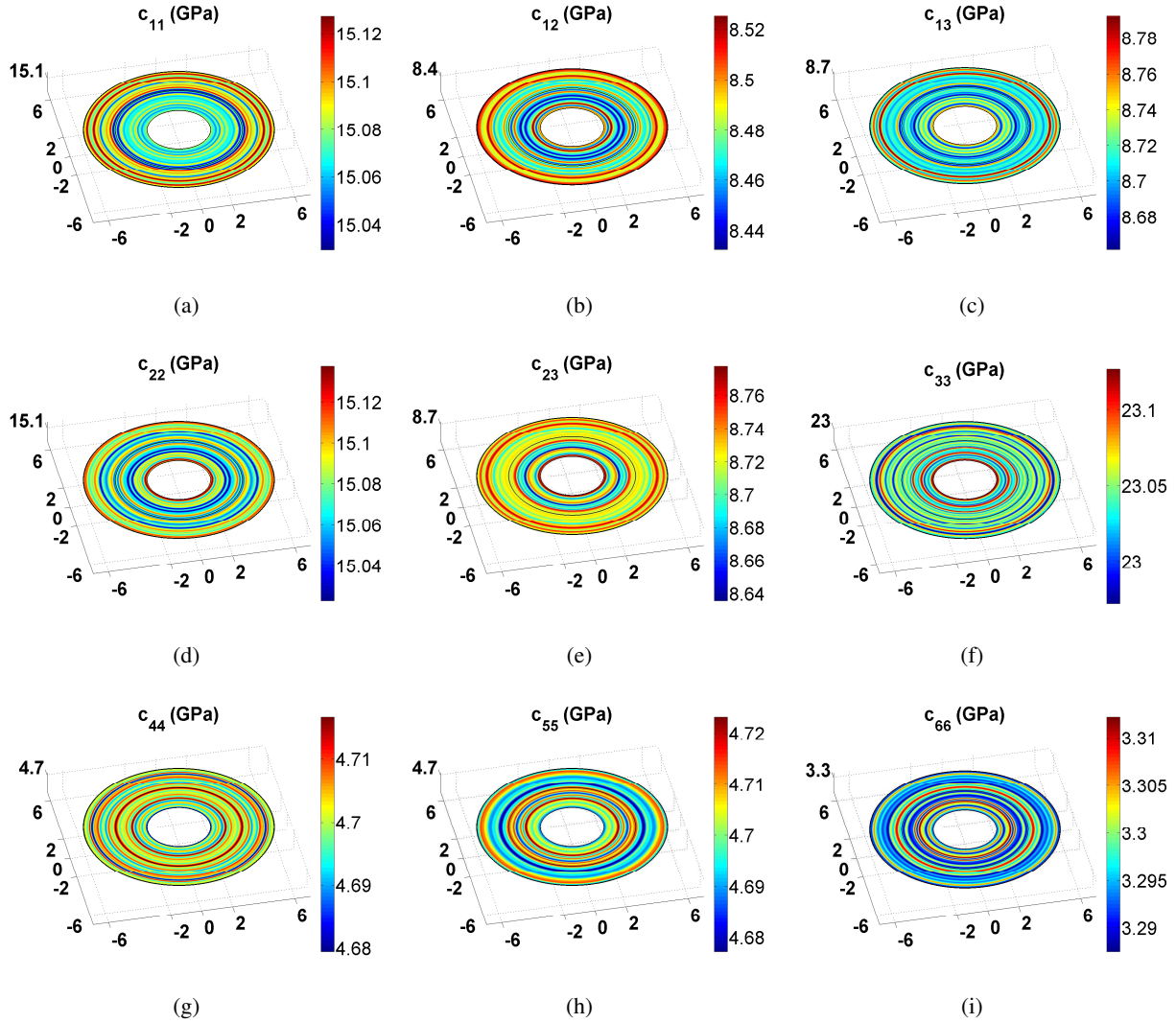

(a) (b) (c)

(d) (e) (f)

(g) (h) (i)

Figure 4.5: Mean components of the random elasticity tensor generated from homogeneous properties.

have similar dispersive behavior than axisymmetric modes $L(0,1)$, $T(0,1)$, $L(0,2)$, respectively. For a statistical sens, $L(0,2)$ and $F(1,3)$ seem to be the more dispersive.

4.5.3 Validation

4.5.3.1 Homogeneous cylinder

In this section the proposed three-dimensional approach is validated by extracting the dispersion curves obtained for homogeneous isotropic and transversely isotropic cylinders, respectively. Results are compared against those calculated in Disperse software. For homogeneous steel cylinder ($\rho_{steel} = 7932$ kg.m^{-3}, $c_T = 3260$ m.s^{-1} and $c_L = 5960$ m.s^{-1}), dispersion curves are plotted in Fig. 4.7(a). Results show a good agreement.

In Fig. 4.7(b), phase velocity dispersion curves are plotted for homogeneous transversely isotropic

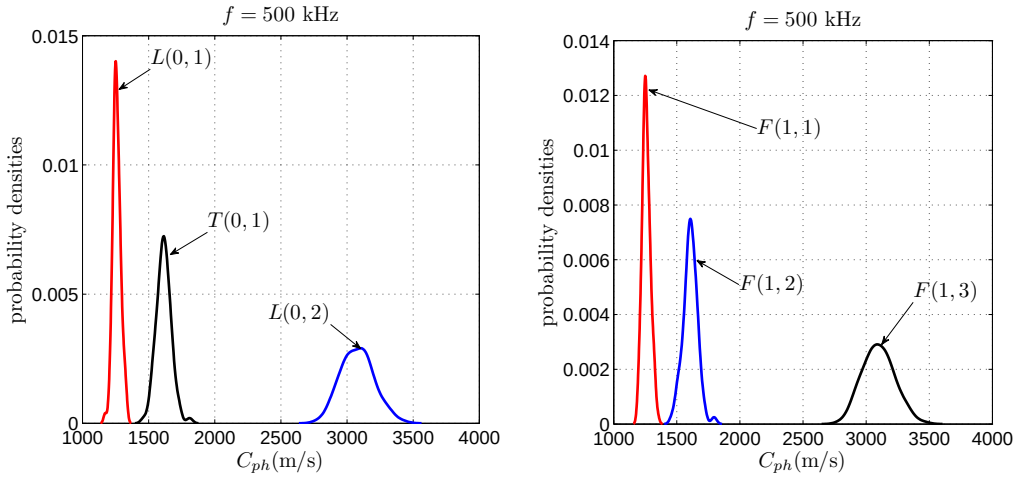

(a) (b)

Figure 4.6: (a) (Color online) (a) Probanility density functions of axisymmetric modes. (b) Probability density functions of non-axisymmetric modes. $n_r = 200$ and $\delta = 0.1$.

layer having material properties given in Table. 4.2. Results show a good agreement between Disperse and SAFE results except on low frequencies, where the agreement is relatively poorer. In addition, with the SAFE procedure, the branches of two modes that not given by Disperse, are detected near high frequency equal (e.g., $f = 2$ MHz).

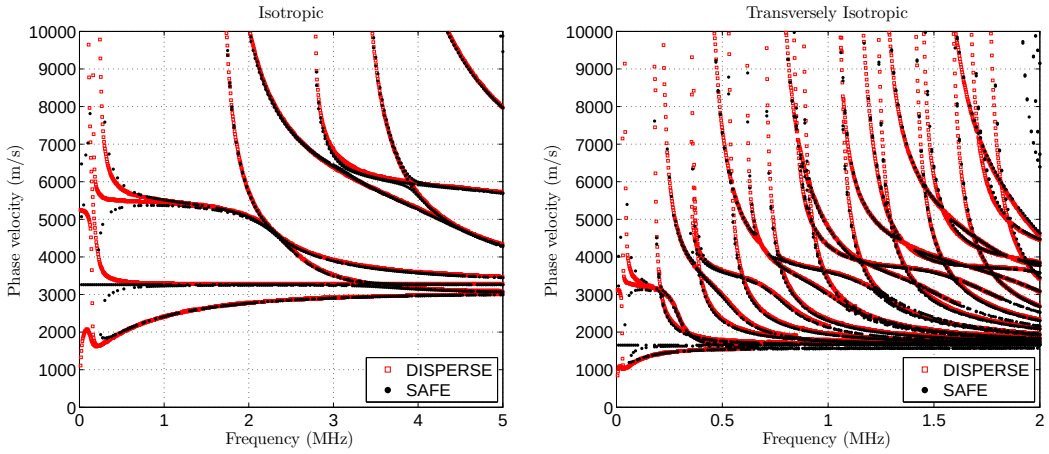

(a) (b)

Figure 4.7: (a) Transversely isotropic bone material properties $h = 4$ mm, $R_i = 12$ mm. (b) Isotropic steel material properties $h = 1$ mm, $R_i = 5$ mm.

4.5.4 Phase velocity and real wavenumber

Among the different projections for expressing the dispersion characteristics, the phase velocity dispersion curves is the most widely used. In this section we present both phase velocity and real wavenumber

Table 4.2: Transversely isotropic layers properties.

Property	ρ (kg.m^{-3})	c_{11} (GPa)	c_{33} (GPa)	c_{13} (GPa)	c_{55} (GPa)	c_{66} (GPa)
Bone	1722	15.1	23.05	8.7	4.7	3.3

dispersion curves for the two first circumferential wavenumbers n. In general, the circumferential order of most interest in ultrasonic study are low order. Indeed, due to the fact that practical measurement systems usually don't have enough resolution around the cross-section to be able to accurately segregate high circumferential orders, only the lower circumferential order modes are mostly used in NDT. In this thesis, we focus only on low circumferential order modes such $n = 0$ related to axisymmetric longitudinal and torsional modes , and $n = 1$ corresponding to the first orders non-axisymmetric flexural modes. The behavior of higher order modes is briefly discussed.

In Fig. 4.8(a) the dispersion phase velocity of the $n = 0$ order axisymmetric modes are presented. The corresponding real wavenumber projection is shown in Fig. 4.8(b). It well known that curves appears more linear on this last projection. Such like linearity justifies the utility of this projection in the context of experimental measurements. The dispersion phase velocity and real wavenumber dispersion curves for $n = 1$ order flexural modes are plotted in Fig. 4.9(a) and Fig. 4.9(b), respectively. It is well known and observed in theses figures that Cylindrical modes that have an odd circumferential wavenumber is like anti-symmetric A_m bone plate modes. Whereas, cylindrical Lamb modes with an even circumferential order resemble to symmetric S_m plate modes.

In addition, we may notice that, the only modes that can exist for all frequencies are the lowest longitudinal, torsional and flexural modes. In general, these lowest modes are the modes required to describe free isotropic cylinder vibration for frequencies below a so called "hoop" frequency (or "ring" frequency: $f = c_L/2\pi R_i$). For higher frequency, the number of higher modes becomes important and can be used in Quantitative Ultrasound bone evaluation.

The first torsional mode $T(0, 1)$ has the advantage of being non-dispersive whatever the frequency. Furthermore, this mode generates only a tangential displacement (i.e., non orthogonal to the circumference) called also circumferential displacement. Therefore, its propagation characteristics should not be influenced by the presence of a fluid (soft tissue or marrow).

4.5.5 Cylindrical to plate model approximation: effect of curvature

In this section, we investigate the influence of the curvature (due to cylindrical geometry) on dispersion curves. Note that such study is performed in some previous works (Lefebvre et al., 2002; Baron, 2011). Here we confirm theses results by validating our approach, and, we provide some detailed explanations. Changing the ratio between inner radius R_i and the wall thickness $h = R_e - R_i$, the three-dimensional model can be approximated by a plate model in certain conditions. Investigating the behavior of cylindrical Lamb wave when changing radius may allows us to reveal when it is acceptable to model bone

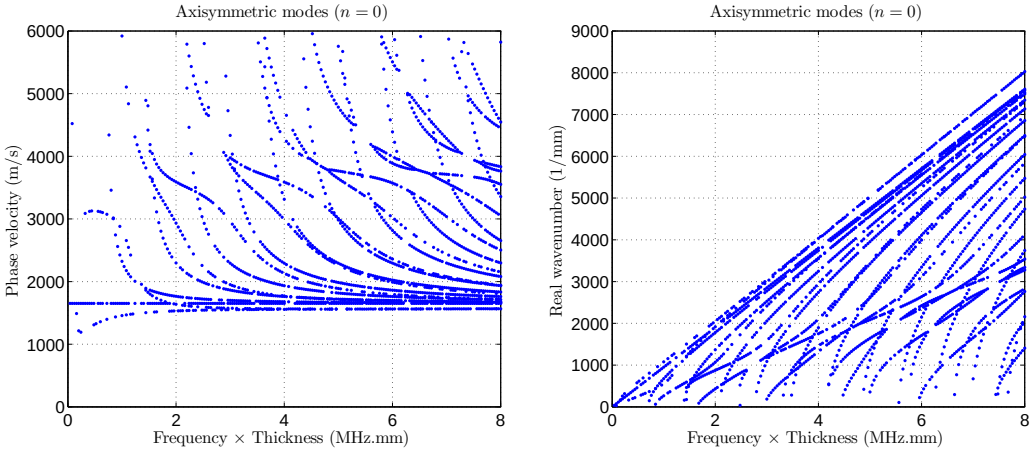

(a) (b)

Figure 4.8: Phase velocity (a) and real wavenumber (b) projections for axisymmetric modes $L(0, m)$ and $T(0, m)$. $h = 4$ mm, $R_i = 12$ mm.

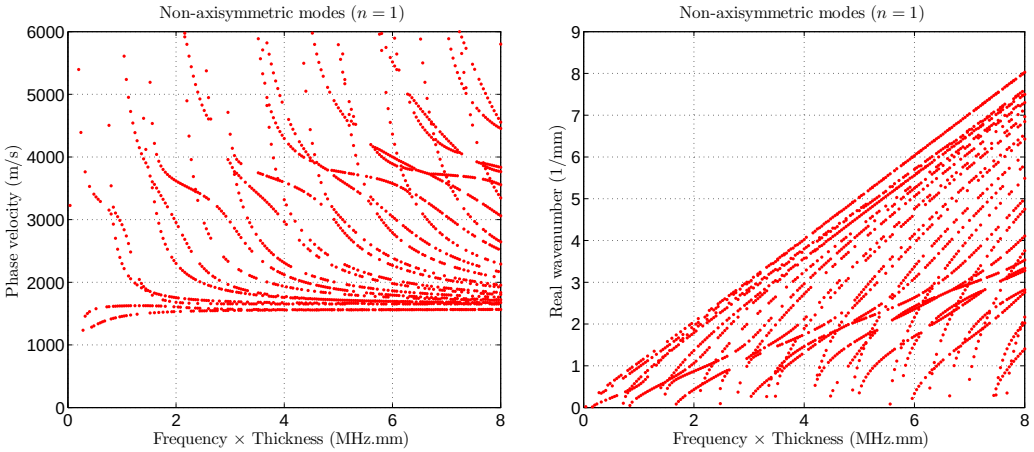

(a) (b)

Figure 4.9: Phase velocity (a) and real wavenumber (b) projections for non-axisymmetric modes $F(1, m)$. $h = 4$ mm, $R_i = 12$ mm.

as a simplified plate model instead of cylinder which is more difficult to analyze. The substitution of a complex system having cylindrical nature like bone by one simplistic system that behave like a plate is a key issue to investigate.

It has been shown that as the inner radius increases and becomes large compared to the wall thickness, the cylinder begin to behave like a plate. In Fig. 4.10, the trend of the phase velocity dispersion curves when increasing inner radius is shown for a homogeneous cylindrical bone waveguide. In these figures only axisymmetric ($n = 0$) and the non-axisymmetric ($n = 1$) modes are plotted. The wall thickness is fixed at 1 mm. Six values of inner radius are investigated (from $R_i = 1$ mm to $R_i = 32$ mm). From these figures it is well shown that the longitudinal modes are trend to the Lamb modes extracted in plate

model having the same thickness. In addition, the effect of curvature (i.e., due to low or higher inner radius) is more perceptible in low frequencies than higher frequencies. (see. Fig. 4.10(a-c)). Indeed, as the frequency increases, the wavelength decreases, as results, the guided waves begin to only percept (or see) the local section of the bone cylinder which can be seen as a plate like, especially with large inner radius (see. Fig. 4.10 (f)). In other words, low frequency will detect the curvature, but high frequency will not. In this model the difference between results derived from plate bone model and cylindrical model are noticeable in frequency-thickness products below 0.6 MHz.mm. From these results, we can deduce that plate model can be used when working with very high frequency with large bone inner radius.

4.5.6 Modes shapes in the waveguide cross-section

As we mentioned previously, guides waves have radial distribution characteristic, known as mode shape. Understand these modes shapes are quite necessary to better understand the behavior of Lamb modes. First we paid our attention on the circumferential displacement over the waveguide cross-section. Next, modes shapes for radial and axial displacements are investigated.

Recall that as describe in the three-dimensional SAFE formulation, the circumferential displacement of the bone cylindrical waveguide is expressed by a complex factor number $\exp(n\theta)$. That is to say, the motion is comprised of $\cos(n\theta)$ and $\sin(n\theta)$ components, where n is the circumferential wavenumber known as the circumferential order. An illustration of the displacement distribution for the first six circumferential order modes are shown in Fig. 4.11(a-f). In general, the circumferential order of most interest in ultrasonic study are low order.

For $n = 0$, ultrasound is radiated very efficiently, where there is no sinusoidal variation of the guided wave around the circumferential cross-section. The corresponding modes are the axially symmetric. Note that the $n = 0$ modes are known as *breathing modes* (or *"modes de respiration"* in French language). Indeed, in such modes, the cylindrical waveguide expands and contracts axisymmetrically as the guided wave propagate.

For the $n = 1$ modes, the cross-section remain undeformed and circular but moves from back and fourth around its normal position. For $n = 2$, the modes is called "*lobar*" mode, where the cross section deforms as a rugby ball (i.e., an oval). As the circumferential order increases, the higher n modes show more complicated displacement with different symmetries around the bone circumference as can be seen in Fig. 4.11. In general, the $n = 0$ and $n = 1$ order modes are the most interests in the context of QUS bone evaluation.

4.5.7 Sensitivity to intra-cortical bone degradation

In this subsection, we explore the feasibility of using guided guides waves to detect cortical alteration (i.e., intracortical loss), which is occur in osteoporosis bone. Fig. 4.12(c) illustrates the degradation of cortical bone *via* a progressive decreasing of bone wall cylindrical thickness. The intact cortical bone is assumed to have 4 mm cylindrical wall thickness. We investigate five values of cortical bone loss (from

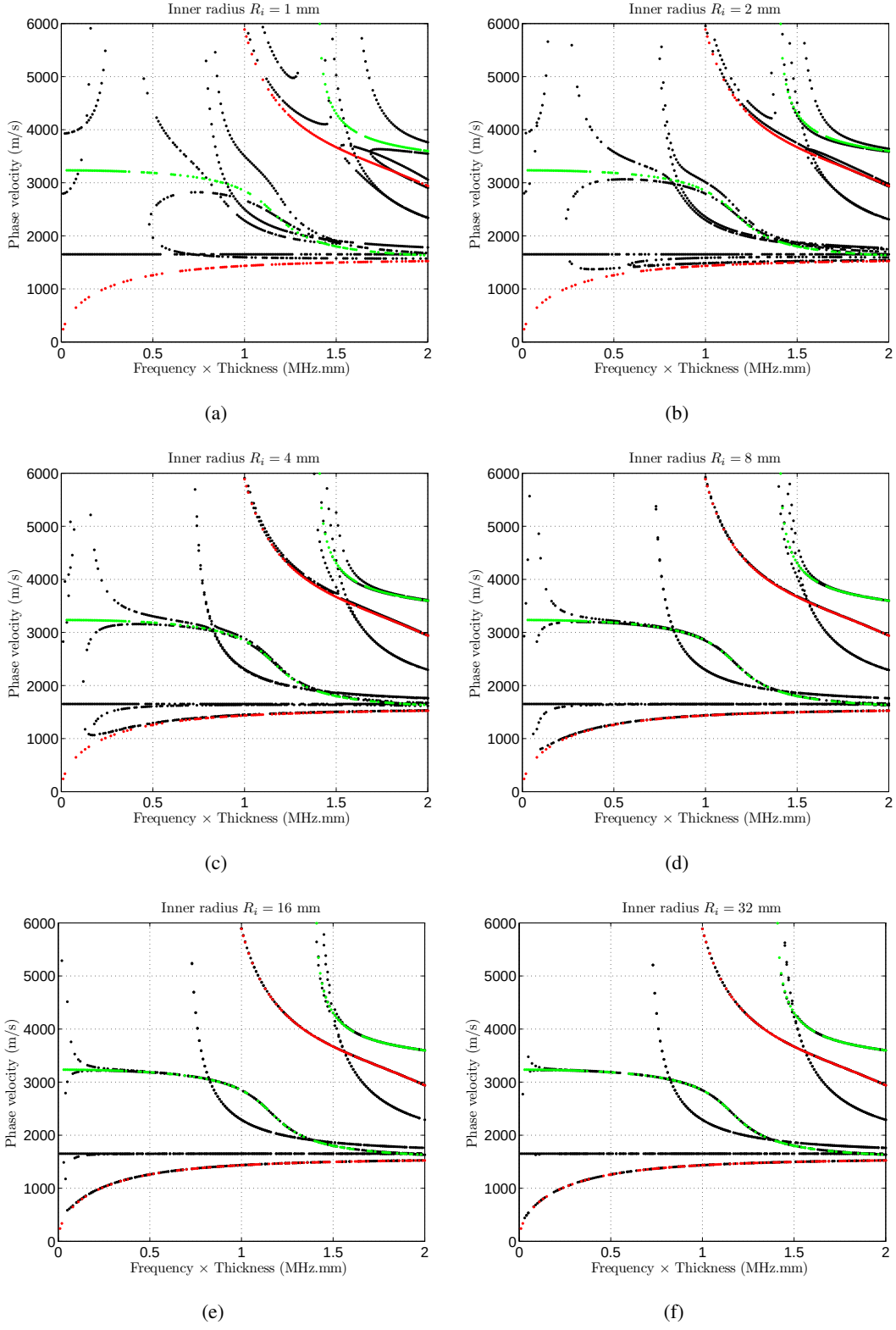

Figure 4.10: The trend of dispersion curves when increasing the inner radius of a 1 mm cortical bone cylinder. The curves in red and green color represent the results obtained with the plate model.

0.5 mm to 2.5 mm loss of bone wall thickness) as illustrated in Fig. 4.12(a). The corresponding phase velocity dispersion curves are plotted in Fig. 4.12(a) and 4.12(b) for $n = 0$ order axisymmetric modes

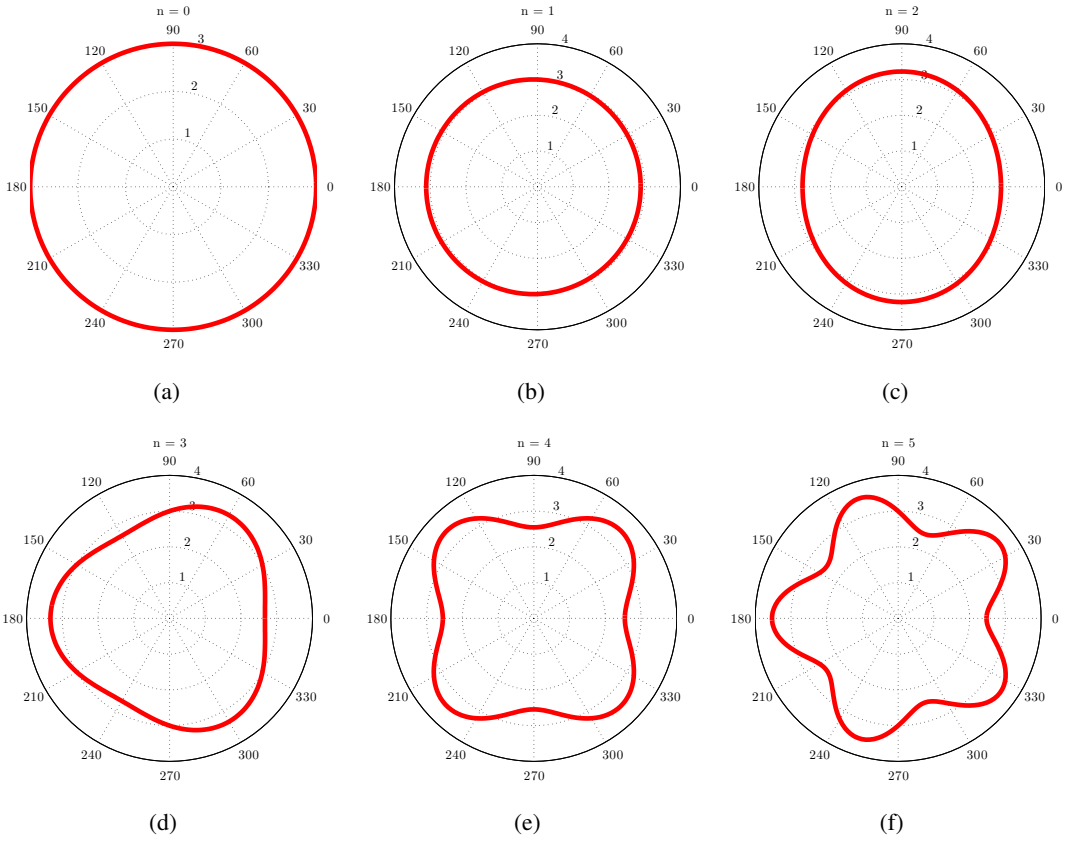

(a) (b) (c)

(d) (e) (f)

Figure 4.11: (Color online) Illustration of the n-th order displacement distribution over the waveguide cross-section.

and $n = 1$ order non-axisymmetric modes, respectively.

The finding show that phase velocity dispersions for axisymmetric as well as non-axisymmetric are sensitive to the cortical loss. This results confirm, observation shown in the 2D model proposed in the previous chapter. Cylindrical guides waves may be suitable for evaluated cortical bone loss in the context of intracortical loss diagnosis.

4.5.8 Fluctuation of phase velocity and axial wavenumber

In this subsection, we investigate the effect of uncertainties on the output random quantities. We paid our attention on the random real wavenumber and phase velocity dispersion curves. We recall that the wavenumber is the first output random quantity to be calculated using the proposed approach. In order to have comprehensible curves, axisymmetric and non-axisymmetric mode are plotted separately in Fig. 4.13 and Fig. 4.14, respectively. A parametric study is performed by changing the dispersion parameter which control the level of fluctuation of the random material properties. Three value of this parameter are explored ($\delta = 0.1$, $\delta = 0.2$ and $\delta = 0.3$) in frequency-thickness products range from 0 to 4 MHz.mm. Probability density functions of the three first flexural modes ($F(1,1)$, $F(1,2)$, $F(1,3)$), the two first longitudinal modes ($L(0,1)$, $L(0,2)$) and the first torsional mode $T(0,1)$ are shown at a fixed

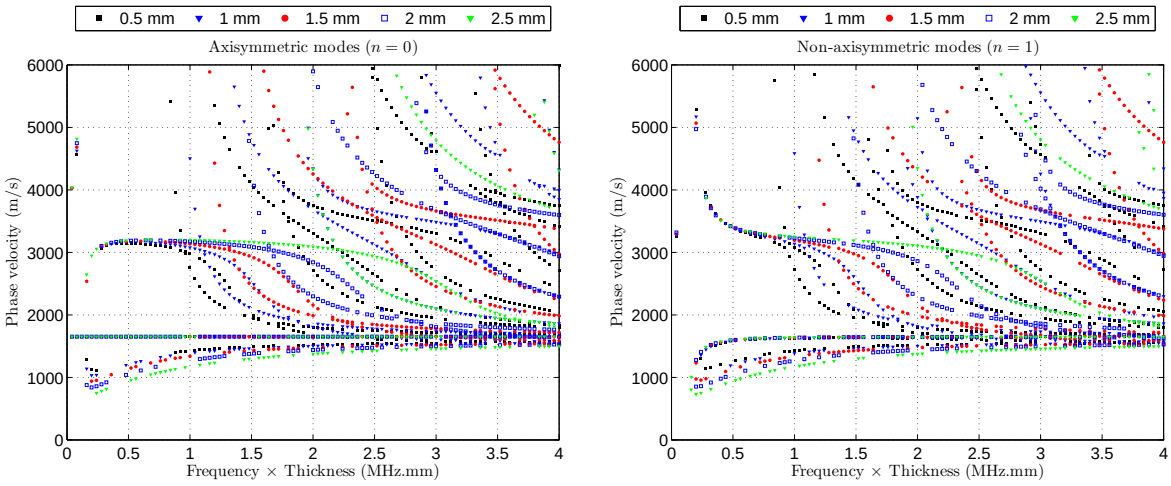

(a) (b)

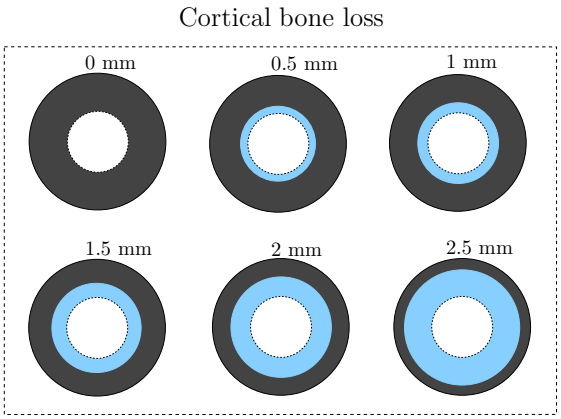

(c)

Figure 4.12: (a) Phase velocity for axisymmetric modes. (b) Phase velocity for non-axisymmetric modes. (c) Schematic illustration of bone cortical loss. The region in light blue color illustrates the lost cortical bone, while the black one is the remaining bone wall thickness.

frequency-thickness product.

We extract all dispersion curves of each realization of the random medium. In Fig. 4.13(a) where axisymmetric mode are plotted, one may notice that dispersion curves are affected by the random properties on cylindrical bone waveguide. The curves in red color marker represent the results obtained by using the deterministic properties. Fig. 4.13(b) is a zoom of Fig. 4.13(a) around 0.2 and 0.6 MHz.mm. Among the three first axisymmetric modes, $L(0,2)$ mode seems to be the more dispersive from probabilistic point of view. The longitudinal mode $L(0,1)$ is the less dispersive in statistical sens. The first torsional mode $T(0,1)$ which is the only non dispersive mode (i.e, there is no dependency with respect to frequency) is here dispersive from probabilistic point of view. To consolidate these observations, the probability density functions of corresponding phase velocities at fixed frequencies are plotted in Fig. 4.13(c) with a low dispersion parmeter when $\delta = 0.1$. From Fig. 4.14, in which non-axisymmetric modes dispersions curves are presented, analogous behavior can be observed. In this case, as the second index m increases,

flexural mode $F(1,m)$ become more dispersive. Thus, $F(1,1)$ mode is the less dispersive flexural mode, at least from a statistical sens. For all axisymmeric modes, as well as non-axisymmetric modes, statistical dispersion increases with the frequencies thickness products (see. Fig. 4.13(b) and 4.14)

Besides, as observed in the two-dimensional plate model (see. the previous chapter), in this three dimensional model, it can be seen that dispersion curves have also complete branches at each random trajectory (i.e., at least a point is captured on each frequency). Such observation confirm that our model can allows to complete the missing branches by predicting an interval in which missing branches should be recovered from the experimental results.

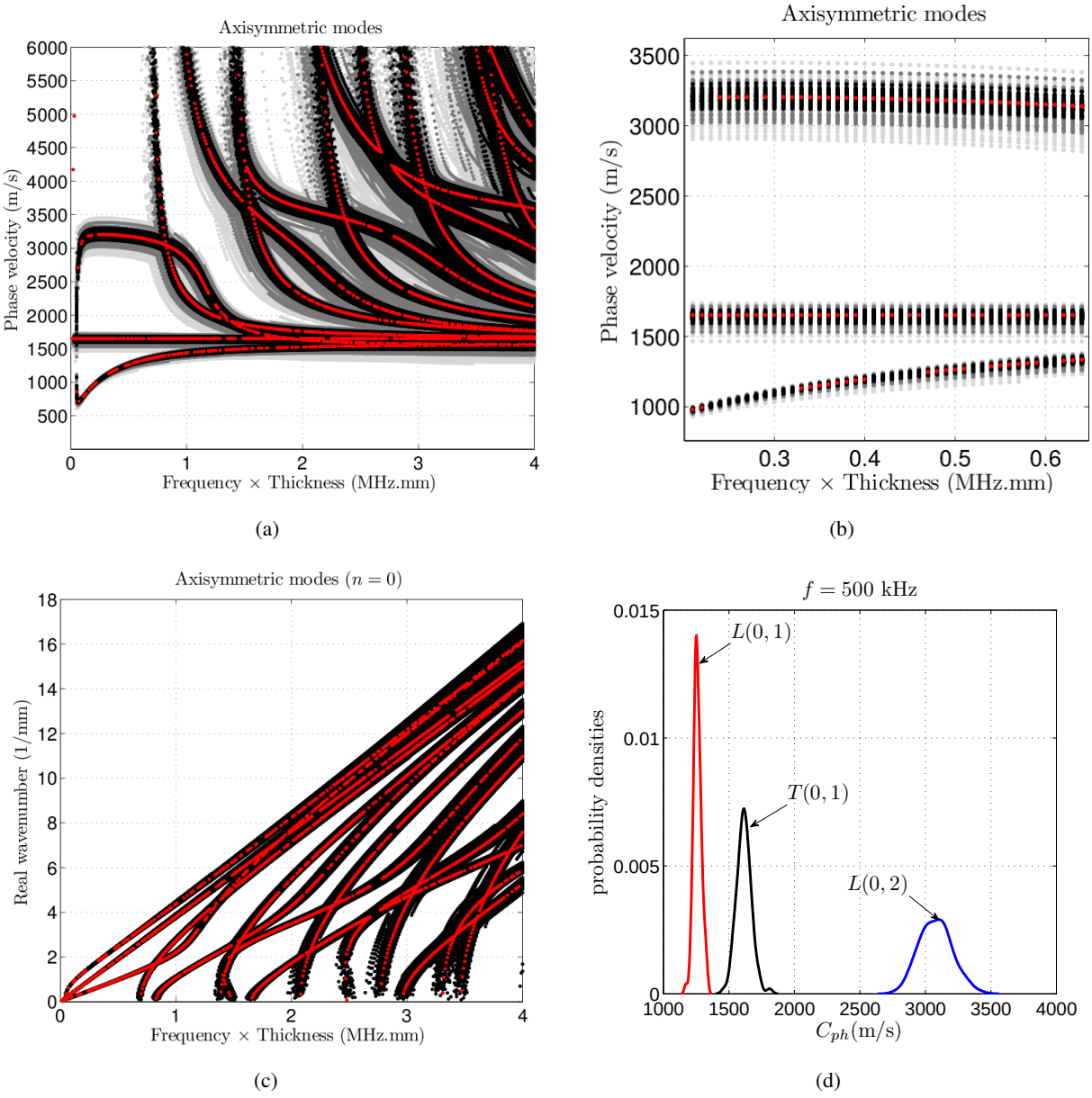

Figure 4.13: (color online) (a) random phase velocity for three value of dispersion parameter (b) Zoom of Fig. 4.13(a). (c) Random real wavenumber for $\delta = 0.1$. (d) Probability density functions of three phase velocity modes. All these curve are plotted with $n = 0$ (i.e., axisymmetric modes).

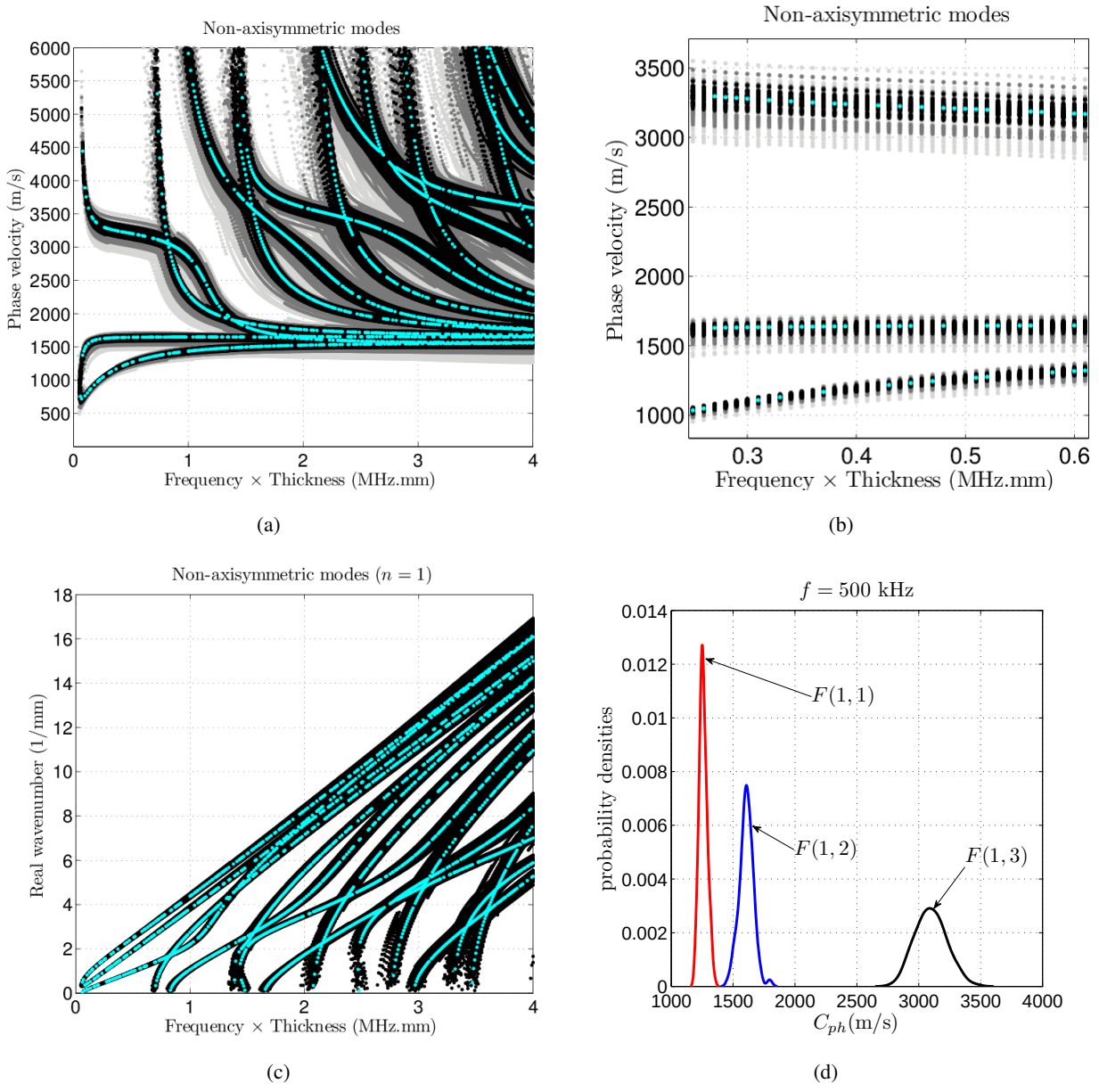

Figure 4.14: (Color online) See caption Fig. 4.13.All these curves are plotted with $n = 1$ (i.e., non-axisymmetric flexural modes)

4.6 Conclusion and perspectives

In this chapter, we presented a three-dimensional numerical model of wave propagation in random cylindrical waveguide mimicking the physical properties of cortical bone. The bone is assumed to be anisotropic and to have random heterogeneity in the radial direction. The application motivation was to give birth to a framework which should be able to take into account both uncertainties on heterogeneity and three-dimensional geometry of bone. We investigate especially the guides waves present in cylinder.

We first validated the proposed three-dimensional formulation against the results calculated using Disperse software. The dispersion curve extracted by our approach agreed well with those calculated *via* Disperse in which the global matrix method is implemented.

Next, we investigated the effect of three-dimensional geometry on the propagation of guides waves. Thus, the effect of curvature is discussed. The trend of cylindrical dispersion curves when increasing the radius of bone cylinder is shown. The convergence of the cylindrical 3D model results to a 2D model results is analyzed. It has been shown that in certain geometric conditions, one can use a two-dimensional plaque model instead of a three-dimensional cylindrical model. The sensitivity of Lamb wave characteristic to an intra-cortical bone degradation is explored. Results show a slight modification on cylindrical dispersion curves with respect to cortical bone loss.

Modes shapes in the cross section are extracted. The lowest axisymmetric modes seem to be more suitable for QUS bone evaluation. The relevance of using the three firsts *Breathing modes* for Quantitative Ultrasound testing is pointed out. The longitudinal mode $L(0,2)$ seems to be more sensitive in statistical sens. Furthermore, the lowest torsional mode $T(0,1)$, which has no dependence with frequency, is now dispersive form probabilistic point of view. This three-dimensional stochastic study shows that, we can used it to help on fitting missing branches on experimentally dispersion curves.

However, one major simplification made in the present model was the assuming of unrealistic boundary condition such free boundary conditions. Thus, it would be more relevant to investigate the influence of soft tissues. Such model should explore the potential of in-vivo testing which may take into account the influence of marrow and as well as soft tissue. This is the subject of the an ongoing study, in which a three-dimensional bone cylinder immersed in fluids is modeled. Reflection/transmission and scattering phenomena of ultrasound waves in the modeled cylindrical structure surrounded by fluids will be investigated in a deterministic and statistical sens.

Appendices

A Explicit forms of the sub-matrices

Box 4.1. Explicit forms of the sub-matrices

$$\mathbf{A}_{rz} = \mathbf{L}_r^T \mathbf{c} \mathbf{L}_z = \begin{bmatrix} c_{15} & c_{14} & c_{13} \\ c_{56} & c_{46} & c_{36} \\ c_{55} & c_{45} & c_{35} \end{bmatrix}, \quad \mathbf{A}_{zz} = \mathbf{L}_z^T \mathbf{c} \mathbf{L}_z = \begin{bmatrix} c_{55} & c_{45} & c_{35} \\ c_{45} & c_{44} & c_{34} \\ c_{35} & c_{34} & c_{33} \end{bmatrix},$$

$$\mathbf{A}_{r0} = \mathbf{L}_r^T \mathbf{c} \mathbf{L}_0 = \begin{bmatrix} c_{12} & -c_{16} & 0 \\ c_{26} & -c_{66} & 0 \\ c_{25} & -c_{56} & 0 \end{bmatrix}, \quad \mathbf{A}_{\theta\theta} = \mathbf{L}_\theta^T \mathbf{c} \mathbf{L}_\theta = \begin{bmatrix} c_{66} & c_{26} & c_{46} \\ c_{26} & c_{22} & c_{24} \\ c_{46} & c_{24} & c_{44} \end{bmatrix},$$

$$\mathbf{A}_{z1} = \mathbf{L}_z^T \mathbf{c} \mathbf{L}_0 = \begin{bmatrix} c_{25} & -c_{56} & 0 \\ c_{24} & -c_{46} & 0 \\ c_{23} & -c_{36} & 0 \end{bmatrix}, \quad \mathbf{A}_{r\theta} = \mathbf{L}_r^T \mathbf{c} \mathbf{L}_\theta, = \begin{bmatrix} c_{16} & c_{12} & c_{14} \\ c_{66} & c_{26} & c_{46} \\ c_{56} & c_{25} & c_{45} \end{bmatrix},$$

$$\mathbf{A}_{\theta z} = \mathbf{L}_\theta^T \mathbf{c} \mathbf{L}_z = \begin{bmatrix} c_{56} & c_{46} & c_{36} \\ c_{25} & c_{24} & c_{23} \\ c_{45} & c_{44} & c_{34} \end{bmatrix}, \quad \mathbf{A}_{rr} = \mathbf{L}_r^T \mathbf{c} \mathbf{L}_r = \begin{bmatrix} c_{11} & c_{16} & c_{15} \\ c_{16} & c_{66} & c_{56} \\ c_{15} & c_{56} & c_{55} \end{bmatrix},$$

$$\mathbf{A}_{\theta 1} = \mathbf{L}_\theta^T \mathbf{c} \mathbf{L}_0 = \begin{bmatrix} c_{26} & -c_{66} & 0 \\ c_{22} & -c_{26} & 0 \\ c_{24} & -c_{46} & 0 \end{bmatrix}, \quad \mathbf{A}_{11} = \mathbf{L}_0^T \mathbf{c} \mathbf{L}_0 = \begin{bmatrix} c_{22} & -c_{26} & 0 \\ -c_{26} & c_{66} & 0 \\ 0 & 0 & 0 \end{bmatrix},$$

$$\mathbf{A}_\rho = \rho \mathbf{I}_d = \begin{bmatrix} \rho & 0 & 0 \\ 0 & \rho & 0 \\ 0 & 0 & \rho \end{bmatrix}.$$

B Strains and stresses in cylindrical coordinates

Box 4.2. Strains and stresses in cylindrical coordinates

Using the notation of Voigt, the Hooke law reads:

$$\mathbf{s} = \mathbf{c}\mathbf{e}, \tag{4.45}$$

where $\mathbf{e}$ and $\mathbf{s}$ are the vectors containing the strain components and the components of the stress tensor $\boldsymbol{\sigma}$, respectively. $\mathbf{c}$ is the matrix containing the components of the anisotropic elasticity tensor.

$$\mathbf{e} = (\epsilon_{rr}, \epsilon_{\theta\theta}, \epsilon_{zz}, 2\epsilon_{\theta z}, 2\epsilon_{rz}, 2\epsilon_{r\theta})^T, \tag{4.46}$$

$$\mathbf{s} = (\sigma_{rr}, \sigma_{\theta\theta}, \sigma_{zz}, \sigma_{\theta z}, \sigma_{rz}, \sigma_{r\theta})^T. \tag{4.47}$$

The strain components are defined as follow:

$$\epsilon_{rr} = \partial_r u_r, \quad \epsilon_{\theta\theta} = \frac{u_r}{r} + \frac{1}{r}\partial_\theta u_\theta, \quad \epsilon_{zz} = \partial_z u_z \quad 2\epsilon_{\theta z} = \partial_z u_\theta + \frac{1}{r}\partial_\theta u_z,$$
$$2\epsilon_{rz} = \partial_z u_r + \partial_r u_z, \quad 2\epsilon_{r\theta} = \frac{1}{r}\partial_\theta u_r + \partial_r u_\theta - \frac{1}{r}u_\theta. \tag{4.48}$$

The strain-displacement relation is given by

$$\mathbf{e} = \mathbf{L}_\epsilon \mathbf{u} \tag{4.49}$$

The operator $\mathbf{L}_\epsilon$ is defined as follows:

$$\mathbf{L}_\epsilon{}^T = \begin{bmatrix} \partial_r & \frac{1}{r} & 0 & 0 & \partial_z & \frac{1}{r}\partial_\theta \\ 0 & \frac{1}{r}\partial_\theta & 0 & \partial_z & 0 & \partial_r - \frac{1}{r} \\ 0 & 0 & \partial_z & \frac{1}{r}\partial_\theta & \partial_r & 0 \end{bmatrix}, \tag{4.50}$$

which can be written in simplified form as

$$\mathbf{L}_\epsilon = \mathbf{L}_r\partial_r + \mathbf{L}_\theta\frac{1}{r}\partial_\theta + \mathbf{L}_z\partial_z + \mathbf{L}_1\frac{1}{r}, \tag{4.51}$$

$$\mathbf{L}_r = \begin{bmatrix} 1 & 0 & 0 \\ 0 & 0 & 0 \\ 0 & 0 & 0 \\ 0 & 0 & 0 \\ 0 & 0 & 1 \\ 0 & 1 & 0 \end{bmatrix}, \quad \mathbf{L}_\theta = \begin{bmatrix} 0 & 0 & 0 \\ 0 & 1 & 0 \\ 0 & 0 & 0 \\ 0 & 0 & 1 \\ 0 & 0 & 0 \\ 1 & 0 & 0 \end{bmatrix}, \quad \mathbf{L}_z = \begin{bmatrix} 0 & 0 & 0 \\ 0 & 0 & 0 \\ 0 & 0 & 1 \\ 0 & 1 & 0 \\ 1 & 0 & 0 \\ 0 & 0 & 0 \end{bmatrix}, \quad \mathbf{L}_1 = \begin{bmatrix} 0 & 0 & 0 \\ 1 & 0 & 0 \\ 0 & 0 & 0 \\ 0 & 0 & 0 \\ 0 & 0 & 0 \\ 0 & -1 & 0 \end{bmatrix}. \tag{4.52}$$

The stresses in radial, azimuthal and longitudinal principal surfaces are

$$\mathbf{s}_{rr} = [\sigma_r, \sigma_{r\theta}, \sigma_{rz}]^T = \mathbf{L}_r^T\sigma, \quad \mathbf{s}_\theta = [\sigma_{r\theta}, \sigma_{\theta\theta}, \sigma_{z\theta}]^T = \mathbf{L}_\theta^T\sigma, \quad \mathbf{s}_z = [\sigma_{rz}, \sigma_{\theta z}, \sigma_{zz}]^T = \mathbf{L}_z^T\sigma. \tag{4.53}$$

$$\rho\ddot{\mathbf{u}} - \mathbf{L}_\sigma^T\mathbf{s} = \mathbf{0}, \quad \forall M \in \Omega^b, \tag{4.54}$$

The operator $\mathbf{L}_\sigma$ in equation (4.3) is defined by:

$$\mathbf{L}_\sigma{}^T = \begin{bmatrix} \partial_r + \frac{1}{r} & -\frac{1}{r} & 0 & 0 & \partial_z & \frac{1}{r}\partial_\theta \\ 0 & \frac{1}{r}\partial_\theta & 0 & \partial_z & 0 & \partial_r + \frac{2}{r} \\ 0 & 0 & \partial_z & \frac{1}{r}\partial_\theta & \partial_r + \frac{1}{r} & 0 \end{bmatrix}, \tag{4.55}$$

$$\mathbf{L}_\sigma = \mathbf{L}_r\partial_r + \mathbf{L}_\theta\frac{1}{r}\partial_\theta + \mathbf{L}_z\partial_z + (\mathbf{L}_r - \mathbf{L}_1)\frac{1}{r}. \tag{4.56}$$

In this model, it is assumed that the physical properties of the solid only depend on r, *i.e.* $\mathbf{c} = \mathbf{c}(r)$.

$$\mathbf{c}(r) = \begin{bmatrix} c_{11} & c_{12} & c_{13} & c_{14} & c_{15} & c_{16} \\ & c_{22} & c_{23} & c_{24} & c_{25} & c_{26} \\ & & c_{33} & c_{34} & c_{35} & c_{36} \\ & \text{Sym} & & c_{44} & c_{45} & c_{46} \\ & & & & c_{55} & c_{56} \\ & & & & & c_{66} \end{bmatrix}. \tag{4.57}$$

Bibliography

A. Abdoulatuf, V.-H. Nguyen, C. Desceliers, and S. Naili. A probabilistic study of the ultrasonic reflection coefficient from cortical bones. *Computer Methods in Biomechanics and Biomedical Engineering*, 18: 1864–1865, 2015.

G. Bal and L. Ryzhik. Time reversal for classical waves in random media. *Comptes Rendus de l'Académie des Sciences - Series I - Mathematics*, 333(11):1041 – 1046, 2001.

C. Baron. Propagation of elastic waves in an anisotropic functionally graded hollow cylinder in vacuum. *Ultrasonics*, 51(2):123 – 130, 2011.

C. Baron. Using the gradient of human cortical bone properties to determine age-related bone changes via ultrasonic guided waves. *Ultrasound in Medicine & Biology*, 38(6):972 – 981, 2012.

K.J. Bathe. *Finite Element Procedures*. Prentice-hall, 1996.

M.A. Ben Souf, O. Bareille, M.N. Ichchou, F. Bouchoucha, and M. Haddar. Waves and energy in random elastic guided media through the stochastic wave finite element method. *Physics Letters A*, 377(37): 2255 – 2264, 2013.

F. Bouchoucha, M.N. Ichchou, and M. Haddar. Guided wave propagation in uncertain elastic media. *Ultrasonics*, 53(2):303 – 312, 2013.

A. Charalambopoulos, L.N. Gergidis, and G. Kartalos. On the gradient elastic wave propagation in cylindrical waveguides with microstructure. *Composites Part B: Engineering*, 43(6):2613 – 2627, 2012. Homogenization and Micromechanics of Smart and Multifunctional Materials.

J. Chen and Z. Su. On ultrasound waves guided by bones with coupled soft tissues: A mechanism study and *in vitro* calibration. *Ultrasonics*, 54(5):1186 – 1196, 2014.

C. Chree. The equations of an isotropic elastic solid in polar and cylindrical coordinates, their solutions and applications. *Transactions of the Cambridge Philosophical Society*, 14:250 – 369, 1889.

S.C. Cowin. *Bone mechanics handbook*. CRC Press, Boca Raton, FL, 2nd edition, 2001.

C. Desceliers, C. Soize, Q. Grimal, M. Talmant, and S. Naili. Identification of an anisotropic elasticity tensor for an elastic layer using transient wave propagation in a fluid-solid multilayer. model with uncertainties and experiments. *The Journal of the Acoustical Society of America*, 125(4):2027–2034, 2009.

C. Desceliers, C. Soize, S. Naili, and G. Haiat. Probabilistic model of the human cortical bone with mechanical alterations in ultrasonic range. *Mechanical Systems and Signal Processing*, 32:170 – 177, 2012.

X.N. Dong and X.E. Guo. The dependence of transversaly isotropic elasticity of human femoral cortical bone on porosity. *Journal of Biomechanics*, 37:1281–1287, 2004.

A.T. Fabro, N.S. Ferguson, T. Jain, R. Halkyard, and B.R. Mace. Wave propagation in one-dimensional waveguides with slowly varying random spatially correlated variability. *Journal of Sound and Vibration*, 343:20 – 48, 2015.

D.C. Gazis. Three dimensional investigation of the propagation of waves in hollow circular cylinders. i. analytical foundation. *The Journal of the Acoustical Society of America*, 31(5):568–573, 1959.

R.P. Gilbert, P. Guyenne, and J. Li. A viscoelastic model for random ultrasound propagation in cancellous bone. *Computers & Mathematics with Applications*, 66(6):943 – 964, 2013.

C. Gomez. *Wave propagation and time reversal in random waveguides.* PhD thesis, Université Paris-Diderot - Paris VII, December 2009.

M.N. Ichchou, F. Bouchoucha, M.A. Ben Souf, O. Dessombz, and M. Haddar. Stochastic wave finite element for random periodic media through first-order perturbation. *Computer Methods in Applied Mechanics and Engineering*, 200(4):2805 – 2813, 2011.

E.T. Jaynes. Information theory and statistical mechanics. *The Physical Review*, 106(4):620–630, 1957a.

E.T. Jaynes. Information theory and statistical mechanics. II. *The Physical Review*, 108(2):171–190, 1957b.

K.I. Lee and S.W. Yoon. Propagation of time-reversed lamb waves in acrylic cylindrical tubes as cortical-bone-mimicking phantoms. *Applied Acoustics*, 112:10 – 13, 2016.

F. Lefebvre, Y. Deblock, P. Campistron, D. Ahite, and J.J. Fabre. Development of a new ultrasonic technique for bone and biomaterials in vitro characterization. *Journal of Biomedical Materials Research*, 63(4):441–446, 2002.

E. Lunéville and J.-F. Mercier. Finite element simulations of multiple scattering in acoustic waveguides. *Waves in Random and Complex Media*, 20(4):615–633, 2010.

K. Macocco, Q. Grimal, S. Naili, and C. Soize. Elastoacoustic model with uncertain mechanical properties for ultrasonic wave velocity prediction: Application to cortical bone evaluation. *The Journal of the Acoustical Society of America*, 119(2):729–740, 2006.

M.L. Mehta. *Random Matrices*. Academic Press, 2004.

F. Mézière, M. Muller, B. Dobigny, E. Bossy, and A. Derode. Simulations of ultrasound propagation in random arrangements of elliptic scatterers: Occurrence of two longitudinal waves. *The Journal of the Acoustical Society of America*, 133(2):643–652, 2013.

S. Naili, V.-H. Nguyen, M.-B Vu, C. Desceliers, and C. Soize. Modeling of transient wave propagation in a heterogeneous solid layer coupled with fluid: Application to long bones. *The Journal of the Acoustical Society of America*, 137(2):668–678, 2015.

P. Nauleau. *Vers la mesure d'ondes circonférentielles guidées par la coque corticale du col du fémur*. PhD thesis, UPMC, 2013.

M.T. Nguyen. *Multiscale identification of stochastic apparent elasticity field of heterogeneous microstructures : application to a biological tissue*. Theses, Université Paris-Est, October 2013.

V.-H. Nguyen, T. Lemaire, and S. Naili. Poroelastic behaviour of cortical bone under harmonic axial loading: A finite element study at the osteonal scale. *Medical Engineering & Physics*, 32(4):384 – 390, 2010.

V.-H. Nguyen, A. Abdoulatuf, C. Desceliers, and S. Naili. A probabilistic study of reflection and transmission coefficients of random anisotropic elastic plates. *Wave Motion*, 64:103 – 118, 2016.

H. Nishino, S. Takashina, F. Uchida, M. Takemoto, and K. Ono. Modal analysis of hollow cylindrical guided waves and applications. *Japanese Journal of Applied Physics*, 40(1R):364, 2001.

J.O. Parra, C.L. Hackert, R. Ababou, and M.J. Sablik. Dispersion and attenuation of acoustic waves in randomly heterogeneous media. *Journal of Applied Geophysics*, 42(2):99 – 115, 1999.

J. Pochlammer. "uber die fortpflanzungsgeschwindigkeinten kleiner schwingungen in einem unbergrenzien isotropen kreiscylinder" : On the propagation speed of small oscillations in a non-limit isotropic circular cylinder. *J fur reine und angewandte Math*, 81:324 – 336, 1876.

V.C. Protopappas, I.C. Kourtis, L.C. Kourtis, K.N. Malizos, C.V. Massalas, and D.I. Fotiadis. Three-dimensional finite element modeling of guided ultrasound wave propagation in intact and healing long bones. *The Journal of the Acoustical Society of America*, 121(6):3907–3921, 2007.

C. Soize. Non-gaussian positive-definite matrix-valued random fields for elliptic stochastic partial differential operators. *Computer Methods in Applied Mechanics and Engineering*, 195(1-3):26–64, 2006.

L. Wang, S.P. Fritton, S.C. Cowin, and S. Weinbaum. Fluid pressure relaxation depends upon osteonal microstructure: modeling an oscillatory bending experiment. *Journal of Biomechanics*, 32:663–672, 1999.

Chapter 5

Conclusion and perspectives

"Quiconque prétend s'ériger en juge de la vérité et du savoir s'expose à périr sous les éclats de rire des dieux puisque nous ignorons comment sont réellement les choses et que nous n'en connaissons que la représentation que nous en faisons.."

[Albert Einstein.]

Summary

The purpose of this thesis is the development of modeling tools which can be used to study ultrasound waves propagation in bone tissue. The idea is to seek better understanding and fully investigation of all of the phenomena involved in the ultrasound guided waves in the cortical bone. The work is motivated by the increasing needs for monitoring the human bone health status by using quantitative ultrasound (QUS) methods, for example to diagnosis bone decease such as osteoporosis. Such methods are deemed to be a promising good candidate for quantitative bone evaluation. However, due to the complexity of bone structure, the comprehension of guided waves propagation characteristics in such medium is challenge.

Chapter 2 investigated the reflection and transmission phenomena of ultrasound for a bi-dimensional three-layer model consisting of a cortical bone solid layer immersed in two fluids (representing soft tissues and marrow). The bone material properties are randomly varied in the thickness direction. The model is based on semi-analytical finite elements (SAFE) method, which efficiently provides the modeling of structures with continuously varying material properties as well as multilayered structures immersed in a fluid. A probabilistic model based on the maximum of entropy principle has been used for generating the random elasticity tensor. In the proposed approach , the reflection and transmission coefficients are estimated and statistically studied using Monte-Carlo simulation. The findings show that the angle of incidence has an influence on the estimation of the coefficients in statistical sense. Both coefficients are more sensitive to the dispersion parameter which control the random fluctuation level of bone material properties. In addition, it has been shown that the effect of random properties is more important for higher frequency. Finally, the obtained confidence regions which strongly sensitive to the angle of incidence, can

be helpful for the development of strategy in the experimental method measurement of the coefficients of interest. Next, we introduced a gradient of material properties on the bone thickness direction. The effects of this new profile of properties are investigated in statistical sense. The results show drastic changes on the coefficients of interest. Thus the proposed approach can be useful for the determination of the parameter of this gradient of properties.

Chapter 3 described the modal characteristics of ultrasound wave propagating in complexes structures such cortical bone. Precisely, we studied the dispersion of Lamb wave in a bi-dimensional plate (representing cortical bone) having random heterogeneity in the thickness. To do so, the nonlinear problem (with respect to wavenumber) was transformed in a linear eigenvalue problem. An approach based on SAFE method is used to extract the dispersion relations. A validation of the formulation is performed. There is a good agreement between the proposed approach and the validation results for all the cases examined (and by comparing with results obtained by disperse). We discussed the effects of random heterogeneity on the dispersion curves and displacement distribution (mode shapes). The findings show that by introducing uncertainties in bone material properties (random heterogeneity), the SAFE approach can extract relevant dispersion curves (with quasi-completes branches). Thus the proposed model may be useful to overcome lack on experimental data. Moreover, a parametric study is performed highlighting the relevancy of the fundamental A_0 and S_0 modes in the context of ultrasound bone evaluation. It is shown that these modes are more dispersive in statistical sense, and are sensitive on thickness change. Finally, the parametric study shows that such model seems to be a good candidate for the bone thickness evaluation for younger as well as elderly patients.

In chapter 4, a cylindrical model is proposed, in order to explore the effect of the bone three-dimensional geometry. An extension of the model developed in the previous chapter is proposed. The motivation was to propose a framework for analysis of Lamb waves characteristics in a bone cylindrical waveguide having random properties in the radial direction. The effect of curvature is investigated and the sensitivity of Lamb waves characteristic to intra-cortical bone degradation is observed. Modes shapes are extracted. A parametric study is performed, and the effects of bone mechanical and geometrical characteristics on these output quantities are discussed. Thus, the influence of cylindrical geometry as well as material properties are investigated. The results show that the three first axi-symmetric modes may be relevant for quantitative ultrasound testing. The longitudinal mode $L(0,2)$ is more sensitive from probabilistic point of view. Moreover, the lowest torsional mode $T(0,1)$, which is no dispersive with respect frequency, is henceforth dispersive in a statistical sense. The proposed three-dimensional stochastic model may be more suitable on fitting the missing branches on experimentally dispersion curves.

In conclusion, the work presented in this manuscript forms a substantial amount of original research which contributes to the understanding of phenomena involved in the propagation of ultrasound waves in cortical bone tissue.

Suggestions for future work

Based on the understanding of ultrasound guided waves characteristics in the quantitative ultrasound bone evaluation, some possible future directions are listed in the following.

i. **Work in progress (not presented in this manuscript)**. In an ongoing study [P2], we explore the development of a numerical model capable of combining all the characteristics studied in the models developed in this thesis. As discussed in this manuscript, ultrasound waves propagation in cortical bone can be affected by many factors (geometrical and mechanical) related to the bone structure. The aim of this ongoing study is to introduce a single numerical framework for modeling ultrasound wave propagation in cortical bone by taking into account all the characteristics previously studied by different models. Strictly speaking, the idea is to develop a model for propagation of ultrasonic waves in random, heterogeneous, anisotropic and three-dimensional cortical bone having functionally graded material properties, coupling with soft tissue and marrow. Therefore, effort has been spent for development of semi-analytical finite element procedure for ultrasound propagation in solid cylinder coupled with fluid.

   In general, the fluid-solid coupling in the cylindrical model makes the mathematical study much more difficult in comparison with the case of a solid cylinder immersed in vacuum. In this study, the cortical bone is modeled by an anisotropic solid cylinder filled with fluid (representing the marrow) and immersed in another fluid (representing the tissues soft). The cortical bone cylinder is assumed to have random heterogeneity on its radial direction, but remains homogeneous on its longitudinal direction. The propagation of ultrasound wave in both fluids is characterized by the pressure (pressure waves), which is expressed explicitly through the Bessel and Hankel functions for modeling outgoing and incoming waves from the cylinder. In the bone cylinder, waves propagation is mainly related to the displacement (elastic waves). A procedure based on the SAFE method is developed, allowing to propose a formulation of the coupling (between the cylinder and the fluid) and to extract the solutions (pressures and displacements). Next, ultrasound wave scattering phenomenon on contact of bone cylinder is investigated in deterministic and probabilistic point of view. The effect of numerical parameters, material properties, bone geometry and random heterogeneity is being discussed. Finally, a study is initiated in order to explore estimation of the reflection and transmission coefficients in terms of power.

ii. Validate the numerical models with experimental measures. For example, by confirming the relevancy of using the proposed stochastic models to predict missing branches on experimental dispersion curves.

iii. Study the inverse problem for the deterministic model as well as the stochastic one. This would make it possible to estimate dispersion parameters and obtain some material or geometric properties of the bone tissue.

iv. Now that the modeling tools have been developed and validated, their potential application on quantitative ultrasound bone evaluation can be rapidly evaluated by measures.

Appendix A

Summary of research and teaching activities

A.1 Articles in refereed scientific journals

[A1] **A. Abdoulatuf**, V.-H. Nguyen, C. Desceliers, S. Naili. A numerical study of ultrasonic response of random cortical bone plates. *Vietnam Journal of Mechanics*, 39 (1), 79-95, 2017.

[A2] V.-H. Nguyen, **A. Abdoulatuf**, C. Desceliers, S. Naili. A probabilistic study of reflection and transmission coefficients of random anisotropic elastic plates. *Wave Motion*, 64:103 – 118, 2016.

[A3] **A. Abdoulatuf**, V.-H. Nguyen, C. Desceliers, S. Naili. A probabilistic study of the ultrasonic reflection coefficient from cortical bones. *Computer Methods in Biomechanics and Biomedical Engineering*, 18:1864–1865, 2015.

A.2 Conference Proceedings

[C1] **A. Abdoulatuf**, V.-H. Nguyen, C. Desceliers, S. Naili. A numerical study of stochastic ultrasonic response of cortical bone plates. In *13th International Symposium on Computer Methods in Biomechanics and Biomedical Engineering*, Montréal, Canada, September 1-5, 2015.

[C2] **A. Abdoulatuf**, V.-H. Nguyen, C. Desceliers, S. Naili. A probabilistic study of the ultrasonic reflection coefficient from cortical bones. In *40éme Congrès de la Société de Biomécanique*, Paris, France, October 28-30, 2015.

A.3 Courses taught at university

[U1] **Instrumentations sur les ondes ultrasonores et lumineuses**, Licence 2 "BioSanté et CB". Université Paris-Est Créteil, Faculté des Sciences et Technologie, 2016-2017: TP, 9h.
Collaboration avec *Mme. Pascale CHELIN et M. Mokhtar RAY*.

[U2] **Introduction à la Physique**, Licence 1 "Sciences Pour l'Ingénieur". Université Paris-Est Créteil, Faculté des Sciences et Technologie, 2016-2017: 30h/TD, 27h/TP.
Collaboration avec *Mme. Karine PROVOST et plus de 12 enseignants-chercheurs*.

[U3] **Optique géométrique**, Licence 1 "Double licence de Mathématiques et Physique". Université Paris-Est Créteil, Faculté des Sciences et Technologie, 2016-2017: TP, 12h.
Collaboration avec *M. Jacques MOSCOVICI et M. Mokhtar RAY*.

[U4] **Initiation à l'algorithmique et outils informatiques**, Licence 1 "MISIPC". Université Paris-Est Créteil, Faculté des Sciences et Technologie, 2015-2017: TP, 117h.
Collaboration avec *M. Gilles LEBLANC*.

[U5] **Introduction à la Physique**, Licence 1 "Mathématiques et Informatique". Université Paris-Est Créteil, Faculté des Sciences et Technologie, 2013-2015: 50h/TD, 12h/TP.
Collaboration avec *M. Lotfi BESSAIS et M. Abderrahim AYADIM*.

[U6] **Outils informatiques**, Licence 1 "MISIPC". Université Paris-Est Créteil, Faculté des Sciences et Technologie, 2013-2015: TP, 45h.
Collaboration avec *M. Gilles LEBLANC*.

A.4 Papers in preparation for publication

Submitted articles

[S1] **A. Abdoulatuf**, V.-H. Nguyen, C. Desceliers, S. Naili. Dispersion of lamb waves in anisotropic random plates: Application to cortical bone tissues diagnosis. *Philosophical Transactions of the Royal Society A : Mathematical, Physical and Engineering Sciences*, (submitted).

Articles in progress

[P1] **A. Abdoulatuf**, V.-H. Nguyen, C. Desceliers, S. Naili. On ultrasound waves in cylindrical waveguides physically mimicking bones: From deterministic to stochastic three-dimensional model, application to cortical bone diagnosis.

[P2] **A. Abdoulatuf**, V.-H. Nguyen, C. Desceliers, S. Naili. Propagation of ultrasonics waves in a random anisotropic bone cylinder coupled with fluids: study of scattering phenomenon.

[P3] **A. Abdoulatuf**, V.-H. Nguyen, C. Desceliers, S. Naili. Reflection and transmission of ultrasonic waves from an anisotropic functionally-graded random plate: Application to characterization of cortical bones.

List of Figures

List of Tables

Index

U

Union des Comores

Unité - Solidarité - Développement

RÉSUMÉ : Dans ce travail de thèse, nous nous sommes intéressés à la modélisation et la simulation de la propagation d'ondes ultrasonores dans l'os cortical. Plus précisément, nous avons étudié et analysé la technique dite des ultrasons quantitatifs (Quantitative Ultrasound, QUS) pour l'évaluation de la qualité du tissu osseux. Il s'agit d'une technique émergente dont l'application aux tissus osseux suscite un intérêt particulier dans la communauté scientifique. Le tissu osseux étant un tissu vivant, il est sujet au vieillissement et à divers pathologies parmi lesquelles on peut citer ostéoporose, ostéomalacie, ostéoporomalacie, ou encore, la maladie dite de Paget. Pour accompagner les soins à prodiguer au tissu osseux, une surveillance de sa qualité s'avère indispensable. Dans ce contexte, les méthodes ultrasonores sont réputées être intéressantes, de par leurs caractères non-invasif, peu coûteux, portable et non-ionisant. Cependant, utiliser des ultrasons dans le cadre de la caractérisation du tissu osseux, suppose une compréhension profonde des différents phénomènes physiques mis en jeu lors de leur propagation. Dans cette optique, notre travail est développé dans la thématique de la modélisation dédiée à la propagation des ondes ultrasonores dans des guides d'ondes multidimensionnels, hétérogènes, anisotropes, et composés de matériaux dont l'hétérogénéité peut être qualifiée d'aléatoire. Une des originalités de cette thèse concerne l'étude des coefficients de réflexion et de transmission et des courbes de dispersion en présence d'incertitudes dues aux propriétés matérielles. Dans une première partie, nous étudions les phénomènes de réflexion/transmission *via* un modèle tri-couches bidimensionnels prenant en compte les tissus mous et l'hétérogénéité aléatoire du tissu osseux. Nous avons pu analyser l'impact de ces caractéristiques sur les coefficients de réflexion et de transmission. Un gradient de propriétés matérielles de l'os est introduit, et son impact sur les coefficients d'intérêt est examiné. L'aspect modal des ondes est exploré, en étudiant la dispersion des ondes de Lamb. Les résultats obtenus dans une configuration géométrique bidimensionnelle ont permis de discuter l'influence des divers paramètres, en terme de propriétés mécaniques et/ou géométriques, sur la propagation des ondes ultrasonores dans le tissu cortical. Dans une deuxième partie, le modèle est étendu pour une configuration géométrique cylindrique. La discussion est menée afin d'analyser l'influence de la géométrie tridimensionnelle de l'os sur les phénomènes de propagation.

Mots-clés : *ondes ultrasonores, coefficients de réflexion/transmission, méthode semi-analytique des éléments finis, os cortical, ondes de Lamb, hétérogénéité, anisotropie, gradient de propriétés, propriétés aléatoires, guide d'onde.*

ABSTRACT : In this thesis, we are interested in the modeling and simulation of the propagation of ultrasonic waves in the cortical bone. Precisely, we have studied and analyzed the Quantitative Ultrasound (QUS) technique for the evaluation of the quality of bone tissue. It is an emerging technique those the application to bone tissue arouses particular interest in the scientific community. Since bone tissue is a living tissue, it is subject to aging and various pathologies, such osteoporosis, osteomalacia, osteoporomalacia, or the so-called Paget disease. To assist in therapeutic follow-up of the bone, monitoring of quality of bone tissue is essential. In this context, methods based on QUS technique are deemed to be interesting, due of their non-invasive, inexpensive, portable and non-ionizing characteristics. However, use the ultrasound in the context of characterization of bone tissue, requires a deep understanding of the different physical phenomena involved in their propagation. In this perspective, our work is developed in the modeling theme dedicated to the propagation of ultrasonic waves in multidimensional, heterogeneous, anisotropic waveguides, constituted of materials whose heterogeneity can be qualified as random. One of the originalities of this thesis concerns the study of the reflection and transmission coefficients and the dispersion curves in the presence of uncertainties in the material properties. In a first part, we study the reflection/transmission phenomena *via* a two-dimensional tri-layer model taking into account the soft tissues and the random heterogeneity of the bone tissue. We analyzed the impact of these characteristics on the reflection and transmission coefficients. A gradient of material properties is introduced, and its effect on the coefficients of interest is examined. The modal aspect of the waves is explored, by studying the dispersion of Lamb waves. The results obtained in a two-dimensional geometrical configuration made it possible to discuss the influence of the various parameters, in terms of mechanical and/or geometric properties, on the propagation of the ultrasonic waves in the cortical tissue. In a second part, the proposed model is extended for a cylindrical geometric configuration. The discussion is carried out in order to analyze the influence of the three-dimensional geometry of the bone on the phenomena of propagation.

Keywords : *ultrasonic waves, reflection/transmission coefficients, semi-analytical finite element method, cortical bone, Lamb waves, heterogeneous, anisotropic, gradient of properties, random properties, waveguide.*

Antoisse ABDOULATUF
Laboratoire Modélisation et Simulation Multi Echelle, MSME UMR 8208 CNRS, Université Paris-Est,
61, avenue du Général de Gaulle, 94010 Créteil Cedex FRANCE
Mél. : antoisse.abdoulatuf@univ-paris-est.fr